AD/A-004 218

BALLISTIC MISSILE PROPELLANT EVALUATION TEST MOTOR SYSTEM (SUPER BATES)

W. A. Stephen, et al

United Technology Center

Prepared for:

Air Force Rocket Propulsion Laboratory

25 November 1974

Unclassified
SECURITY CLASSIFICATION OF THIS PAGE (When Data Entered)

AD/A004218

REPORT DOCUMENTATION PAGE

READ INSTRUCTIONS BEFORE COMPLETING FORM

1. REPORT NUMBER: AFRPL-TR-74-70	2. GOVT ACCESSION NO.
3. RECIPIENT'S CATALOG NUMBER	
4. TITLE (and Subtitle): Ballistic Missile Propellant Evaluation Test Motor System (Super BATES)	5. TYPE OF REPORT & PERIOD COVERED: Final Report 1 April 74 to 30 Sep 74
6. PERFORMING ORG. REPORT NUMBER	
7. AUTHOR(s): W. A. Stephen, T. C. Warren, J. M. Humphrey	8. CONTRACT OR GRANT NUMBER(s): F04611-74-C-0022
9. PERFORMING ORGANIZATION NAME AND ADDRESS: United Technology Center, 1050 E. Arques Avenue, Sunnyvale, Calif. 94088	10. PROGRAM ELEMENT, PROJECT, TASK AREA & WORK UNIT NUMBERS: JON 305908 WM
11. CONTROLLING OFFICE NAME AND ADDRESS: Air Force Rocket Propulsion Laboratory, Edwards Air Force Base, Calif. 93523	12. REPORT DATE: 25 Nov 1974
	13. NUMBER OF PAGES: ~~218~~ 219
14. MONITORING AGENCY NAME & ADDRESS (if different from Controlling Office)	15. SECURITY CLASS. (of this report): UNCLASSIFIED
	15a. DECLASSIFICATION/DOWNGRADING SCHEDULE

16. DISTRIBUTION STATEMENT (of this Report)

Approved for public release: Distribution unlimited.

17. DISTRIBUTION STATEMENT (of the abstract entered in Block 20, if different from Report)

18. SUPPLEMENTARY NOTES

19. KEY WORDS (Continue on reverse side if necessary and identify by block number)

Super BATES, Ballistic Missile, Propellant, Evaluation Test Motor, Thrust Measurement System, Tradeoff Study

20. ABSTRACT (Continue on reverse side if necessary and identify by block number)

A two phase program was conducted to define requirements and to prepare a preliminary design of a test motor system that will accurately and economically simulate the chamber environments of present and future large solid propellant rocket motors. A segmented motor configuration with 28-in. outside diameter case bonded propellant grains was selected. The nominal grain configuration is an internal burning cylinder with both ends burning. The preliminary design uses UTP-18,803 as the control propellant, operates at 1,000 psi chamber

DD FORM 1 JAN 73 1473 EDITION OF 1 NOV 65 IS OBSOLETE

(Unclassified)
SECURITY CLASSIFICATION OF THIS PAGE (When Data Entered)

20. Abstract

pressure, and has an 8-in-diameter nozzle throat. This baseline motor consists of two 60-in.-long segments and one 30-in. segment. Both submerged and conventional nozzle designs were prepared. Designs of a 0 to 150,000 lb single component thrust stand, and handling and process tooling were also prepared.

SUMMARY

A trade study was conducted to accurately and economically simulate the chamber environments of present and future large solid propellant rocket motors. During the study the acceptable ranges of motor configuration and interna ballistic parameters over which the Super BATES motor is capable of operating were defined.

This study resulted in selection of a segmented motor configuration with case bonded propellant grains. The nominal grain configuration is an internal burning cylinder with both ends burning. The nominal grain for each segment is 60-in. long with an outside diameter of 28 in. A 30-in.-long grain segment is also incorporated to permit flexibility over a range of grain lengths (corresponding to one-half to three segments) without introducing exorbitant heat losses. This configuration results in a motor with desirable pressure neutrality characteristics. The maximum pressure variation over the future range of operating conditions will average less than ±5% from the mean pressure over the entire burning range.

A preliminary design was generated using UTC propellant formulation UTP-18,803 as the control propellant. This propellant has a burning rate of 0.43 in./sec at 1,000 psi. This baseline motor, with an 8-in. diameter throat has a mass flow rate of 317 lb/sec at 1,000 psi; it consists of two 60-in.-long segments and one, half-length (30-in.) segment. The propellant web thickness will be 2.6 in.

Both submerged and conventional nozzles were designed for the motor. The case segments are joined together with individual clevis H-rings using a pinned joint in double shear. The same joint configuration is used to pin the segments to the closures. In this approach a low cost pipe is used for the case segments; this permits case bonding of the propellant instead of the more complicated cartridge loading approach because motor case segment fabrication costs are comparable to cartridge costs. The motor segments will be shipped to the propellant supplier for refurbishing and processing.

The motor incorporates a burst diaphragm system to protect the motor and thrust stand in the event of motor overpressurization. This pressure relief system is installed in the motor forward closure and is designed to vent combustion gases through the forward closure in a radial direction. This precludes damage to the load cells and thrust stand.

The thrust stand preliminary design is a single component, horizontal system capable of measuring axial thrust in the ranges of 0 to 50,000 lb, 0 to 100,000 lb, and 0 to 150,000 lb. The stand incorporates a deadweight calibrator and has a combined thrust measurement accuracy of ±0.15% over the full range.

The motor is designed for vertical assembly on the test pad adjacent to the thrust stand. Preliminary tooling designs have been prepared for motor assembly and for rotating the motor from the vertical position to the horizontal position for transporting to the horizontal test stand. Designs have also been prepared for process tooling and shipping containers.

The technical effort of this program was conducted between 1 April and 30 September 1974.

CONTENTS

ILLUSTRATIONS

ILLUSTRATIONS (Continued)

ILLUSTRATIONS (Continued)

TABLES

1.0 INTRODUCTION

The evaluation of solid rocket propellants for applications to ballistic missile or large solid motors is a difficult problem in the solid rocket motor industry. Scaleup of data from small test motors is undesirable because of the many large performance corrections which are necessary. Computer program approximations of performance are inaccurate because of limited knowledge of combustion and loss mechanisms. A full-scale prototype test motor is the best approach; however, evaluation of the actual system is generally prohibitive due to cost and schedule.

Propellants specifically formulated for large motor applications are currently being developed. A reusable test motor is not available to permit a full-scale evaluation of these propellants. A program was conducted to analyze the requirements for such a motor, and preliminary motor and thrust stand designs were generated.

2.0 OBJECTIVES

This program was divided into two tasks: (1) tradeoff analysis, and (2) preliminary design.

The objective of the task 1 tradeoff analysis was to identify the ranges of motor configuration and internal ballistic parameters over which the test motor must operate to adequately and economically simulate all large solid propellant motor chamber environments.

The objective of the second task was to produce a preliminary design of test motor, thrust stand, and casting and handling hardware.

3.0 SUPER BATES TASK 1 TRADE STUDY

3.1 Motor

3.1.1 System Trade Study

The objective of the system trade study was to identify the ranges of motor configuration and internal ballistic parameters over which the Super BATES motor must be capable of operating so that the full spectrum of chamber environments in present and future large solid rocket motors could be accurately and economically simulated. This objective was accomplished in several steps.

First, the characteristics of large solid motors that would be likely candidates for Super BATES simulation were tabulated. A trade study was then conducted to define the range of motor design parameters that would best simulate the candidate motors. This was done by matching the designs' primary performance variables. The parameter range specified by the contract served as a starting point and recommendations were made in several areas to extend the ranges of important parameters to cover the full range of present and future large solid motors. The recommended motor case and nozzle designs resulting from this trade study were summarized and an evaluation summary of the Super BATES performance accuracy (including scaleup considerations where important) was presented.

The details of the trade study are presented in Appendix A. This appendix includes (1) a list of performance related parameters, (2) the mechanism by which each parameter affects performance, and (3) the relative importance of that parameter in achieving an accurate simulation of large motor combustion environments.

3.1.1.1 Identification of Candidate Large Solid Motor Design Characteristics - The Super BATES motor will be used primarily to simulate the chamber environment of the stages of future large ballistic missiles like MX, C4, and successive generations of ballistic missiles. Important additional candidates for Super BATES testing include operational strategic ballistic missiles (e.g., Minuteman III and Poseidon C-3), large battlefield support rockets (e.g.,

Pershing), large solid boosters (e.g., the 156-in. motor), the Titan IIIC 120-in. solid strap-ons, the NASA shuttle booster, and the lower stages of the NASA Scout vehicle. The most significant performance related parameters for these motors are listed in Table 1.

Data supplied by AFRPL on the MX and C4 were particularly valuable. Although the design characteristics of these systems, particularly the MX, have not been frozen, the data provided give a firm indication of the likely range of future large ballistic missile design parameters. For large ballistic missiles chamber pressures range from roughly 400 psia to 1,500 psia, throat diameters range from 5 to 15 in., and chamber residence times are all greater than 40 msec and usually greater than 100 msec. Grain length to diameter ratio ranges from 0.6 to 4 while nozzle submergence (as a fraction of grain length) ranges from 0% to 30%. Burning rates at average pressure range from 0.3 to 0.6 in./sec.

In contrast, booster motors operate at chamber pressures around 550 psia with large throat diameters. Residence times of a few hundred milliseconds are typical. The motors generally have long grain length to diameter, little or no nozzle submergence, and burning rates from 0.22 to 0.34 in./sec.

3.1.1.2 Recommended Operating Range for Super BATES – A preliminary trade study was conducted to evaluate the range of motor parameters required to simulate large solid rocket motors. Particular emphasis was on the prime candidate motors described in Section 3.1.1.1. The two primary motor simulation variables (chamber pressure and throat diameter) are shown in Figure 1. Candidate large motors are located on the figure to indicate primary areas of interest.

Chamber pressures are clearly trending upward as better case materials become available. With the exception of the second stage Polaris (which was designed for a low pressure to overcome the high base burning rate limitations of early double base propellants), no operational or proposed large solid motor operates at a pressure below 440 psia. The MX and C4 stages are optimizing at pressures 200 to 300 psia higher than the earlier Minuteman and Polaris. The predicted pressure for the first stage MX is 1,400 to 1,500 psia.

TABLE 1. CANDIDATE LARGE SOLID MOTORS FOR SUPER BATES SIMULATION TESTS*

	$\bar{P}_c$, psia	D_T, in.	$\dot{W}$, lb/sec	$\bar{L}^*$, in.	tr, msec	D_{GRAIN}, in.	Grain, L/D	Submergence, %	Burn time, sec	$\dot{r}$ at $\bar{P}$, in./sec	n
MX 66-in. diameter – 1st Stage	1,500	10.5	787.0	4,730	180	64.5	3.7	4.5	60	0.40	0.67
– 2nd Stage	1,200	8.56	413.4	2,530	97	64.7	1.3	14	40	0.45	0.67
– 3rd Stage	800	5.14	99.6	2,960	115	65.0	0.6	18	70	0.35	0.67
MX 88-in. diameter – 1st Stage	1,420	14.7	1,433	4,570	175	87.1	2.8	4.5†	60	0.54	0.67
– 2nd Stage	1,200	11.8	781	2,570	100	83.3	1.2	14†	40	0.61	0.67
– 3rd Stage	719	8.0	219	2,760	106	87.7	0.6	18†	71	0.47	0.67
	1,275	10.3	648	4,225	160	72.76	2.23	15.1	63.5	0.43	0.63
	1,080	7.39	275	3,404	130	72.60	1.06	22.8	65.6	0.41	0.63
	930	4.92	109	1,819	70	29.44	3.22	5.4	35.11	0.31	0.63
	741	4 at 7.23	782	2,540	98	65.3	3.7	–	59.4	0.31	0.23
	445	9.63	207	1,610	62	51.8	2.4	13.6	65.75	0.31	0.27
	510	6.9	118	1,640	67	51.7	1.3	23.7	62.0	0.32	0.27
	780	11.6	616	3,170	105	73.1	2.3	15	65.1	0.44	0.35
	330	11.9	240	1,270	45	73.6	0.9	27	67.2	~0.6	0.6
	575	6.24	116.2	1,590	61	39.7	1.8	–	38.3	0.31	~0.25
	395	5.97	71.4	1,060	41	39.8	1.1	–	39.0	0.31	~0.25
156-in. booster motor Model L-71	555	37.6	3,920	8,200	320	151.6	6.8	–	114	0.22	~0.25
NASA shuttle booster	580	53.6	8,100	5,300	200	141.2	10	~2	124	0.35	0.25
120-in. booster motor	545	37.7	3,720	4,200	160	120	6.0	–	114	0.34	0.25
ALGOL III First stage Scout	550	12.6	434	2,250	87	44.7	7.1	–	64.5	0.22	0.20

* Data from AFRPL and CPIA Motor Manual. Engineering estimates used where data was unavailable
† Estimate

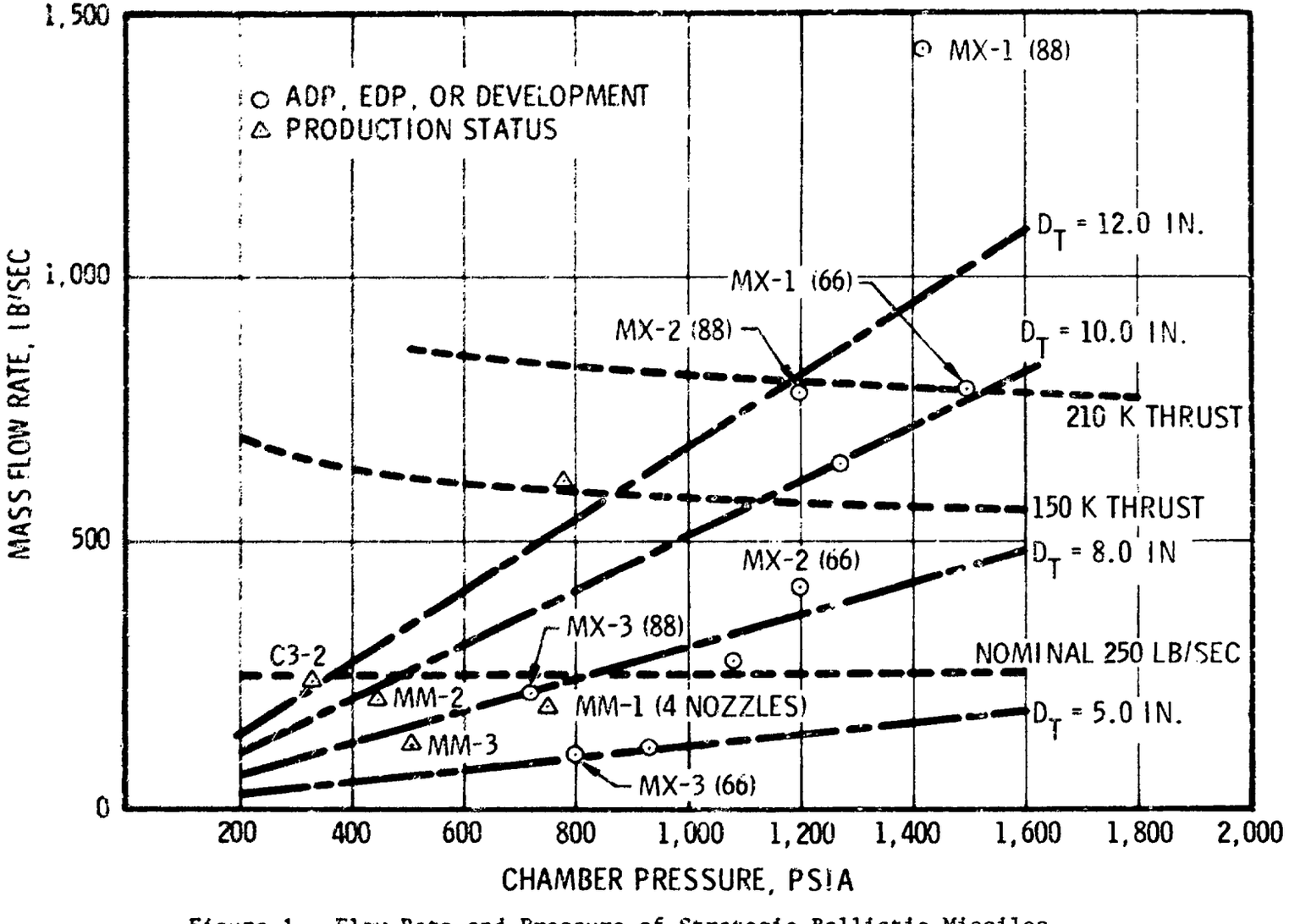

Figure 1. Flow Rate and Pressure of Strategic Ballistic Missiles

05749

With the introduction of carbon filaments, ballistic missiles in the 1980's could easily be optimized at pressures above the 1,600 psia maximum pressure proposed for Super BATES. Since chamber pressure acting directly on combustion processes and indirectly through propellant burning rate is such a fundamental parameter, it is recommended that the Super BATES motor be designed for a maximum pressure of 2,200 psia. This allows direct pressure simulation of large solid motors presently in use as well as those anticipated in the near future. The system is not noticeably penalized either from cost or handling weight considerations for this increased pressure capability.

Throat diameter selection depends on the range of chamber pressure and flow rate required. A throat diameter of 8 in. matches a number of large solid motors and appears to be an excellent choice for the nominal throat size. A throat diameter of 5 in. covers all planned motors, but future increases in pressure may require throat diameters as small as 4 in. on ballistic missiles. This should be provided for on Super BATES.

Several large solid motors including all first stage ballistic missiles have thrust levels that exceed the standard limit of 150,000 lb. However, these motors can be scaled down at constant pressure to operate with throat diameters of 10 in. or less at the maximum thrust stand capability for all MX and C4 stages. The scaled first stages of Minuteman and Polaris would operate at flow rates from 350 lb/sec to 400 lb/sec with 10-in. throats. Therefore, a 10-in. throat size appears to be adequate unless high flow rates at low pressure are expected or the maximum thrust level is raised above 150,000 lb.

The Super BATES should be designed to cover as wide a pressure range as practicable. The principal design problem at low pressure comes from accommodating throat diameters capable of handling large flow rates. Large throats require larger motor diameters to keep low port to throat ratios. However, in the interest of flexibility the Super BATES should be designed to accommodate throat diameters of up to 12 in. with the baseline submerged conical nozzle. A standard closure can be designed to accommodate the submerged nozzle to 10-in. diameter. A special closure would be required to increase the nozzle diameter to 12 in. A 12-in. throat would allow flow rates of 240 lb/sec at the minimum pressure of 200 psia and would be capable of simulating the second stage Polaris to provide a

data point for double base propellants. More important, an aft closure designed to accommodate a 10-in. conical nozzle will be able to handle smaller diameter contoured nozzles. For specific tests where exact full-scale performance simulation is required, Super BATES' ability to match the nozzle exit cone profile would be an important asset.

UTC recommends maintaining the present 150,000 lb thrust stand limitation although increasing the thrust to 210,000 lb would allow direct simulation of several first and second stage ballistic missiles (see Figure 1). A typical specific impulse efficiency curve versus mass flow rate is shown in Figure 2; it is based on 16% aluminum propellant in motors at 500 to 800 psia. The flow rates of several large solid rocket motors are also shown although their efficiencies generally will not fall on the 16% aluminum curve. The large motor data points that appeared to lie well beyond the 150,000 thrust level in Figure 1 in reality only require a specific impulse scaleup of roughly 0.1%. The large increase in cost required to achieve flow rates up to 800 lb/sec cannot be justified to eliminate the small specific impulse scaleup for very large solid motors.

The curve for specific impulse efficiency provides a preliminary indication of the value of the Super BATES motor as a performance tool in large solid motor design. By covering the critical large motor flow rate range from slightly under 100 lb/sec to roughly 550 lb/sec, the Super BATES permits direct performance measurements of most large solid motors with only small scaleups (a few tenths of a percent) for even very large solid motors. Data from 70-lb BATES motors require scaleups of 1% to 2% to cover the Super BATES range.

Burning rate characteristics of large solid motors were evaluated to determine the primary burning rate range for Super BATES. Where data were not available, a propellant b/a ratio of 4.0 was assumed to establish maximum web. The burning rates at average pressure for the candidate large solid ballistic and booster motors ranged from 0.31 to 0.6 in./sec as shown in Figure 3. Based on the large number of motors with burning rates below 0.4 in./sec, UTC recommends extending the proposed burning rate range down to 0.3 in./sec to cover

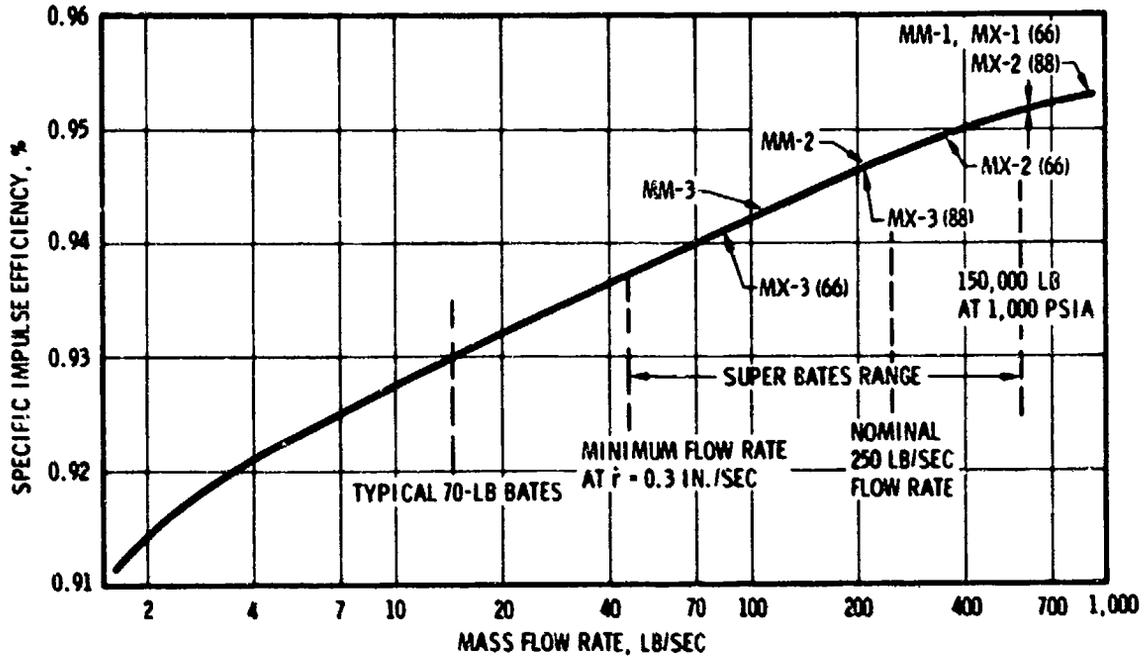

Figure 2. Typical Efficiency vs Flow Rate for 16% Aluminum Propellants

05750

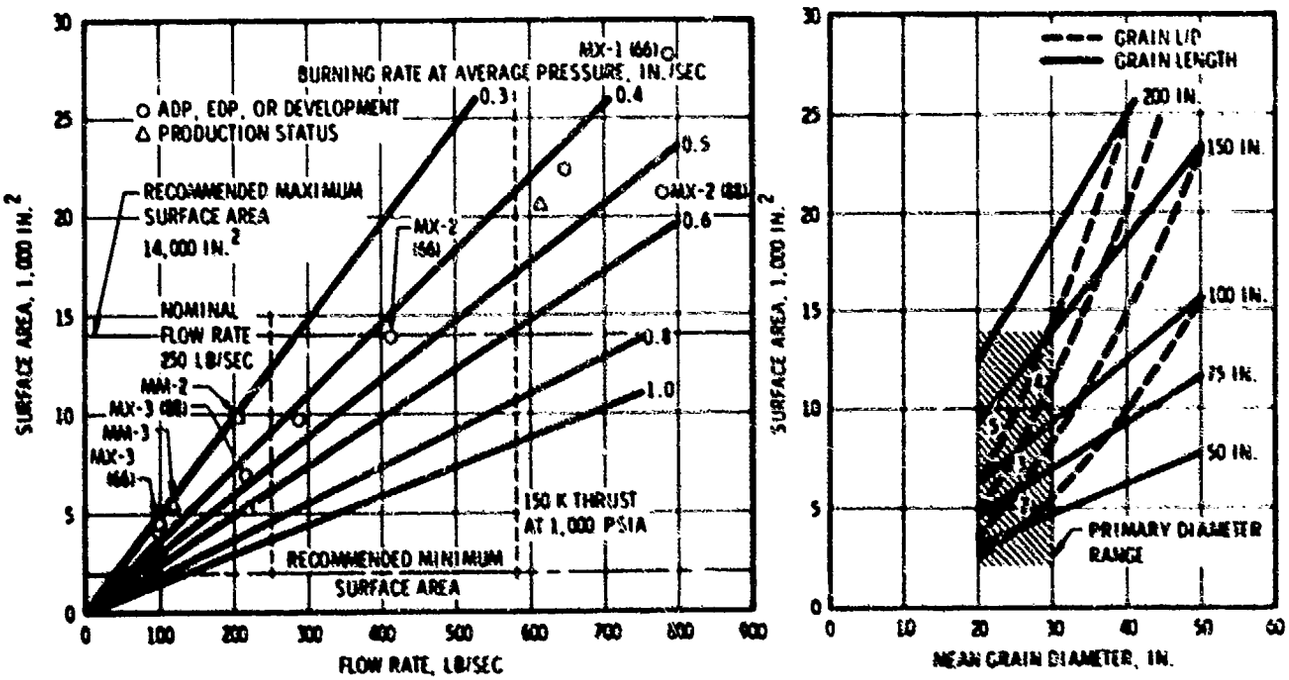

Figure 3. Super BATES Grain Geometry for Segmented Tubular Grains

05751

these motors. The complete absence of motors with burning rates above 0.6 in./sec suggests that the high burning rate range should not be overemphasized. Trying to achieve long burntimes (i.e., 5 to 6 sec) with burning rates of 0.8 to 1.0 in./sec requires thick webs (up to 6 in.) which will compromise the overall design. Thick webs require larger motor diameters and more complicated grain geometries to achieve a neutral pressure trace. UTC recommends a maximum web of 3.5 in. which allows a 5-sec burn time at burning rates up to 0.7 in./sec. At higher burning rates the maximum burn time will be proportionately reduced. However, in general high burning rate motors will have low L* and will require shorter burn times to minimize the effects of ignition and tailoff and achieve accurate performance measurements.

The motors within the primary Super BATES flow rate range of 100 to 500 lb/sec can best be simulated with average port diameters from 20 to 30 in. and a maximum surface area of 14,000 $in.^2$ as shown in Figure 3. Within this region Super BATES motor lengths range from approximately 50 to 200 in. Motor geometry provides another reason for not attempting to directly simulate the flow rate of very large solid motors. In addition to the facility and recurring cost required to achieve flow rates up to 800 lb/sec, Super BATES motor diameters of up to 40 in. would be required to achieve reasonable grain lengths with these high flow rates. Selection of a large diameter would compromise the operation of the Super BATES at lower flow rates by creating an excessively short length to diameter motor with long ignition and tailoff transients.

Preliminary operating range recommendations were prepared for the Super BATES based on the results of this design trade study. Major parameters listed in Table 2 were split into two ranges, primary and complete. The primary range of each parameter encompassed the most likely range of operating conditions required to simulate large solid rocket motors. Within this range the motor will be optimized for performance accuracy, ease of handling, and minimum operating cost. However, each major parameter also includes a much wider range to allow maximum flexibility. The motor will be designed to provide accurate performance over this complete range, but motors which require extreme values for several parameters (e.g., a 2-sec burn time with a 1-in. web) can not be expected to be as accurate as motors in the primary operating range. The recommended operating ranges of several important ballistic and geometric parameters

TABLE 2. SUPER BATES OPERATING RANGE PRELIMINARY RECOMMENDATIONS

Parameter	Baseline Range	Recommended Range
Chamber pressure, psia	200 to 1,800	Primary: 400 to 1,800 Complete: 200 to 2,200
Maximum thrust, lb	150,000	150,000
Burning rate, in./sec	0.4 to 1.0	Primary: 0.3 to 0.7 Complete: 0.3 to 1.0
Throat diameter, in.		Primary: 5.0 to 10.0 Complete: 4.0 to 12.0
Web, in.		Primary: 1.5 to 3.5 Complete: 1.0 to 4.0
Duration, sec		Primary: 4.0 to 7.0 Complete: 2.0 to 8.0
Average port diameter, in.		20 to 30

are shown in Figure 4. A nominal design point of 323 lb/sec for 6.2 sec at a burning rate of 0.43 in./sec at 1,000 psia was selected. With a web of 2.6 in. and an average port diameter of 25.4 in. (grain outside diameter = 28 in.) the grain length would be 150 in.

3.1.2 Recommended Motor Case Configuration

UTC recommends a nominal grain diameter of 28 in. and a maximum grain length of 180 in. Based on the trade studies presented in previous sections a grain diameter of 28 in. meets all the requirements for neutrality, efficiency of aluminum combustion, transient impulse, flow field and erosive burning modeling, and chamber heat losses. With a maximum grain length of 180 in., the Super BATES can achieve the maximum surface area of 14,000 $in.^2$ which is consistent with the burning and flow rate ranges of the motor.

The Super BATES trade study has clearly shown the need for configurational flexibility in order to model the operating characteristics of a wide range of large solid motors. The most practical approach to achieve this flexibility is through motor case segmentation. A segmented motor case can match the surface area requirements without either excessive free volume that would contribute to

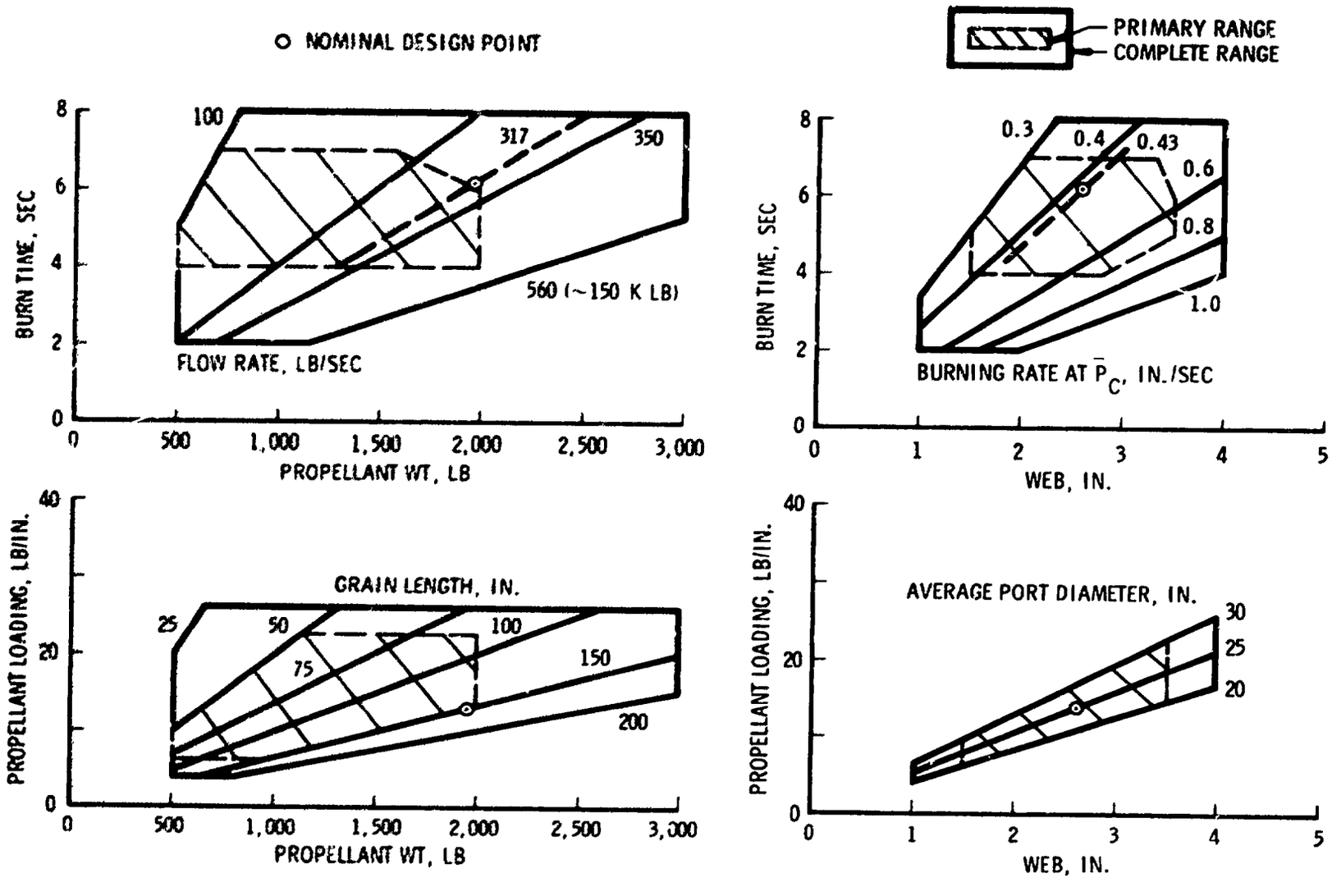

Figure 4. Preliminary Super BATES Parameter Range

05802

ignition and tailoff inaccuracies or large exposed areas of insulation that would substantially increase chamber heat losses.

Propellant grain processing requirements provide the most compelling reason for motor case segmentation. In order to achieve a neutral trace the end burning circular perforated grain must have the correct number of end burning surfaces; this is dependent upon the overall grain length. These neutrality characteristics present formidable processing problems with a monolithic case (see Figure 21, Appendix A). The slots could be formed either in the grain using foam wafers or machined in the grain after cure. Although both approaches are feasible, they require manpower and equipment specialization and neither are attractive for a low cost, widely used test motor. A segmented case allows the grain to be easily cast with two end faces which may be inhibited if desired.

A baseline grain segment length of 60 in. is recommended with three segments used to achieve the maximum grain length of 180 in. A half segment with a grain length of 30 in. is recommended to allow complete length flexibility while minimizing heat losses and transient impulse effects. The recommended segmentation approach (Figure 5) provides for grain lengths from 25 in. (roughly 2,000 $in.^2$) to 180 in. (roughly 14,000 $in.^2$). For grain lengths between 25 and 30 in. a single half segment would be used with the upstream face inhibited. From 30 to 60 in. a single 60-in. segment would be used. The upstream face would be inhibited up to a grain length of roughly 45 in. (depending on the web and neutrality desired). For longer grains, the 60-in. segments together with one 30-in. segment (for 60 in. $\leq L \leq$ 90 in. and 120 in. $\leq L \leq$ 150 in.) would be used up to three 60-in. segments with a total grain length of 180 in. The number and range of grain lengths for which inhibited faces would be used to achieve the desired neutrality is indicated in Figure 5.

A detailed investigation of motor case design approaches was conducted to determine the fabrication and assembly method that would allow high accuracy consistent with lowest program cost. The original design approach used plastic propellant cartridges secured inside clevis pin motor cases. Cartridge loaded

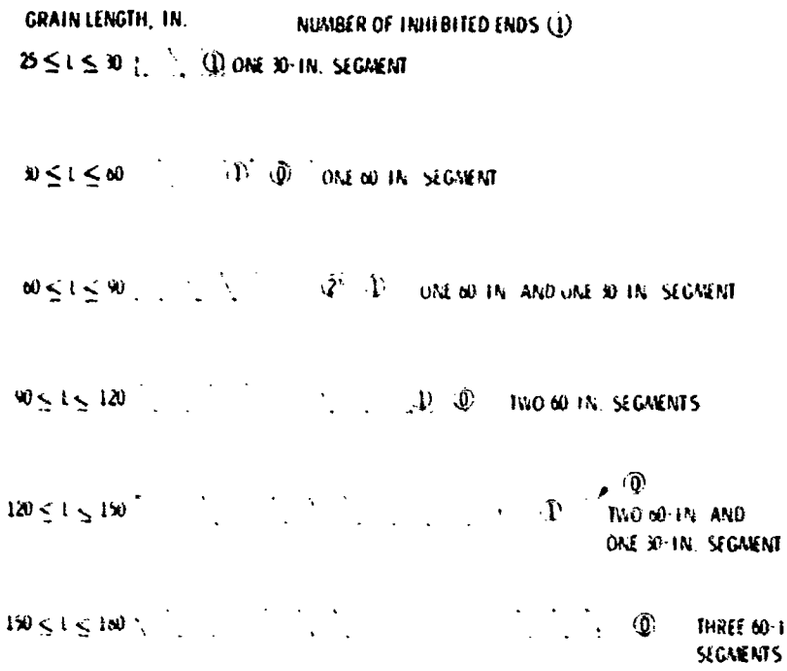

Figure 5. Recommended Grain Segmentation Approach

05752

grains have been successfully used on many programs and represent a straightforward approach to large motor static testing. However, the relatively small size (28-in. inside diameter) and high pressure (~2,000 psia) of the Super BATES motor together with the high degree of performance measurement accuracy required makes cartridge loading less attractive.

Heat losses to the motor case are a significant effect in the Super BATES. An earlier contractural study for Super HIPPO showed that cartridges with single gas seals must have either relatively large annular gaps to allow backside pressurization without a large pressure drop across the cartridge or use a flexible case that can expand to the wall on ignition. Heat losses for large gaps are unacceptable. Even for relatively small gaps, the heat losses can be as high as 0.5% for some conditions; therefore an expensive reusable flexible glass reinforced cartridge with seals at both ends would be required.

Tolerances and dimensional stability are problems with a cartridge loaded grain. A uniform web is essential to achieve rapid tailoff and minimum transient impulse. Producing a cartridge to tight tolerances and holding those tolerances through storage, insulation, and propellant casting could be difficult and costly.

Cartridge inspection would be required at least once during each reprocessing cycle when a decision would be made to (1) accept the cartridge, (2) reject the cartridge, or (3) rework and reinspect the cartridge. Cartridge loading also complicates the handling and motor assembly procedures.

Direct case bonding to segmented motor cases is preferrable to cartridge loading in terms of performance and design simplicity, but several cost aspects must be considered. A steel case can be produced and held to close tolerances over long periods of use. A motor composed of at most three case bonded grains can be easily handled and assembled. However motor cases are traditionally much more expensive than cartridges. With Super BATES, the case segments with integral clevis joints would cost approximately $10,000 and the glass reinforced cartridges (reusable a maximum of 10 times) about $3,000. With the anticipated use rate of 12 firings per year (as given in the SOW), more than 20 segments could be required to account for shipping, processing, setting up, testing, and cleaning schedules. Although the costs are not prohibitive at this level, there is a strong incentive to provide a more cost effective alternate to the cartridge loaded configuration than a case bonded case which incorporates an integral female clevis joint. A logical solution is to fabricate separate attach joints such as H-joints; in this way, the cost of the segment is not burdened with relatively complex joint costs.

Low cost, commercially available pipe offers the best approach for an inexpensive case segment. Medium alloy steel pipe sells for 25 to 35 cents a pound. After being cut to length and bored to produce close tolerance internal dimensions, a 60-in. case segment should cost no more than $2,500 or roughly the same as a glass cartridge which is far less durable. Shipping costs are not a significant factor despite the sizable weight differences between cartridges and steel case segments because a 5,000-lb minimum weight limit exists for shipments of live propellant. A cost study was conducted to determine the round trip shipping costs of one, two, and three segment motors between AFRPL and several solid rocket companies. The results, shown in Table 3, indicate that the difference in transportation costs between cartridges and case segments is not significant (at most $200 per segment).

TABLE 3. SUPER BATES TRANSPORTATION COST STUDY

Shipping Configuration	Quantity Per Shipment	Gross Weight, lb	Net Explosive Weight, lb	Estimated Transportation Costs AFRPL to Vendor to AFRPL, $			
				UTC	Aerojet	Hercules	Thiokol
300-lb plastic cartridges	1	500 /1,250	0/750	154	154	414	443
	2	1,000/2,500	0/1,500	181	181	460	492
	3	1,500/3,750	0/2,250	208	208	506	541
2,000-lb steel case segment	1	2,400/3,150	0/750	254	254	556	605
	2	4,800/6,300	0/1,500	332	332	766	823
	3	7,200/9,450	0/2,250	422	422	1,120	1,203
Round trip cost differential	1			100	100	152	162
	2			151	151	306	331
	3			214	214	614	662

* 1974 rates shown
Shipping weight from RPL to contractor which includes shipping containrer tare weight
Shipping weight from contractor to RPL which includes 750 lb of propellant

UTC-DC - Coyote, California
Aerojet - Nimbus, California
Hercules - Baccus, Utah
Thiokol - Thiokol, Brigham City, Utah

The motor case joints would be produced only in small quantities (no more than two would be needed) and would remain in the assembly/test area. These joints would be machined either from flat plate or from roll ring forgings. Two candidate joints, shown in Figure 6 , are representative of the type of configurations that could be used. The shear ring design uses a split ring mating with circumferential grooves in each segment; it is retained by a cylindrical collar. The double clevis pin joint offers simplified assembly, but the joint adds about 10 in. of free volume to the motor.

3.1.3 Nozzle Design Study

The nozzle design has an extremely important effect on motor performance. Consequently accurate modeling of all major nozzle design variables is important to properly simulate the performance of large solid rocket motors The four most important nozzle parameters are:

A. Throat Diameter

The throat size affects two phase flow losses and should be closely modeled to minimize scaleup. The nozzle should accommodate throat diameters from 4 to 12 in. One closure can be used to accommodate nozzles with throat diameters from 4 to 12 in. However, a special closure will be required for nozzles with throat diameters from 8 to 12 in.

B. Expansion Ratio

Since the motor will operate at pressures from 200 to 2,200 psia, expansion ratio flexibility is required to avoid over expansion and to achieve close to the optimum expansion ratio.

C. Submergence

Variable submergence is required to model the flow field around the nozzle entrance. Since submergence losses tend to flatten out for nozzle submergence length/chamber length of 5% to 10%, a maximum nozzle submergence of 18 in. is recommended based on 10% of the maximum chamber length of 180 in.

D Throat Radius of Curvature

The throat radius of curvature (especially in the entrance region) has a significant effect on two phase flow losses. The nozzle should be designed

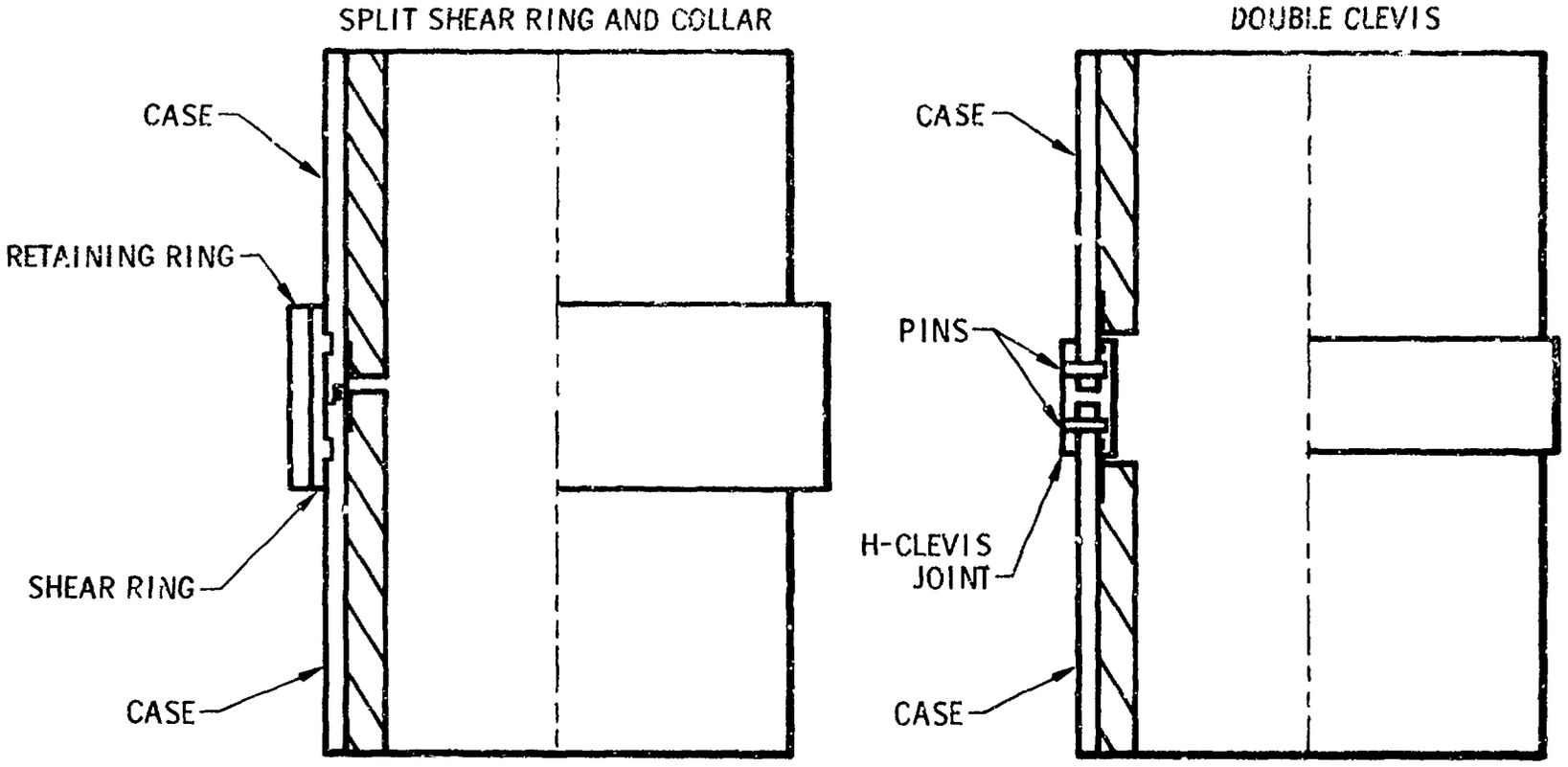

Figure 6. Typical Joints for Extruded Pipe Motor Cases

05753

to model throat curvatures from 1.5 times the throat radius up to roughly 4 times the throat radius.

The nozzle throat presents the greatest design challenge to achieving performance accuracy and cost effectiveness. The throat must withstand chamber pressures up to 2,200 psia with high energy propellants for up to 8 sec with little erosion. The nozzle operating range of pressure and throat diameter is shown in Figure 7. Medium erosion resistant throat materials could be used for the larger throat sizes (10 to 12 in.) where thrust and burn time limitations will restrict the severity of the thermal environment. However, the baseline throat size must operate over the full pressure range. Throat materials like pyrolytic graphite are recommended to minimize erosion effects especially for maximum duration tests at high pressure with the smaller 4- to 8-in. throats.

Reuse of the throat package is considered a cost effective design approach for the Super BATES. Although instantaneous heat fluxes equal or exceed the full-scale motor values requiring an expensive high performance throat, the total nozzle heat transfer during a 5 to 8 sec Super BATES firing is small compared to the nozzle heat transfer in a full-scale motor; therefore, char penetration and thermal soakout will be much less severe in Super BATES. Multiple reuse of the throat package would help amortize the nozzle cost over several firings and could contribute significantly to achieving minimum motor operating expense.

The Super BATES motor operating range is shown in terms of surface area and nozzle flow rate in Figure 8. The grain segmentation approach allows continuous operation from 2,000 $in.^2$ to 14,000 $in.^2$ However, there is no easy way to continuously vary throat diameter over the full range of 4 to 12 in. nor is this necessary. The use of a small number of Super BATES throat sizes (three to five) is recommended rather than trying to exactly model the throat diameter of each motor. A set of four nozzles with throat diameters of 5, 6.5, 8, and 10 in. could adequately cover the Super BATES range. This does not preclude use of a special nozzle for a particular test. However, for the majority of tests, the small scaleup introduced by using standard nozzles would not significantly affect performance accuracy.

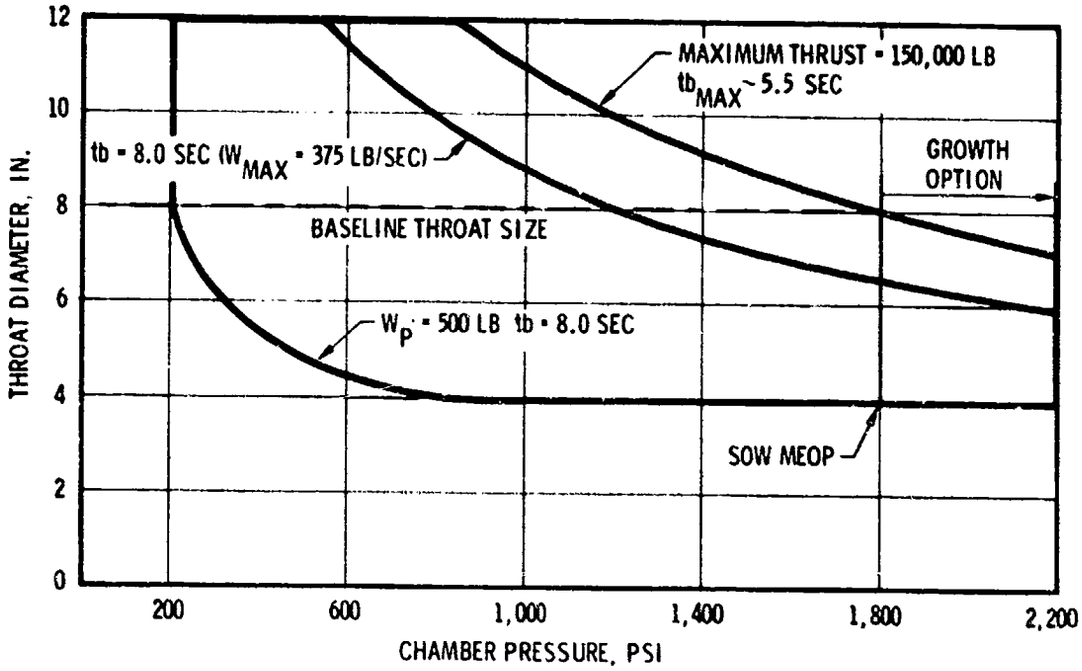

Figure 7. Super BATES Operating Range ($W_{p_{max}}$ = 3,000 lb)

05754

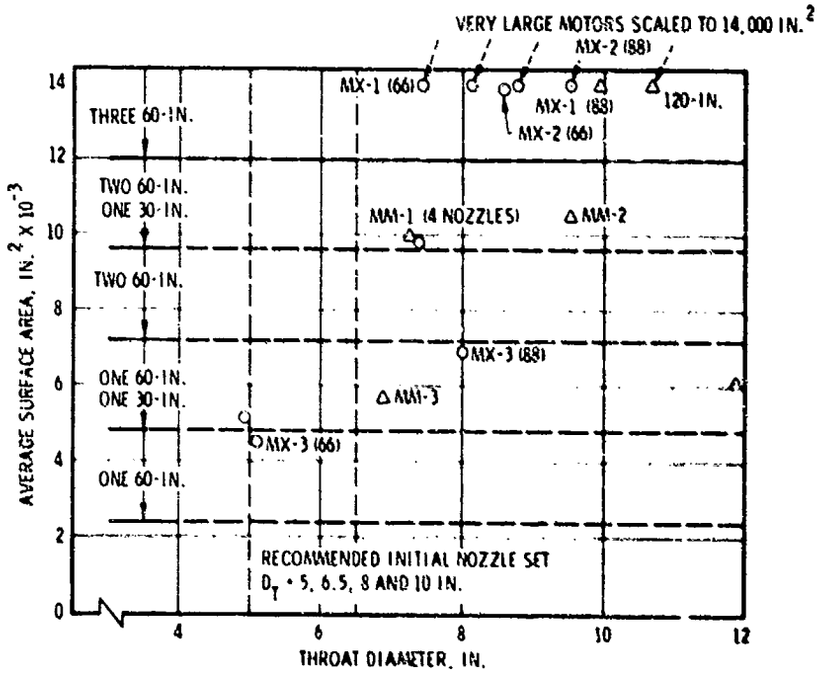

Figure 8. Super BATES Operating Range

05755

The recommended submerged nozzle design shown in Figure 9 allows flexibility in expansion ratio, submergence depth, and throat radius of curvature.

Expansion ratio flexibility is essential to minimize separated flow effects and to achieve a near optimum expansion ratio based on the chamber to exit pressure ratio of a particular test. The recommended design uses a silica phenolic exit cone that is free standing from an area ratio of 5:1. The exit cone would be set at the correct expansion ratio for each test and discarded after the test. By using a partially free standing exit cone that is pinned to the steel support at a low area ratio, a single nozzle can cover the complete range of expansion ratios for each throat size.

Nozzle submergence depth (as a fraction of chamber length) must be modeled to simulate submergence losses. Fortunately submergence losses reach a threshold value by about 10% submergence and increase only slightly thereafter. Consequently, a maximum submergence depth of 18 in. will provide 10% submergence for the longest grain.

Adapter rings were evaluated to provide flexibility in submergence depth. The adapter rings, manufactured to various lengths, control the axial position of the nozzle and therefore the depth of submergence. The adapter length can be increased until the nozzle is nearly unsubmerged.

Flexibility in radius of curvature of the nozzle can be achieved without building several nozzles in each throat size. The plastic insulation parts in the nozzle entrance and throat can be machined to achieve an entrance radius of curvature range using a common steel support piece. UTC recommends that a nominal radius curvature of approximately 1.6 times the throat radius be used for most firings to allow reuse of the throat. However, whenever particular test conditions (especially for a test series) require a different radius of curvature, the nozzle insulation pieces can be configured to meet new radius of curvature requirements.

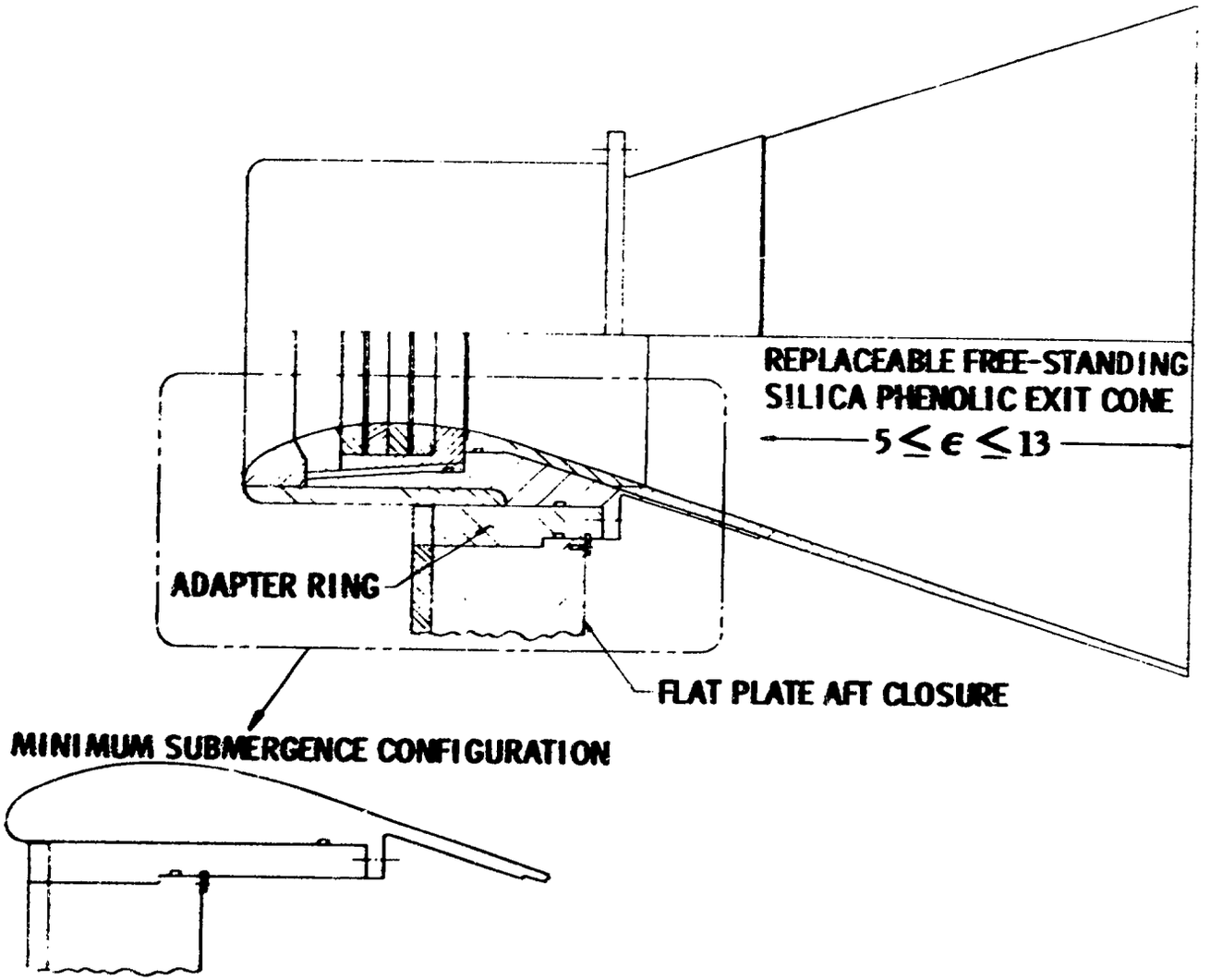

Figure 9. Variable Submergence Nozzle

05756

3.1.4 System Performance Accuracy

The projected accuracy of the Super BATES test motor and thrust stand to define the solid rocket propellant performance is summarized in Table 4. This table is a summary of the detailed trade studies presented in Appendix A. The table shows projected variations in (1) the ability to model exactly, (2) the scaleup effects for pertinent performance parameters, and (3) the error introduced by analytically correcting these variations.

The trade study analyses indicate that the delivered performance for the actual flight motors may be defined quite accurately without applying any correction factors. The rationale is that the variations in performance due to parameters such as heat loss, combustion efficiency, etc., are well within the range experienced in an actual flight motor. The scaleup and configuration factors such as throat size, erosive burning due to low port to throat, etc., are not major contributors and do not justify the additional effort to apply corrections.

For tests whose purpose is to define the actual propellant performance as accurately as possible, corrections for variations may be made analytically. Combining these projected uncertainties results in an overall estimated system accuracy of 0.35%. This estimate is based on the two and one-half segment baseline motor with an 8.0-in.-diameter throat described in section 4.0

Table 5 presents the accuracy with which the Super BATES motor delivered performance can be measured. This summary considers the measurable items listed in Table 4. As shown, the actual performance is estimated to be within 0.19% of measured performance.

3.2 Thrust Stand

A study was conducted to identify a single component horizontal system capable of measuring thrust in three ranges: 0 to 50,000 lb, 0 to 100,000 lb, and 0 to 150,000 lb. The maximum thrust is 150,000 lb; the stand structure is capable of force loads to 200% of maximum without damage.

TABLE 4. ACCURACY ANALYSIS OF SUPER BATES PERFORMANCE

Parameter	Variation		Uncertainty of Performance Correction	
	All Configurations	Baseline Motor	All Configurations	Baseline Motor
Pressure	None; model directly	0	0	0
Throat diameter	None up to D_t = 12 in.; model directly	0	0	0
	<0.5% up to 156-in. diameter (motor nozzle size)	-	<0.1%	-
Burning rate	<2.0% due to erosive burning and port diameter	0	Negligible	0
Nozzle submergence	None; model directly	0	0	-
Combustion efficiency	0.2%	0	<0.05%	0
Heat loss	Up to 2.5%	1.9% submerged 1.6% conventional	0.20%	0.15%
Thermal Nonequilibrium	4.0%	4.0%	0.1%	0.1%
Pressure neutrality	±10.0% maximum ±3.0% nominal	±10.0 maximum ±3.8% nominal	<0.05%	<0.05%
Transient impulse	5.0%	2.6%	<0.10%	<0.05%
Expended inerts	1.25%	1.00%	<0.30%	<0.25%
Thrust stand	-	-	<0.15%	<0.15%
Overall RMS accuracy	-	-	0.43%	0.35%

TABLE 5. ACCURACY ANALYSIS OF SUPER BATES MEASUREMENT

Parameter	Magnitude of Variation	Estimated Tolerance
Pressure neutrality	±10.0% maximum ±3.0% nominal	<0.05%
Transient impulse	5.0%	<0.10%
Thrust stand accuracy		<0.15%
Overall RMS accuracy		0.19%

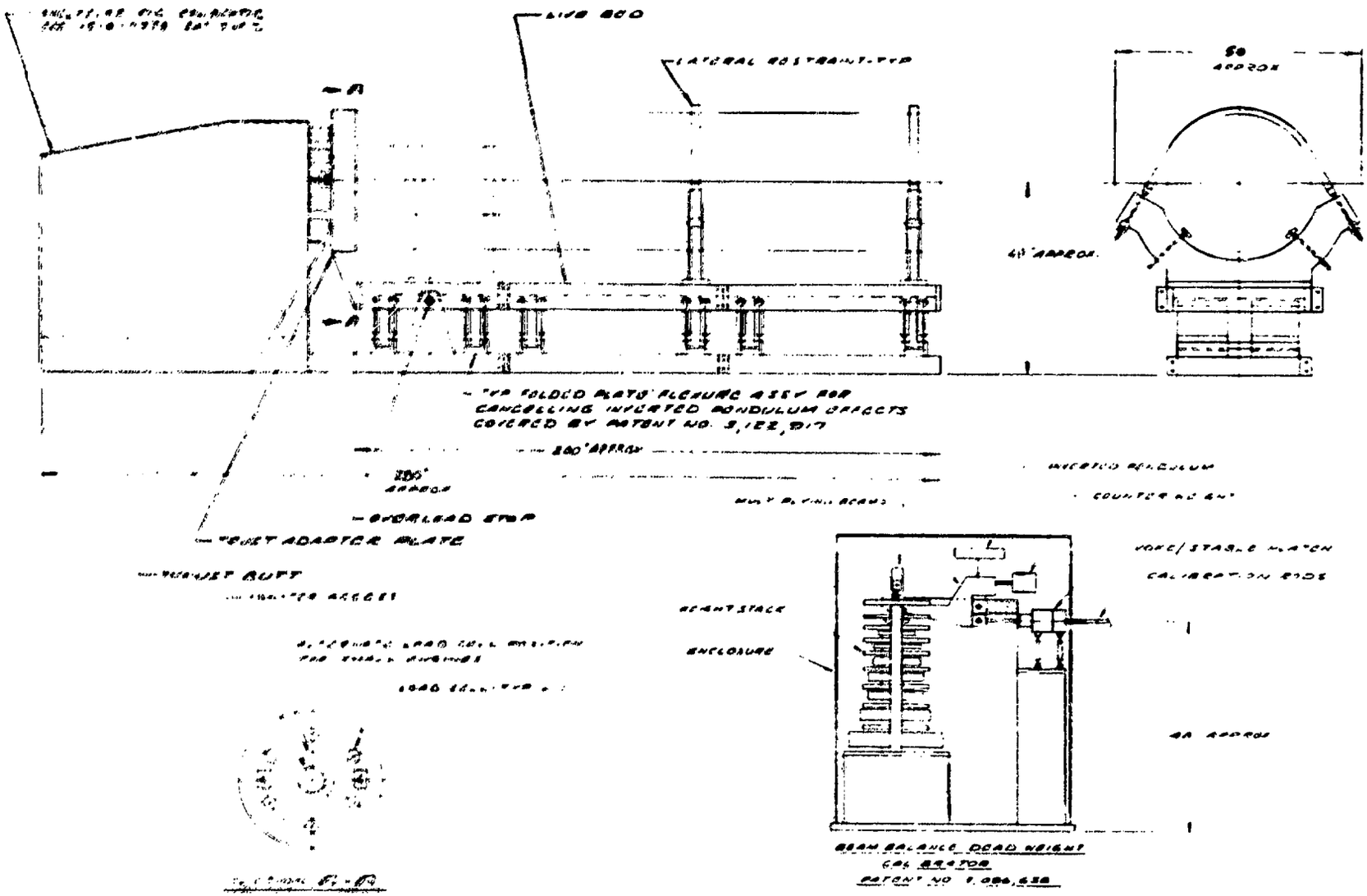

Figure 10. Single Component Thrust Stand

The axial thrust measurement system accuracy has an initial design goal of ±0.10 percent of full-scale (for each of the ranges) with a three sigma confidence based on in-place calibration with a stand resonant frequency of 25 cycles per second or higher.

After identifying the characteristics of the thrust stand, an analysis was conducted to determine cost versus thrust stand accuracy.

3.2.1 Thrust Stand Definition

3.2.1.1 Design Flexibility - The thrust system design has a large degree of flexibility for (1) interchanging load cells for different capacities, (2) installing motors of various sizes, (3) easily removing and installing motors and load cells, and (4) easily calibrating the system (see Figure 10).

Various combinations of load cells can be installed between the thrust adapter plates and thrust abutments to accommodate motors of different sizes and capacities (see Figure 10). Load cells are doweled and bolted into place; all locating holes are precisely jig bored in both thrust adapter plates and thrust abutments so that load cells can be interchanged without positioning or alignment. Thrust adapter plate locations are related to thrust abutments and are positioned with tooling bars jig bored at the same time.

The thrust system is designed in three sections allowing complete removal of one or two sections to accommodate motors of various lengths. All joints are bolted and locked using dowel pins so that alignment is maintained and realignment will not be necessary during subsequent installations. Motors can be removed without upsetting the alignment; however, center lines and dowel pins are located on the structure so that periodic alignment checks can be made using a surveyor's transit, scales, and levels.

Motors of various diameters can be installed using appropriate cradles which in turn can be bolted to the thrust bed. These cradles will be manufactured to match and accommodate the selected motor configuration.

3.2.1.2 Accuracy – The design goal accuracy of the thrust system is 0.10% of full-scale for each of the three ranges with a three-sigma confidence level based on in-place calibration. This accuracy is possible because of the folded flexures used; these cancel the inverted pendulum effects and interaction quantities that result from changes in the length of the thrust system due to temperature changes. The folded flexures also reduce the redundancy of the thrust measuring system by a factor of 2.0. The thrust system has been designed around the simple technique of supporting the thrust bed and motor on folded flexures. The system has 1 degree of freedom and 5 degrees of fixity. The motor can be installed so that the head end of the motor can face directly against the thrust adapter plate or a special adapter to interface between the motor and the plate as required by the user. This allows the motor to be installed and aligned without affecting the accuracy of the thrust measuring system since motor installation is virtually independent of the measuring system. Misalignment of the motor by an angle of 1° introduces an error of less than 0.015% of thrust.

Ultra-precision load cells are furnished for measuring thrust. These load cells were developed in the last four or five years at Ormond, Inc., and are now used in sophisticated weighing systems, some of which have been checked by deadweight to one part in 30,000. These load cells have superb linearity, repeatability, and hysteresis characteristics.

An in-place calibration system with a beam balance deadweight is provided as shown in Figure 10. The prime limitation of this calibration system is its calibration. Some systems installed by Ormond, Inc., have been checked with deadweights to tolerances better than 0.002% of load, including repeatability, hysteresis, and linearity, using a deadweight compensation technique. To calibrate this deadweight calibrator, load cells must be used since the calibration force is applied horizontally instead of vertically.

A load cell calibration system (including load cells for each of the full-scale ranges) is used which is calibrated by deadweights traceable to NBS. Using this technique a transfer of calibration constants should have an accuracy

of 0.03% full-scale or better. Error terms include repeatability, linearity, hysteresis, and non-return to zero.

3.2.1.3 Calibration – A deadweight calibrator is furnished with the system. This calibration system includes the cancellation technique outlined in Ormond's patent No. 3,449,947. This technique eliminates the interaction terms that result from the redundancy associated with attaching the calibrator to a fixed structure.

The thrust stand includes a deadweight calibrator with a range accuracy of ±0.03% which is used to calibrate the thrust measuring system.

The calibrator, which can be operated manually or from a programmed computer, is a multiple beam arrangement whereby the weights are raised and lowered using flexure bellows. The control panel is mounted in the block house. The solenoid for actuating the bellows is mounted on the calibrator and is potted to obtain an hermetic seal. All lines are run in conduit without plugs. Lead connections are made on a barrier strip mounted on the calibrator.

The weights are in binary coded decimals which allow the selection of increments from 1,000 to 150,000 lb. The weights are certified to class C tolerances approximately 0.006% of weight. The Bureau does not certify weights of this type to 0.001%, but this accuracy is not required.

The calibration factor is established by calibrated load cells mounted in the pull rod. Three load cell ranges are furnished and delivered along with the calibration instrument. This equipment can be used to verify the beam balance calibrator at any future date. Flexures are used on both ends of the load cell in order to eliminate bending moments. The thrust stand can be calibrated in 15 equal steps up and down in less time than 1 min/step.

Limit stops are mounted on the beam; these prevent the calibrator from applying additional loads as long as the stop is engaged. This safety feature prevents inadvertent application of loads in excess of that selected by the operator. It does not prevent the calibrator from running in the opposite direction to unload the system.

The calibration system has the minimum following specified accuracies (at a one-sigma confidence level):

A. Linearity – ±0.03% of applied load from 50,000 to 150,000 lb
B. Hysteresis – ±0.006 of applied load
C. Repeatability – ±0.006% of applied load
D. Accuracy – (including combined effects of linearity, hysteresis, and repeatability errors) within 0.08% of applied load or 0.03% or range, whichever is greater, where the ranges are 50,000, 100,000, and 150,000 lb. The primary limitation of the calibrator's accuracy is the difficulty of calibrating the system load cells to a higher level.

The calibrator is designed to prevent load cell and thrust stand overloading by including a digital selector switch on the panel. The electrical circuitry prevents the application of any load in excess of that selected and dialed into the system by the operator. The calibrator is mounted on support structures completely independent of the thrust measuring system.

The control circuit for the calibrator is equipped with logic so that it can be interfaced with Hewlett-Packard's 2100 mini-computer. The interface is TTL compatible. All power supplies and other control elements are furnished with the calibrator. Switch closures on the calibrator indicate when a weight has been applied and the beam is balanced. Under these conditions the calibrator load can be recorded. Through proper programming the complete system can be calibrated automatically by using the computer and the beam balance calibrator.

3.2.1.4 Alignment – The thrust system is manufactured using jig boring techniques to establish dowel pin and tooling bar locations; this will provide precise alignment of all components.

Centerline dowel pin holes are jig bored at the same time and can be used to align the system after final assembly using transits, levels, and scales. In a single-component thrust stand of this type, alignment is not critical since the error for a 1° misalignment of the motor is 0.0015% of thrust.

The load cells are manufactured as ball-ball types which do not have flexures on the end. Therefore, the ends of the load cell can be drilled and tapped on the centerline so that installations can be made without precise alignment being required.

3.2.2 Trade Study of Cost versus Measurement Accuracy

This thrust stand system is state-of-the-art in thrust measuring equipment that has been installed and used for several years. If the evaluation of accuracy is based on in-place calibration, allowing ±0.1% of full-scale load for the thrust stand, there is no difference in cost between a thrust stand having this accuracy and one having 0.25% full-scale at the three-sigma level. The above values are based on in-place calibration and do not include the 0.03% allowed for the calibrator. Since this equipment is standard and a beam balance deadweight calibrator is required for calibration, the cost of a 0.1% system would be the same as the cost for a 0.25% system. The only difference is that more tests are required to establish a three-sigma confidence level for a 0.1% system than for the same confidence level at 0.25% of full-scale. Tests could be run at a cost of about $10.00 per data point using the calibrator provided with the system. Over 100 data points would be required to establish a three sigma confidence level at 99% reliability factor.

4.0 BASELINE SYSTEM DESCRIPTION

The baseline BATES system consists of motor assembly, thrust stand, processing and handling equipment, and shipping containers for motor segments and nozzles. The test motor was designed to accommodate a wide range of propellants and simulate combustion chamber environments for a large variety of ballistic and large solid motors (see Section 3.0, trade study).

By using various combinations of segments with 60- and 30-in.-long propellant grains up to a maximum of three 60-in. grains, the motor will operate with propellants having burning rates from 0.3 to 1.0 in./sec. The motor case is designed to operate at pressures to 2,200 psia with a design safety factor of 1.5 on yield.

Motor flexibility is achieved by using the segmented case approach. This permits great variation in propellant surface area (and thrust) without resulting in a large free chamber volume at low flow rate conditions. (The latter condition represents an unrealistically large L* which greatly affects chamber heat loss and ignition and tailoff impulse.) The maximum total combined weight of the three 60-in. propellant grain segments is 3,000 lb; maximum design thrust is 150,000 lb. Weight of the maximum size loaded motor assembly with conventional nozzle is less than 20,000 lb (see Table 6); this weight is below the maximum specified in the RFQ (25,000 lb).

The motor grain design uses double end-burning, center-perforated grains with a cylindrical bore. Design simplicity and casting ease were primary design considerations.

The motor has relatively neutral pressure-time and thrust-time histories. The maximum pressure variation over the entire range of operating conditions (i.e., pressure, burning rate, burn time, etc.) averages less than ±5% from the mean pressure over the entire burn time. In addition, for any point within the range, the operating pressure does not vary more than ±10% from the mean pressure. Combined ignition and tailoff transients contribute less than 5% of the motor's total impulse.

TABLE 6. WEIGHT SUMMARY OF THREE SEGMENT MOTOR WITH MAXIMUM PROPELLANT WEIGHT

Component	Weight, lb
Forward closure	2,490
Case	9,950
Case attachments	1,140
Aft closure	1,291
Nozzle (conventional)	400
Nozzle attach ring	40
Insulation and liner	170
Igniter	2
Propellant	3,000
Total loaded motor	18,483
Handling tooling	750
Total weight	19,231
Maximum weight allowing for design growth	20,000

The propellant grains are case bonded to the motor segments. This approach simplifies the motor design and minimizes the cost of motor components and processing since pressure grade carbon steel pipe is used for the case segments. The segments are insulated at both ends in the area where the wall is exposed to the combustion gases during propellant burnback.

Forward and aft closures are fully insulated to minimize heat loss and the resultant loss in accuracy of data. The aft closure is designed so that the submergence depth of the nozzle can be varied by using an adapter.

Two nozzle designs are provided at the nominal operating condition (8-in. throat). The conventional nonsubmerged design employs a converging section with a 45° half-angle and a diverging section with a 15° half-angle. The submerged configuration has a diverging section with a 15° half-angle. The submerged nozzle is designed for variable submergence. Both nozzle designs use

graphite G-90 throats so that erosion effects on performance measurements are minimized.

A burst disc is used as a relief device to prevent overpressurization of the motor. The device will adequately vent the motor if the chamber pressure exceeds 1.25 times the maximum expected operating pressure. The pressure relief passages are radially oriented so that overpressurization will not cause sudden large changes in motor axial thrust. The motor is designed with provisions for measuring chamber pressure at two locations in the forward and aft closures.

Drawings of motor components have been prepared for the preliminary motor design based on use of the UTC control propellant UTP-18,803; this propellant has a burning rate of 0.43 lb/sec at 1,000 psia. These baseline designs are shown in Figures 11 and 12. The motor, consisting of two full-length and one 25.6-in. length propellant grains, has a mass flow rate of 323 lb/sec at a chamber pressure of 1,020 psi with the nominal 8-in.-diameter nozzle throat. Propellant web thickness is 2.6 in., nominal burn time is 6.2 sec. This two and one-half segment motor design has a maximum pressure variation of less than 4% from the mean pressure over the entire burn time. A summary of weights for the baseline motor with conventional nozzle is given in Table 7.

Submerged and conventional nozzles were designed with a radius of curvature of the nozzle throat equal to 1.6 times the throat radius. The maximum submergence depth is 18 in. Motor case segments are joined with a pinned, double shear H-clevis as described in Section 4.1.1. The pinned joint design is similar to that used with the AFRPL HIPPO and Super HIPPO test motors. The segments have only male joints, thus substantially reducing manufacturing costs.

Motor ignition is achieved with a pyrotechnic device inserted through the nozzle and placed on the propellant cylindrical perforation. The igniter propellant is packaged in a perforated phenolic tube. Igniter size is controlled by motor size and propellant formulation. This inexpensive and reliable type of igniter has been used successfully on numerous UTC/AFRPL test motors.

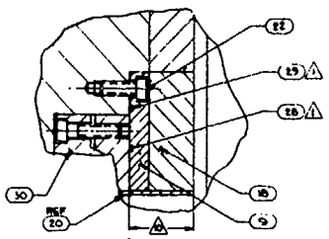
DETAIL A
SCALE: 1/1

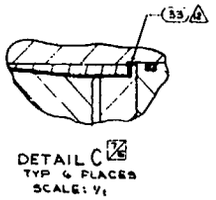
DETAIL C
TYP 4 PLACES
SCALE: 1/1

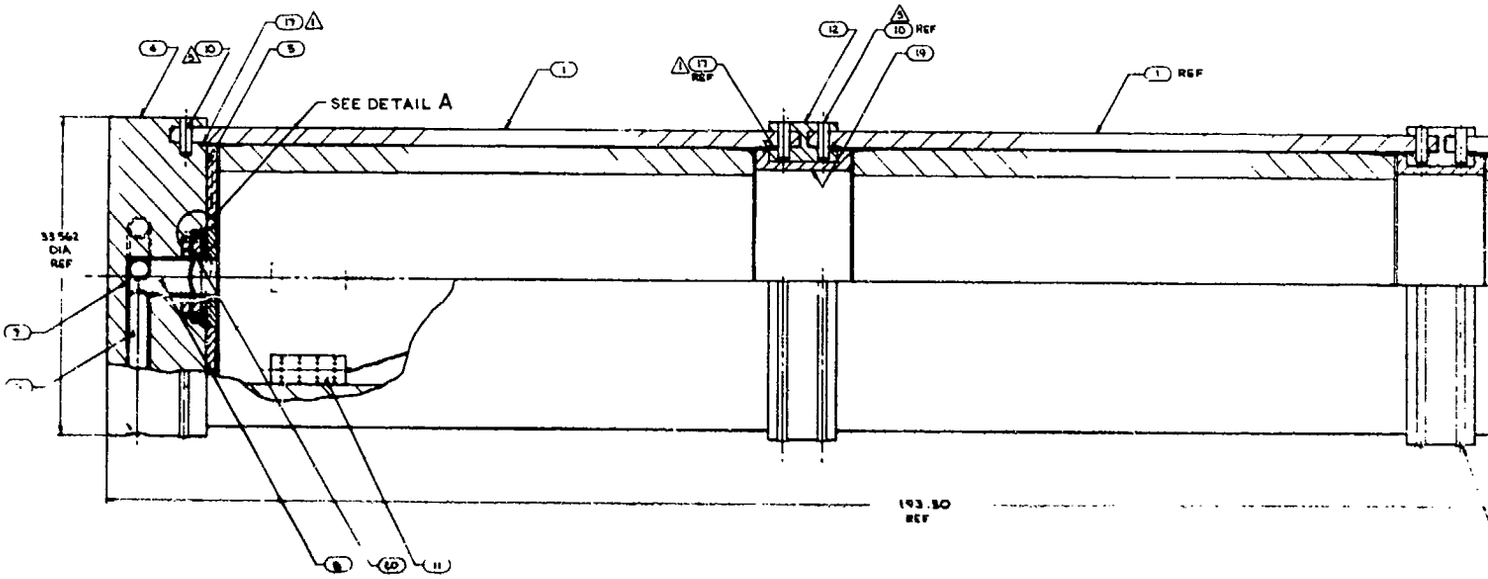
SEE DETAIL A
33.562
DIA
REF
193.50
REF

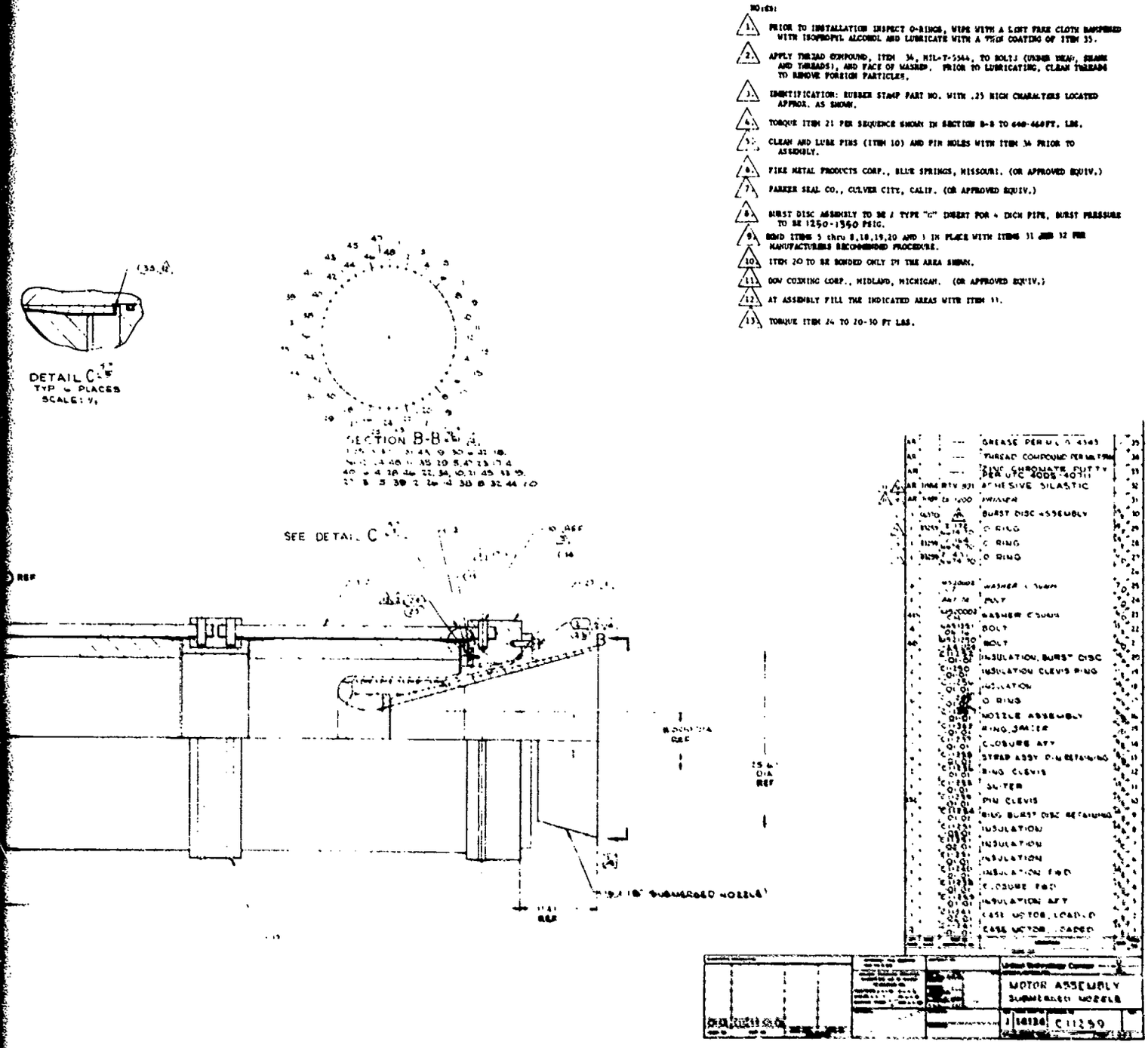

Figure 11. Motor Assembly, Submerged Nozzle Baseline Design

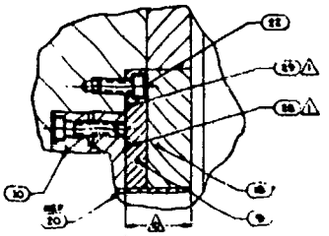

DETAIL A
SCALE

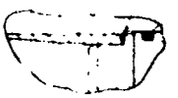

DETAIL C
TYP 6 PLACES
SCALE

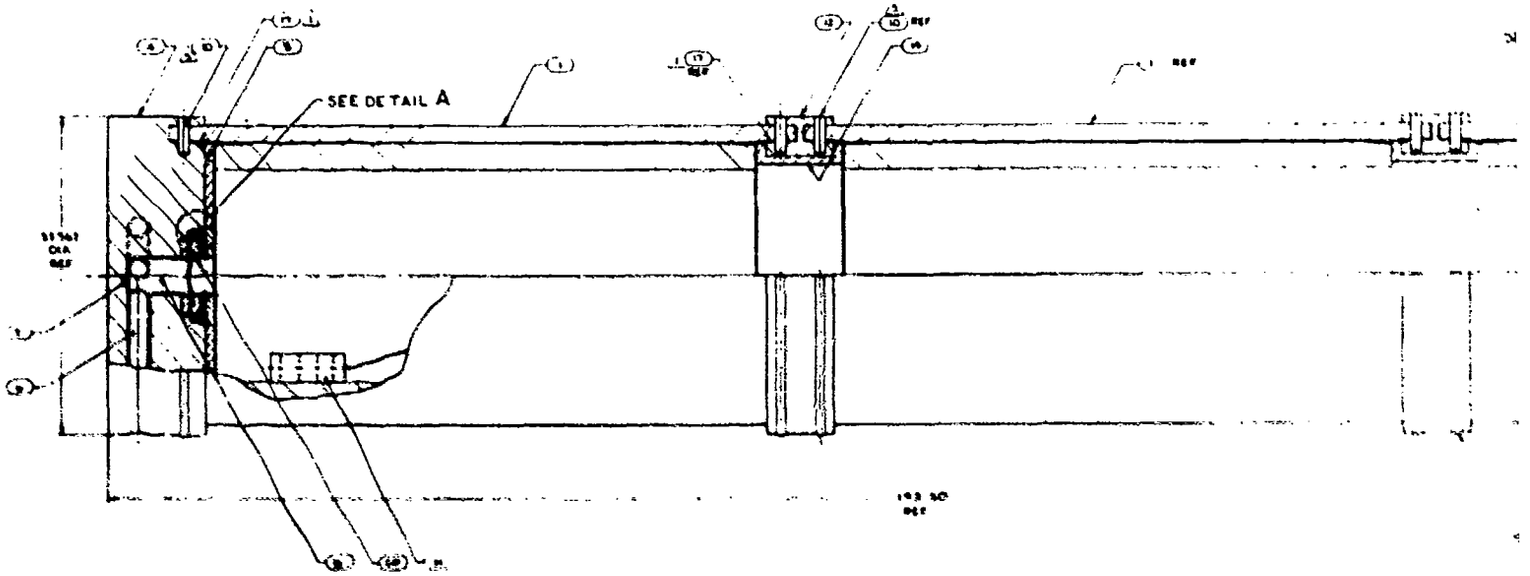

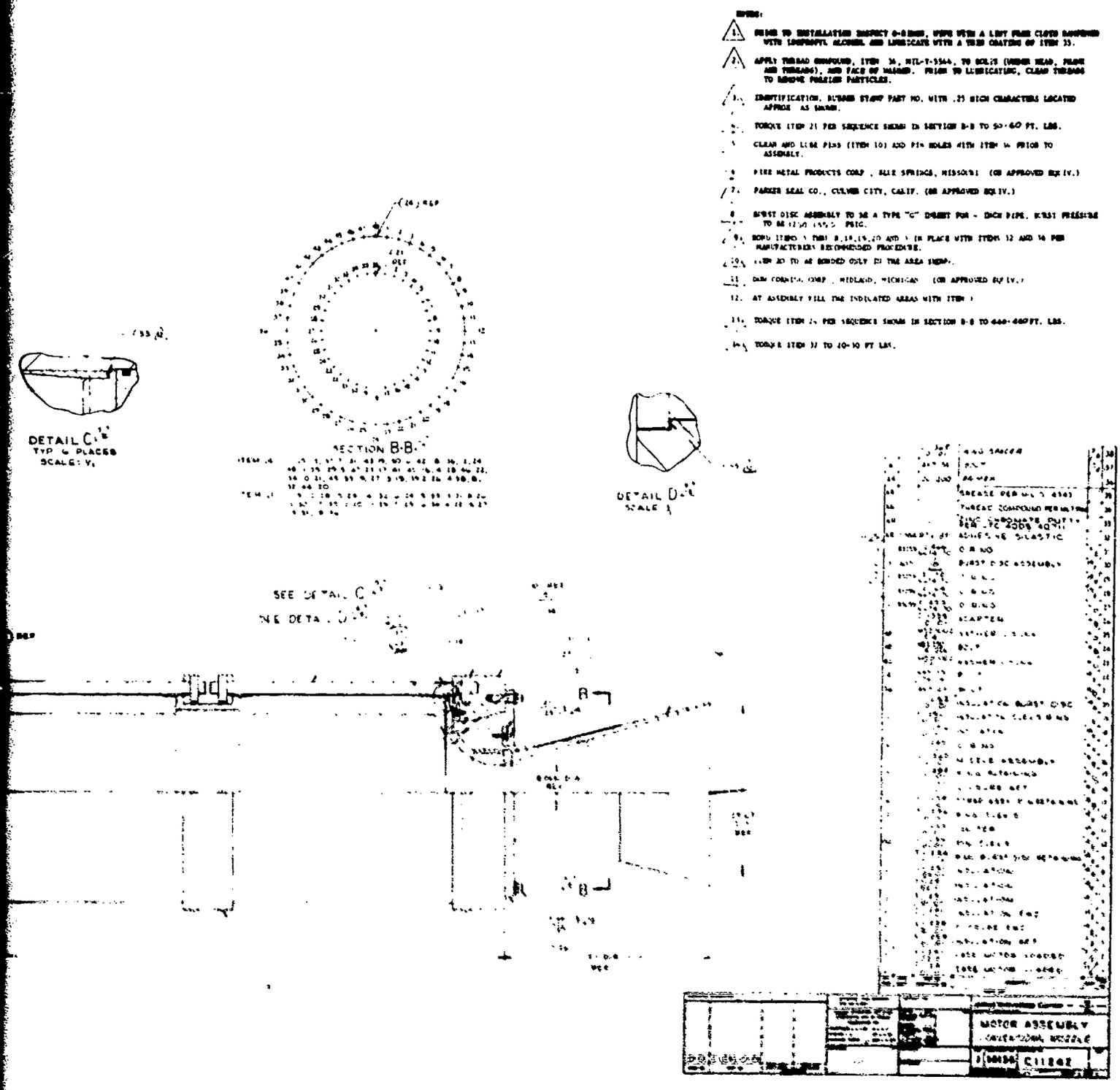

Figure 12. Motor Assembly, Conventional Nozzle Baseline Design

TABLE 7. BASELINE MOTOR WEIGHT SUMMARY

Component	Weight, lb
Forward closure	2,490
Case	8,570
Case attachments	1,140
Aft closure	1,291
Nozzle (conventional)	400
Nozzle attach ring	40
Insulation and liner	168
Igniter	2
Propellant	1,997
Total loaded motor	16,068
Handling tooling	750
Total weight	16,818
Maximum weight allowing for design growth	17,660

Motor processing equipment designs include casting mandrels for the centrally perforated double end-burning grain design, casting base plate, casting spider, and casting bell. Fixtures and shipping and storage pallets were designed for handling the loaded and unloaded motor segments. The loaded segments will be shipped and stored in approved shipping containers.

Conceptual designs were prepared for motor component handling and assembly equipment for use at the AFRPL test pad. This equipment is designed for vertical assembly of the motor adjacent to the thrust stand. The assembled motor will then be lowered horizontally with a rotating fixture and an overhead 15-ton crane. Design concepts have been generated for all equipment required for motor handling and assembly with the exception of the overhead crane which is already on the test pad.

The thrust stand is a single component, horizontal system capable of measuring axial thrust in ranges of 0 to 50,000 lb, 0 to 100,000 lb, and 0 to 150,000 lb. Thrust stand accuracy is within ±0.15% over the full range. The stand includes a deadweight calibrator for accurate calibration of axial thrust measurements.

The test motor is supported by flexures and cradle supports mounted on the thrust stand rails. To accommodate the various motor lengths, sections of the thrust stand rails with associated flexures and cradles will be removable. Accurate alignment upon assembly of these railings will be accomplished using tooling bars and dowel pins. This removable feature eliminates the need for thermal protection of the exposed rails. Protection may still be required for the concrete pad and the metal rails embedded in the pad. During the final design phase of the program a thermal analysis of the pad will be conducted to define the extent of necessary protection.

4.1 Motor Design

4.1.1 Case, Closure, Double Clevis, and Hardware Design Requirements

The preliminary design meets all AFRPL requirements, incorporates the results of performance optimization studies, and makes maximum use of UTC's experience. The design requirements that most influence motor case component design are shown in Table 8.

4.1.2 Design Description

4.1.2.1 Motor Case Assembly - The baseline configuration consists of a forward closure which contains the pressure relief subsystem, two full-length motor case segments, one one-half length segment, an aft closure, a nozzle assembly, and two double clevis rings (see Figures 11 and 12).

The segment-to-segment and segment-to-closure attachments use the clevis joint while a segmented key or bolts (depending on configuration) are used to attach the nozzle assembly to the aft closure.

The clevis pins are retained with circumferential straps and the segmented key is secured with standard high strength threaded fasteners. All joints use conventional O-rings to maintain internal pressure during motor firing.

A preliminary stress analysis has been performed on all motor case components to assure component structural capabilities and eliminate the need for major redesign during design review and final design phases. All motor case

TABLE 8. CRITICAL MOTOR CASE COMPONENT DESIGN REQUIREMENTS

Item	Requirement
MEOP, psia	200 to 1,800*
Overpressurization	Pressure relief system (1.25 x MEOP)
Factor of safety	1.5 on yield 3.0 on ultimate
Proof pressure, psia	1.3 x MEOP
Motor case inside diameter, in.	28.0 nominal
Motor case propellant grain lengths, in.	60 and 30
Total motor weight, lb	20,000

* Based on trade studies discussed in Section 3.1.3 of this report, the recommended chamber pressure range for the Super BATES motor is 200 to 2,200 psia. Therefore, an MEOP of 2,200 psia has been used as a design requirement.

components will be hydrotested to a proof pressure of 1.3 times MEOP (2,860 psia) to demonstrate structural integrity. This pressure is well below the pressure required to cause permanent deformation of case components. Corrosion and environmental protection of all components will be provided by an acrylic coating system.

All components will be identified with the following:

A. Serial number

B. Pressure rating

C. Weight

D. Factor of safety (minimum)

E. Date of manufacture.

4.1.2.2 Motor Case - The basic motor case segment is 70.54 in. long with a 28-in. inside diameter and a 1.75-in. minimum wall thickness. The case is fabricated from high pressure steel pipe per ASTM 135 class 1. The length and diameter of the case were selected based on performance optimization studies presented in Section 3.0. The case wall is sized for an MEOP of 2,200 psia with the required

factor of safety of 1.5 on yield stress. The ASTM specification governing the high pressure pipe requires a normalizing procedure after welding; therefore, no efficiency loss is encountered in the weld joint.

The case ends are machined to close tolerance on the inside diameter to provide the required sealing surface to mate with the O-ring seal(s) located in the double clevis ring(s) and closures. The case is pinned to both closures and clevis rings using 32 clevis pins at each interface. The case material and fabrication process were selected to minimize cost and to provide high reliability for extended use.

4.1.2.3 Closures - Flat plate closures were selected for the motor to minimize fabrication costs and simplify the closure-insulation interface. Although more raw material is required, flat plate closures are less expensive than dished heads welded to joint-area forgings. By avoiding curved interfaces with insulation, cost of fabricating the insulators is greatly reduced. If closure insulation contours typical of flight motors are required, the insulation may be machined to contour without a contoured structural shell. Two closures (one forward and one aft) will be provided to meet all program requirements for the various nozzle configurations; submerged and nonsubmerged nozzles are to be accommodated with nozzle throat diameters up to 12 in. The 11-in. plate thickness is needed for the forward closure to withstand bending stresses from internal pressure and to accommodate the pressure relief system described in Section 4.1.9. The resulting forward closure weight is 2,490 lb. The aft closure is 8-in. thick and weighs 1,291 lb. The closure material is ASTM A266 steel, at an ultimate tensile strength of 60 ksi and a yield strength of 30 ksi. Two pressure taps are provided in each closure.

All closures include clevis joint features for attachment to the segment cylinder; these are identical in design philosophy to that successfully demonstrated on the HIPPO motor. Since the motor closures are heavyweight and extremely rigid, no problem exists in withstanding the thrust vector loadings of nozzles during the startup transient when the nozzle is usually unsymmetrically separated.

A stress analysis was conducted on the forward and aft closures to ensure that yield stresses are not exceeded under loading with a factor of safety of 1.5. The possible loading includes internal pressurization with an MEOP of 2,200 psia and motor restraint due to contact between a thrust plate and the forward closure.

4.1.2.4 Double Clevis Ring - A clevis type pin joint was selected to connect the closures to the motor case and the segments to each other. This configuration has been used on the HIPPO test motor and is a highly reliable, easily assembled, simple configuration. The clevis pin joint contributes to low case fabrication cost since a simple cylindrical configuration can be used.

The double clevis rings are fabricated from ASTM A266 steel forgings with 60-ksi ultimate tensile strength and 30-ksi yield. The ring incorporates O-ring glands which interface with the inside diameter of the motor case to provide the required seal for internal operating pressure. Thirty-two pins are used at each segment/ring interface. The pins are 1.25 in. in diameter and are fabricated from 4340 steel heat treated to 180-ksi ultimate tensile strength. The pins are retained by a circumferential strap around each pin joint.

4.1.2.5 Nozzle Attachment Joints - Two basic attachment joint designs provide the desired variability in motor-nozzle configurations while using only one aft closure configuration. These are the standard bolted flange type joint and a segmented ring (or segmented key) type joint. UTC-designed segmented ring joints have demonstrated reliable performance and ease of assembly in 16-, 42-, and 45-in.-diameter test motors. For assembly, four ring segments are engaged in a circumferential slot either in the nozzle outside diameter or adapter inside diameter depending upon the desired motor nozzle configuration. Bolts hold the ring segments in place before motor pressurization. Under pressure, nozzle ejection forces are resisted by the shear strength of the ring segments.

Examples of the attachment methods for various nozzle configurations that can be tested with this design are shown in Figures 13 through 17. Using a single aft closure and one adapter, submerged nozzles with throat diameters ranging from 4 to 10 in. can be tested at degrees of submergence of 3, 6, 10, 14, and 18 in. With a second adapter, conventional nozzles with a 45° entrance angle and 4 to 10 in. throat diameters can be tested with the same aft closure. A conventional nozzle with a 12-in. throat diameter can be attached to the closure with a bolted flange type joint. If testing of 12-in.-diameter submerged nozzles is desired, a separate aft closure design would be required; the aft closure will probably be an integral part of the nozzle flange.

The adapter configurations are shown in Figures 18 and 19. These configurations are designed to function under a motor MEOP of 2,200 psia with a safety factor of 3 based upon a minimum ultimate tensile strength of 125,000 psi.

4.1.2.6 Joint Seals - Because of their many advantages, O-rings are used almost exclusively in solid rocket motors for pressure integrity. Conventional elastomeric O-ring seals were selected because they reliably seal joints with relatively loose tolerances. Reliability of O-ring seals has been demonstrated on the HIPPO motor at pressure levels over 3,000 psia using both Viton and Buna-N O-rings. Design parameters including tolerance control, surface finish, and material property requirements for O-rings have been well established by past experience. A test program will be conducted to verify seal integrity and provide additional data on allowable sealing surface tolerances. If required, seal wedge rings to prevent O-ring extension can be incorporated with minimum design change at a later time.

4.1.2.7 Structural Analysis - Although the Super BATES motor design (UTC assembly drawing C-11242) is considered to be a preliminary design, structural analysis has been performed on all major motor components and they have been structurally approved for manufacturing and test operations. The major components which have been analyzed in detail are

A. Segment cases
B. H-clevis joint
C. Forward closure

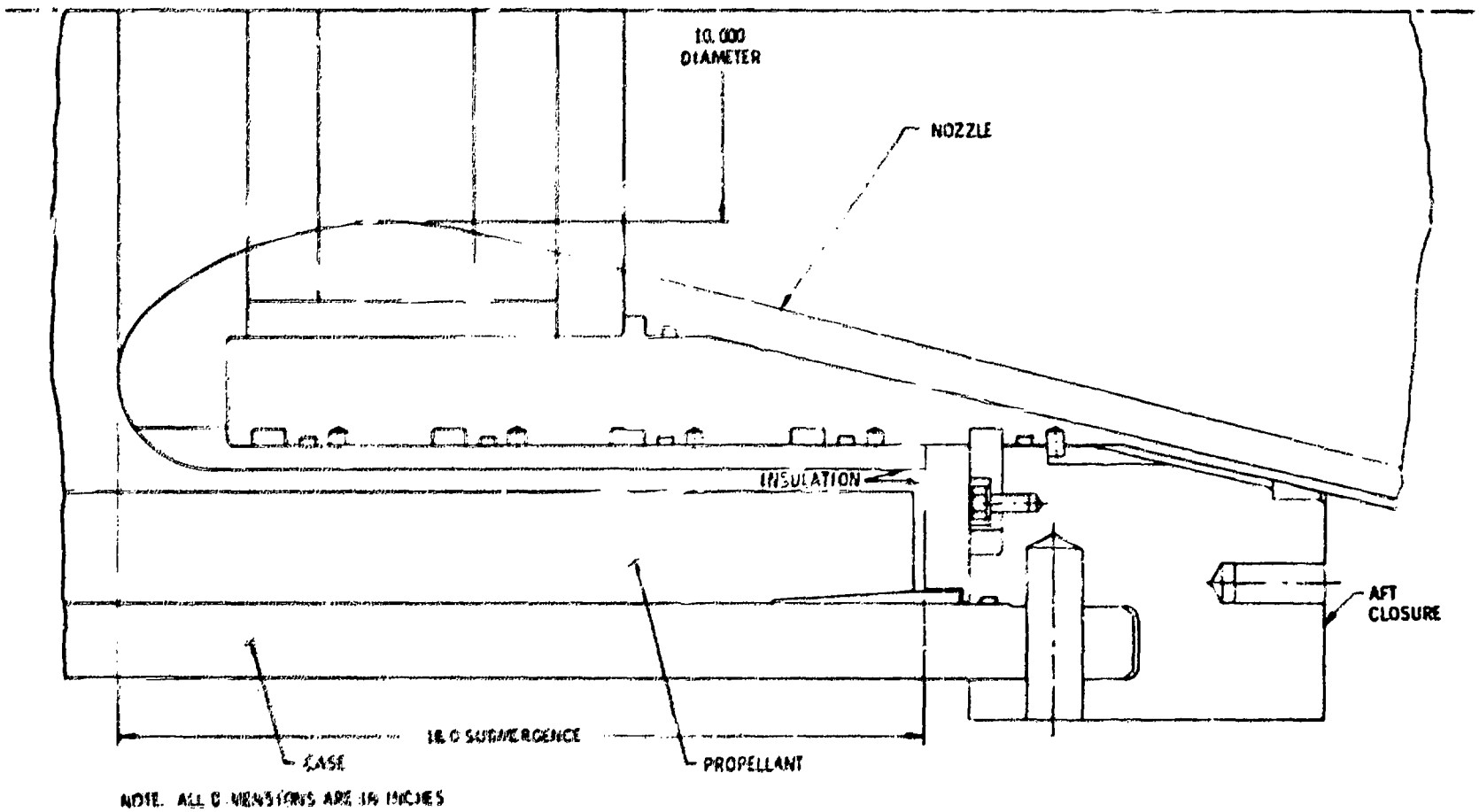

Figure 13. 10-In.-Diameter Submerged Nozzle

05904

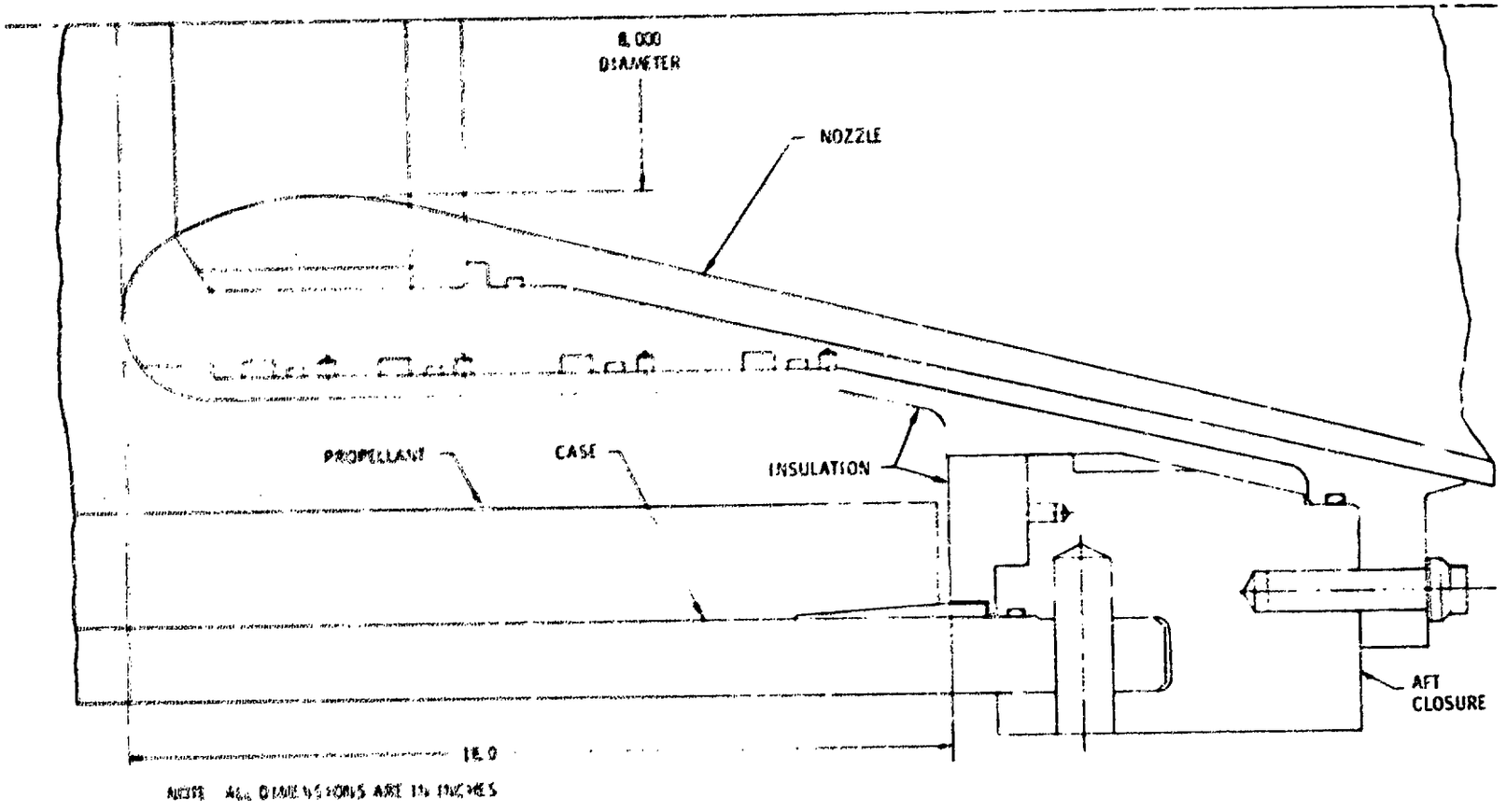

Figure 14. 8-In.-Diameter Nozzle Submerged 18 In.

05905

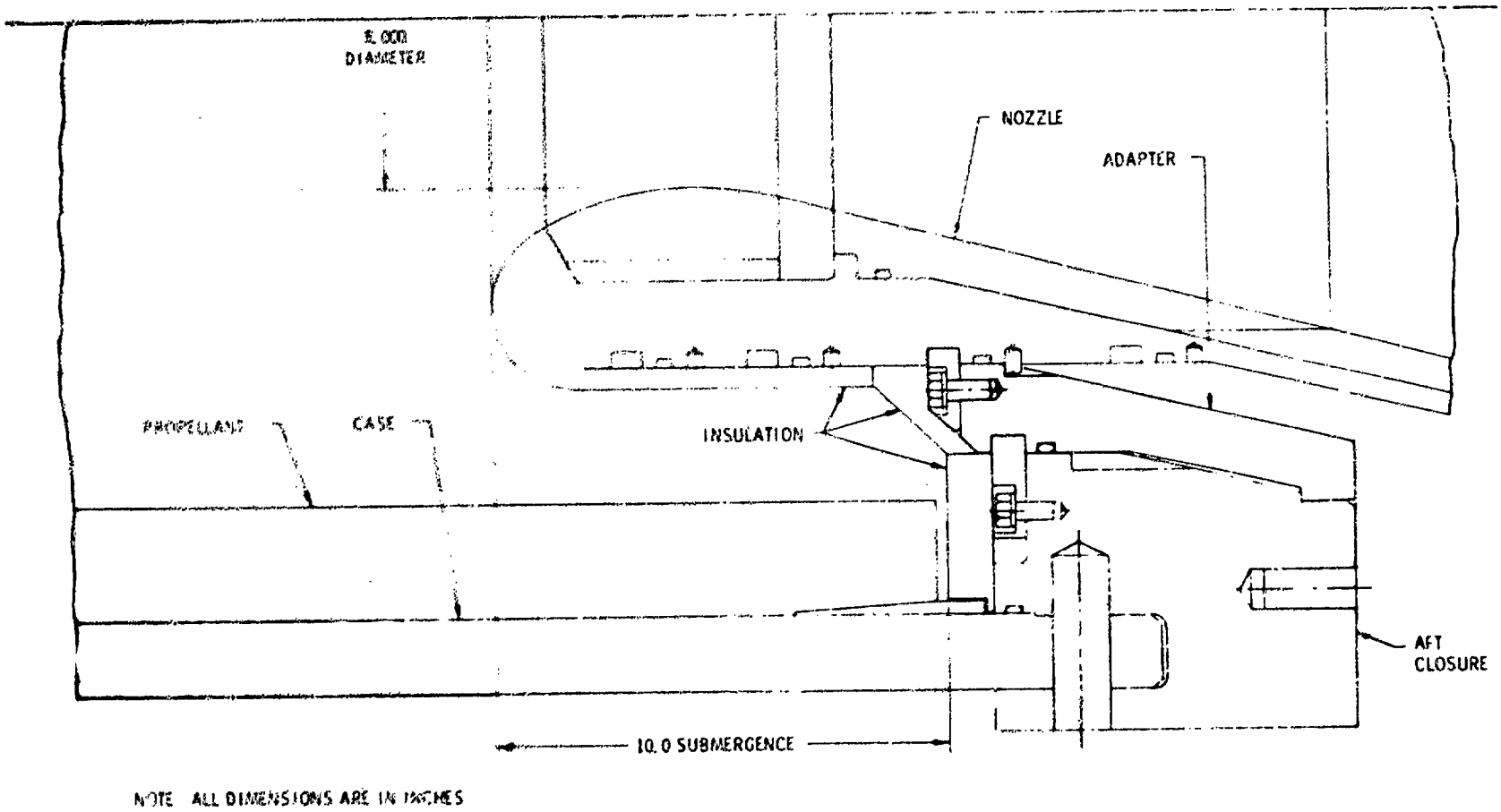

Figure 15. 8-In.-Diameter Nozzle Submerged 10 In.

05906

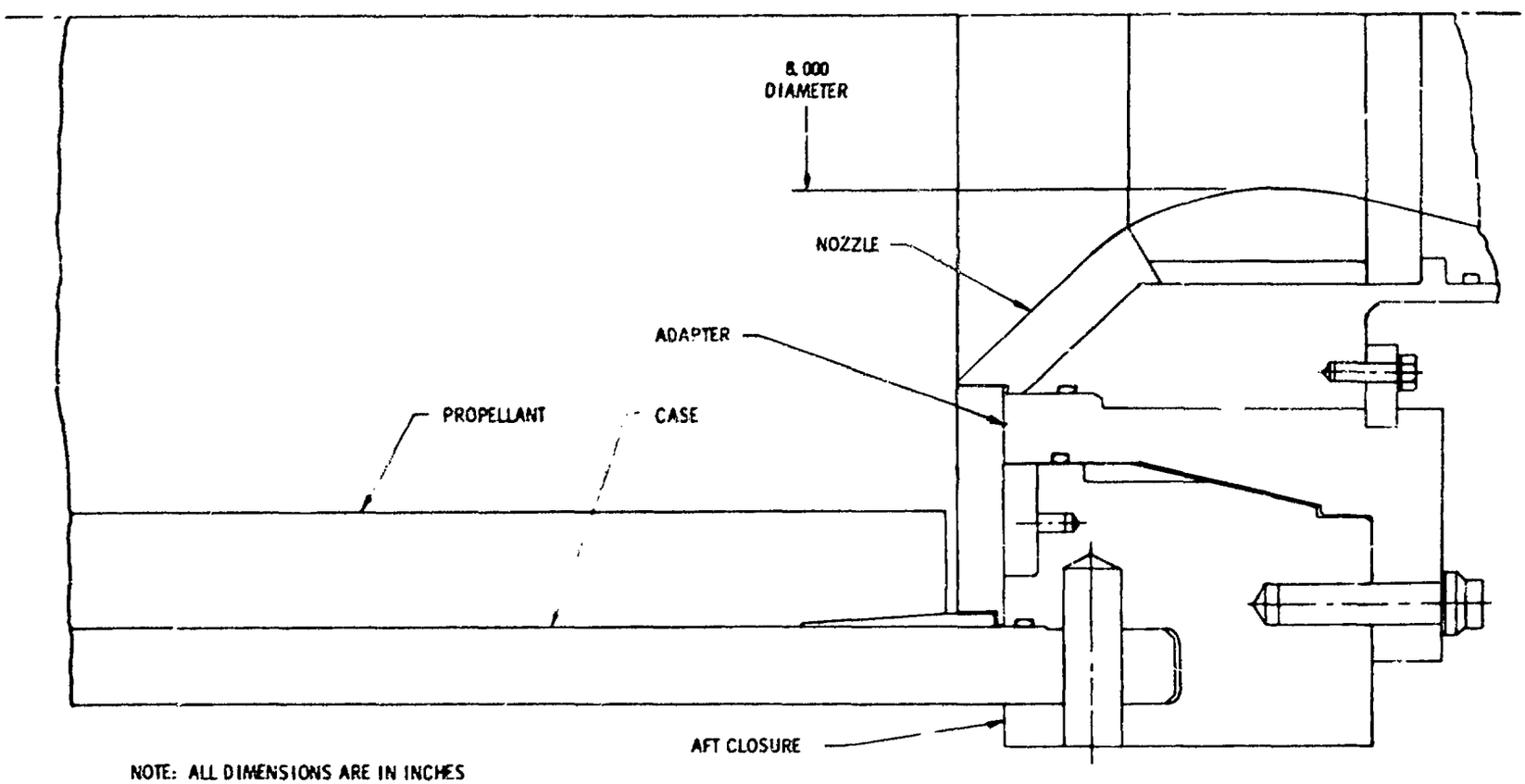

Figure 16. 8-In.-Diameter Conventional Nozzle

05907

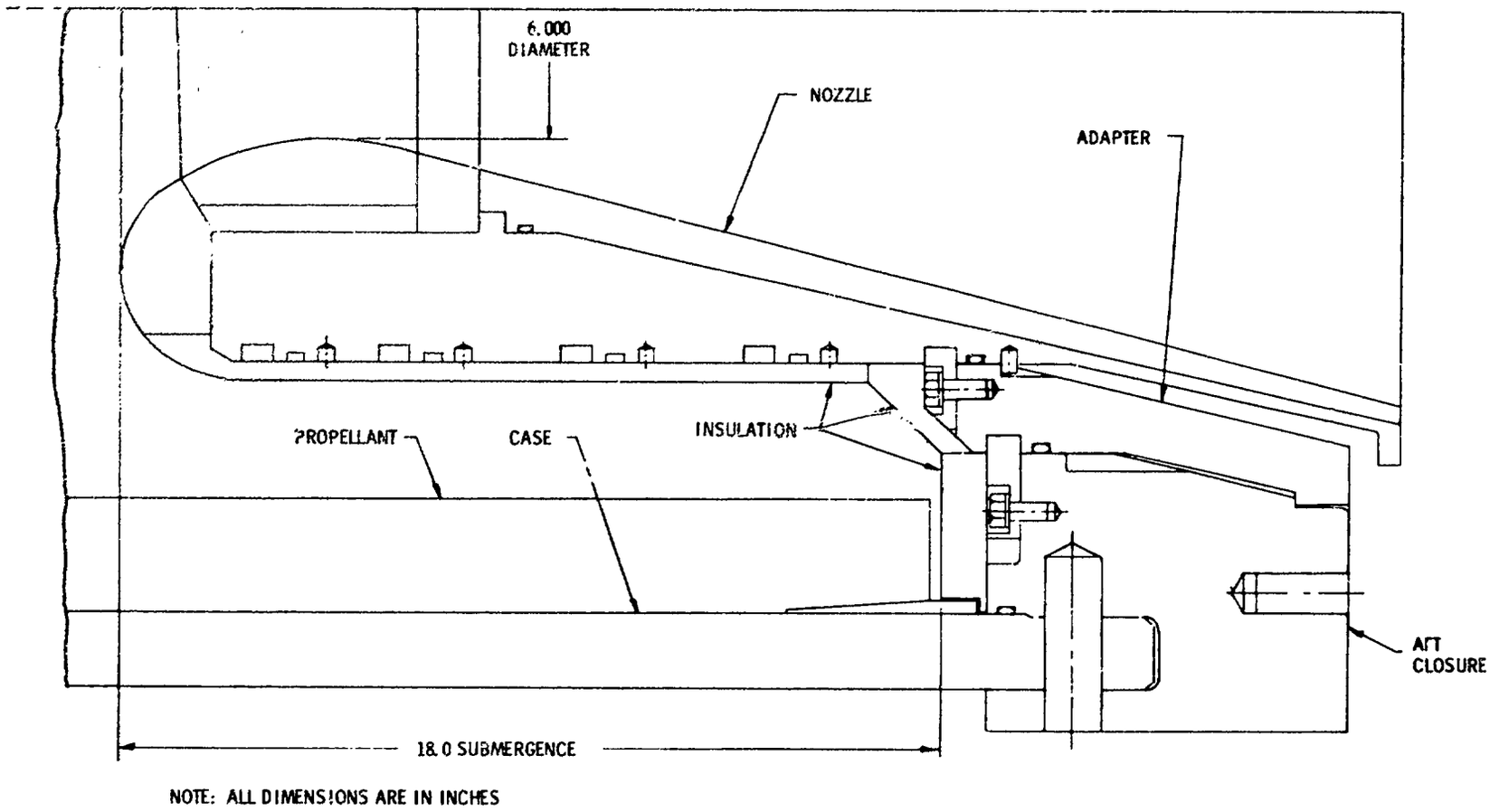

Figure 17. 6-In.-Diameter Nozzle Submerged 18 In.

05908

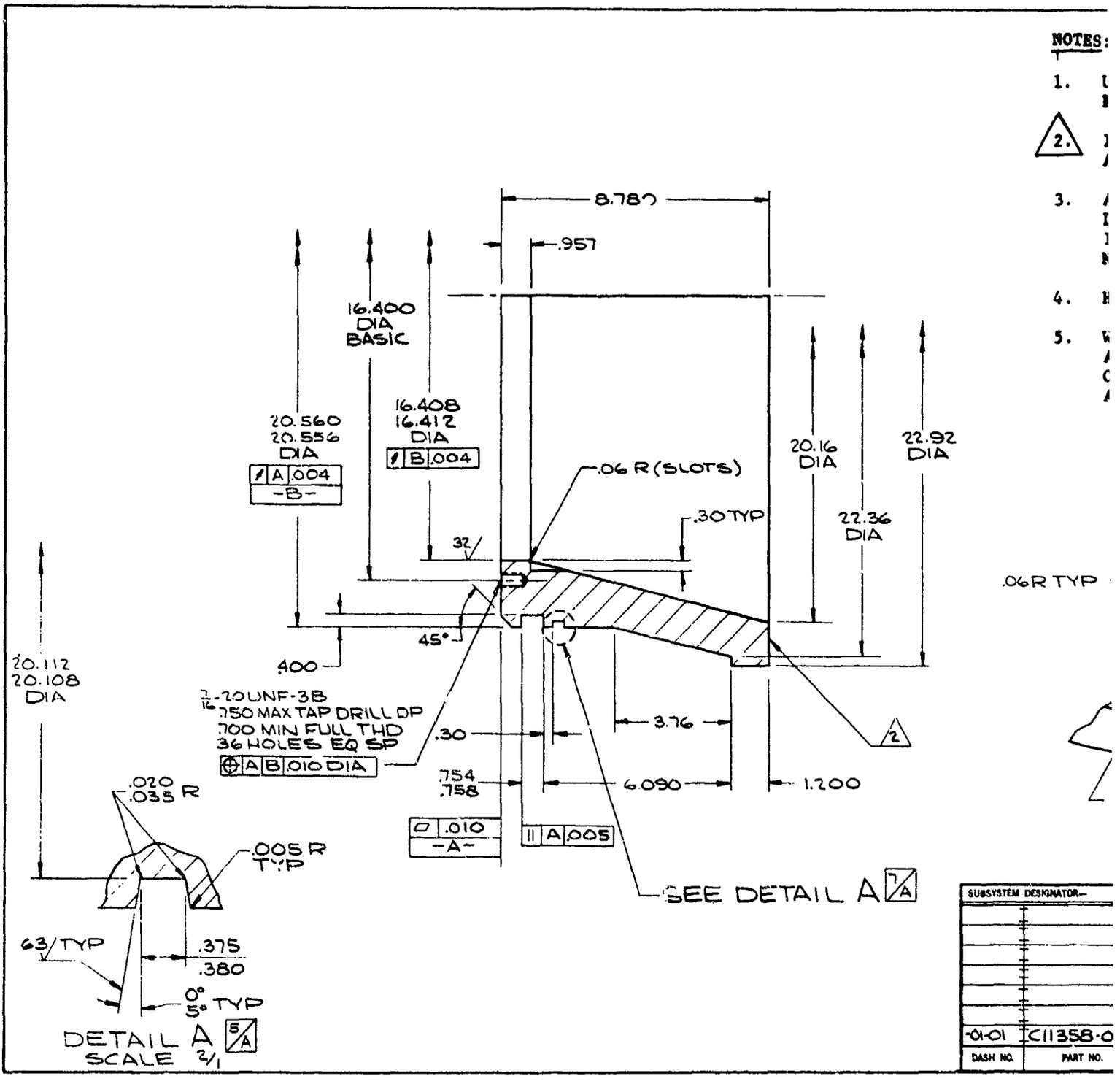
8.780
.957
16.400
DIA
BASIC
20.560
20.556
DIA
⌀ A .004
-B-
16.408
16.412
DIA
⌀ B .004
.06 R (SLOTS)
.30 TYP
20.16
DIA
22.92
DIA
22.36
DIA
32
45°
.400
20.112
20.108
DIA
7/16-20 UNF-3B
.750 MAX TAP DRILL DP
.700 MIN FULL THD
36 HOLES EQ SP
⌖ A B .010 DIA
.30
3.76
.754
.758
6.090
1.200
⌭ .010
-A-
// A .005
.020
.035 R
.005 R
TYP
63/TYP
.375
.380
0°
5° TYP
DETAIL A
SCALE 2/1
5/A
SEE DETAIL A 7/A
2
.06R TYP
NOTES:
1.
2.
3.
4.
5.
SUBSYSTEM DESIGNATOR—
-01-01
DASH NO.
C11358-0
PART NO.

NOTES:

1. UNLESS OTHERWISE SPECIFIED: REMOVE ALL BURRS, BREAK ALL SHARP EDGES .0050-.030. ALL FILLET RADII TO BE .030 RAD. MAX.

2. IDENTIFY BY STEEL STAMPING PART NUMBER USING ¼ INCH HIGH CHARACTERS LOCATED APPROXIMATELY AS SHOWN.

3. ACCEPTABLE ALTERNATE IS 4340 STEEL PER MIL-S-5000 FABRICATED AS A WELDMENT WITH LOCATION AND TYPE OF WELDS TO BE APPROVED BY UTC. WELDS SHALL BE RADIOGRAPHICALLY INSPECTED PER MIL-STD-453. ACCEPTANCE CRITERIA SHALL BE PER NAS 1514, CLASS III. NO CRACKS OR CRACKLIKE DEFECTS ARE ALLOWED.

4. HEAT TREAT PER MIL-H-6875 TO 125,000 PSI MINIMUM ULTIMATE TENSILE STRENGTH.

5. WET CONTINUOUS MAGNETIC PARTICLE INSPECT ALL SURFACES PER MIL-I-6868. CONCENTRATION AND VISCOSITY OF SUSPENSION SHALL BE WITHIN THE LIMITS OF PARAGRAPH 5.1.2. METHOD OF MAGNETIZATION TO BE AC TO TWO DIRECTIONS. USE FLUORESCENT PARTICLES. NO CRACKS ALLOWED.

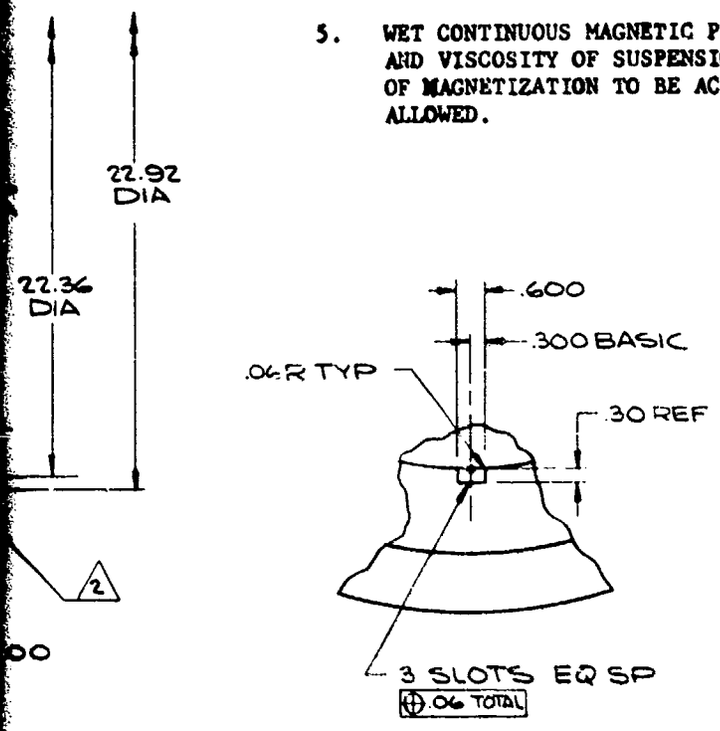

QTY REQD	CODE IDENT	PART OR IDENTIFYING NO.	DESCRIPTION	ZONE	ITEM NO.

PARTS LIST

SUBSYSTEM DESIGNATOR—

INTERPRET THIS DRAWING PER MIL-D-1000

UNLESS OTHERWISE SPECIFIED DIMENSIONS ARE IN INCHES
TOLERANCES ON:
FRACTIONS ± 1/16 .X ± .1
ANGLES ± 2° .XX ± .03
SURFACE FINISH 125 √ .XXX ± .005

CONTRACT NO.

United Technology Center — U
A.

ADAPTER, NOZZLE
SUBMERGED
NOZZLE

MATERIAL
STEEL 4130
PER MIL-S-6758

DASH NO.	PART NO.	NEXT ASSY	USED ON
-01-01	C11358-01-01		

APPLICATION

SIZE	CODE IDENT NO	DRAWING NO.	REV
D	14134	C11358	

SCALE 1/8 WEIGHT SHEET 1 OF 1

Figure 18. Adapter, Submerged Nozzle

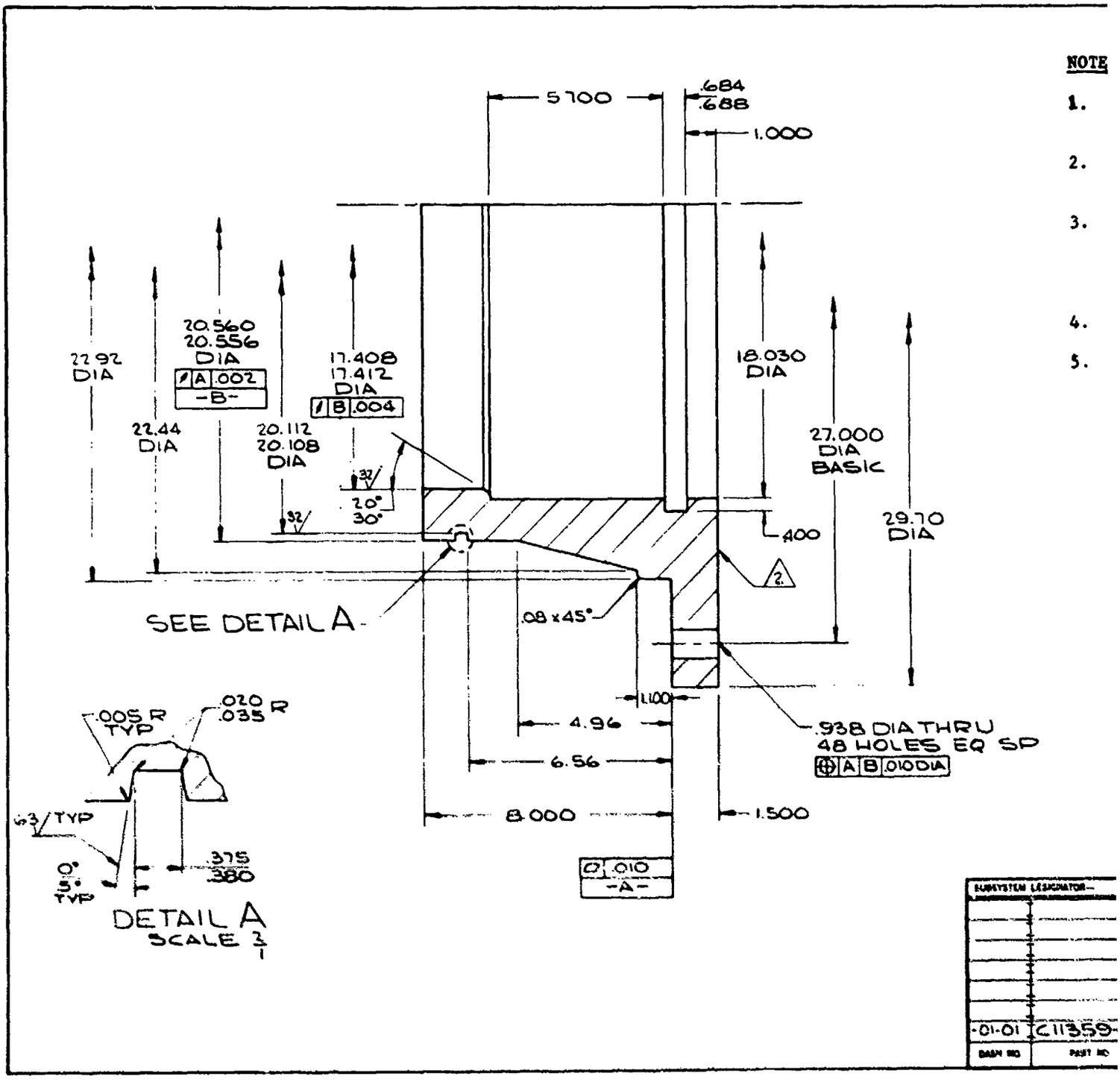
NOTE
1.
2.
3.
4.
5.
5.700
.684
.688
1.000
22.92
DIA
20.560
20.556
DIA
A .002
-B-
17.408
17.412
DIA
B .004
18.030
DIA
22.44
DIA
20.112
20.108
DIA
32
32
20°
30°
27.000
DIA
BASIC
29.70
DIA
.400
2.
SEE DETAIL A
.08 x 45°
1.100
4.96
6.56
8.000
1.500
.938 DIA THRU
48 HOLES EQ SP
⌖ A B .010 DIA
0 .010
-A-
.005 R
TYP
.020
.035 R
63
TYP
0°
5°
TYP
.375
.380
DETAIL A
SCALE 3/1
SUBSYSTEM DESIGNATOR
-01-01
C11359-
DASH NO
PART NO

NOTES:

1. UNLESS OTHERWISE SPECIFIED: REMOVE ALL BURRS, BREAK ALL SHARP EDGES .005 -.030. ALL FILLET RADII TO BE .030 RAD. MAX.

2. IDENTIFY BY STEEL STAMPING PART NUMBER USING ¼ INCH HIGH CHARACTERS LOCATED APPROXIMATELY AS SHOWN.

3. ACCEPTABLE ALTERNATE IS 4340 STEEL PER MIL-S-5000 FABRICATED AS A WELDMENT WITH LOCATION AND TYPE OF WELDS TO BE APPROVED BY UTC. WELDS SHALL BE RADIOGRAPHICALLY INSPECTED PER MIL-STD-453. ACCEPTANCE CRITERIA SHALL BE PER NAS 1514, CLASS III. NO CRACKS OR CRACKLIKE DEFECTS ARE ALLOWED.

4. HEAT TREAT PER MIL-H-6875 TO 125,000 PSI MINIMUM ULTIMATE TENSILE STRENGTH.

5. WET CONTINUOUS MAGNETIC PARTICLE INSPECT ALL SURFACES PER MIL-I-6868. CONCENTRATION AND VISCOSITY OF SUSPENSION SHALL BE WITHIN THE LIMITS OF PARAGRAPH 5.1.2. METHOD OF MAGNETIZATION TO BE AC TO TWO DIRECTIONS. USE FLUORESCENT PARTICLES. NO CRACKS ALLOWED.

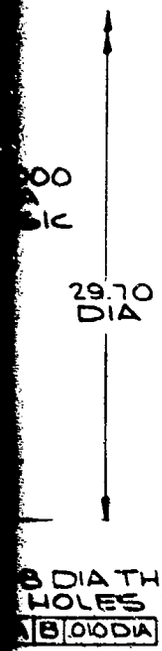

QTY REQD	CODE IDENT	PART OR IDENTIFYING NO	DESCRIPTION	ZONE	ITEM NO
			PARTS LIST		

DASH NO	PART NO	NEXT ASSY	USED ON
-01-01	C11359-01-01		

APPLICATION

SUBSYSTEM DESIGNATOR—

INTERPRET THIS DRAWING PER MIL-D-1000

UNLESS OTHERWISE SPECIFIED DIMENSIONS ARE IN INCHES
TOLERANCES ON:
FRACTIONS ± 1/16 .X ± .1
ANGLES ± 2° .XX ± .03
SURFACE FINISH √ .XXX ± .010

MATERIAL STEEL, 4130 PER MIL-S-6758

CONTRACT NO

DRAWN
CHECKED
DESIGN
APPROVED
APPROVED

DATE

United Technology Center — U A.

ADAPTER NOZZLE
CONVENTIONAL NOZZLE

SIZE	CODE IDENT NO	DRAWING NO.	REV
D	14134	C11359	

SCALE 1/2 WEIGHT SHEET 1 OF 1

Figure 19. Adapter, Conventional Nozzle

D. Aft closure

E. Case bonded propellant grain

F. Nozzle.

A thermal stress analysis of the nozzle insert has yet to be performed for temperature gradients induced immediately after ignition. Previous experience with similar crystalline graphite rings (on contract No. F04611-70-C-009) has shown that these thermal stresses will not be a limiting factor where there is stiff structural support for the ring such as the steel shell used for this design.

Further structural analysis will be done on the burst disc assembly and on thermal stresses in the crystalline graphite throat inserts mentioned above.

Methods of analysis included:

A. Case, closures, H-clevis - A standard finite element analysis for axisymmetric isotropic bodies was used because of the need to calculate displacements. Displacements are used to calculate seal margins of safety, and to analyze clevis joints. A finite element analysis is performed for each of the joint components for two arbitrarily selected distributions of the axial load on the female lugs. The finite methods used and the deformed outlines calculated are shown in Figures 20 through 27.

The first distribution assumes that both female lugs in a clevis joint carry equal loads; the second assumes that the inside lug carries 60% of the axial load and the outer lug 40%. By using the influence coefficients obtained from these solutions, the correct load distribution and the correct displacements at the clevis joint seals are obtained.

Pin shear bearing and tear-out margins were determined by hand calculations.

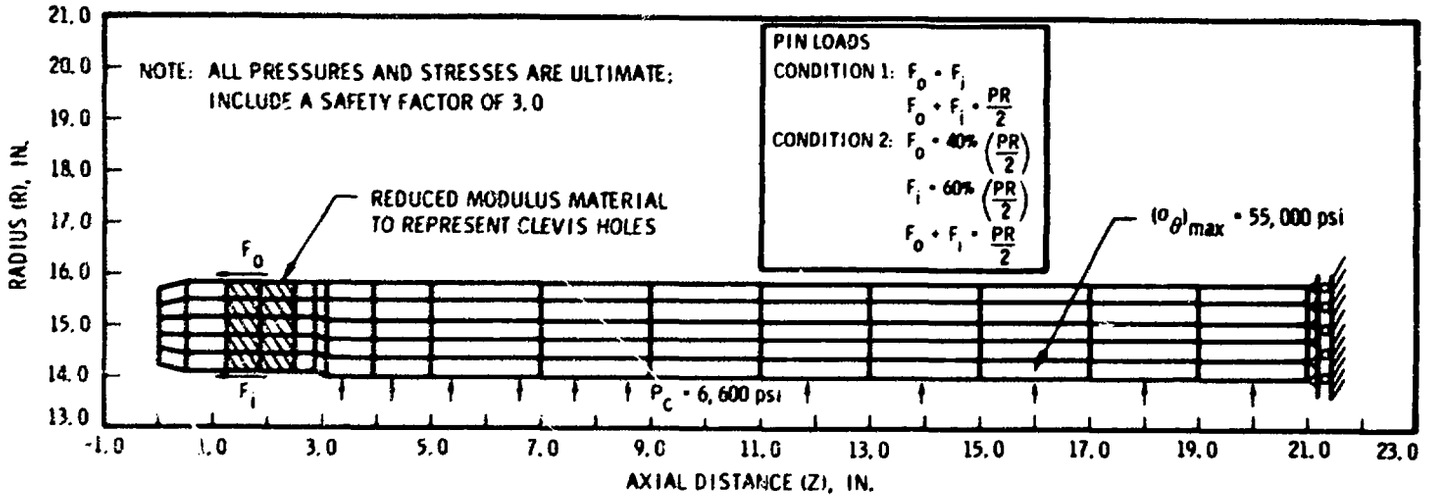

Figure 20. Motor Case Loads and Maximum Stresses

05882

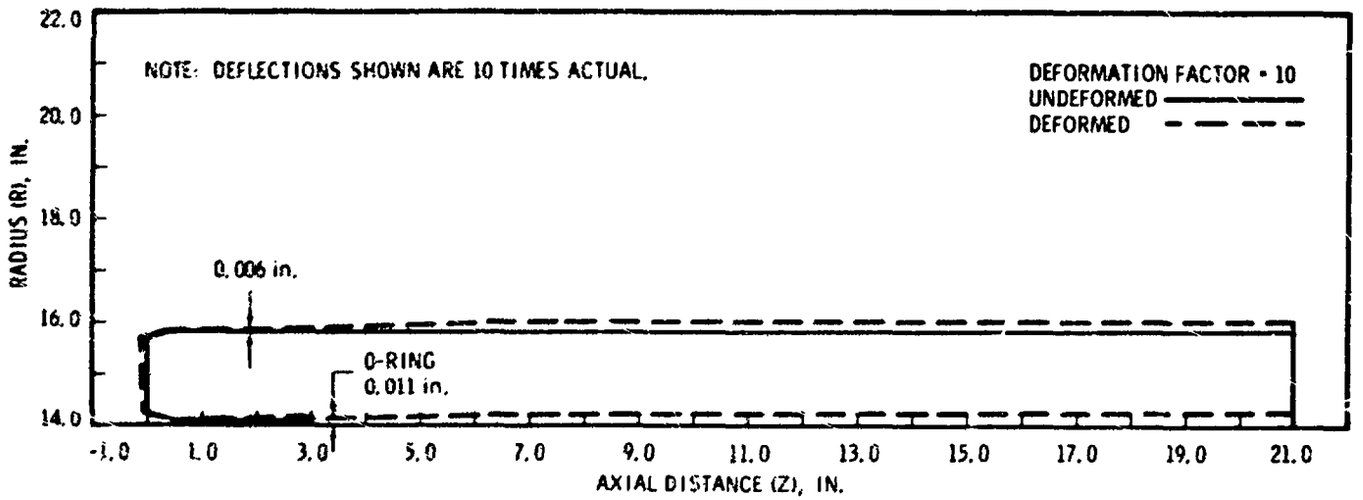

Figure 21. Motor Case Deformed Outline

05883

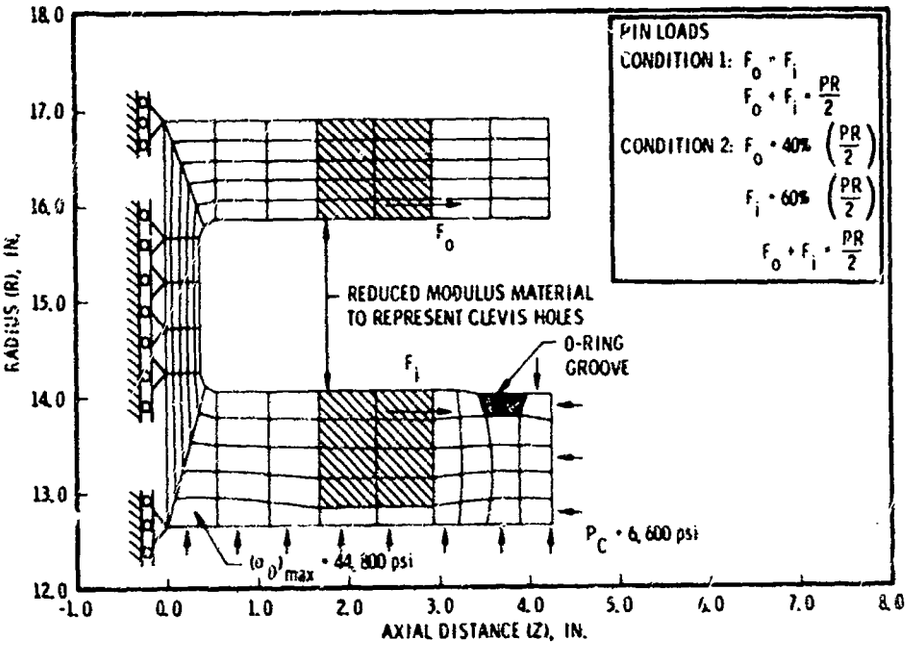

Figure 22. Clevis Ring Loads and Maximum Stresses

05884

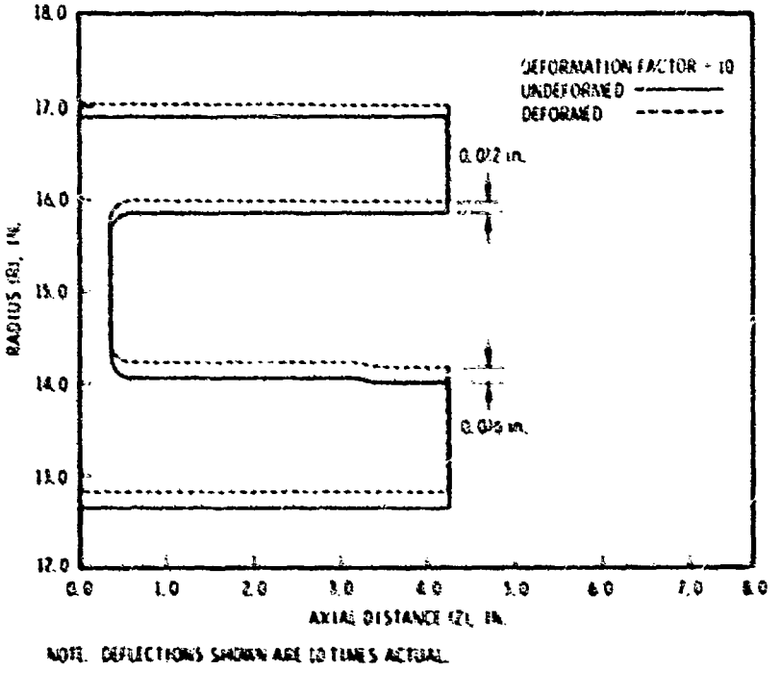

Figure 23. Clevis Ring Deformed Outline

05885

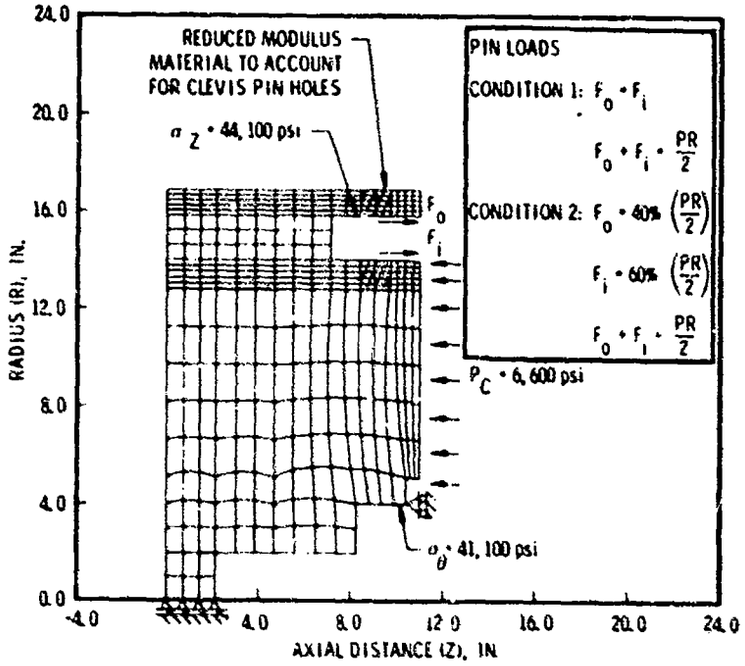

Figure 24. Forward Closure Loads and Maximum Stresses

05886

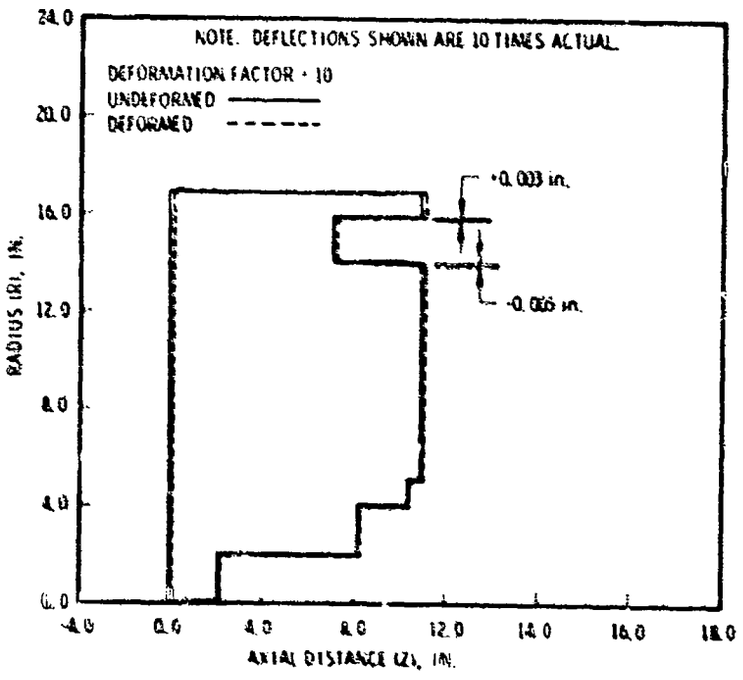

Figure 25. Forward Closure Deformed Outline

05887

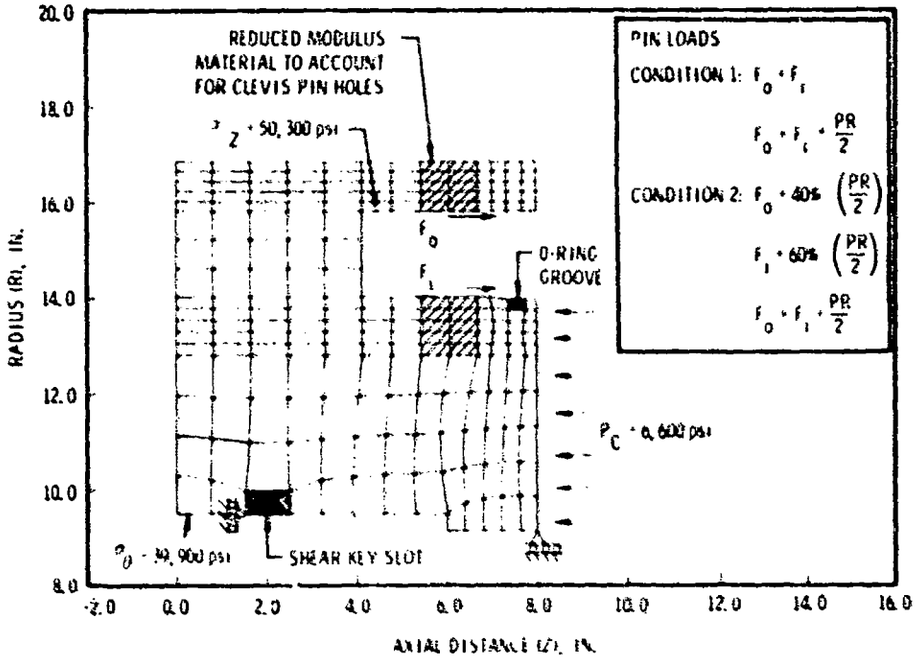

Figure 26. Aft Closure Loads and Maximum Stresses

05888

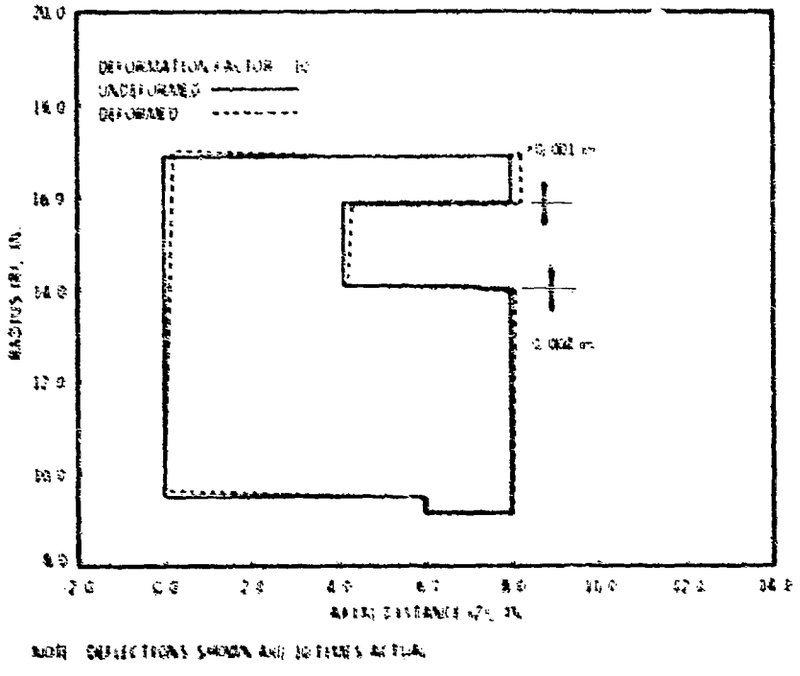

Figure 27. Aft Closure Deformed Outline

05889

B. Nozzle – Structurally analyzed primarily for ejection loads since no thermal stress problems are anticipated in the insulation due to the heavyweight steel shell.

C. Propellant grain – Analyzed by hand calculations.* Because of the very low case/bore diameter ratio and moderate storage conditions, grain margins of safety are high.

All components analyzed have positive margins of safety after required factors of safety have been applied. A safety factor of 3 is applied to loads to determine the ultimate load which the hardware is required to carry; a safety factor of 1.5 is applied to give the loads at which there should be no yield in the metal structures.

A comprehensive list of margins of safety will be provided with the final design configuration.

The deformation of all clevis joint lugs is determined to be sufficiently small so there will be no leakage past properly installed O-rings.

4.1.3 Case, Closure, and Clevis Ring

4.1.3.1 Materials and Properties – The Super BATES motor case is composed of three case segments, forward and aft closures, and clevis rings. High strength steel forgings per ASTM-A-266 are used for the closures and clevis joint. The material for the segments is ASTM-A-515, ASTM-A-516 or equivalent, capable of being heat treated to a minimum ultimate tensile strength of 60,000 psi and a minimum 0.2% offset yield strength of 30,000 psi. This material is fabricated into either extruded or fusion-welded pipes per ASTM-A-155 class 1.

These ASTM grades were selected on the basis of availability, cost, reliability, and related experience with similar applications and configurations. The primary material for the motor case is ASTM-A-516 grade 60 with an alternate

* Hufferd, W. L., and J. E. Fitzgerald, NASNAF Solid Propellant Structural Integrity Handbook, CPIA Publication 230, September 1972.

material of ASTM-A-515 grade 60. Both of these materials are intended for pressure vessel applications, however the ASTM-A-516 meets the fine grain requirements, is more amenable to fabrication (i.e., rolling, welding, machining, etc.), and has been fabricated into pressure vessels by UTC for its heavyweight 45-in. motor program (test motor for C4). Chemical and mechanical properties for these alloys are shown in Table 9.

The material for the forward and aft closures and clevis rings is a carbon steel forging conforming to ASTM-A-266 class 1. This material has been used extensively for heads and covers in thicknesses proposed for the design. Chemical and mechanical properties are shown in Table 10.

4.1.3.2 Fabrication and Material Testing - The Super BATES motor case is fabricated either as an extruded pipe or as an electric fusion welded steel pipe per ASTM-A-155 class 1. The roll and weld method is the primary method. This process has been selected because of the high quality requirements of this specification and related experience of similar configurations. The selected plate material, ASTM-A-516, is rolled and fusion welded per ASME code VIII (qualified per Section IX, and stress relieved per Section VIII, paragraph UW-40). The welded cylinder is heat treated (normalized and tempered) and radiographically inspected per ASME code, Section VIII, paragraph UW-51. The welded pipe is machined on the entire inside diameter surface and on the ends for the mechanical joints. The remaining outer surface is as-fabricated provided weld mismatch is within that allowed by the design. The motor case is 100% magnetic particle inspected and the longitudinal weld is radiographically inspected before and after hydrotest. The accepted case is cleaned and coated with a suitable protective compound for storage.

The forward and aft closures are machined from normalized and tempered steel per ASTM-A-266 class 1. After machining, all surfaces are 100% magnetic particle inspected per MIL-I-6868. The clevis ring is also finish-machined from a pierced blank or ring rolled forging and tested in like manner.

TABLE 9. PROPERTIES OF CANDIDATE MATERIALS, GRADE 60

	ASTM-A-515	ASTM-A-516
Chemistry, %		
C, maximum	0.29	0.25
Mn, maximum	0.90	1.20
P, maximum	0.35	0.035
S, maximum	0.040	0.040
Si	0.15/0.30	0.15/0.30
Mechanical Properties		
Ultimate tensile strength, ksi	60/72	60/72
Yield strength, minimum, ksi	32	32
Elongation (2 in.), minimum, %	25	25
Grain size, per ASTM-E-112	1-5	5 or finer

TABLE 10. CHEMICAL AND MECHANICAL PROPERTIES OF CANDIDATE MATERIALS, CLOSURES, AND CLEVIS RING

	ASTM-A-266
Chemistry, %	0.35
C, maximum	0.35
Mn	0.40/0.90
P, maximum	0.040
S, maximum	0.040
Si	0.15/0.35
Mechanical Properties	
Ultimate tensile strength, ksi	60 minimum
Yield strength, ksi	30 minimum
Elongation (2 in.), minimum, %	23
R/A, minimum, %	38

4.1.4 Nozzle Design

4.1.4.1 Design Requirements - The following requirements were established for the nozzle designs:

A. Two nozzle configurations are required: a submerged nozzle that allows for 3, 6, 10, 14, and 18 in. submergence; and a conventional nozzle with a 45° inlet angle. Both have a throat diameter of 8 in.

B. The expansion ratio for both nozzle designs is optimum for sea level conditions with the exit cone half-angle equal to 15°.

C. The nozzle structural housings are designed to a motor MEOP of 2,200 psi. The ablative and insulative components are designed for operation using the control propellant at chamber conditions of 1,000 psi for 6.2 sec.

D. The inlet radius of curvature on both nozzles is 1.5 to 2.0 times the throat radius.

4.1.4.2 Design Description - The two nozzle configurations are shown in Figures 28 and 29 (UTC drawings C11357 and C11360).

The nozzles are designed with heavyweight, low-cost steel shells with a safety factor of 3.0 on MEOP (2,200 psia) based on a minimum ultimate tensile strength of 125,000 psi. The shells provide structural support for all the nonmetallic components. The submerged nozzle shell attaches to an adapter that also attaches to the aft closure with a segmented r taining ring joint. The conventional nozzle shell mounts to an adapter with a segmented retaining ring joint; the adapter attaches to the aft closure with a bolted joint.

The submerged nozzle is shown at the maximum degree (18 in.) of submergence in Figure 14. A reduced degree of submergence is achieved by installing the adapter between the nozzle and aft closure as shown in Figure 15.

In keeping with current design practices, the entrance contour of the submerged nozzle is defined by circular arcs approximating a 3 to 2 ellipse with the nose tip stagnation point at an area ratio of 3 to 1 and the throat

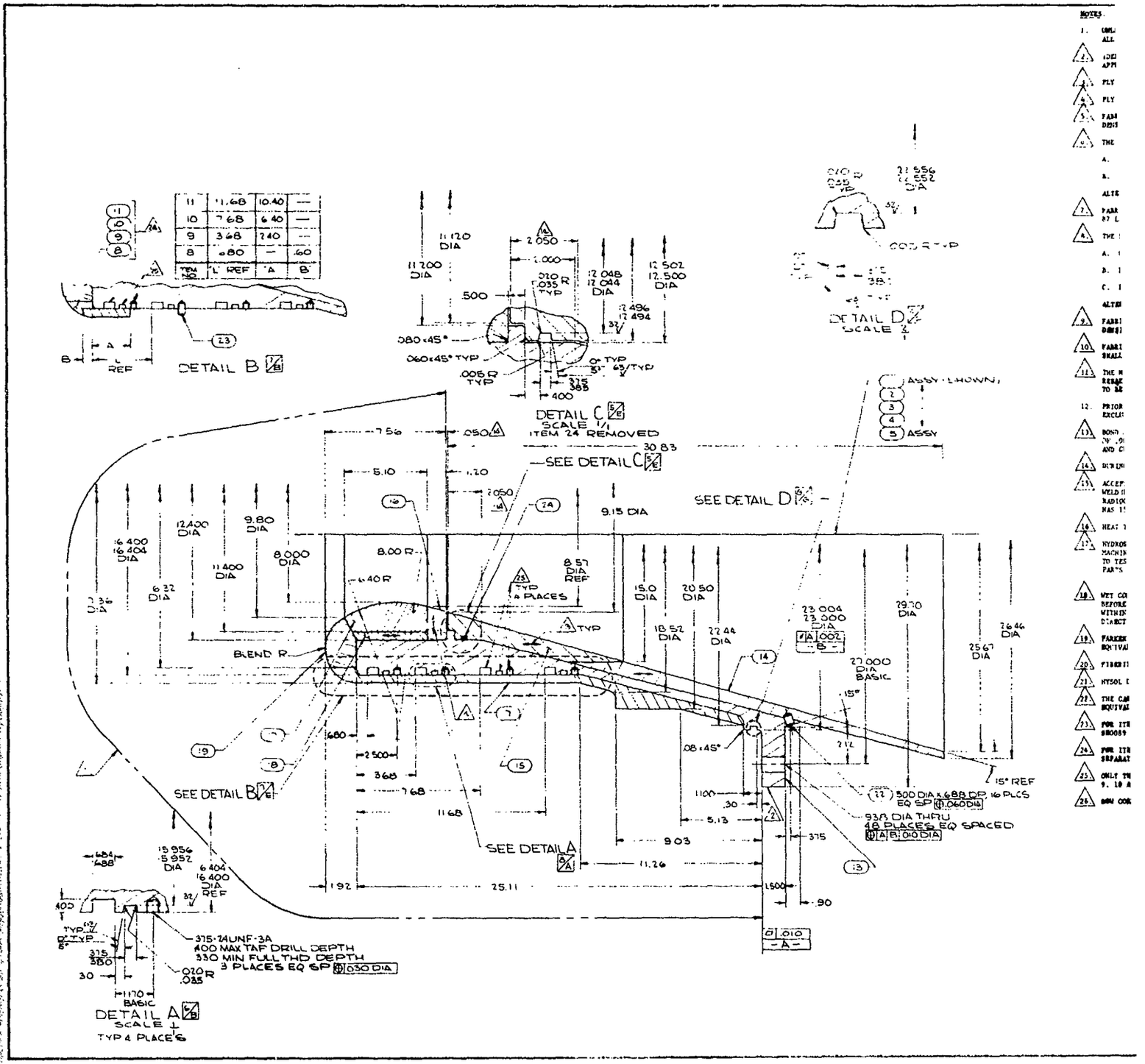
DETAIL B
DETAIL C
SCALE 1/1
ITEM 24 REMOVED
DETAIL D
SCALE 1/1
DETAIL A
SCALE 1
TYP 4 PLACES
SEE DETAIL A
SEE DETAIL B
SEE DETAIL C
SEE DETAIL D
ASSY (SHOWN)
ASSY
BLEND R
.375-24UNF-3A
.400 MAX TAP DRILL DEPTH
.330 MIN FULL THD DEPTH
3 PLACES EQ SP
.030 DIA
93A DIA THRU
48 PLACES EQ SPACED
.010 DIA
.300 DIA x .688 DP
EQ SP .060 DIA
15° REF
1.170 BASIC

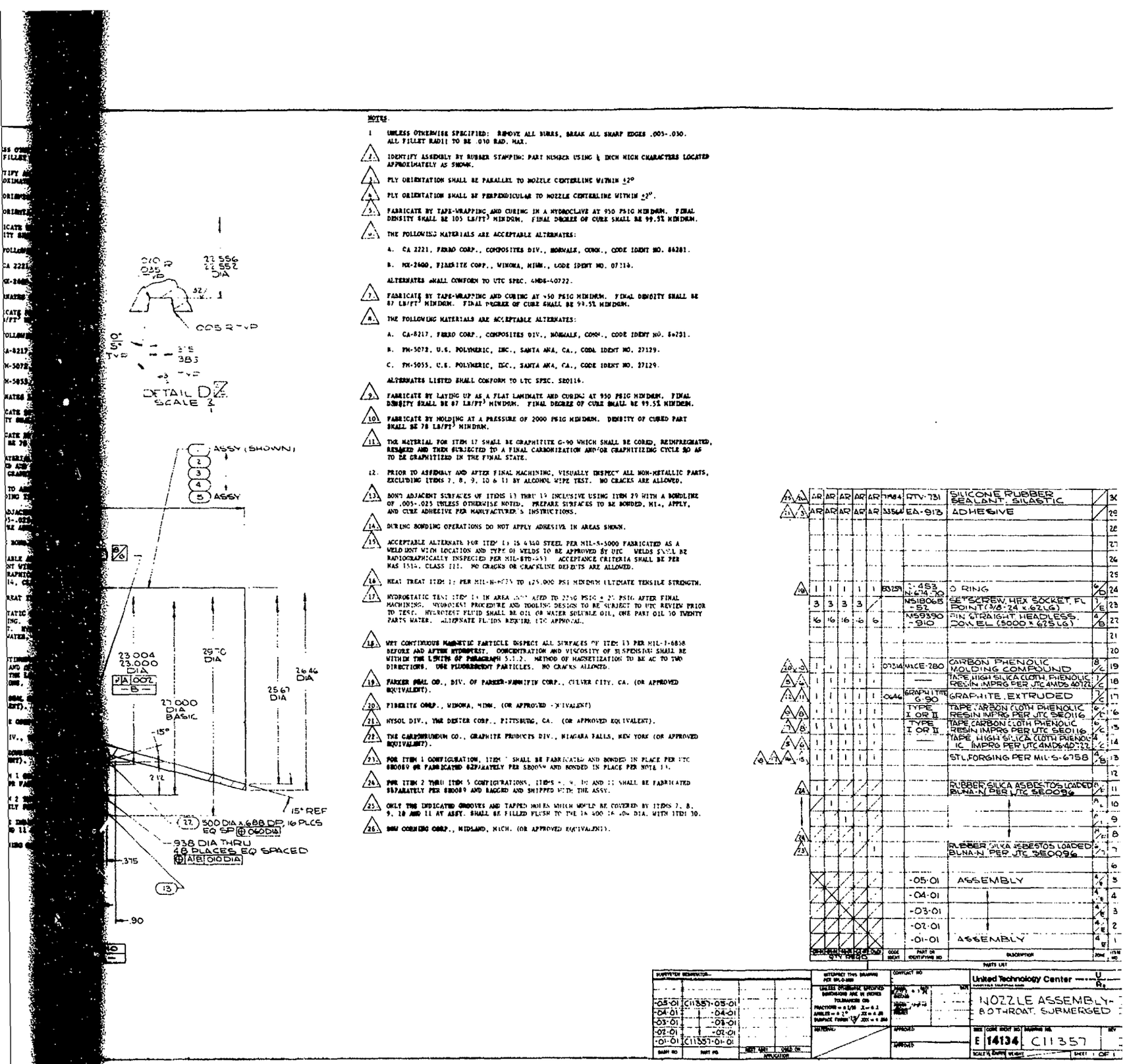

Figure 28. Submerged Nozzle Assembly

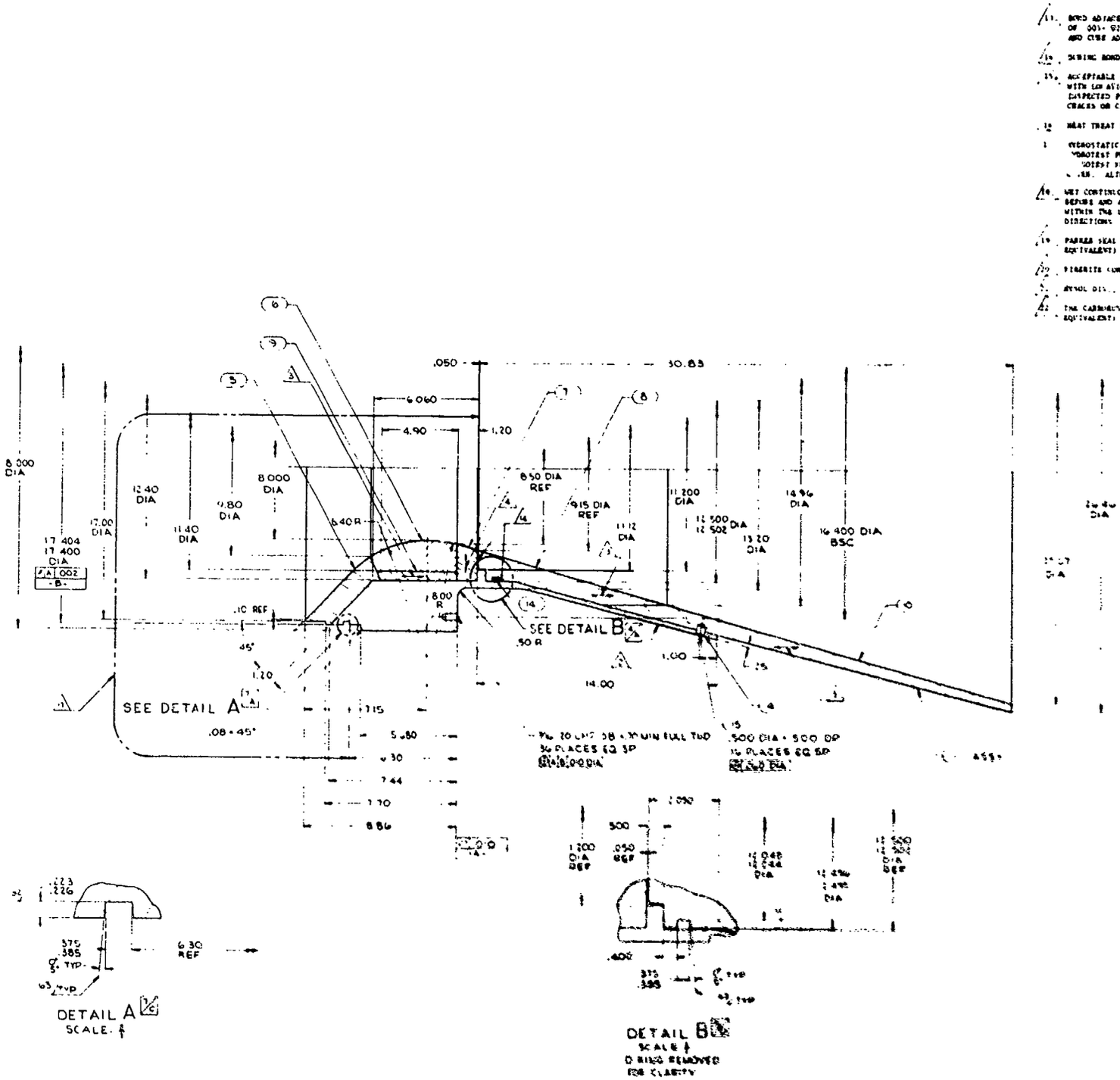
SEE DETAIL A
SEE DETAIL B
DETAIL A
SCALE 4
DETAIL B
SCALE 4
.050
30.83
6.060
4.90
1.20
8.000 DIA
12.40 DIA
8.000 DIA
11.40 DIA
12.00 DIA
17.404
17.400
DIA
.640 R
8.50 DIA REF
9.15 DIA REF
11.200 DIA
11.12 DIA
12.500
12.502 DIA
13.20 DIA
14.96 DIA
16.400 DIA BSC
.10 REF
45°
1.20
8.00 R
.50 R
1.00
14.00
.08 x 45°
5.80
6.30
7.44
7.70
8.86
.575
.585
6.30 REF
.050 REF
1.200 DIA REF
16.048
16.244 DIA
.400
.375
.395

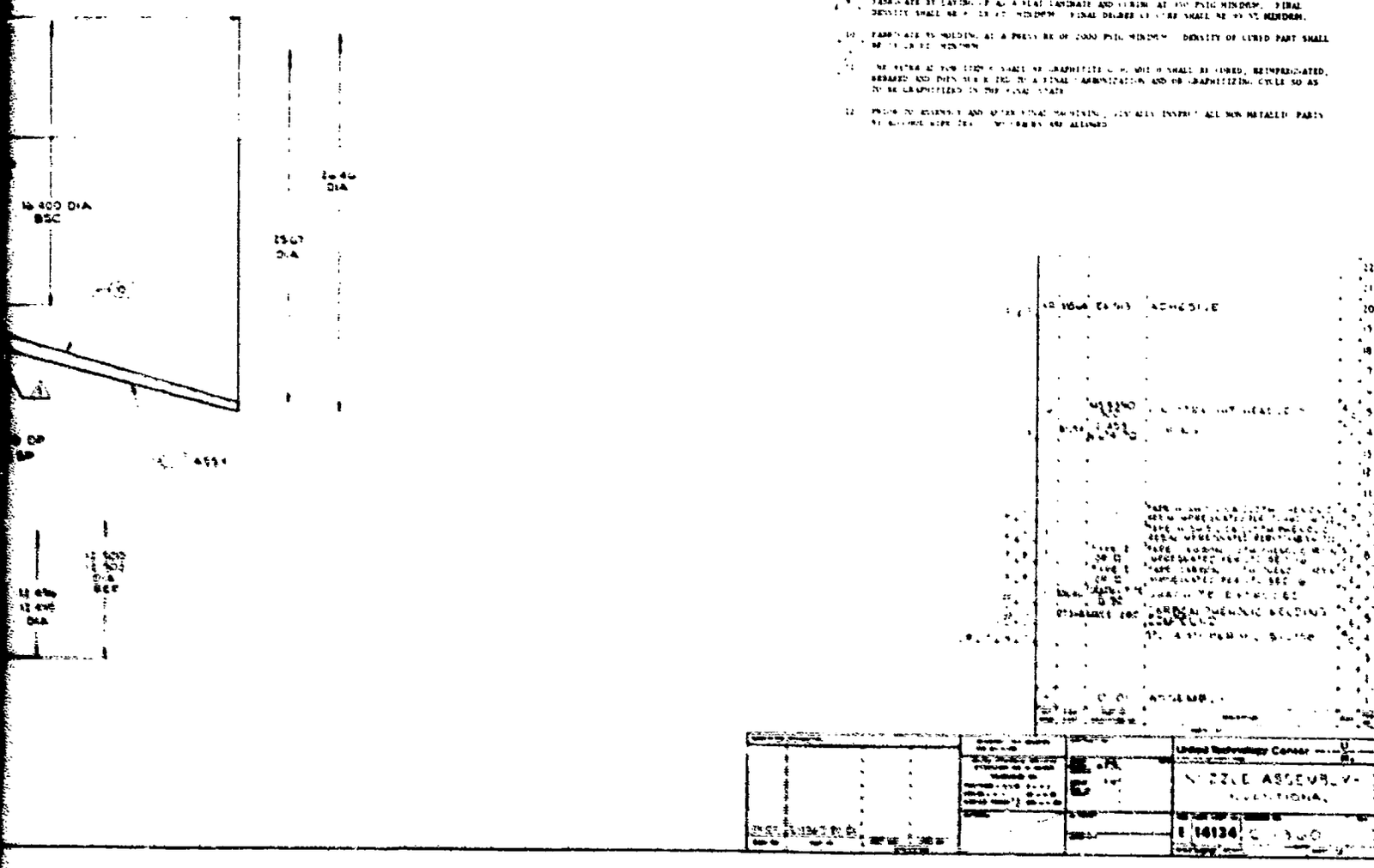

Figure 29. Conventional Nozzle Assembly

inlet radius equal to 1.6 times the throat radius. This inlet contour is the same as that tested on the 7-in.-diameter submerged nozzles (contract No. F04611-70-C-0009). The exit cone has a half-angle of 15° and an overall expansion ratio of 10.3 to 1.

The contour of the conventional nozzle is identical to that of the submerged nozzle except for the 45° entrance angle. The same ablative and insulative materials are used in both nozzles. Silica-asbestos filled NBR insulation is used to protect the backside of the submerged nozzle housing and to protect the aft closure when the conventional nozzle is used.

Elastomeric modified carbon-phenolic (MXCE 280) is used for the nozzle entrance material up to an area ratio of 1.5. This material has performed well in many similar applications. The throat insert package extends from a subsonic area ratio of 1.5 to a supersonic area ratio of 1.3 and consists of a Graph-i-tite G-90 throat insert contained in a silica phenolic sleeve which provides thermal protection for the steel housings.

A carbon phenolic ring with tape plies oriented at 90° to the nozzle centerline is located just aft of the throat insert and transmits throat ejection loads to the steel housing. This is a well proven method of throat retention; the good ablation resistance of the material provides for a smooth transition to the exit cone.

The exit cone has plies tapewrapped parallel to the centerline. Carbon-phenolic is used from an area ratio of 1.5 to 3.5 and silica-phenolic is used from an area ratio of 3.5 to the exit plane. This is a standard exit cone configuration: the materials are used in regions where their ablation resistance is adequate to minimize contour changes that could adversely affect delivered motor performances. To provide structural redundancy the exit cone liner is pinned to the steel shell and bonded in place.

4.1.4.3 Nozzle Fabrication - Fabrication of the ablative material is the same for both nozzles. Tapewrapped and laminated parts are debulked and

cured in a hydroclave at 950 psi (minimum) and 300°F, and machined to final dimensions. All molded parts are molded in a press at 2,000 psi and 300°F, and machined to final dimension. Each part is alcohol wiped and dimensionally inspected prior to assembly to assure its structural integrity. The Graph-i-tite G-90 is cored and reimpregnated to obtain a density of 1.90 or greater. The graphite billets will be X-rayed and alcohol wiped. After acceptance, the components are final machined and again subjected to NDT before assembly. All the ablatives are assembled and bonded with an epoxy adhesive. As previously mentioned, exit cone pins are included to retain the ablative liner should an inadequate adhesive bond exist.

The steel shells are fabricated from ASTM-A-266 steel, which possesses good properties, has good machinability, and is readily available. The shell is a heavyweight design which reduces the cost and provides easy fabrication. A weldment or alternate material may be used at the vendor's option and with UTC approval.

The rubber insulation used on the submerged nozzle is fabricated by laying up unvulcanized sheets of rubber to the required thickness, vacuum bagging the layup, and autoclave curing (vulcanizing) the part at 200 psi (minimum) and 300°F. Curing the material in place on the nozzle shell (vulcanized bond) or curing it separately and bonding it in place with epoxy adhesive are allowable options.

4.1.4.4 Nozzle Thermal Analysis – A preliminary thermal analysis was conducted on the throat of the submerged nozzle configuration using four materials that were selected for study as potential throat candidates. These candidates were Graph-i-tite G-90, ATJ graphite, edge-oriented pyrolytic graphite (high thermal conductivity direction normal to nozzle centerline), and MX-4926 carbon phenolic. Table 11 lists ablation results for throat heat transfer conditions and includes the maximum and average ablation rates. The analysis was conducted using the thermodynamic and thermochemical properties of UTP-18,803 (a 21% aluminum HTPB propellant) at 1,000 psia for 6.2 sec. The maximum ablation rates occurred at 6.2 sec because of the constant pressure trace assumed and the transient nature

TABLE 11. RESULTS OF THROAT ABLATION STUDIES

Throat Material	Ablated Depth, in.	Maximum Ablation Rate,* mils/sec	Average Ablation Rate,† mils/sec
G-90	0.067	15.0	11.55
ATJ	0.079	16.9	13.62
PG-edge oriented	0.0105	4.7	1.81
MX-4926	0.135	26.3	23.28

* Ablation rate at the end of firing, 5.8 sec
† Ablation rate determined by dividing ablated depth by 5.8 sec

of the surface temperature responses of the various materials. For the short firing duration, the surface temperature and thermal penetration is significantly transient. Figure 30 shows the surface temperature of the G-90 throat plotted as a function of time. Correspondingly, the ablation rate is also quite transient in nature (see Figure 31 for a plot of the G-90 throat ablation rate versus time). The average ablation rate in Table 11 is the total ablated depth divided by the assumed firing time of 6.2 sec.

This analysis procedure included a boundary layer analysis to determine throat heat transfer coefficients, a thermochemical analysis of the exhaust gas and ablating wall interaction, and an in-depth heat conduction analysis including surface thermochemical ablation. The boundary layer program is an integral energy deficit computer program from UARL called UARLED. The boundary layer is started at the nozzle stagnation point as a turbulent boundary layer, assuming that Mach number can be described by one-dimensional gas dynamics up to the throat. This program yields a heat transfer coefficient which is subsequently used in the kinetic controlled thermochemistry and heat conduction analysis. The one-dimensional heat conduction analysis computer program, CMA[1] requires both heat transfer and thermochemical boundary conditions in order to predict thermochemical ablation responses in the materials evaluated. The

[1] User's Manual, "Aerotherm Charring Material Thermal Response and Ablation Program," Version 3, AFRPL-TR-70-92, Vol. I, April, 1970.

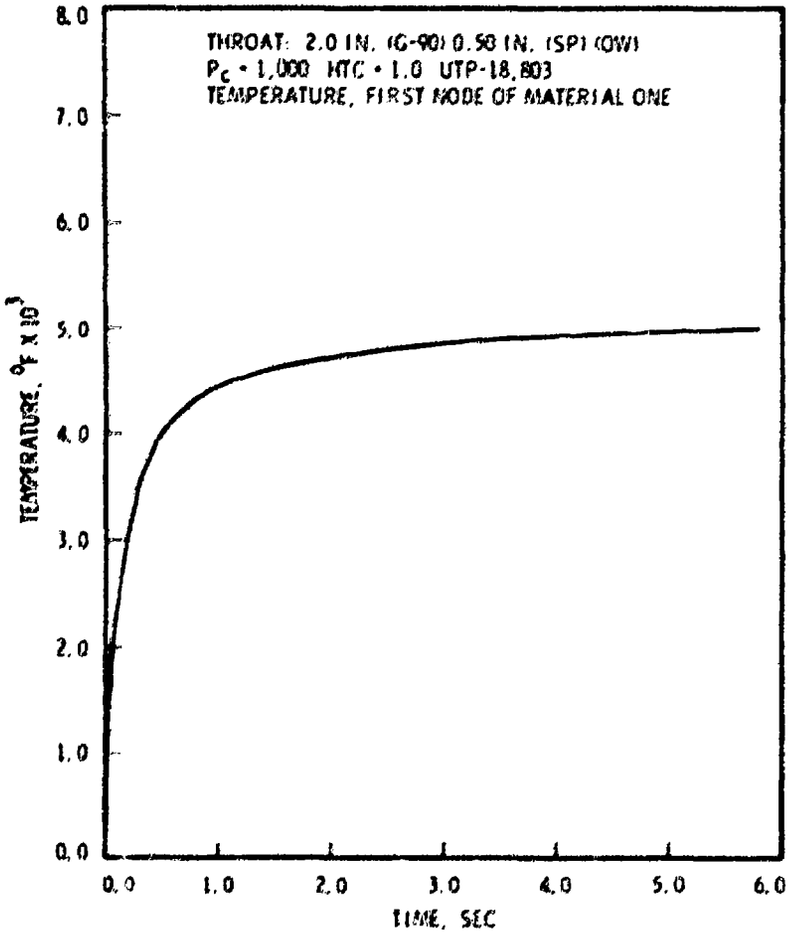

Figure 30. Super BATES G-90 Throat Temperature vs Time

05902

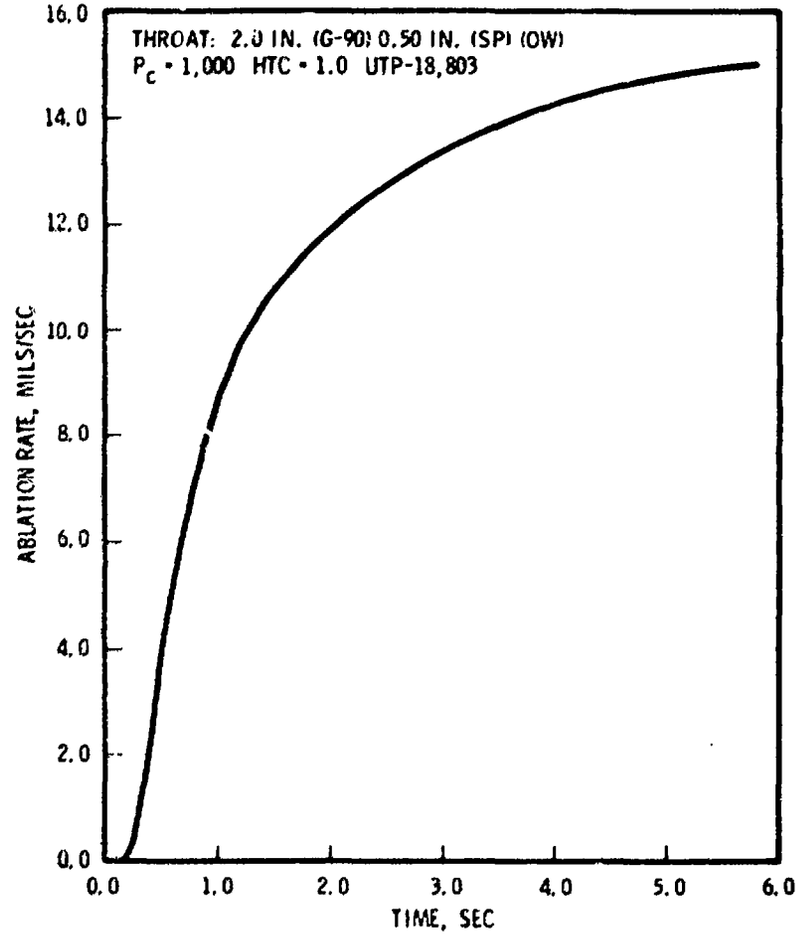

Figure 31. Super BATES G-90 Throat Ablation Rate vs Time

05903

thermochemical boundary conditions are computed using either program GASKET[2] for G-90, ATJ, or pyrolytic graphites, or program EST[3] for carbon phenolic material. The elemental composition of the propellant exhaust gas and other thermodynamic properties are required as input for these thermochemistry programs. The output from each program is a map of nondimensional ablation rates, enthalpies, and chemical generation terms used in program CMA for the surface thermochemical energy balance. With this data, and with the heat transfer results from program UARLED, the radiation boundary condition, and the appropriate thermal properties (as a function of material temperature), program CMA can be executed. It yields transient surface temperature, ablation, and in-depth temperature response. In the case of carbon phenolic (MX-4926), the CMA program also predicts char depth since that material decomposes in depth as a function of heat transfer rate and time.

The programs described above and this general analytical approach will be used on the entire nozzle during final design analysis to insure nozzle thermal adequacy. In the throat region, two-dimensional heat conduction analysis may be employed in support of the structural analysis.

4.1.5 Insulation

The insulation design, shown in Figures 11 and 12, provides complete thermal protection for the motor case components so that structural integrity is not degraded during test motor operation. Fully characterized materials and state-of-the-art fabrication and assembly techniques assure a design of high reliability and low cost. Specific features incorporated in the design are:

A. A demonstrated ablative/insulative material (silica- and asbestos-loaded NBR) is used.

B. Most insulation components are designed for more than one test firing (two reuses).

C. Premolded insulators secondarily bonded to motor case components are used for easy refurbishment.

---

[2] User's Manual, "Aerotherm Graphite Surface Kinetics Computer Program," AFRPL-TR-72-23, Vol. 1, January, 1972

[3] User's Manual, "Aerotherm Equilibrium Surface Thermochemistry Computer Program," Version 3, AFRPL-TR-70-93, Vol. 1, April, 1973.

4.1.5.1 Design Requirements – The following design requirements were considered in arriving at the selected configuration:

A. Thermal protection must and will be provided for all motor case components for the most severe anticipated motor operating conditions (worst combination of chamber pressure and duration)
B. The insulation design must and will minimize heat loss and resultant loss of data accuracy (minimize insulation surface areas)
C. Insulation, where possible, will be designed for two reuses; the temperature rise at the case-to-insulation interface will not exceed 100°F during motor operation
D. A factor of safety of 1.25 will be applied to predicted ablation
E. Segment insulation design will be compatible with a case-bonded grain
F. Ease of installation and refurbishment will be a major design consideration.

4.1.5.2 Design Description – All insulation components are fabricated from silica- and asbestos-loaded NBR per UTC specification SE0096 except for the pressure relief ports. This material has been selected for its demonstrated ablative/thermal performance in numerous motors at UTC. It is relatively low in cost, compatible with propellant/liner systems to be tested in the motor, and easily fabricated.

The insulation consists of seven major components:

A. Aft closure insulator
B. Segment insulator (one installed at each end of the segment)
C. Clevis ring insulator
D. Forward closure insulator
E. Burst disc insulator
F. Pressure relief port insulators in forward closure
G. Adapter insulator.

The aft closure insulator is a flat, annular ring of insulation 1.93 in. thick. This thickness will allow the insulator to be used three times (two reuses). Interface between the aft insulator and the segment insulator is a stepped butt joint filled with zinc chromate putty to prevent the structural

components from being exposed to chamber exhaust gas. This type of joint configuration has been used extensively at UTC and where possible is used between all insulation components for this motor.

Each segment is insulated at both ends with a tapered insulator which is 0.32 in. thick at full exposure locations and tapers to 0.05 in. at a point approximately 0.5 in. beyond the point of web burnout. This insulation will be replaced after each firing to ensure that propellant volume and surface area are the same for each firing.

The insulator over the clevis ring (0.75 in. thick) is designed to be reused twice. The insulation thickness at the ends of the ring (fore and aft faces) is 1.03 in. (the same as the aft closure insulation); allowing for segment interchangeability, the interface with the segment is the same as that at the aft closure.

Insulation at the forward end of the motor consists of an outer annular ring (1.03 in. thick) protecting the forward closure, a second inner, annular ring (1.03 in. thick) insulating the burst disc retainer, and a cup-shaped insulator (0.125 in. thick) for the burst disc itself. The outer and inner insulators can be reused four times. The thickness of the forward closure insulator is the same as the aft closure so that the segments are interchangeable. The burst disc insulator is designed to be replaced each time. The pressure relief ports will be insulated with commercially available tubing of asbestos paper-phenolic simply cut to length and inserted into the ports. Several commercial materials such as Micarta tubing are available and will be selected for final design.

The insulation is fabricated per UTC specification SE0089. All insulators are premolded and cured using either a forming tool in an autoclave or by the matched die-formed press-cure method. After cure, the insulators are checked for proper cured hardness and inspected visually and dimensionally. The port insulators are cut to length from stock diameter tubing. All insulators are bonded to the motor case component with a silicone rubber adhesive. This relatively low strength adhesive facilitates removal of the insulators when they must be refurbished. If a higher strength bond is desired an epoxy adhsive can be used.

4.1.6 Propellant

4.1.6.1 Baseline Propellant - The baseline propellant for the Super BATES motor is UTP-18,803. The composition is one of a family of UTC propellants containing an R-45M/IPDI binder. The composition was selected on the basis of (1) no burning rate catalyst, (2) immediate availability, (3) good ballistic and hazard properties, (4) high density, and (5) good processability. The propellant is a high energy system with high solids loading which is believed to be typical of future compositions and therefore ideal for use in the Super BATES. The propellant was developed for ballistic motor applications and for the Super HIPPO motor. This propellant has been characterized and released for production in large quantities. The physical properties are currently being documented and will be available in time for the Super BATES motor.

The basic composition consists of 10% R-45M binder, 21% aluminum, and 69% AP. Table 12 lists the complete composition and properties.

4.1.6.2 Liner Formulation - UTC has evaluated Thiokol liner, TL-H755A, developed under USAF contract No. F04611-73-C-0069, and has found it to be an excellent selection for use with R-45M propellants. TL-H755A has been designated UTL-0040 and is used for the Super BATES motor. The composition of UTL-0040 is presented in Table 13.

4.1.6.3 Grain Configuration - The grain for the Super BATES motor is a segmented, internal burning, cylindrical configuration having a relatively small web fraction and a pressure neutrality of approximately 4%. Two and one-half segments are used with burning taking place in the center bore and on the ends of each segment. A slight gain in neutrality may be accomplished by restricting one face of a half segment; however, for this configuration it is not considered necessary. Figure 32 shows a sketch of the grain along with the significant dimensions. Table 14 lists the grain design parameters.

The design web of 2.6 in. was tentatively selected as the best compromise between propellant weight and neutrality. As noted in Figure 33, if a slight increase in neutrality is sacrificed (about 0.3%), the web thickness can decrease

TABLE 12. UTP-18,803 COMPOSITION

Ingredient	Function	Weight, %
R-45	Prepolymer	6.51
IPDI	Curative	0.49
IDP	Plasticizer	2.60
HX-752	Bonding agent	0.30
PRO-TECH® 3002	Antioxidant	0.10
Al, 25μ	Fuel	21.00
AP, 200μ	Oxidizer	48.30
AP, 8μ	Oxidizer	20.70
	Properties	
Ballistic		
I^{o}_{sps} (theoretical, standard), sec		264.3
c* (theoretical), ft/sec		5,172
Chamber temperature, °K		3,730
Chamber temperature, °F		6,260
Burning rate (1,000 psia), in./sec		0.43
Pressure exponent, n		0.33
Physical		
Density (70°F), g/cm^3		1.843
Density (70°F), $lb/in.^3$		0.0666
Hazard		
Impact sensitivity, kg-cm		35
Autoignition temperature, °F		
Ignition in 10 sec		670
Ignition in 30 sec		580
DOT classification		pending

TABLE 13. UTL-0040 COMPOSITION

Ingredient	Wt-%
R-45M	41.85
DDI	12.15
HX-868	6.00
Thermax	40.00

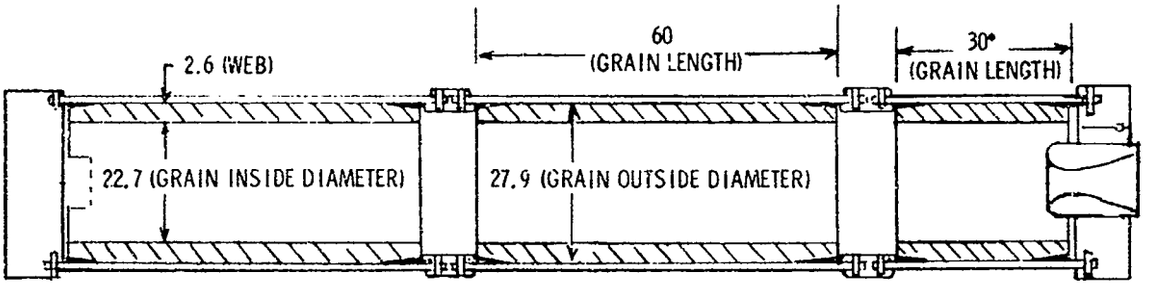

* MAX. LENGTH FOR CONFIGURATION: NOMINAL = 25.6
NOTE: ALL DIMENSIONS ARE IN INCHES

Figure 32. Super BATES Grain Configuration

05758

TABLE 14. GRAIN DESIGN PARAMETERS

Web thickness, in.	2.6
Web fraction*	0.228
b/a ratio†	1.23
Port/throat ratio	8.1
Initial K_n	225.7
Average K_n	225.5
Propellant weight, lb	1,996.5
Volumetric loading, %	34
Surface area neutrality‡	1.002
Pressure neutrality	1.0377

* Ratio of web thickness to outer radius
† Ratio of outer radius to inner radius
‡ Ratio of maximum to average surface area

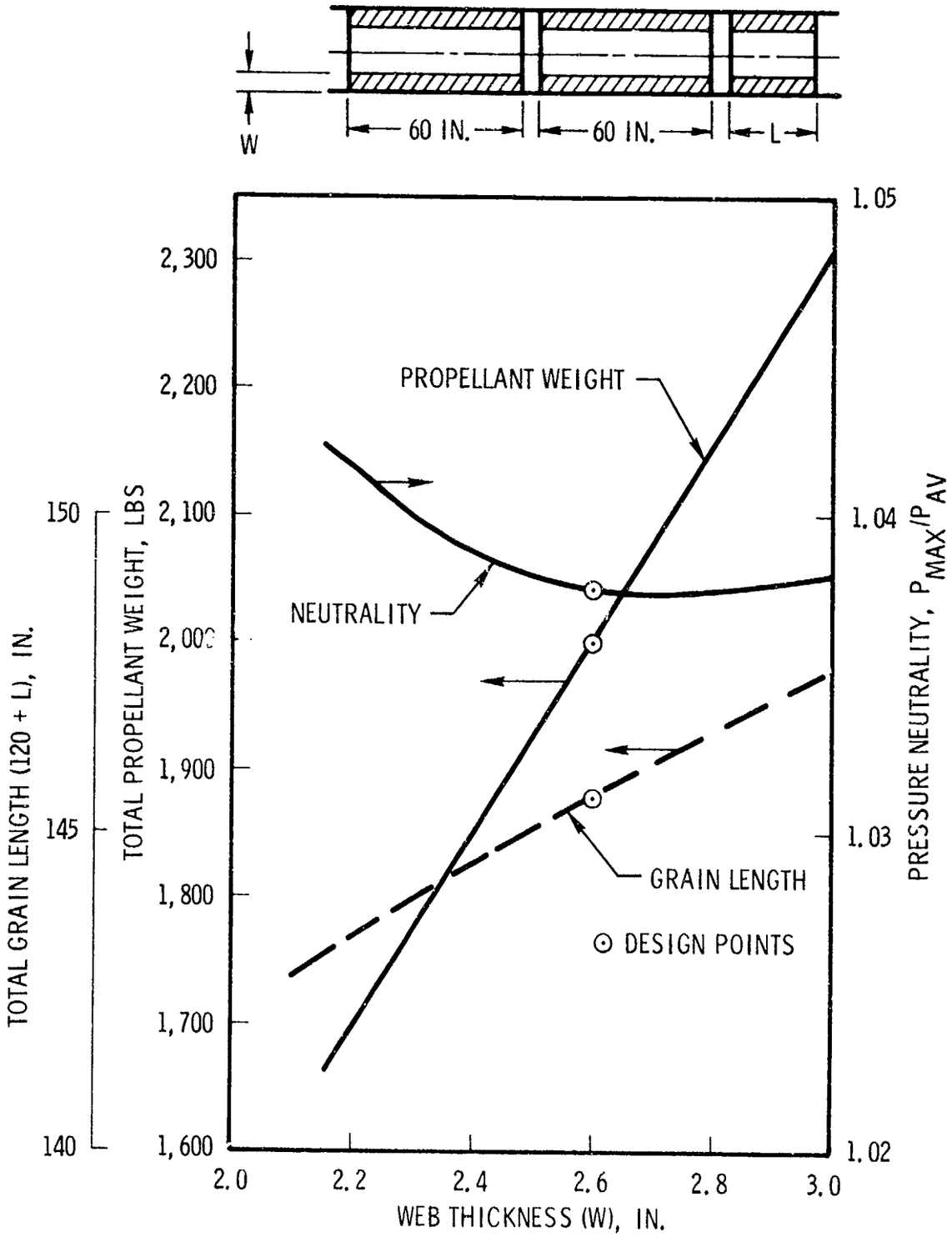

Figure 33. Propellant Weight, Grain Length, and Neutrality vs Web Thickness

05890

to 2.2 in. and almost 300 lb of propellant per motor can be saved. A 3-in. web will give the same neutrality as the 2.6-in. design, but a larger amount of propellant (300 lb) is required to maintain the 320 lb/sec average flow rate.

The grain configuration is the result of a trade study where the parameters of pressure neutrality and half-segment length were determined for web thicknesses in the range of 2 to 3 in. Figure 33 shows the results of the study.

The actual grain length for the aft segment is 25.6 in. based on preliminary burning rate data on UTP-18,803. The reported burning rate is based on 4-lb motor firings from 5-gal batches. This value is expected to change slightly (1) when production size batches are made, and (2) due to the effect of motor size. The preliminary design length was set at a value slightly less than the maximum possible to permit a grain length increase in the last segment if necessary. The half length segment will provide greater flexibility with respect to possible combinations of segments for future Super BATES configurations. Figure 34 shows the required grain length versus burning rate for a web thickness of 2.6 in. and the desired operating conditions. As noted, the entire range of possible burning rates can be employed with some combination of segments using the proposed configuration.

The tapered insulation at the ends of each segment improves the shape of the pressure trace just prior to tailoff. Straight insulation pieces would cause a sharp increase in chamber pressure when the propellant burns into the region between the end pieces. Since this would affect both neutrality and tailoff impulse, the insulation will be tapered to provide a smooth transition into tailoff.

4.1.6.4 Internal Ballistics and Performance - Curves of pressure and thrust versus time are shown in Figure 35. The single number ballistic parameters are listed in Table 15. Because of the simple grain shape and large port to throat ratio, ballistic predictions are straightforward; no anomalies due to erosive burning or pressure drop are anticipated. UTC's single module ballistic

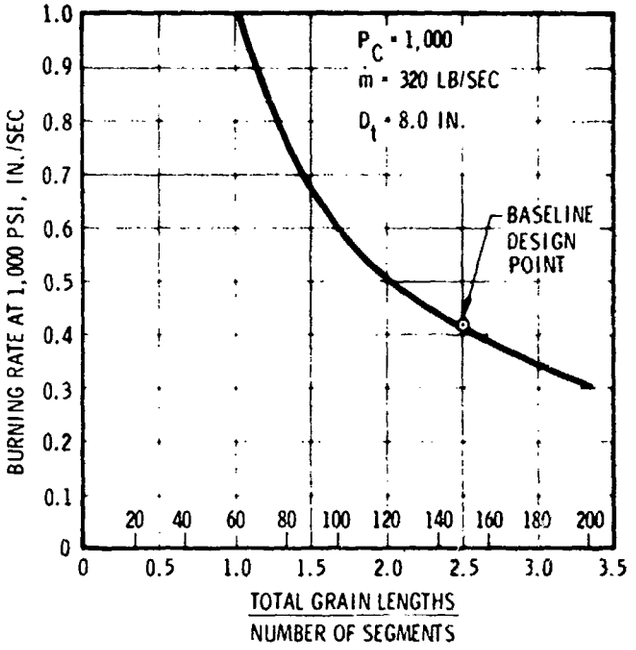

Figure 34. Burning Rate vs Number of Segments

05759

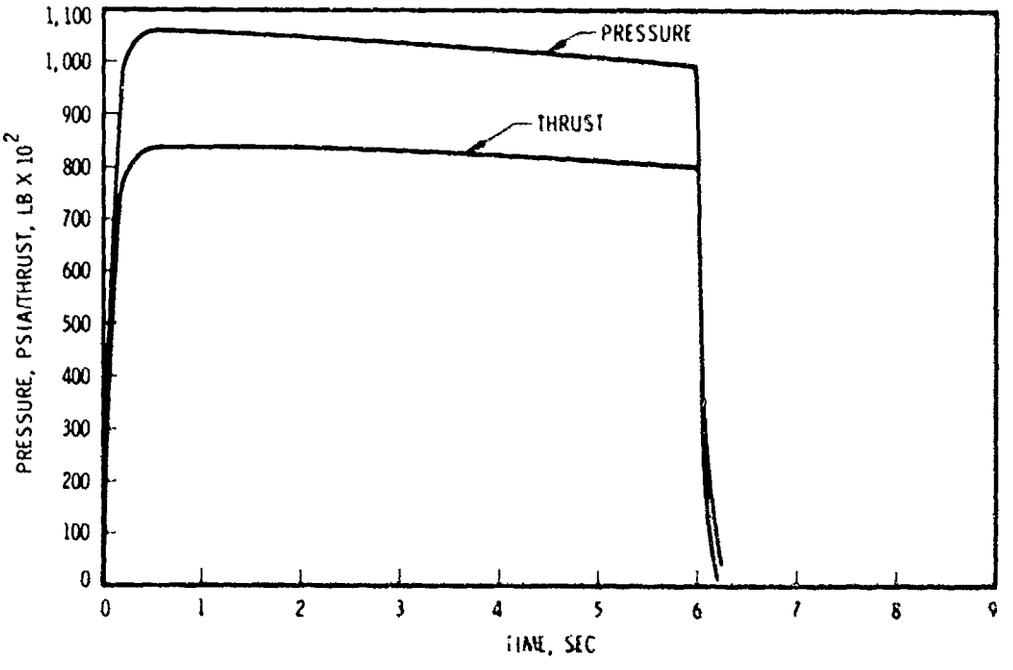

Figure 35. Thrust and Pressure vs Time

05891

TABLE 15. SEA LEVEL BALLISTIC PERFORMANCE PARAMETERS, 70°F

Web time, sec	6.02
Action time, sec	6.19
Average pressure, psia*	1,003
Total impulse, lb-sec*	492,023
Tailoff impulse, lb-sec	5,273
Average thrust, lb*	79,197
Delivered specific impulse, sec*	246.69
Average mass flow rate, lb/sec*	322.5
Maximum pressure, psia	1,058
Maximum pressure/average pressure†	1.0377
Motor Parameters	
Throat diameter, in.	8.0
Expansion ratio	10.3
Nozzle half-angle, °	15
Propellant weight, lb	1,996.5
Nozzle erosion rate, mils/sec	11.5

* Over action time
† Over web time

---

program was used for the performance prediction. This program inputs grain and insulation coordinates and automatically calculates the end-to-end ballistic prediction including ignition rise and tailoff at blowdown. Time dependent functions such as throat erosion rate, igniter flow rate, and nozzle efficiency are also considered in the calculation.

Gas dynamic analyses were conducted to determine the pressure and flow field in (1) the radial slot between the burning propellant and the segment insulator, and (2) the annulus between the propellant and a submerged nozzle whose outside diameter approaches the inside diameter of the burning propellant.

Figure 36 shows the predicted pressure and Mach number in the radial slot at ignition over a range of slot widths. The reported pressure drop is actually

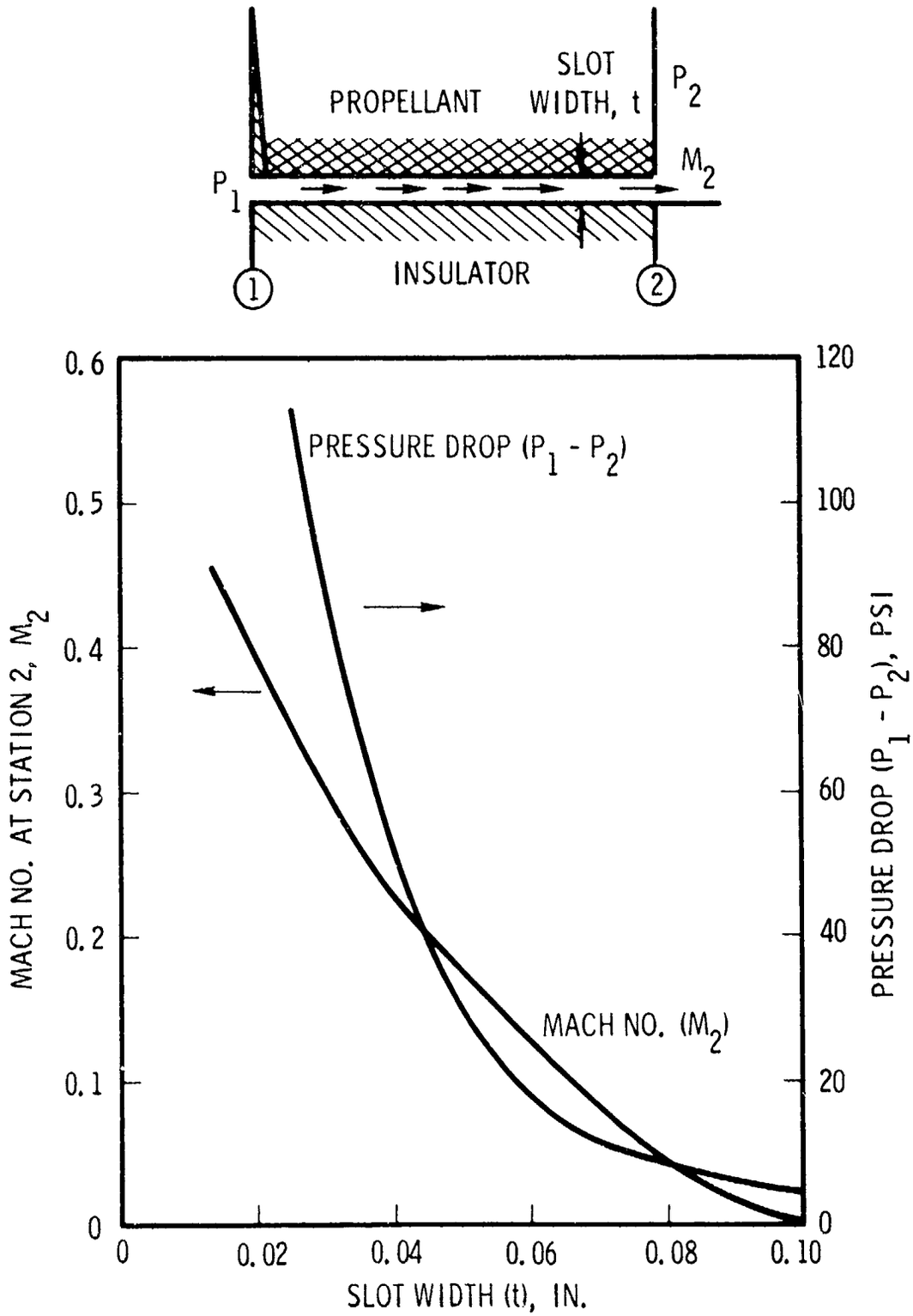

Figure 36. Pressure Drop and Mach Number vs Slot Width

05892

the pressure buildup which occurs at station 1 since the exit static pressure (P_2) must adjust to the chamber pressure. As shown, no serious problem exists with the pressure buildup until the slot width decreases to 0.03 in. or approximately 1/32 in.

The results of the submerged nozzle analysis are shown in Figure 37. Because of the larger burning surface area, the minimum annulus width must be significantly larger than that of the radial slot to permit safe operation. As shown, the pressure buildup becomes prohibitive when the annulus width decreases to 0.2 in.

Both of the above analyses are for conditions at ignition, before the propellant surface has receded. For a 0.03-in. radial slot, the high pressure buildup will disappear after 0.2 sec of operation. For a 0.2-in. submerged nozzle annulus, the pressure buildup will become negligible in approximately 0.5 sec.

4.1.6.5 Process Tooling - Criteria have been established and detailed designs prepared for the tooling required to process the Super BATES motor. Figure 38 presents the assembly and details of the propellant casting tooling.

Process tooling is based on criteria obtained from past HIPPO, BATES, and Super HIPPO programs and accepted industry practices. The tooling is designed to produce the Super BATES motors efficiently, with the best reproducibility obtainable, at any reasonably well-equipped propellant processing facility.

The Super BATES process tooling consists of a mandrel, a base plate, a mandrel centering device, a casting head, a propellant casting manifold, and an insulation locating fixture. A pallet is provided for storage, processing, and in-plant transportation. The design allows maximum interchangeability in handling equipment between the processing plant and the testing area.

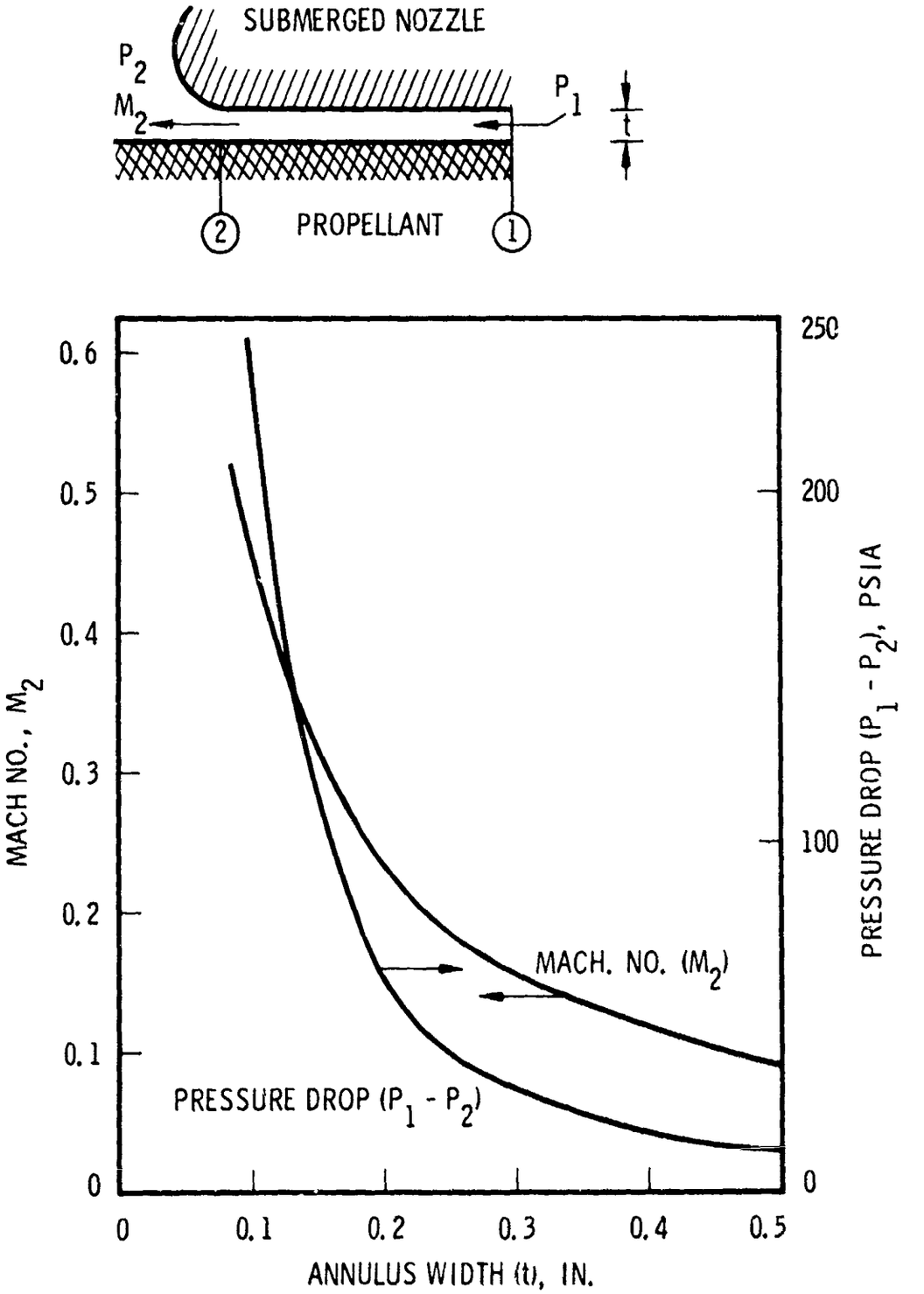

Figure 37. Pressure Drop and Mach Number vs Annulus Width for Submerged Nozzle

05893

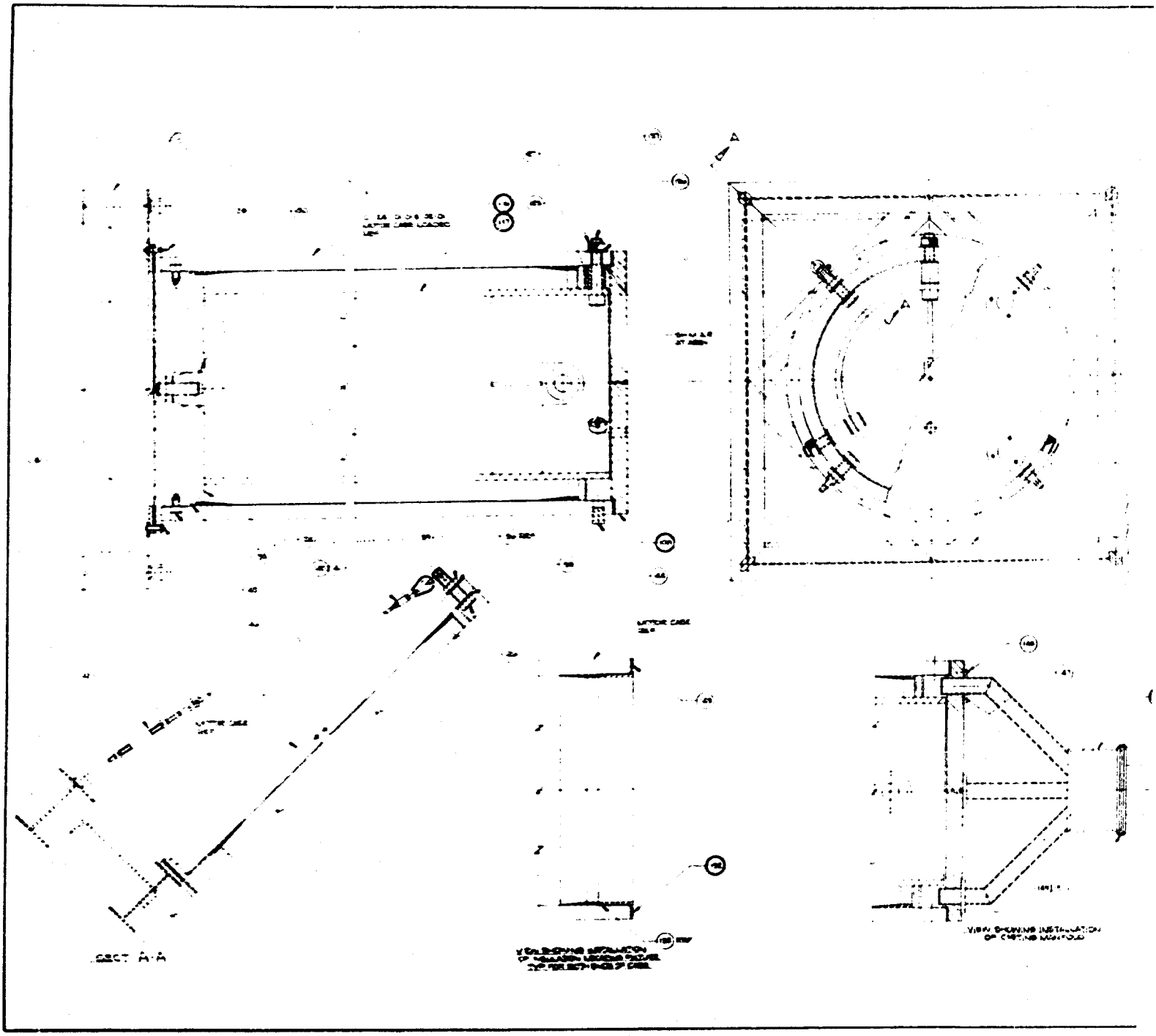

NOTES:

1. THIS TOOLING USED FOR CASTING SUPER BATES MOTOR
2. MATERIALS IN LIM ARE PREFERRED ANY ITEMS SUBSTITUTED MUST BE EQUAL & SUBJECT TO APPROVAL BY UTC
3. DIMENSIONS IN LIM ARE NET SIZES STOCK ALLOWANCE MUST BE MADE FOR FINISHING
4. BREAK ALL SHARP EDGES & DEBURR
5. QUANTITIES IN LIM ARE THE QUANTITIES REQUIRED TO MAKE ONE COMPLETE TOOL
6. STAMP TOOL NO. ON TOOL AND ON ALL LOOSE PARTS USING 1/4 INCH CHARACTERS, MIN HEIGHT. USE ELECTRO ETCH AS REQ'D TO PREVENT DISTORTION OR DAMAGE. (BAS & TAB ALL LOOSE ITEMS)
7. PREPARE ALL SURFACES (BY SANDBLASTING) FOR DUPONT "TEFLON PRIMER "850-204 TO BE FOLLOWED WITH DUPONT TEFLON HIGH BUILD GREEN ENAMEL" 851-224. TOTAL COATS .004 MIN - .007 MAX
8. ALL DIMENSIONS APPLY AFTER TEFLON COATING
9. STRESS RELIEVE TO TEMPERATURE REQ'D FOR TEFLON COATING PRIOR TO FINAL MACHINING
10. STRESS RELIEVE PRIOR TO FINAL MACHINING
11. PAINT ONE COAT SHERWIN WILLIAMS KEM A & A EPOXY PRIMER & ONE COAT SHERWIN WILLIAMS KEM A & A EPOXY ENAMEL UTC AQUA
12. NO PAINT IN HOLES ON THREADS OR FINISHED SURFACES COAT THESE SURFACES WITH A RUST PREVENTIVE.
13. CROSBY - LAUGHLIN, FORT WAYNE, INDIANA.
14. LADISH CO., TRI-CLOVER DIV., KENOSHA, WISCONSIN.
15. PARKER SEAL CO., CULVER CITY, CA.
16. CF & I STEEL CORP., TRENTON, NEW JERSEY.
17. BOND ITEM 110 TO ITEM 109 USING EASTMAN 934 ADHESIVE
18. BOND ITEM 107 TO ITEM 105 USING EASTMAN 934 ADHESIVE.

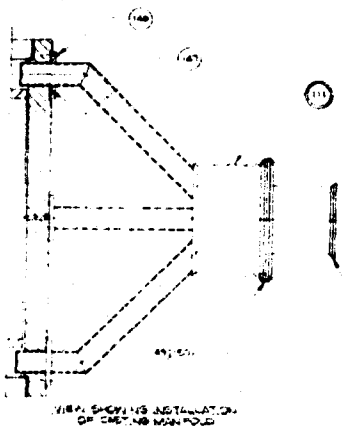

VIEW SHOWING INSTALLATION OF CASTING MANIFOLD

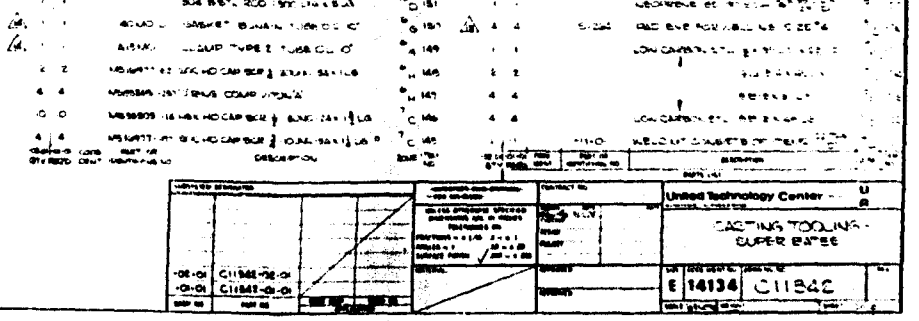

ITEM	QTY	PART NO	DESCRIPTION
1	1	M88524	304 STAINLESS STEEL COMP WELDING
2	1		304 STAINLESS STEEL ROD
3	1	40 CAD	GASKET
4	1	A-S-M-C	CLAMP TYPE 2
5	2	M5	SOCKET HEAD CAP SCREW
6	4	M5	STAINLESS STEEL COMP WELDING
7	10	M5	SOCKET HEAD CAP SCREW
8	4	M5	SOCKET HEAD CAP SCREW

ITEM	QTY	PART NO	DESCRIPTION
B	182		
D	181		
G	180		
A	179		
H	178		
H	177		
C	176		
C	175		

ITEM	QTY	PART NO	DESCRIPTION
1	1		
2	1		
3	1		
4	1		
5	1		
6	4		
7	4		
8	4		
9	2		
10	1		
11	1		
12	1		
13	1		
14	1		
15	1		
16	1		
17	1		
18	1		
19	1		
20	1		
21	1		
22	1		
23	1		
24	1		
25	1		
26	1		
27	1		
28	1		
29	1		
30	1		
31	1		
32	1		
33	1		
34	1		
35	1		
36	1		
37	1		
38	1		
39	1		
40	1		
41	1		
42	1		
43	1		
44	1		
45	1		
46	1		
47	1		
48	1		
49	1		
50	1		
51	1		
52	1		
53	1		
54	1		
55	1		
56	1		
57	1		
58	1		
59	1		
60	1		
61	1		
62	1		
63	1		
64	1		
65	1		
66	1		
67	1		
68	1		
69	1		
70	1		
71	1		
72	1		
73	1		
74	1		
75	1		
76	1		
77	1		
78	1		
79	1		
80	1		
81	1		
82	1		
83	1		
84	1		
85	1		
86	1		
87	1		
88	1		
89	1		
90	1		
91	1		
92	1		
93	1		
94	1		
95	1		
96	1		
97	1		
98	1		
99	1		
100	1		
101	1		
102	1		
103	1		
104	1		
105	1		
106	1		
107	1		
108	1		
109	1		
110	1		
111	1		
112	1		
113	1		
114	1		
115	1		
116	1		
117	1		
118	1		
119	1		
120	1		
121	1		
122	1		
123	1		
124	1		
125	1		
126	1		
127	1		
128	1		
129	1		
130	1		
131	1		
132	1		
133	1		
134	1		
135	1		
136	1		
137	1		
138	1		
139	1		
140	1		
141	1		
142	1		
143	1		
144	1		
145	1		
146	1		
147	1		
148	1		
149	1		
150	1		
151	1		
152	1		
153	1		
154	1		
155	1		
156	1		
157	1		
158	1		
159	1		
160	1		
161	1		
162	1		
163	1		
164	1		
165	1		
166	1		
167	1		
168	1		
169	1		
170	1		
171	1		
172	1		
173	1		
174	1		
175	1		
176	1		
177	1		
178	1		
179	1		
180	1		
181	1		
182	1		
183	1		
184	1		
185	1		
186	1		
187	1		
188	1		
189	1		
190	1		
191	1		
192	1		
193	1		
194	1		
195	1		
196	1		
197	1		
198	1		
199	1		
200	1		
201	1		
202	1		
203	1		
204	1		
205	1		
206	1		
207	1		
208	1		
209	1		
210	1		
211	1		
212	1		
213	1		
214	1		
215	1		
216	1		
217	1		
218	1		
219	1		
220	1		
221	1		
222	1		
223	1		
224	1		
225	1		
226	1		
227	1		
228	1		
229	1		
230	1		
231	1		
232	1		
233	1		
234	1		
235	1		
236	1		
237	1		
238	1		
239	1		
240	1		
241	1		
242	1		
243	1		
244	1		
245	1		
246	1		
247	1		
248	1		
249	1		
250	1		
251	1		
252	1		
253	1		
254	1		
255	1		
256	1		
257	1		
258	1		
259	1		
260	1		
261	1		
262	1		
263	1		
264	1		
265	1		
266	1		
267	1		
268	1		
269	1		
270	1		
271	1		
272	1		
273	1		
274	1		
275	1		
276	1		
277	1		
278	1		
279	1		
280	1		
281	1		
282	1		
283	1		
284	1		
285	1		
286	1		
287	1		
288	1		
289	1		
290	1		
291	1		
292	1		
293	1		
294	1		
295	1		
296	1		
297	1		
298	1		
299	1		
300	1		
301	1		
302	1		
303	1		
304	1		
305	1		
306	1		
307	1		
308	1		
309	1		
310	1		
311	1		
312	1		
313	1		
314	1		
315	1		
316	1		
317	1		
318	1		
319	1		
320	1		
321	1		
322	1		
323	1		
324	1		
325	1		
326	1		
327	1		
328	1		
329	1		
330	1		
331	1		
332	1		
333	1		
334	1		
335	1		
336	1		
337	1		
338	1		
339	1		
340	1		
341	1		
342	1		
343	1		
344	1		
345	1		
346	1		
347	1		
348	1		
349	1		
350	1		
351	1		
352	1		
353	1		
354	1		
355	1		
356	1		
357	1		
358	1		
359	1		
360	1		
361	1		
362	1		
363	1		
364	1		
365	1		
366	1		
367	1		
368	1		
369	1		
370	1		
371	1		
372	1		
373	1		
374	1		
375	1		
376	1		
377	1		
378	1		
379	1		
380	1		
381	1		
382	1		
383	1		
384	1		
385	1		
386	1		
387	1		
388	1		
389	1		
390	1		
391	1		
392	1		
393	1		
394	1		
395	1		
396	1		
397	1		
398	1		
399	1		
400	1		
401	1		
402	1		
403	1		
404	1		
405	1		
406	1		
407	1		
408	1		
409	1		
410	1		
411	1		
412	1		
413	1		
414	1		
415	1		
416	1		
417	1		
418	1		
419	1		
420	1		
421	1		
422	1		
423	1		
424	1		
425	1		
426	1		
427	1		
428	1		
429	1		
430	1		
431	1		
432	1		
433	1		
434	1		
435	1		
436	1		
437	1		
438	1		
439	1		
440	1		
441	1		
442	1		
443	1		
444	1		
445	1		
446	1		
447	1		
448	1		
449	1		
450	1		
451	1		
452	1		
453	1		
454	1		
455	1		
456	1		
457	1		
458	1		
459	1		
460	1		
461	1		
462	1		
463	1		
464	1		
465	1		
466	1		
467	1		
468	1		
469	1		
470	1		
471	1		
472	1		
473	1		
474	1		
475	1		
476	1		
477	1		
478	1		
479	1		
480	1		
481	1		
482	1		
483	1		
484	1		
485	1		
486	1		
487	1		
488	1		
489	1		
490	1		
491	1		
492	1		
493	1		
494	1		
495	1		
496	1		
497	1		
498	1		
499	1		
500	1		
501	1		
502	1		
503	1		
504	1		
505	1		
506	1		
507	1		
508	1		
509	1		
510	1		
511	1		
512	1		
513	1		
514	1		
515	1		
516	1		
517	1		
518	1		
519	1		
520	1		
521	1		
522	1		
523	1		
524	1		
525	1		
526	1		
527	1		
528	1		
529	1		
530	1		
531	1		
532	1		
533	1		
534	1		
535	1		
536	1		
537	1		
538	1		
539	1		
540	1		
541	1		
542	1		
543	1		
544	1		
545	1		
546	1		
547	1		
548	1		
549	1		
550	1		
551	1		
552	1		
553	1		
554	1		
555	1		
556	1		
557	1		
558	1		
559	1		
560	1		
561	1		
562	1		
563	1		
564	1		
565	1		
566	1		
567	1		
568	1		
569	1		
570	1		
571	1		
572	1		
573	1		
574	1		
575	1		
576	1		
577	1		
578	1		
579	1		
580	1		
581	1		
582	1		
583	1		
584	1		
585	1		
586	1		
587	1		
588	1		
589	1		
590	1		
591	1		
592	1		
593	1		
594	1		
595	1		
596	1		
597	1		
598	1		
599	1		
600	1		
601	1		
602	1		
603	1		
604	1		
605	1		
606	1		
607	1		
608	1		
609	1		
610	1		
611	1		
612	1		
613	1		
614	1		
615	1		
616	1		
617	1		
618	1		
619	1		
620	1		
621	1		
622	1		
623	1		
624	1		
625	1		
626	1		
627	1		
628	1		
629	1		
630	1		
631	1		
632	1		
633	1		
634	1		
635	1		
636	1		
637	1		
638	1		
639	1		
640	1		
641	1		
642	1		
643	1		
644	1		
645	1		
646	1		
647	1		
648	1		
649	1		
650	1		
651	1		
652	1		
653	1		
654	1		
655	1		
656	1		
657	1		
658	1		
659	1		
660	1		
661	1		
662	1		
663	1		
664	1		
665	1		
666	1		
667	1		
668	1		
669	1		
670	1		
671	1		
672	1		
673	1		
674	1		
675	1		
676	1		
677	1		
678	1		
679	1		
680	1		
681	1		
682	1		
683	1		
684	1		
685	1		
686	1		
687	1		
688	1		
689	1		
690	1		
691	1		
692	1		
693	1		
694	1		
695	1		
696	1		
697	1		
698	1		
699	1		
700	1		
701	1		
702	1		
703	1		
704	1		
705	1		
706	1		
707	1		
708	1		
709	1		
710	1		
711	1		
712	1		
713	1		
714	1		
715	1		
716	1		
717	1		
718	1		
719	1		
720	1		
721	1		
722	1		
723	1		
724	1		
725	1		
726	1		
727	1		
728	1		
729	1		
730	1		
731	1		
732	1		
733	1		
734	1		
735	1		
736	1		
737	1		
738	1		
739	1		
740	1		
741	1		
742	1		
743	1		
744	1		
745	1		
746	1		
747	1		
748	1		
749	1		
750	1		
751	1		
752	1		
753	1		
754	1		
755	1		
756	1		
757	1		
758	1		
759	1		
760	1		
761	1		
762	1		
763	1		
764	1		
765	1		
766	1		
767	1		
768	1		
769	1		
770	1		
771	1		
772	1		
773	1		
774	1		
775	1		
776	1		
777	1		
778	1		
779	1		
780	1		
781	1		
782	1		
783	1		
784	1		
785	1		
786	1		
787	1		
788	1		
789	1		
790	1		
791	1		
792	1		
793	1		
794	1		
795	1		
796	1		
797	1		
798	1		
799	1		
800	1		
801	1		
802	1		
803	1		
804	1		
805	1		
806	1		
807	1		
808	1		
809	1		
810	1		
811	1		
812	1		
813	1		
814	1		
815	1		
816	1		
817	1		
818	1		
819	1		
820	1		
821	1		
822	1		
823	1		
824	1		
825	1		
826	1		
827	1		
828	1		
829	1		
830	1		
831	1		
832	1		
833	1		
834	1		
835	1		
836	1		
837	1		
838	1		
839	1		
840	1		
841	1		
842	1		
843	1		
844	1		
845	1		
846	1		
847	1		
848	1		
849	1		
850	1		
851	1		
852	1		
853	1		
854	1		
855	1		
856	1		
857	1		
858	1		
859	1		
860	1		
861	1		
862	1		
863	1		
864	1		
865	1		
866	1		
867	1		
868	1		
869	1		
870	1		
871	1		
872	1		
873	1		
874	1		
875	1		
876	1		
877	1		
878	1		
879	1		
880	1		
881	1		
882	1		
883	1		
884	1		
885	1		
886	1		
887	1		
888	1		
889	1		
890	1		
891	1		
892	1		
893	1		
894	1		
895	1		
896	1		
897	1		
898	1		
899	1		
900	1		
901	1		
902	1		
903	1		
904	1		
905	1		
906	1		
907	1		
908	1		
909	1		
910	1		
911	1		
912	1		
913	1		
914	1		
915	1		
916	1		
917	1		
918	1		
919	1		
920	1		
921	1		
922	1		
923	1		
924	1		
925	1		
926	1		
927	1		
928	1		
929	1		
930	1		
931	1		
932	1		
933	1		
934	1		
935	1		
936	1		
937	1		
938	1		
939	1		
940	1		
941	1		
942	1		
943	1		
944	1		
945	1		
946	1		
947	1		
948	1		
949	1		
950	1		
951	1		
952	1		
953	1		
954	1		
955	1		
956	1		
957	1		
958	1		
959	1		
960	1		
961	1		
962	1		
963	1		
964	1		
965	1		
966	1		
967	1		
968	1		
969	1		
970	1		
971	1		
972	1		
973	1		
974	1		
975	1		
976	1		
977	1		
978	1		
979	1		
980	1		
981	1		
982	1		
983	1		
984	1		
985	1		
986	1		
987	1		
988	1		
989	1		
990	1		
991	1		
992	1		
993	1		
994	1		
995	1		
996	1		
997	1		
998	1		
999	1		
1000	1		

-02-01	C11842-02-01		
-01-01	C11842-01-01		

United Technology Center

CASTING TOOLING - SUPER BATES

E 14134 C11842

Figure 38. Super BATES Casting Tooling Assembly and Details (Sheet 1 of 3)

DETAIL ITEM 155

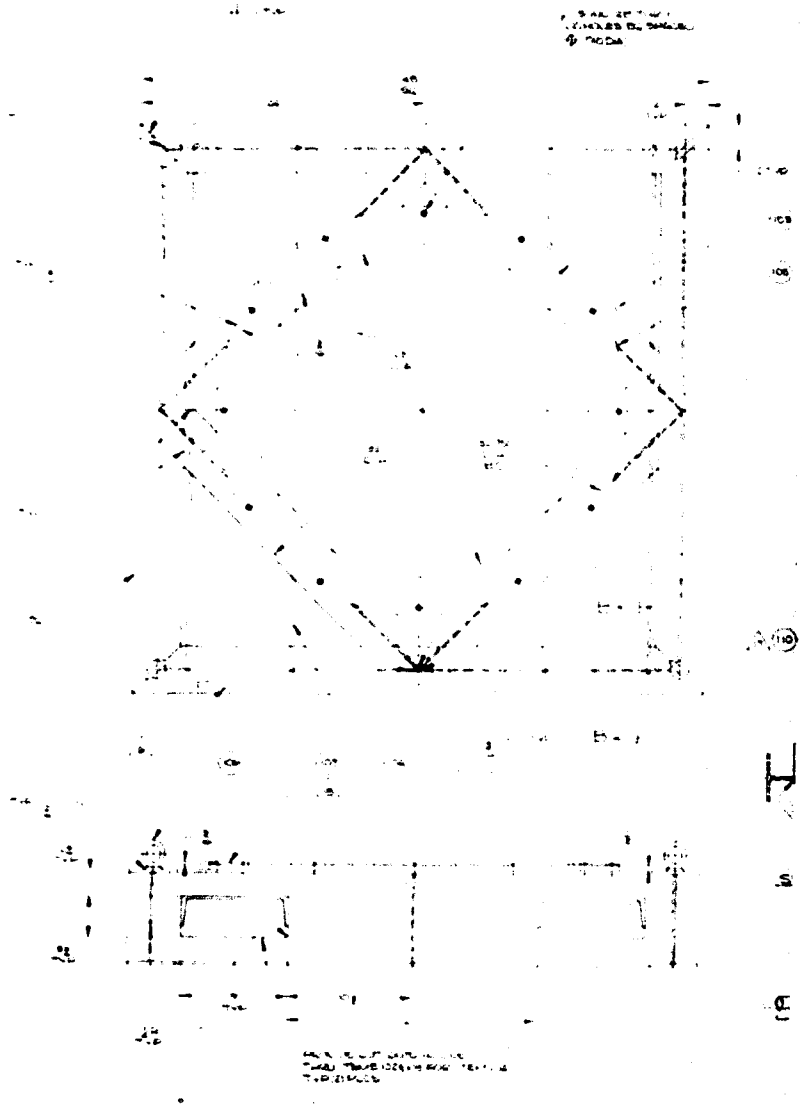

DETAIL WELDMENT ITEM 01

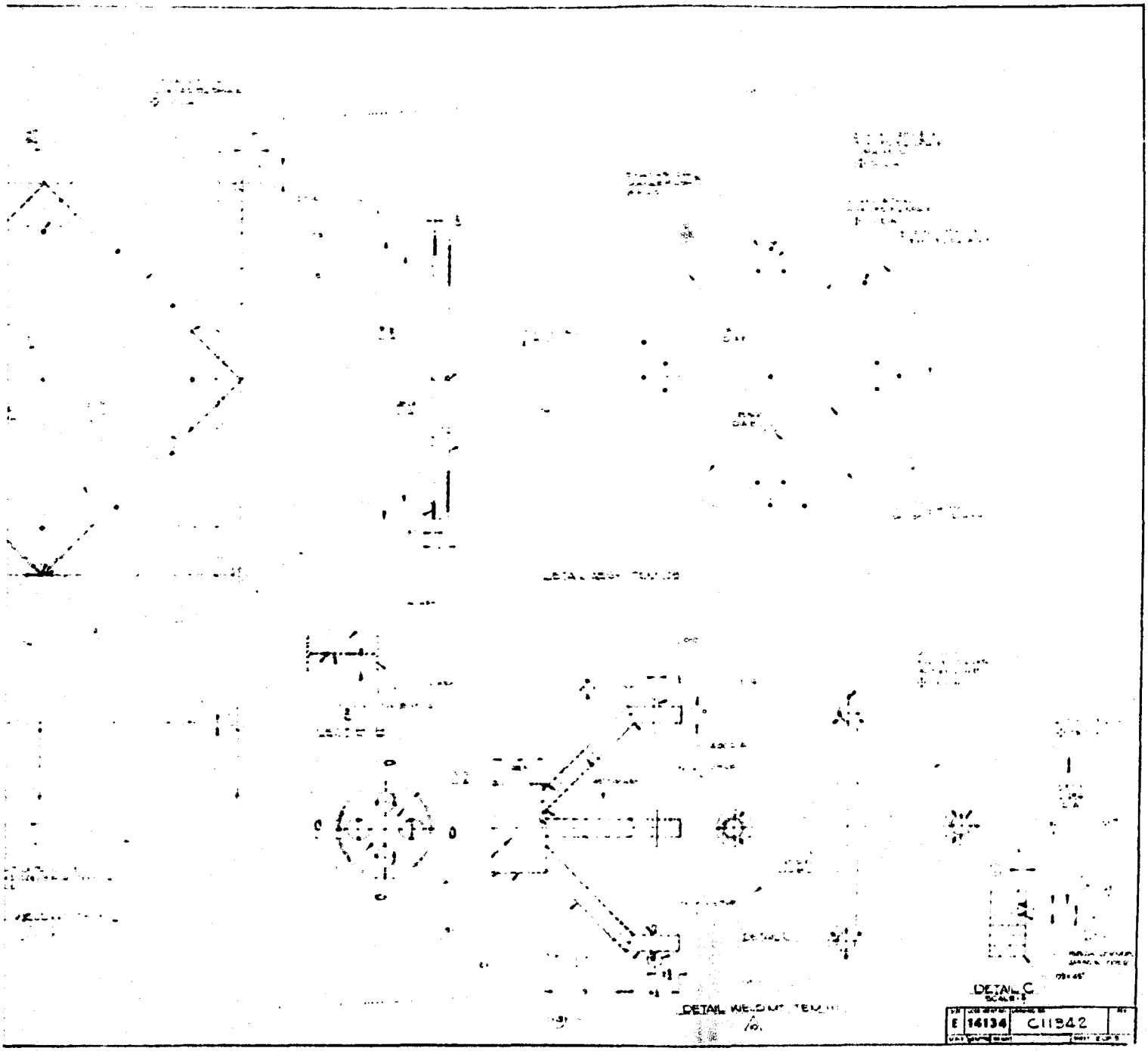

Figure 38. Super BATES Casting Tooling Assembly and Details (Sheet 2 of 3)

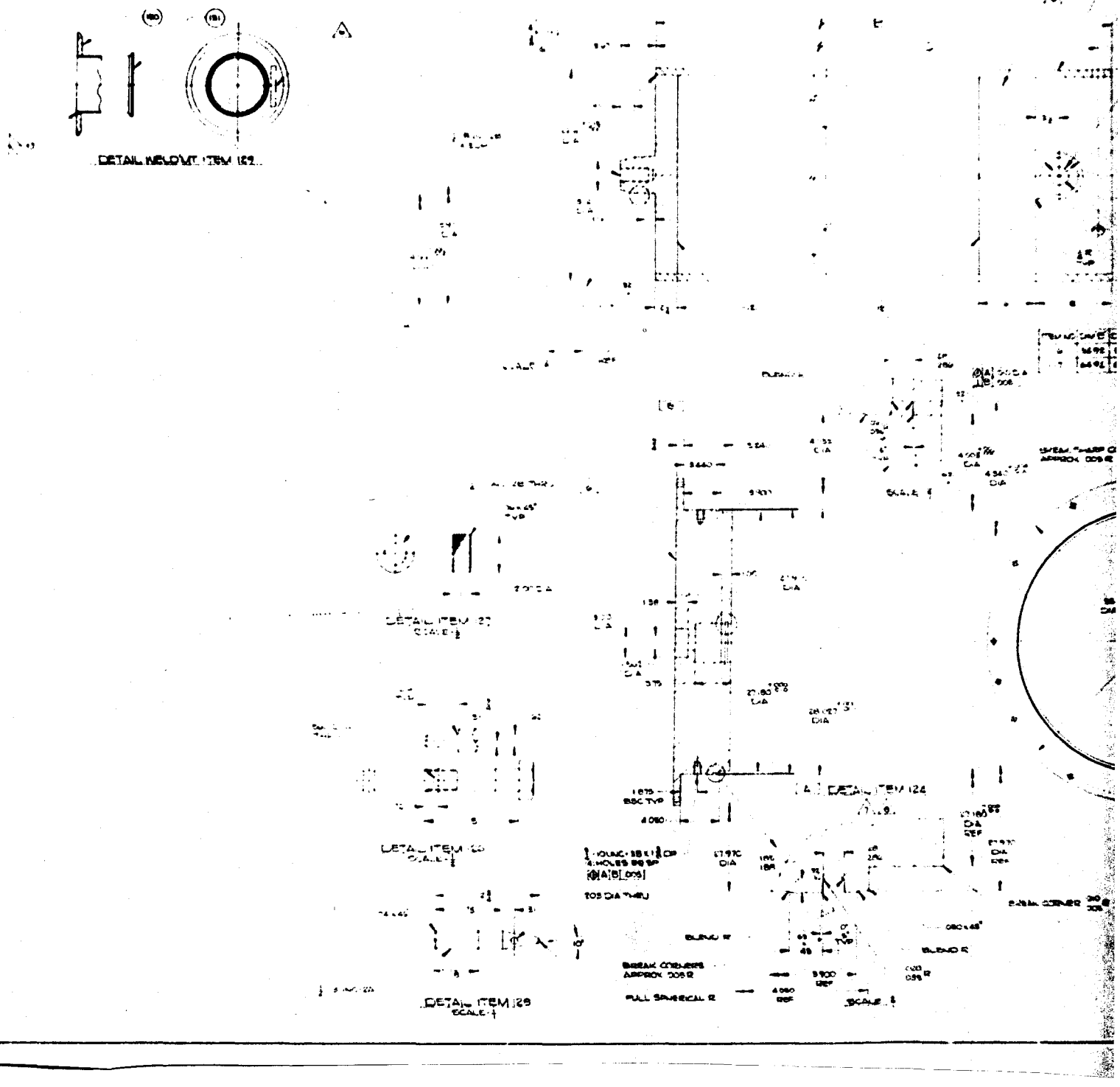
DETAIL ITEM 122
DETAIL ITEM 123
DETAIL ITEM 124
DETAIL ITEM 125
DETAIL ITEM 126
SCALE 1
SCALE 1
SCALE 1
SCALE 1
SCALE 1
BREAK CORNERS
APPROX .005 R
FULL SPHERICAL R
BREAK CORNER

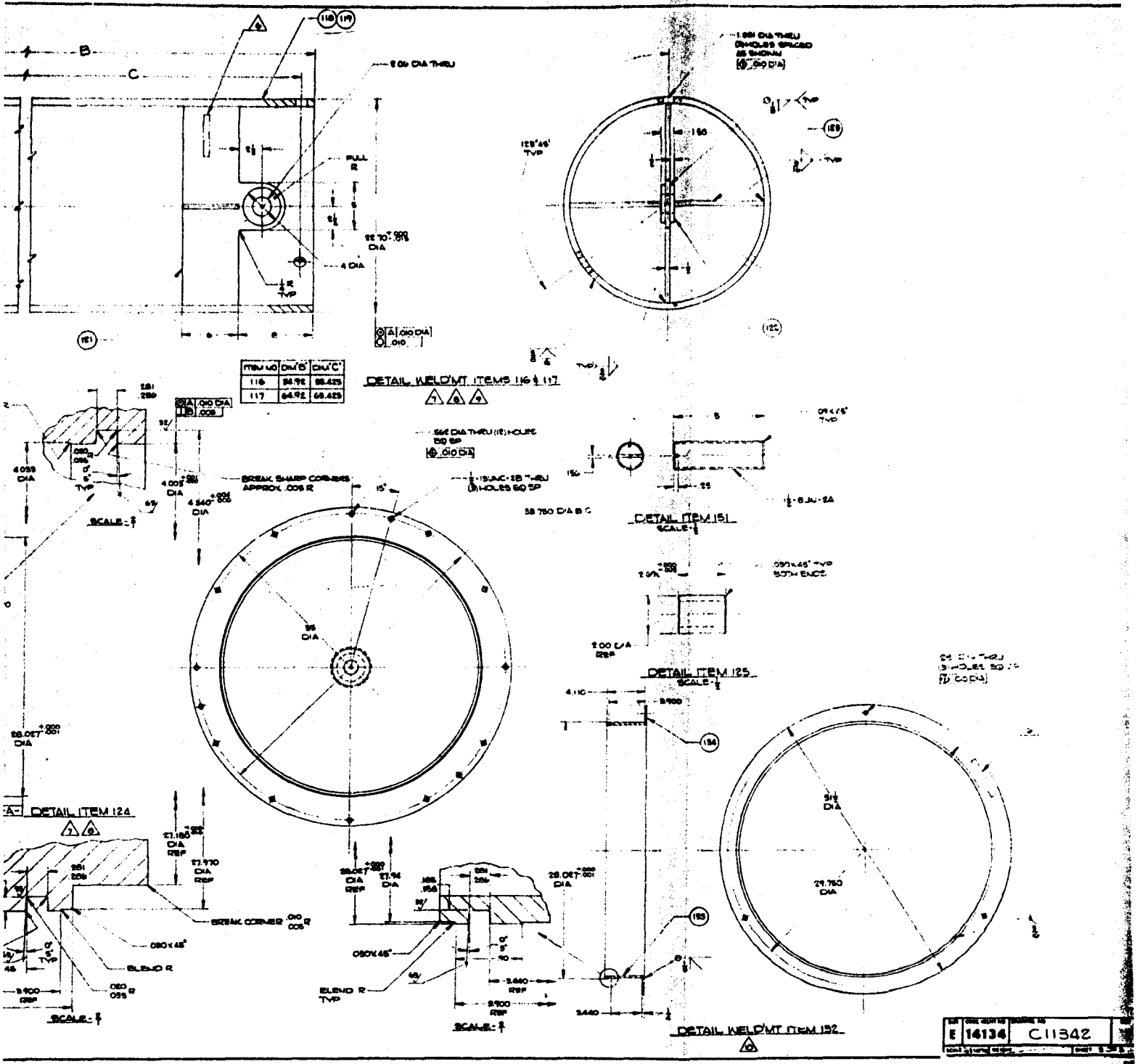

Figure 38. Super BATES Casting Tooling Assembly and Details (Sheet 3 of 3)

The mandrels required to form the propellant perforation are made from aluminum, machined to a close tolerance, and permanently coated with Teflon as a release agent. Mandrels may be made in any shape and size required by a specific motor design without alteration of the other tooling. The permanently coated metal mandrels ensure the maximum reproducibility of close tolerance grains. Mandrels are centered on both ends (and in proper relation to the motor case) by fixed metal registers to ensure uniform thickness of the grain web.

Casting base plates form one end of the propellant grain and provide registers for locating the mandrel in relation to the motor case. These plates are made from aluminum, machined to a close tolerance, and Teflon coated. The base plates will normally be fastened to a fork lift pallet for in-plant handling, but will be detachable if required.

The mandrel centering rods are close tolerance stainless steel rods and sleeves used to position the upper end of mandrel and motor case during casting.

The casting head covers the top end of the motor case during casting. The head is made from Teflon-coated aluminum with ports provided for the casting and vacuum lines. View ports are provided to monitor the casting. The tooling concept uses the case as a vacuum chamber, thus eliminating the need for a separate casting bell.

Propellant is introduced into the Super BATES motor through a stainless steel casting manifold which divides the incoming propellant into four separate streams; this facilitates deaeration and distribution. When casting is completed, the motor is cured with the casting head removed. The mandrel is extracted using a facility crane or hoist. The Teflon coating may be solvent cleaned indefinitely without damage.

Segment insulation is positioned for bonding inside the Super BATES by means of an insulation locating tool. This tool fixes the outer surface of the insulation in relation to the end of the motor case. The insulation location fixture is made of Teflon-coated steel.

Within the processing area, the Super BATES motor case is handled both vertically and horizontally using a strongback with web slings. The case is handled and stored on a shipping container pallet. Trunnions and a strongback are used to lift the motor to a vertical attitude. Trunnion supports are used when inverting the case. All handling will be identical to that described in section 4.1.10.

All materials used in tooling are selected to provide accuracy and long productive life with minimum maintenance. All product-sensitive tooling dimensions will be machined to a tolerance of ±0.005 in. or less. All fasteners used will be AN or MS designation. Safety factors of at least 3 to 1 at yield strength are provided. Commercially available parts are used wherever possible.

4.1.7 Igniter

A basic pyrotechnic, tube type igniter was designed for igniting all configurations of the Super BATES motor. The design is basically the same as that used on the HIPPO motor at AFRPL. The igniter size is varied for various lengths of Super BATES by modifying the igniter length and pellet charge weight. The method of initiation is the same for all configurations. A forward-mounted pyrogen and a spark-initiated system gas-gas (Oxygen/ethylene) were considered but excluded primarily due to considerations of cost, physical size, and test facility complexity.

4.1.7.1 Basic Design Descriptions - The igniter for the nominal motor configuration (Figure 39) consists of a thin walled paper-phenolic tube containing a total of 650 g of $BKNO_3$ pellets as the main ignition charge and 2 g of Mag-TFE granules as the pellet ignition charge. The ignition sequence is started on the initiation of two U.S. Flare 207A squibs, one in each booster charge subassembly.

The pellets are heat sealed in static-free polyethylene bags. Before sealing, each bag is purged with dry nitrogen to drive out any residual moisture. This results in a fully weather-tight assembly and provides electrostatic protection of the squibs and pellets.

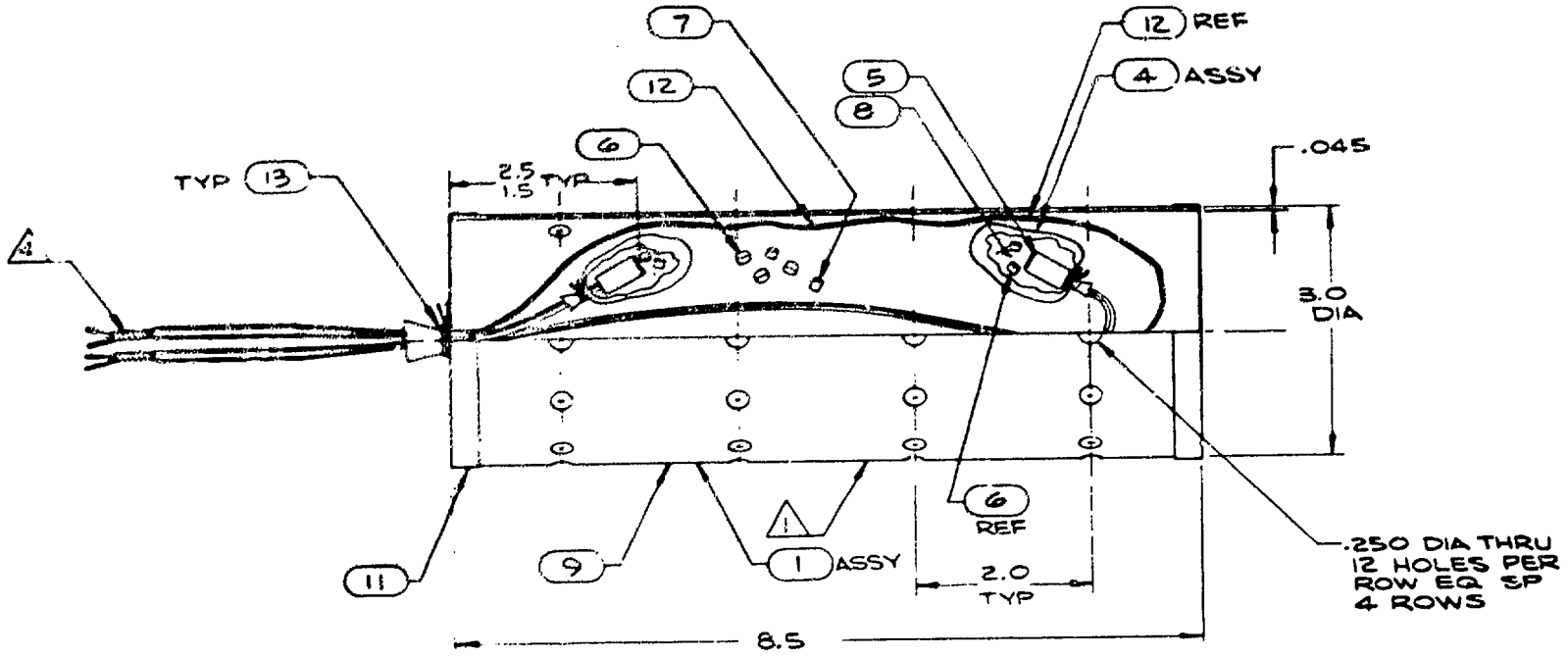

	AR	AR		—	STRING, COTTON	7/C	13
3	AR	AR	7325		VELOSTAT CUSTOM FILM 1 MIL THK NOMINAL	6/C	12
		AR		—	TAPE, ADHESIVE, GLASS CLOTH	7/B	11
							10
5		1	72694	—	TUBING, PAPER PHENOLIC	7/A	9
2	1G		06202	Mg/TFE	POWDER	6/C	8
1		350 G	06202	FND 2D	PELLETS, $BKNO_3$		7
	25 G	300 G	06202	FND 2A	PELLETS, $BKNO_3$		6
2	1		06202	FND 207A	SQUIB	6/C	5
		2		-11-01	SQUIB ASSEMBLY	5/C	4
							3
							2
				-01-01	ASSEMBLY	6/B	1
11-01 QTY REQ'D	G1-01 QTY REQ'D	COAT IDENT	PART OR IDENTIFYING NO.		DESCRIPTION	ZONE	ITEM NO.

PARTS LIST

NOTES:

1. IDENTIFICATION PER OTC 4OOB-9O4O4, METHOD 14A.
2. ATLANTIC RESEARCH CORP ORDNANCE DIV, FLARE/MORTREN DEPT SANDES, CALIF (OR APVD EQUIV).
3. COSTON MATERIALS INC. CHELMSFORD, MASS. (OR APVD EQUIV).
4. SHORT THE TWO LEAD WIRES OF EACH SQUIB TOGETHER.
5. STRITMARK-TAYLOR CORP, AN ALCO STANDARD CO VALLEY FORGE PLANT, VALLEY FORGE, PA, (OR APVD EQUIV).

Figure 39. Igniter Assembly

The U. S. Flare 207A squibs are shelf items and have a demonstrated 1 amp no-fire capability. With a recommended 5 amp firing current applied, the functioning time is less than 2 msec. Two squibs are incorporated in the design for redundancy and increased reliability. Electrical lead wires of sufficient length for the firing circuit connection will be provided with each squib. Either a series or a parallel circuit can be used.

The igniter tube housing is a commercially available paper-phenolic tube with a wall thickness of 0.045 in. The tube has a 3-in. outside diameter and is 8.5 in. long. The tube is perforated to allow a portion of the pellet exhaust products to discharge radially and impinge directly on the propellant surface for increased heat transfer. The ends of the tube are sealed with a durable glass tape to retain the bagged pellets and to provide additional weather protection.

4.1.7.2 Igniter Sizing – The pellet charge weight was determined from an empirical equation developed by the Naval Ordnance Laboratory, White Oaks, Maryland. This equation was used to size the HIPPO pyrotechnic igniter among others and is satisfactory for ignition pellet sizing. This equation appears as follows and results in a calculated pellet weight of 650 g.

$$W = \frac{38}{\Delta H}\left[A_B\, q_c \left(\frac{L}{A_B}\sqrt{4\pi A_p} \right)^{0.59} \right]^{1.06}$$

where W = pellet weight, g

ΔH = heat of reaction, cal/g

A_B = exposed surface area, cm^2

q_c = ignition energy, cal/cm^2

L = exposed grain length, cm

A_p = port area, cm^2

4.1.7.3 Predicted Ignition Transient – The predicted ignition transient for the baseline configuration is shown in Figure 40, and was determined from well characterized computer models at UTC. The time from zero to 75% of maximum forward motor chamber pressure was calculated to be 180 msec at a nominal temperature of 70°F; this meets the requirement of 250 msec.

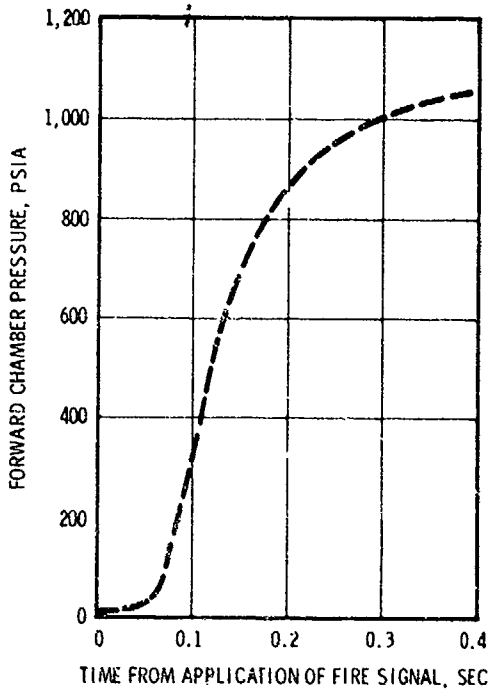

Figure 40. Predicted Ignition Transient for Super BATES Baseline Configuration, 70°F

05762

4.1.8 Pressure Relief System

The pressure relief system, located in the forward closure, consists of a standard off-the-shelf disc assembly, a 4-in.-diameter entrance port, and three equally spaced radial exit passageway [illegible] in. in diameter (Figures 11 and 12). The passageway system is sized for the 2,200 MEOP case while burst disc assemblies will be selected for individual test requirements.

The single burst disc assembly is submerged in the internal side of the forward closure at the motor axial centerline and is held in place by a removable ring assembly. The 4-in.-diameter port is located immediately ahead of the disc assembly. The internal radial passageways intersect the 4-in. port to provide a radial exhaust path which eliminates large changes in motor axial thrust during venting of motor chamber overpressure. All internal passageways of the system are lined with easily replaceable paper-phenolic tubing to provide thermal protection. A single, centrally located burst disc assembly was selected to eliminate the possibility of unequal side force loads which could occur if a 3-disc system were used; the discs did not rupture simultaneously.

The burst disc is sized to rupture at 1.25 times MEOP. For the baseline motor this pressure will be 1,250 psia. Insulation will be used on the upstream side of the burst disc for thermal protection during test; however the burst disc will be replaced after each test firing.

An analysis was conducted to determine the response of the motor to debonding of one complete segmented grain. These results, shown in Figure 41, were used to size the burst disc and associated porting. The analysis shows that the pressure approaches the equilibrium pressure and never exceeds the case proof pressure.

The assumptions used in the analysis are:

A. 1,800 psia chamber pressure
B. 150,000 lb thrust at the above pressure
C. 8-in.-diameter throat
D. 4-in.-diameter burst disc
E. Three segments burning with one segment completely debonded
F. Burst disc ruptures instantaneously at maximum design pressure of 2,250 psia
G. Flow fully stabilized through the burst disc at rupture
H. Case proof pressure at 2,860 psia
I. Surface area and volume held constant.

Burst disc rupture and flow stabilization do not occur instantaneously; however, a more realistic approach would not alter the final conclusions. Assumption I is conservative because the area is continually decreasing while the free volume is increasing.

The pressure-time history was calculated from the following equation using the above specified assumptions:

$$\frac{dP}{dt} = (\dot{\rho}^{n} a A_b - \frac{P_c A_t \zeta}{c^*}) \frac{RoT}{MV} - \frac{P}{V} \frac{dV}{dt}$$

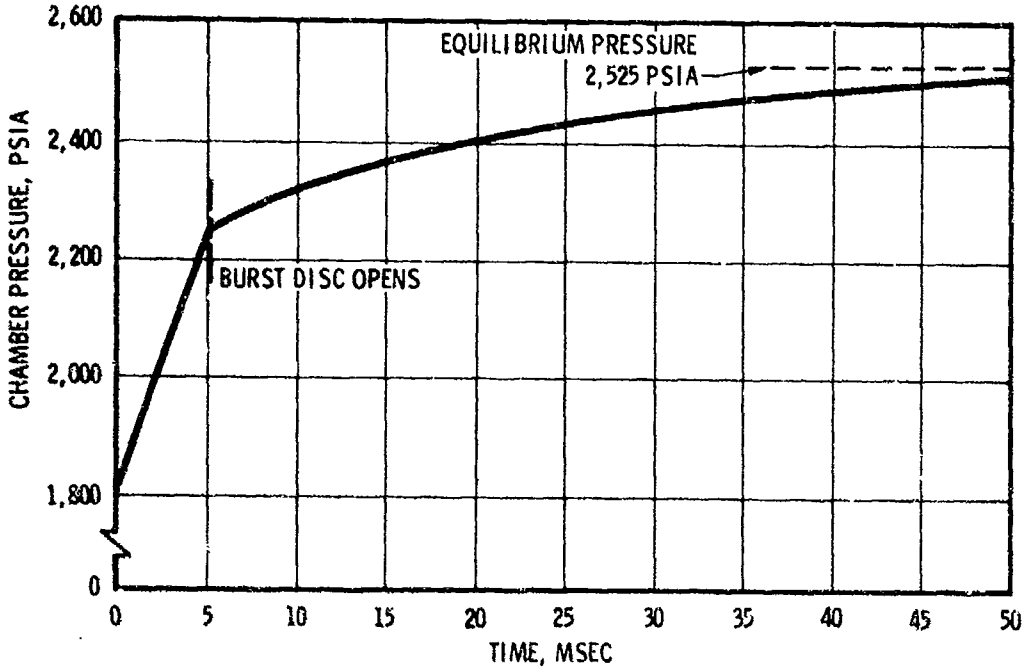

Figure 41. Super BATES Burst Disc Pressure-Time History

05748

4.1.9 Handling Equipment and Motor Assembly

Handling equipment requirements for assembling and installing the Super BATES motor on the thrust stand have been identified and preliminary designs prepared.

The test motor handling equipment is based on concepts developed jointly between UTC and AFRPL for use on the Super HIPPO program. A system of trunnions, slings, and adapters is used to move the components of the motor and the assembled motor. The Super BATES motor is assembled vertically to simplify alignment between case segments and clevis pin rows, then lowered to the horizontal position and moved to the thrust stand. The thrust stand is installed in the test area I-32, pad 2. The Super BATES motor is installed on the right-hand half of the test pad and assembly platforms are located against the back wall on the left hand side of the test pad (see Figure 42). The motor components are delivered to the stand, off-loaded, and assembled.

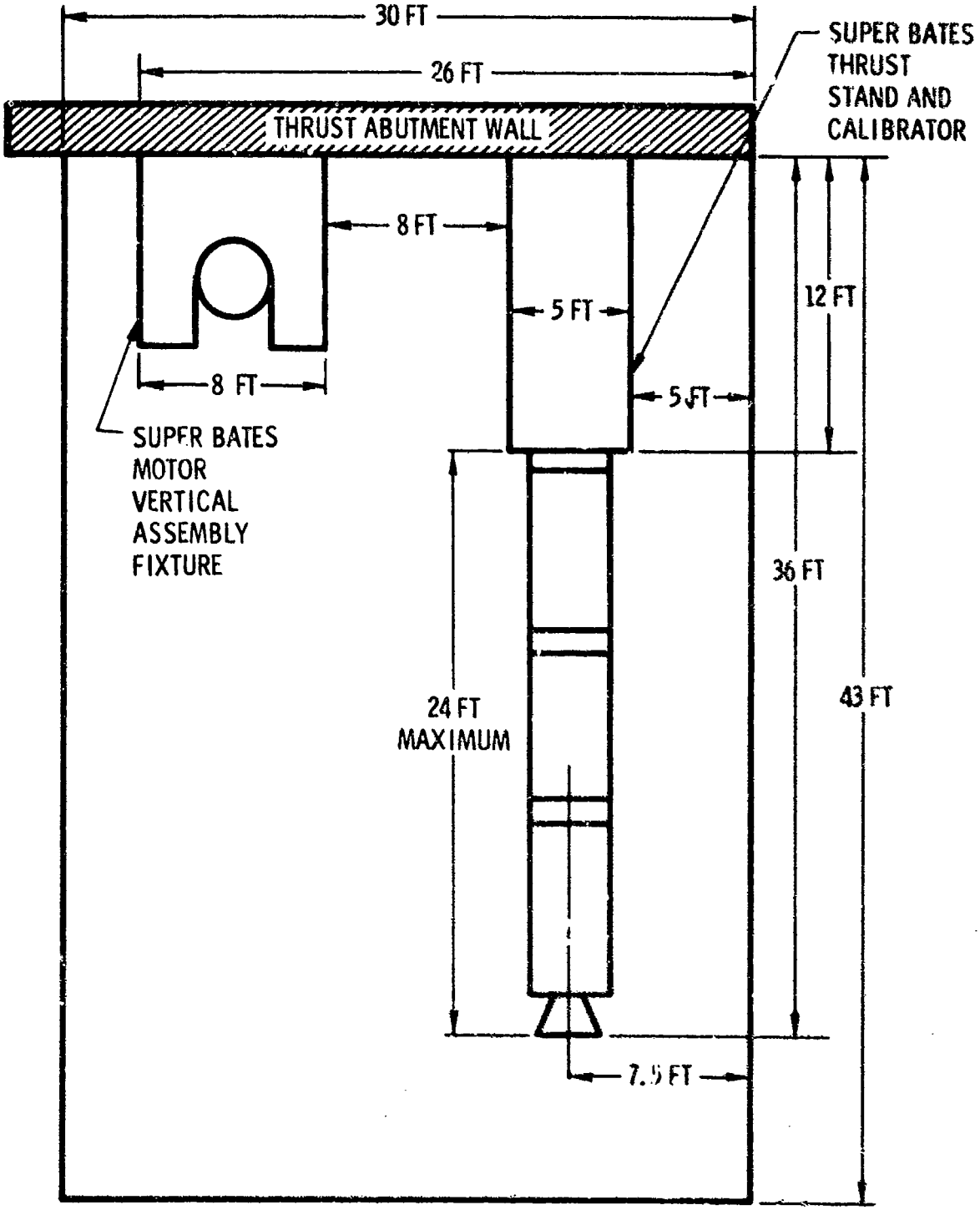

Figure 42. Top View of Super BATES Motor Assembly on Thrust Stand (Area I-32, Pad 2)

05804

The assembly sequence is as follows:

A. The forward closure has two trunnions which are mounted off-center of the closure; those trunnions are lifted with a spreader bar, stirrups, and a tag leg. The purpose of mounting the trunnions off-center on the closure is the same as with Super HIPPO: to generate a three-point lift so that the closure will not revolve on the lifting pins. The tag leg goes to an eye hook located between the trunnions as shown in Figure 43.

B. The frame is set on a trunnion base near the back wall under the assembly work platform as shown in Figure 44. A support positions the forward closure and prevents it from rotating.

C. The O-ring and insulation are installed on the forward closure.

D. The overpressurization venting system, burst disc, and insulation are installed.

E. A loaded case is installed. The propellant case is packed in a reusable shipping container and delivered to the test pad on a flat bed truck, or fork lift, in a vertical position. The complete top of the container is removed to expose the segment on the base of the container. The propellant case stands on the base of the shipping container. Case lift adaptors are installed on the top end of the case. The spreader bar and stirrups are then installed on the case lift adapters and the case is lifted clear of the shipping container base (see Figure 45). Two additional lift adapters are installed on the lower end of the case and the case set down on two pairs of trunnion bases. The trunnion bases engage the case lift adapter shafts as shown in Figure 46.

The motor segment can be moved in the vertical position directly to the forward closure for motor assembly. However the motor is more easily examined in the horizontal position, and this step is necessary for inverting the segment. For motor assembly, the case is rotated to the vertical position. The lifting adapter on the lower end of the segment is removed (see Figure 47) and the assembly is then installed on the forward closure in the assembly area.

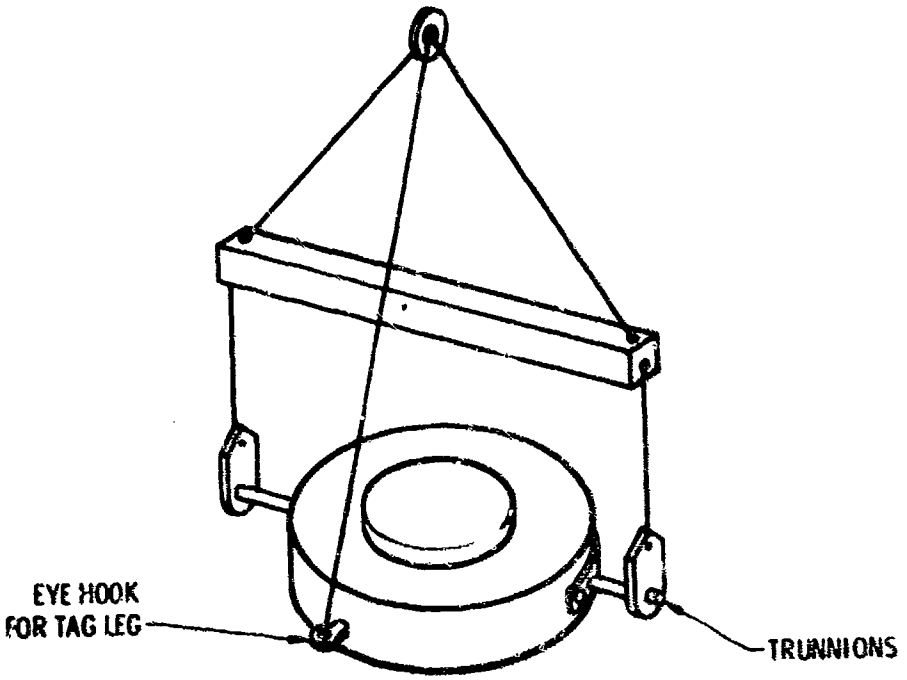

Figure 43. Forward Closure with Lifting Trunnions and Spreader Bar

05805

F. An H-clevis coupling ring is installed,

G. The coupling ring insulation is inspected, the O-ring grooves are inspected and cleaned as required, and new O-rings are installed.

H. The coupling ring is lifted by using the opposite (male) end of the case lift adapter and pinning the coupling to the case lift adapter. External eyes or lift features on a coupling ring are avoided to prevent the possibility of lifting the motor by these eyes.

I. The coupling ring is attached to the closure lift adapter, lifted with a spreader bar, and installed on the segment.

J. A second segment, a second coupling ring, and a third segment are installed in the same fashion. Attachment braces at each of the work platforms may be used to secure the motor assembly during buildup.

K. The aft closure and nozzle assembly are built up on the ground using the trunnion bases that were used for inverting the propellant cases. The closure is lifted by its trunnions with a spreader bar and tag leg and set in a trunnion base set. The tag leg is used to position the aft closure face up.

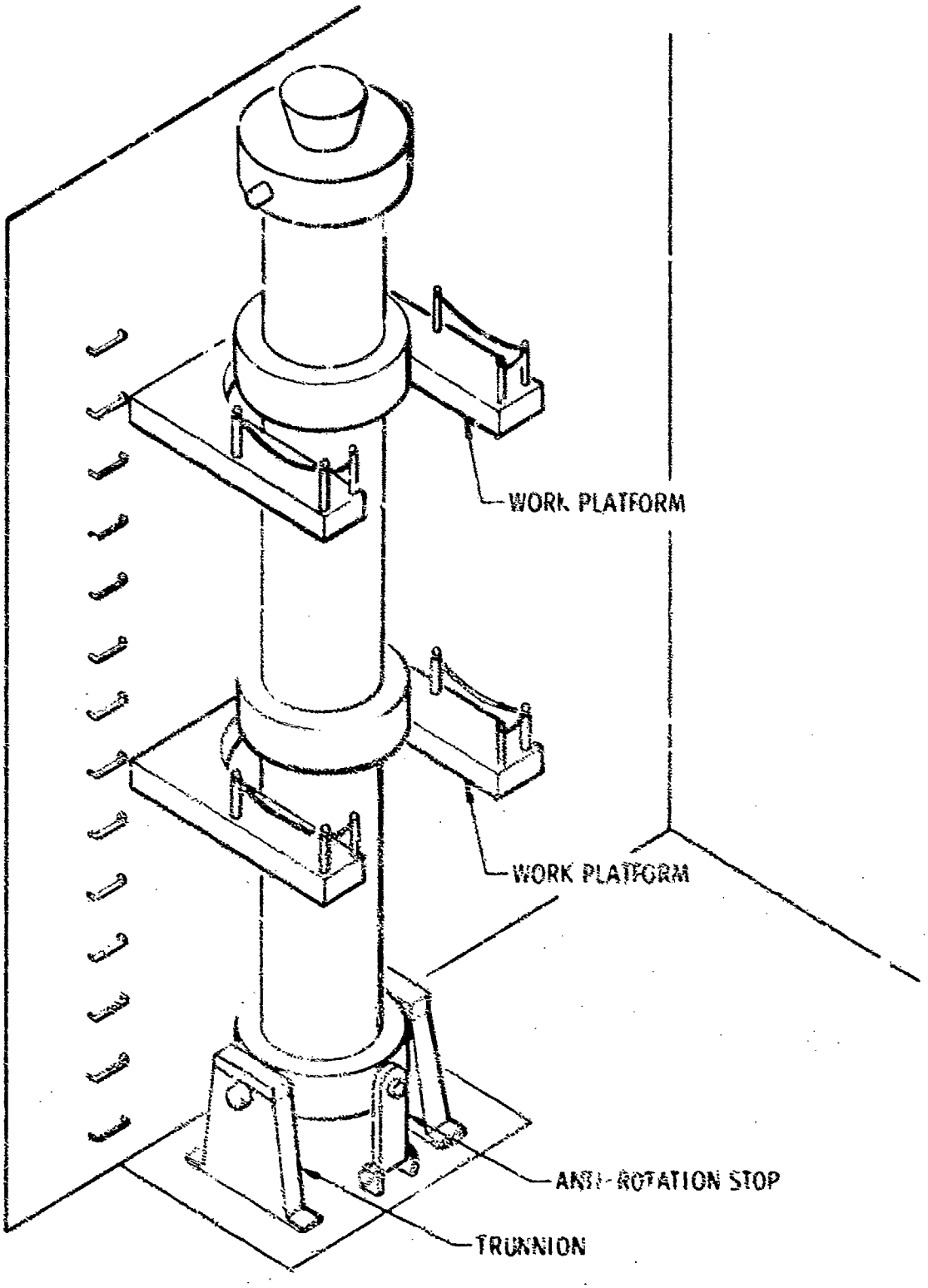

Figure 44. Test Motor Assembly in Vertical Assembly Fixture

05806

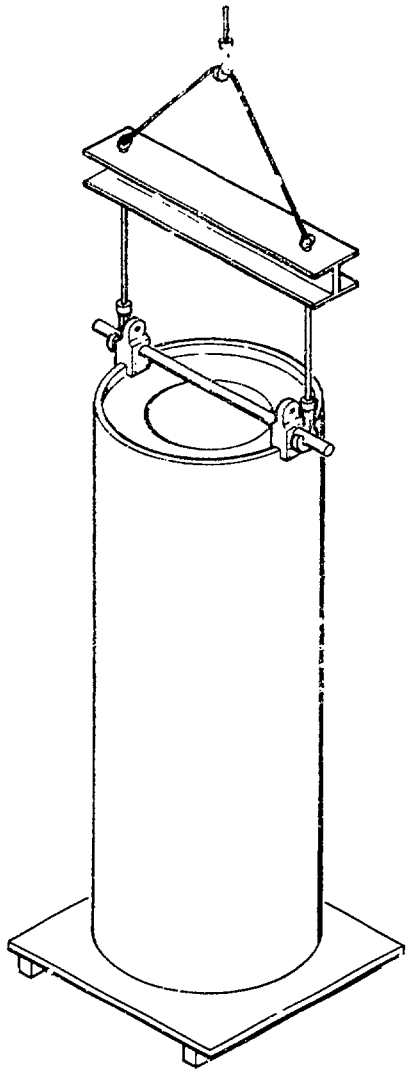

Figure 45. Removing Loaded Motor Case from Shipping Container

05894

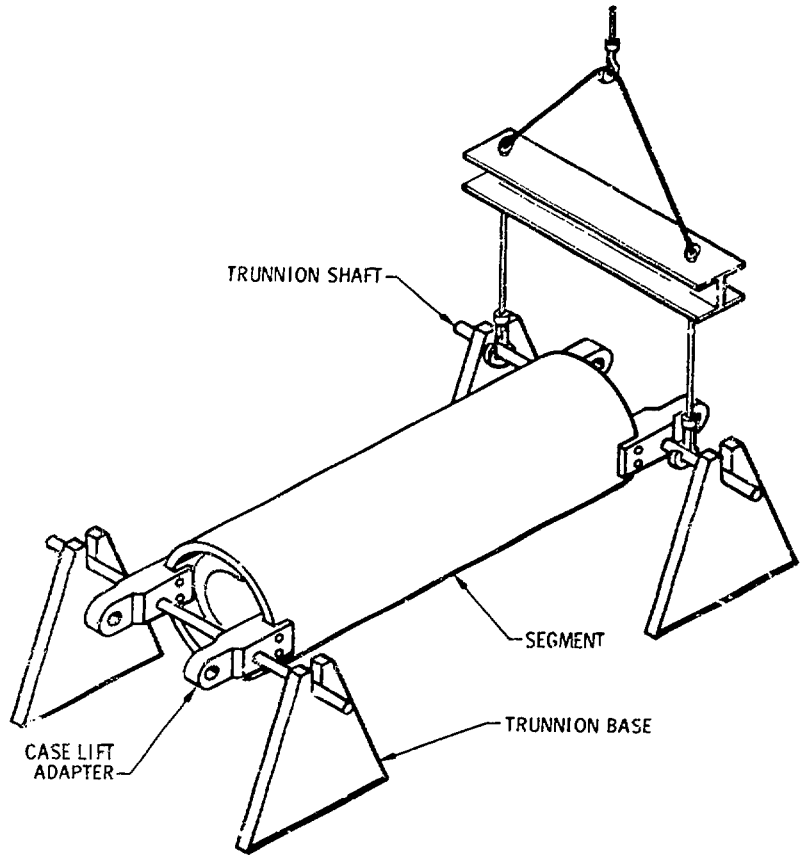

Figure 46. Motor Case on Trunnion Support

05808

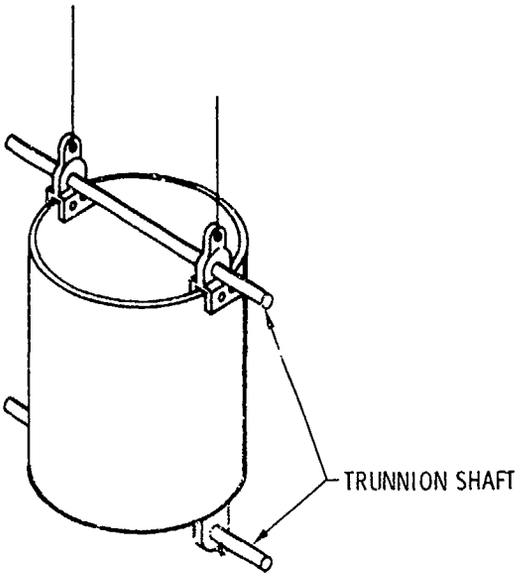

REMOVE LOWER TRUNNION SHAFT FROM
CASE SEGMENT AND LOWER ONTO FORWARD CLOSURE

Figure 47. Removing the Lifter Adapter

05810

L. The insulation is inspected and replaced as necessary.

M. The sealing O-ring is examined and replaced as necessary.

N. The aft closure is inverted using eye hook and tag leg to the nozzle up position and the nozzle assembly is installed in the aft closure using a nozzle lift fixture as shown in Figure 48. The actual nozzle insulation procedure varies depending on nozzle type (conventional or submerged), size, and degree of submergence.

O. The aft closure and nozzle assembly are lifted with a spreader beam and tag leg and positioned on top of the motor.

P. Clevis pins are installed and the two securing brackets on the work platforms are released.

Q. The securing bracket under the forward closure is removed and the motor is rotated to the horizontal position and set on a trunnion base (see Figure 49).

R. A strongback is then attached to the trunnions on the forward and aft closures for lifting (see Figure 50).

S. The motor assembly is moved from the assembly zone and installed on the thrust stand flexure frame.

Disassembly between firings is performed in the same manner but with operations reversed. Shorter motors with fewer segments are assembled in the same fashion. The work platforms are positioned so that by using two platforms and the ground level as working bases, any combination of half- and full-length cases can be accommodated. A strongback will be able to pick different lengths of motors simply by relocating and pinning the cross arms. A flatbed truck with forklift will be adequate for moving loaded case segments. It is recommended that AFRPL provide a trailer for moving motor components and handling fixtures to and from the test stand. The handling equipment required is identified in Table 16.

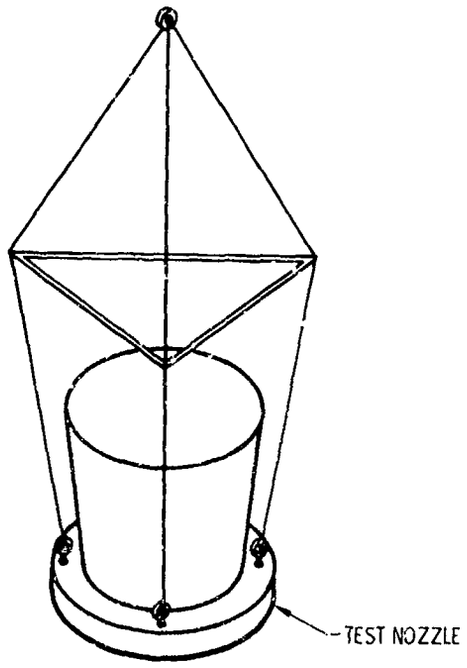

Figure 48. Nozzle Lift Fixture

05811

4.1.10 Motor Case Segment Shipping Container

The shipping container, shown in Figure 51 (taken from UTC packaging data card No. 2509, sheets 2 through 9),* is designed to be reusable and to accept either a full- or half-length segment in the vertical attitude. Acceptance of either a full- or half-length segment is accomplished using adjustable tie-down devices.

The container consists of three major components: (1) base assembly: (2) tie-down assembly; and (3) closure assembly. The base provides total segment load support, horizontal restraint, and tie-down fittings for vertical restraint. Two-way forklift entry pockets and towing attach holes are part of the base structure. The tie-down components consist of four chain and turnbuckle assemblies attached to the base and hooked to the segment cover assembly.

* Sheet 1 details the segment packaging instructions.

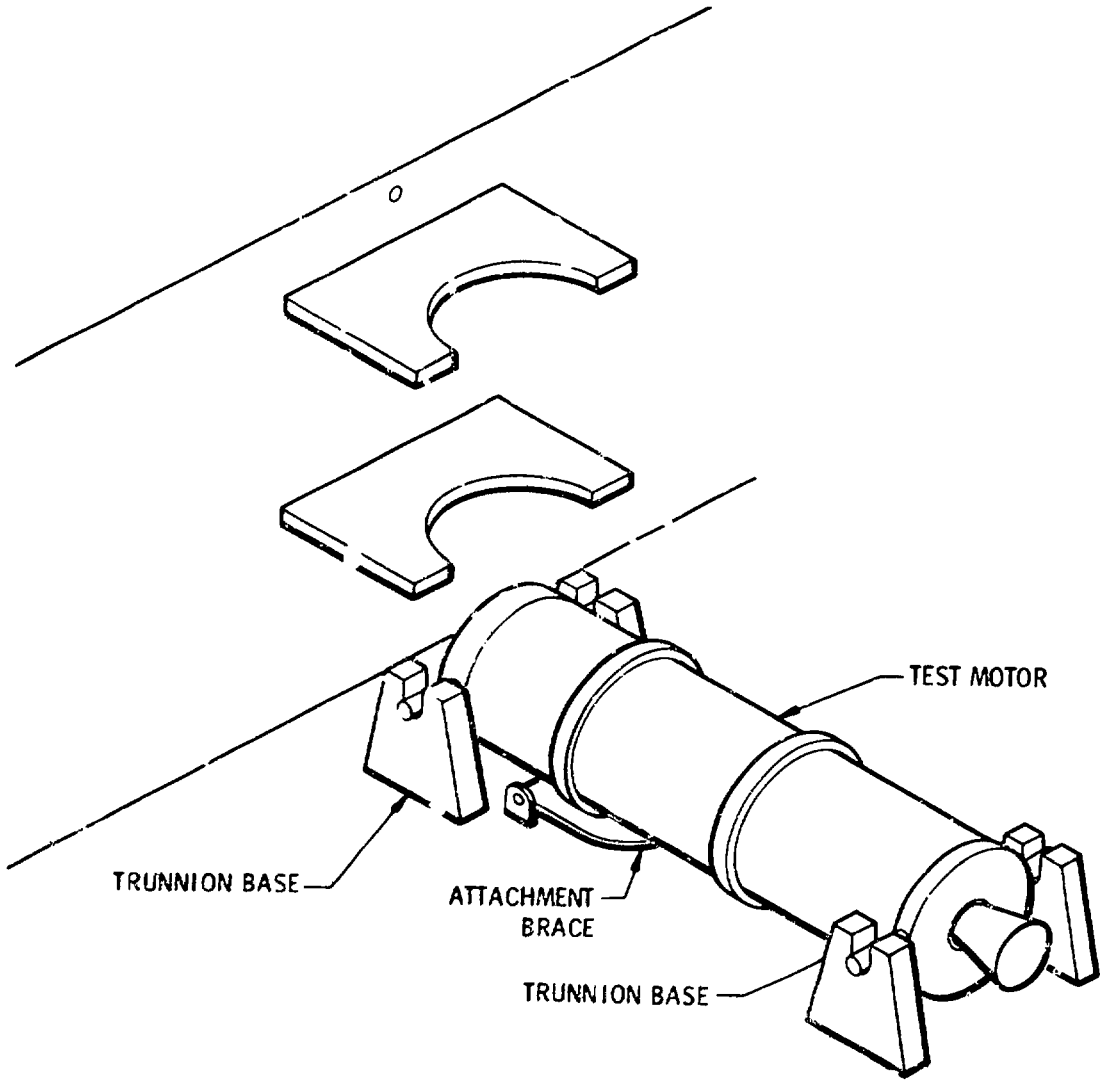

Figure 49. Motor Assembly Lowered to Horizontal Position

05812

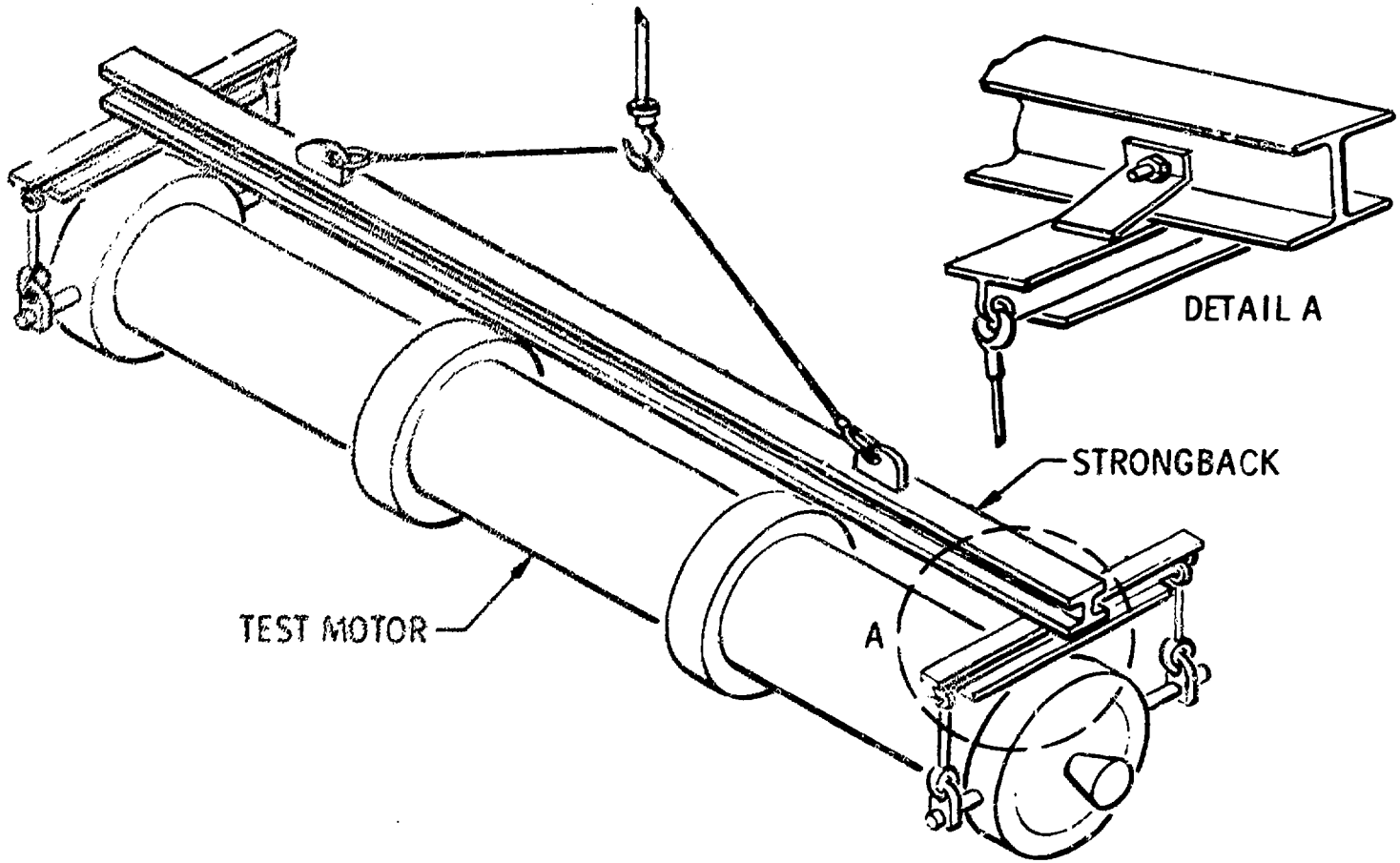

Figure 50. Motor Assembly Being Moved to Thrust Stand

05813

TABLE 16. HANDLING EQUIPMENT

Item	Quantity
Two point sling and tag line	1
Nozzle lift fixture	1
Spreader bar and stirrups	2
Trunnions (mount to closure)	4
Case lift adapters	4
Trunnion base set	4
Base support (anti-tilt)	1
Assembly platforms	1 set
Strongback	1
Pin puller	2
Reusable shipping boxes	
Case	38
Coupling	2
Nozzle insert	3
Transport trailers	
Closure and miscellaneous	2

The closure assembly (patterned after a federal specification PPP-B-601 cleated plywood panel wooden box), indexes to the base and is secured in place using two standard tensioned steel straps installed through the base structure over and around the closure. The straps will be replaced each time the container is reused. The closure is removed and installed by an overhead lifting device and wire-rope slings attached to four lifting grips located at the top corners of the closure.

Container design will be submitted to the Bureau of Explosives for approval and issuance of an approval number; this number will appear on each container.

NOMENCLATURE

SHIPPING CONTAINER, MOTOR CASE SEGMENT, SUPER. BATES

PAR

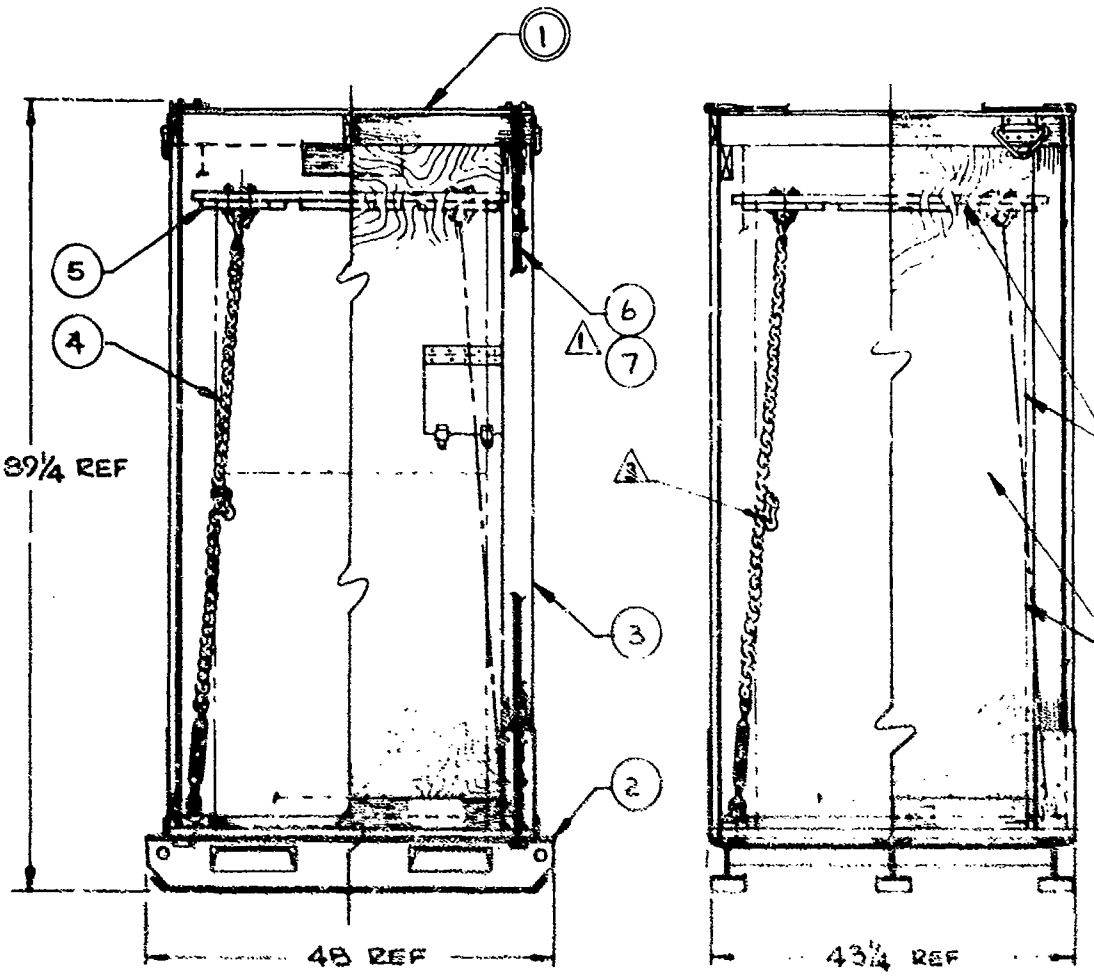

SHIPPING CONTAINER ASSY.

SCALE : ¾" = 1'

NO

QTY	ITEM
1	1
1	2
4	4
1	3
1	5
2	6
2	7

4.2

TOR CASE SEGMENT, SUPER BATES	PART NO.	PD FORM NO. 2509	REV.

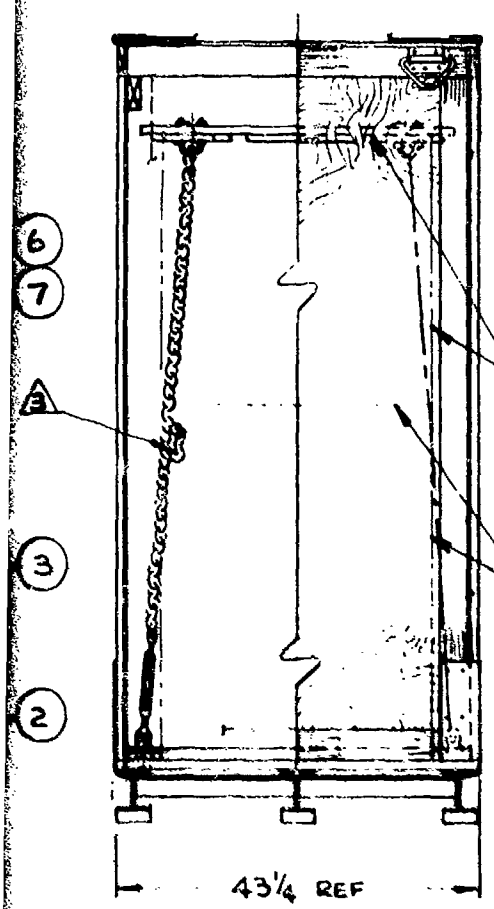

TAINER ASSY.
¾" = 1'

NOTES:

1. ITEMS 6 & 7 ARE USED TO SECURE THE CONTAINER CLOSURE TO THE BASE. ITEM 6 & 7 SHALL BE FURNISHED BY THE MOTOR CASE PACKER.
2. THE SHIPPING CONTAINER ASSY. SHALL BE SUPPLIED COMPLETLY ASSEMBLED, EXCEPT FOR ITEMS 6 & 7, INCLUDING MARKINGS 4.
3. FOR TIE-DOWN OF THE HALF-LENGTH MOTOR CASE USING ITEM-5.
4. SEE SHEET-9 FOR CONTAINER MARKING ARRANGEMENT AND REQUIREMENTS.

	QTY	ITEM	PART NUMBER	DESCRIPTION	SHEET
1	2	7	COMMERCIAL	SEAL, (OPTIONAL TYPE), ¾ SIZE	
1	2	6	COMMERCIAL	STRAP, TENSION, STL. ¾ X .035 X	
	1	5	PDC2509-	COVER ASSY	5
	4	4	PDC2509-	TIE-DOWN ASSY	4
	1	3	PDC2509-	CLOSURE ASSY.	3
	1	2	PDC2509-	BASE ASSY.	2
4 1 2		1	PDC2509	SHIPPING CONTAINER ASSY. CONSISTS OF ITEMS 2 THRU 5	

Figure 51. Shipping Container for Motor Case Segment (Sheet 1 of 7)

05895

MANUFACTURE

SHIPPING CONTAINER, MOTOR CASE SEGMENT, SUPER BATES

PART NO.

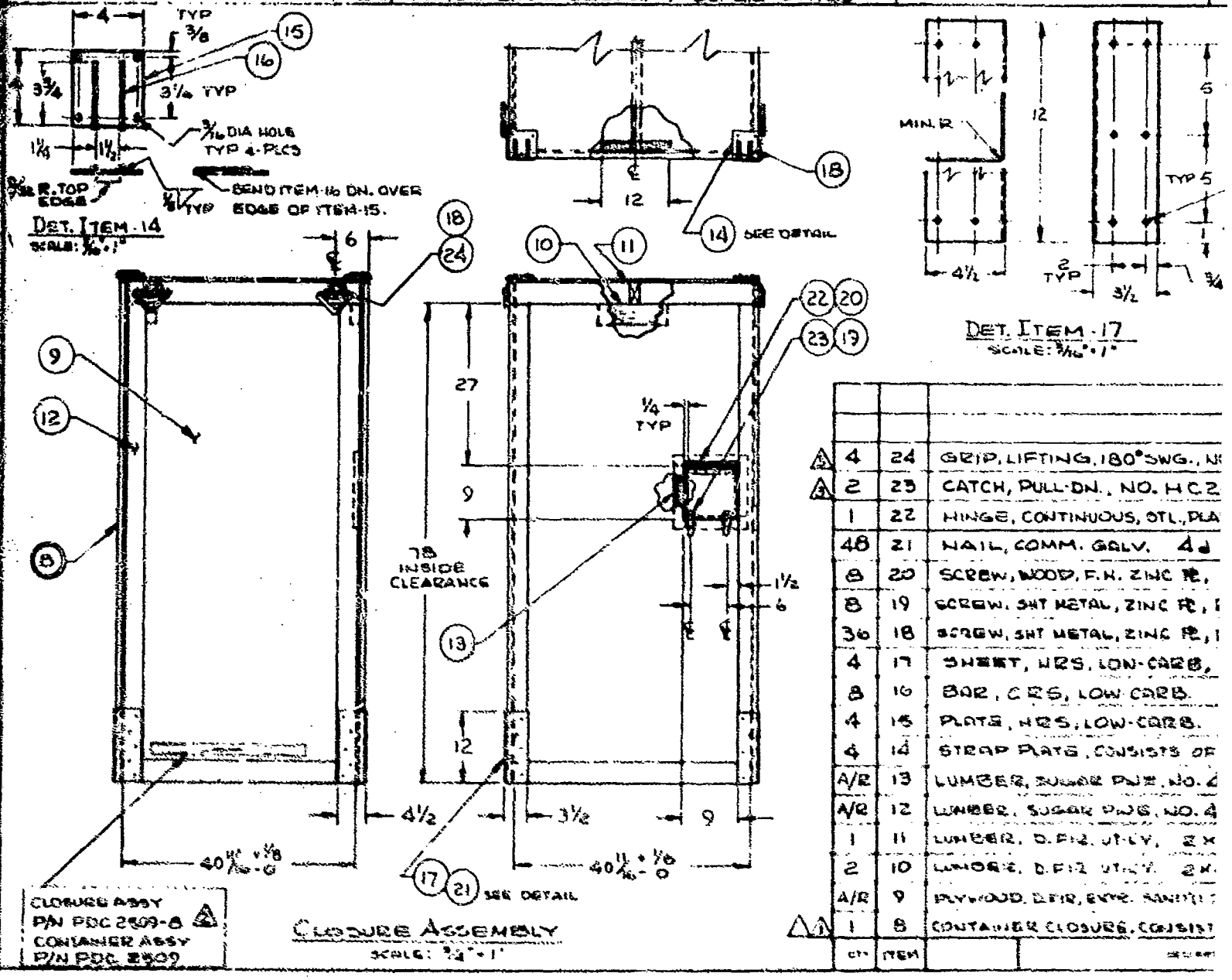

QTY	ITEM	
4	24	GRIP, LIFTING, 180° SWG., N
2	23	CATCH, PULL-DN., NO. HC2
1	22	HINGE, CONTINUOUS, STL., PLA
48	21	NAIL, COMM. GALV. 4d
8	20	SCREW, WOOD, F.H. ZINC PL,
8	19	SCREW, SHT METAL, ZINC PL, I
36	18	SCREW, SHT METAL, ZINC PL, I
4	17	SHEET, HRS, LOW-CARB,
8	16	BAR, CRS, LOW CARB.
4	15	PLATE, HRS, LOW-CARB.
4	14	STRAP PLATE, CONSISTS OF
A/R	13	LUMBER, SUGAR PINE, NO. 2
A/R	12	LUMBER, SUGAR PINE, NO. 4
1	11	LUMBER, D. FIR, ST-LV, 2 x
2	10	LUMBER, D. FIR ST-LV, 2 x
A/R	9	PLYWOOD, D. FIR, EXTR. SANITI
1	8	CONTAINER CLOSURE, CONSIST

PD FORM NO	REV
2509	

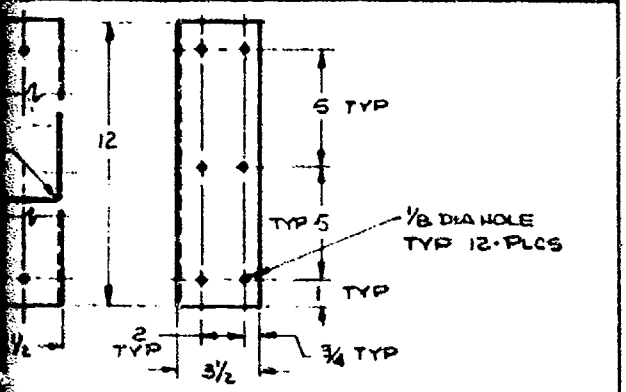

DET. ITEM-17
SCALE: 3/16"=1"

SEE SHEET 4 FOR △ NOTES

RIP, LIFTING, 180° SWG., NO. HA976-LSW, ZINC PL	
ATCH, PULL-DN., NO. HC200ZE	
NGE, CONTINUOUS, STL., PLAIN, W/HOLES, 1½ X 9 LG	
AIL, COMM. GALV. 4d	
REW, WOOD, F.H. ZINC PL, NO. 6 X ⅜ LG	
REW, SHT METAL, ZINC PL, R.H. NO. 4 X ⅜ LG	
REW, SHT METAL, ZINC PL, R.H. NO. 10 X 1 LG	
EET, HRS, LOW-CARB, 12-GA X 8 X 12	
AR, CRS, LOW-CARB. 3/16 X 3/16 X 4 LG	
ATE, HRS, LOW-CARB. 3/16 X 4 X 4	
AP PLATE, CONSISTS OF ITEM 15 AND 16	
IBER, SUGAR PINE, NO. 4 1 X 3 X DEVEL. LGTH	
IBER, SUGAR PINE, NO. 4 1 X 4 X DEVEL. LGTH	
IBER, D.FIR, UTILY. 2 X 4 X 40 ⅜ LG	
IBER, D.FIR UTILY. 2 X 4 X 12 LG	
WOOD, D.FIR, EXTR. SANDED SHOE, ⅜ X DEV. L & W	
TAINER CLOSURE, CONSISTING OF ITEM 9 THRU 34	
	DESCRIPTION

PD FORM NO	REV
2509	

NOMENCLATURE SHIPPING CONTAINER, MOTOR CASE SEGMENT,

NOTES FOR SHEETS 2 & 4:

△ MATERIAL & CONSTRUCTION SHALL BE PER FEDERAL SPECIFICATION PPP-B-601, STYLE-I, AND AS SHOWN ON THIS DRAWING. ALSO, ALL SIDE-TO-END AND TOP TO SIDE & END PANELS SHALL BE GLUED, USING POLYVINYL GLUE, TO AFFECT A WATER RESISTANT JOINT.

△2 STENCIL IN 7/16 IN. (MIN) HIGH CHARACTERS, BLACK COLOR.

△3 NIELSON HARDWARE CORP., HARTFORD, CONN.

△4 NAIL ITEM-36 TO UNDERSIDE OF ITEM-35 USING ITEM-54: NAILS SHALL BE DRIVEN THRU ITEM-35 INTO ITEM-36.

△5 NAIL ITEM-38 TO ITEM-35 USING ITEM-55; LOCATE NAILS APPROX. AS SHOWN.

△6 GLUE ITEMS-38 AND-39 TO ITEM-35, USING ITEM-50 TO AFFECT A WATER-RESISTANT JOINT.

△7 BOND ITEMS-48 AND-49 TO ITEM-35 USING ITEM-51.

Figure 51. Shipping Container for Motor Case Segment (Sheet 2 of 7)

05896

NOMENCLATURE SHIPPING CONTAINER, MOTOR CASE SEGMENT, SUPER BATES

PART

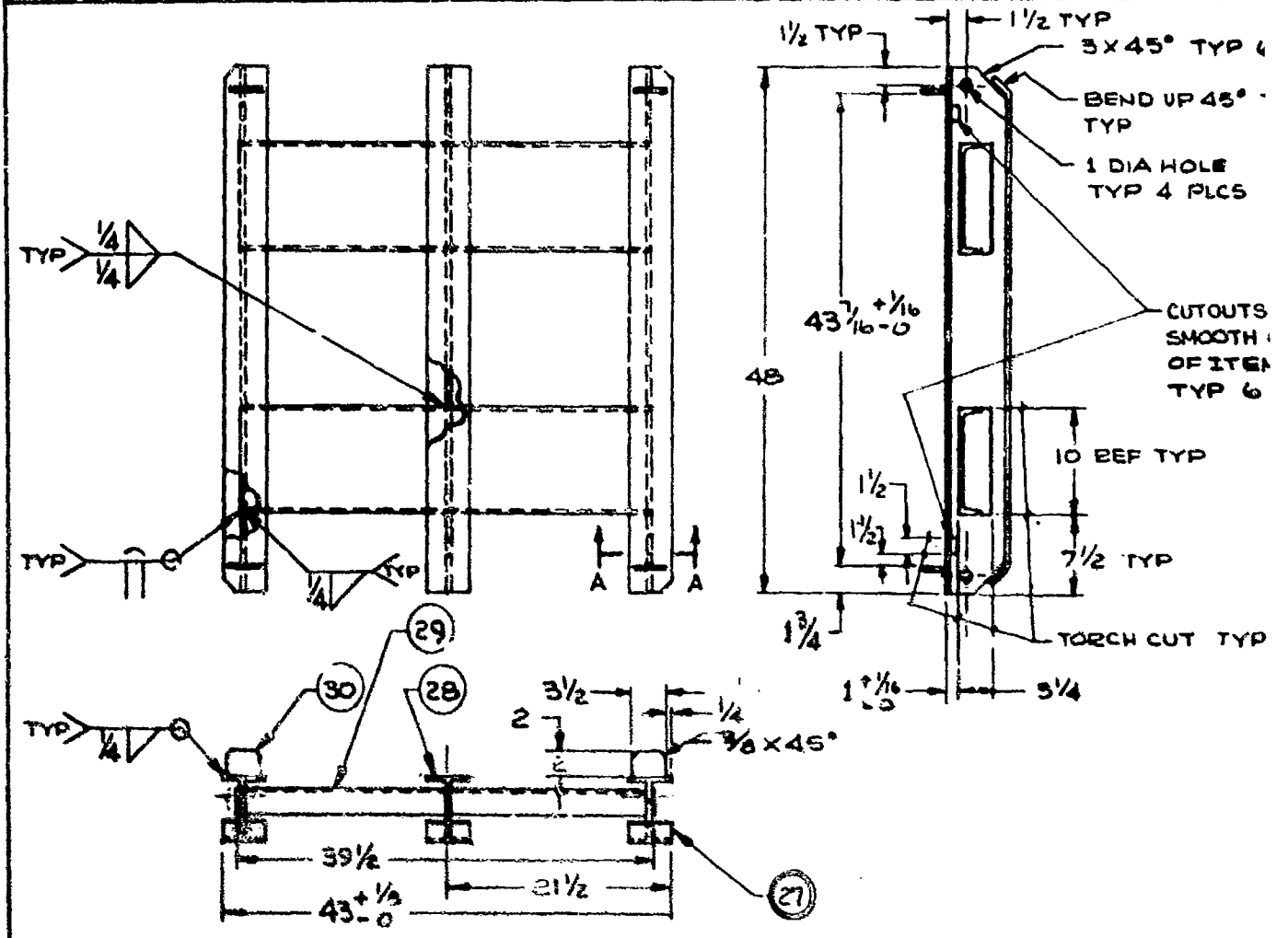

BASE WELDMENT
SCALE: 1"=1'

QTY	ITEM	
A/R	31	
4	30	
2	29	
3	28	
1	27	

NOTES:

4. PAINT WITH ONE COAT OF ITEM 31 PER MANUFACTURERS INSTRUCTIONS.
3. DIMENSIONS GIVEN ARE NOMINAL FINISHED SIZES. ALLOWANCES MUST BE MADE FOR FINISHING
2. REMOVE ALL BURRS AND BREAK ALL SHARP EDGES
1. WELD PER LATEST SPECIFICATIONS OF THE A.W.S.

OTOR CASE SEGMENT, SUPER BATES	PART NO.	PD FORM NO. 2509	REV.

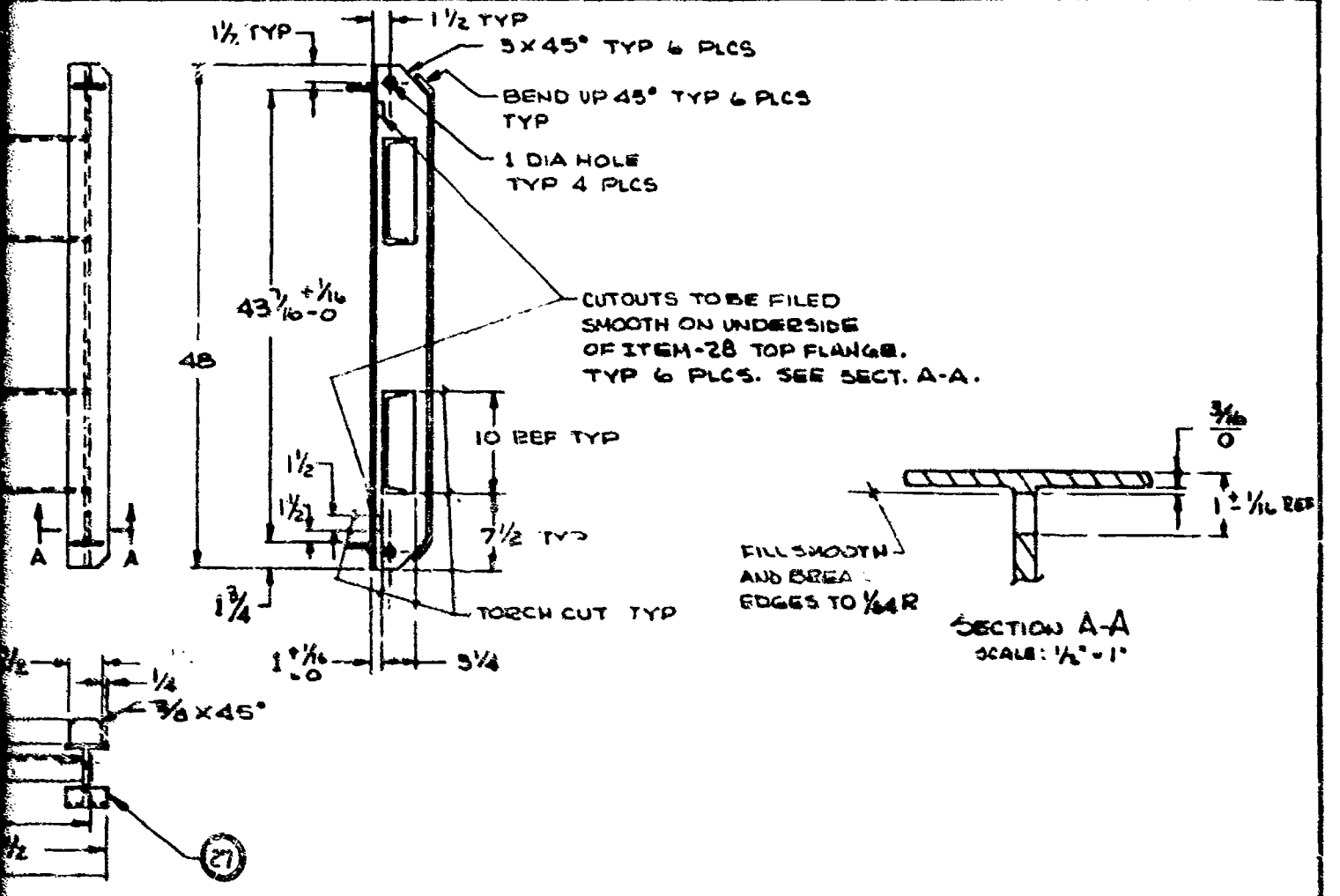

T

M 51 PER MANUFACTURERS INSTRUCTIONS.

NAL FINISHED SIZES. ALLOWANCES

ING.

AK ALL SHARP EDGES

CATIONS OF THE A.W.S.

QTY	ITEM	DESCRIPTION
A/R	51	PRIMER,
4	30	PLATE, HRS, ½ x 5½ x 2, ASTM-A36
2	29	CHANNEL, STRUCTURAL, 10 x 15.3 LB ASTM-A36
3	28	BEAM, WIDE FLANGE 6 x 8.5 LB. ASTM A36
1	27	BASE WELDMT. CONSISTS OF ITEMS 28 THRU 31

Figure 11. Shipping Container for Motor Case Segment (Sheet 3 of 7)

05897

NOMENCLATURE: SHIPPING CONTAINER, MOTOR CASE SEGMENT, SUPER BATES

PART NO.

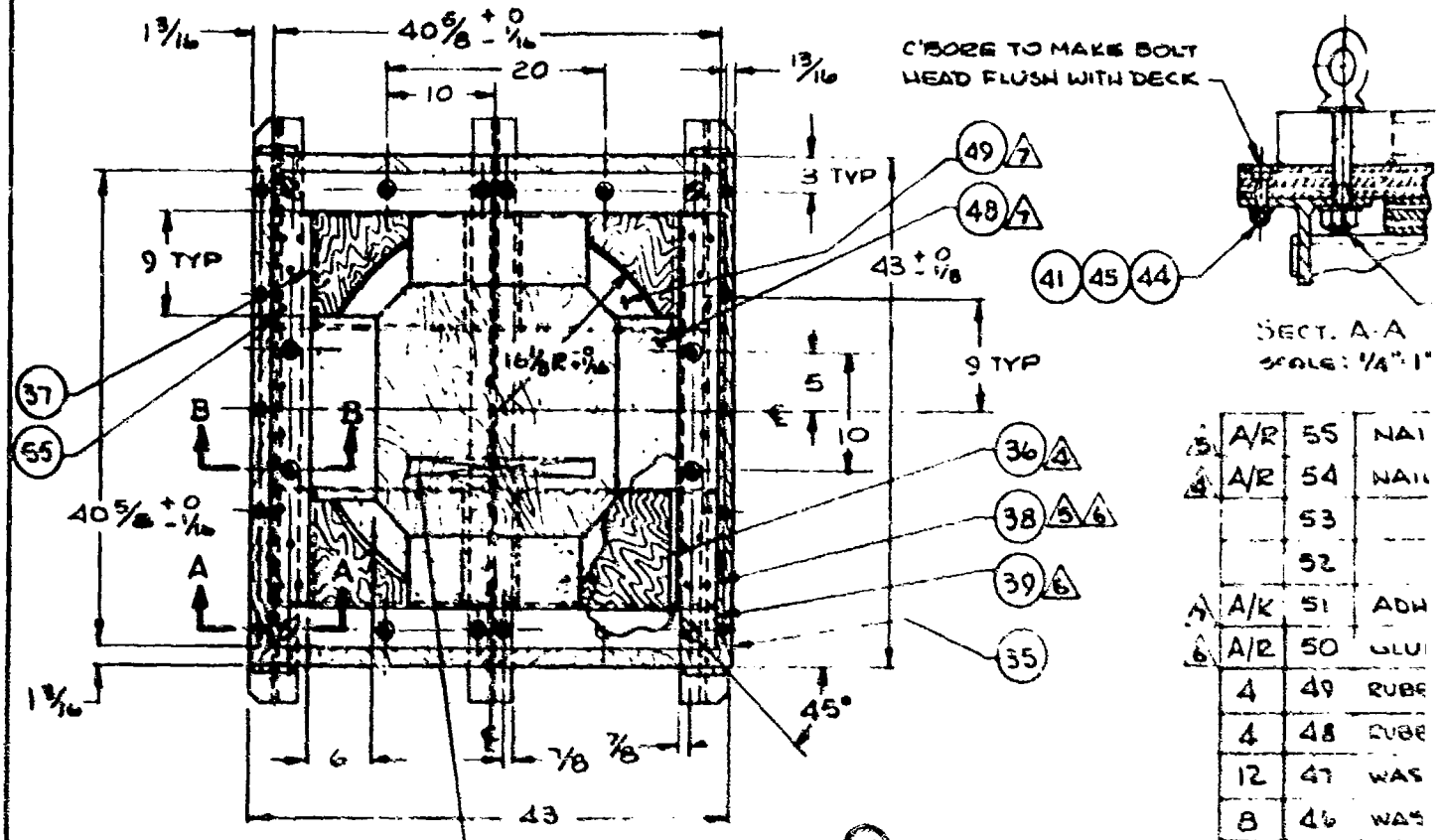

CONTAINER BASE ASSY P/N PDC-2609-54 1

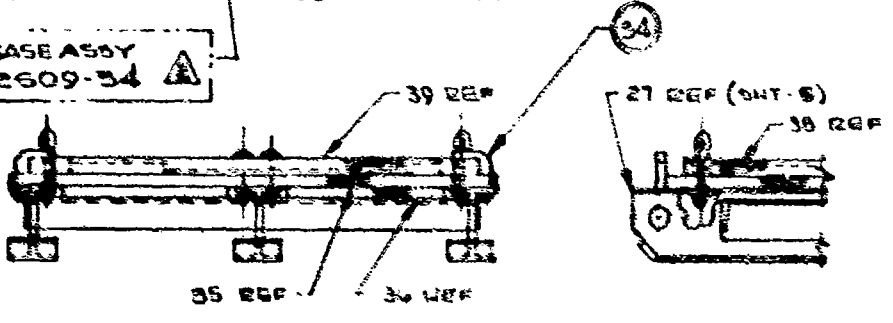

BASE ASSEMBLY

SCALE: 1"=1'

	QTY	ITEM	
5	A/R	55	NAI
4	A/R	54	NAI
		53	
		52	
1	A/R	51	ADH
6	A/R	50	GLU
	4	49	RUBB
	4	48	RUBB
	12	47	WAS
	8	46	WAS
	22	45	WAS
	14	44	NUT
	4	43	NUT
	4	42	BOL
	10	41	BOL
	4	40	BO
	2	39	LUG
	2	38	LUG
	4	37	PLY
	4	36	PLY
	1	35	PLY
	1	34	PLA
	QTY	ITEM	

SEE SHEET 4 FOR NOTES

E SEGMENT, SUPER BATES	PART NO.	PD FORM NO 2509	REV.

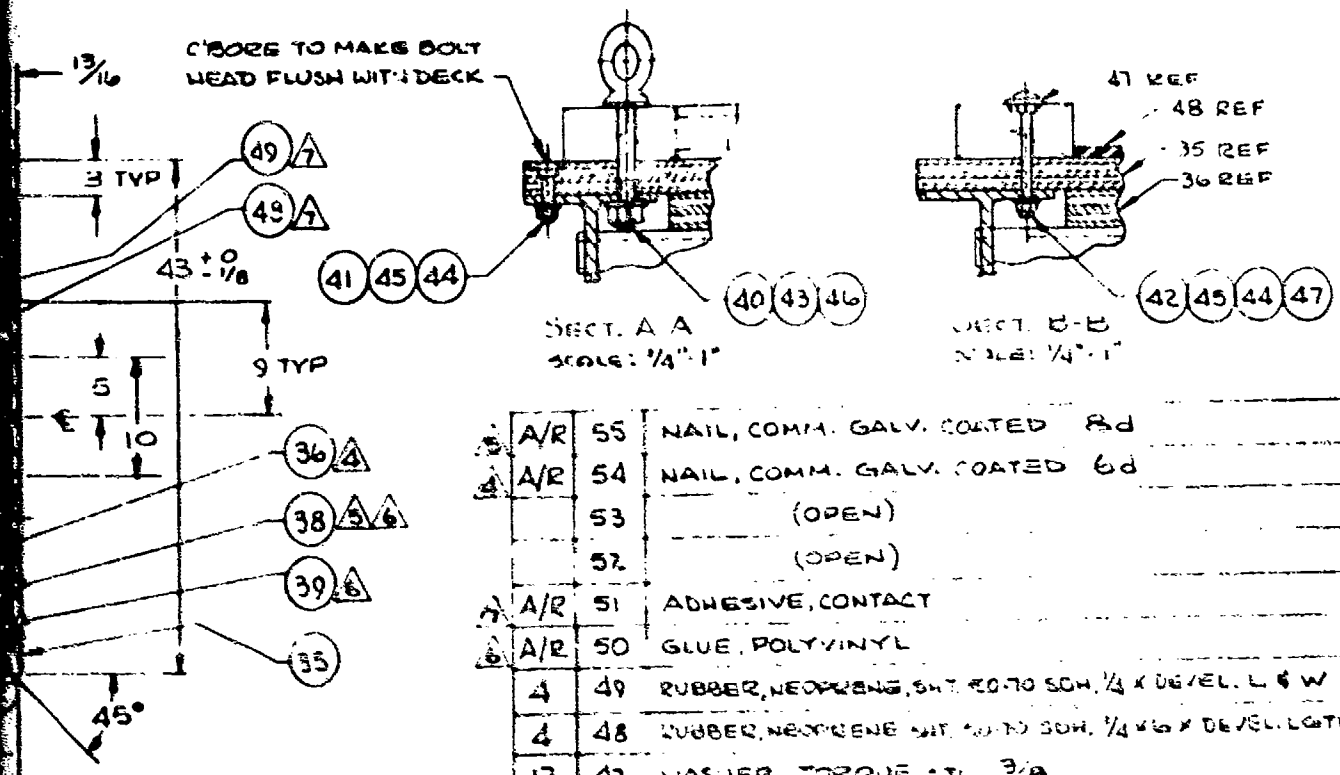

SEE SHEET 4 FOR △ NOTES

5	A/R	55	NAIL, COMM. GALV. COATED 8d
4	A/R	54	NAIL, COMM. GALV. COATED 6d
		53	(OPEN)
		52	(OPEN)
3	A/R	51	ADHESIVE, CONTACT
6	A/R	50	GLUE, POLYVINYL
	4	49	RUBBER, NEOPRENE, SHT. 60-70 SDH, 1/4 X DEVEL. L & W
	4	48	RUBBER, NEOPRENE SHT. 60-70 SDH, 1/4 X 6 X DEVEL. LGTH.
	12	47	WASHER, TORQUE, STL 3/8
	8	46	WASHER, FLAT, STL, ZINC PL 1/2 NOM. I.D.
	22	45	WASHER, FLAT, STL, ZINC PL 3/8 NOM I.D.
	14	44	NUT, LOCK, HEX, STL 3/8-16 UNC
	4	43	NUT, LOCK, HEX, STL 1/2-13 UNC
	4	42	BOLT, CARR & SQ, STL, ZINC PL 3/8 X 3 1/2 LG
	10	41	BOLT, CARRIAGE, STL, ZINC PL 3/8 X 1 1/2 LG
	4	40	BOLT, SHOR, EYE, GALV, FORGED STL 1/2 X 3 1/4 LG
	2	39	LUMBER, D FIR UTILITY 2 X 4 X 40 5/8
	2	38	LUMBER, D FIR UTILITY 2 X 4 X DEVEL LGTH.
	4	37	PLYWOOD, D FIR, EXT [illegible] SANDED 1 X 9 X 9
	4	36	PLYWOOD, D FIR, EXT [illegible] SANDED 1 X 10 X 14
	1	35	PLYWOOD, D FIR, EXT, SMOOTH SANDED 1 X 43 X 43
	1	34	BASE ASSY [illegible] ITEMS W/ THRU 35, AND 27
QTY	ITEM		DESCRIPTION

Figure 11. Shipping Container for Motor Case Segment (Sheet 4 of 7)

05898

NOMENCLATURE: SHIPPING CONTAINER, MOTOR CASE SEGMENT, SUPER BATES

PART NO.

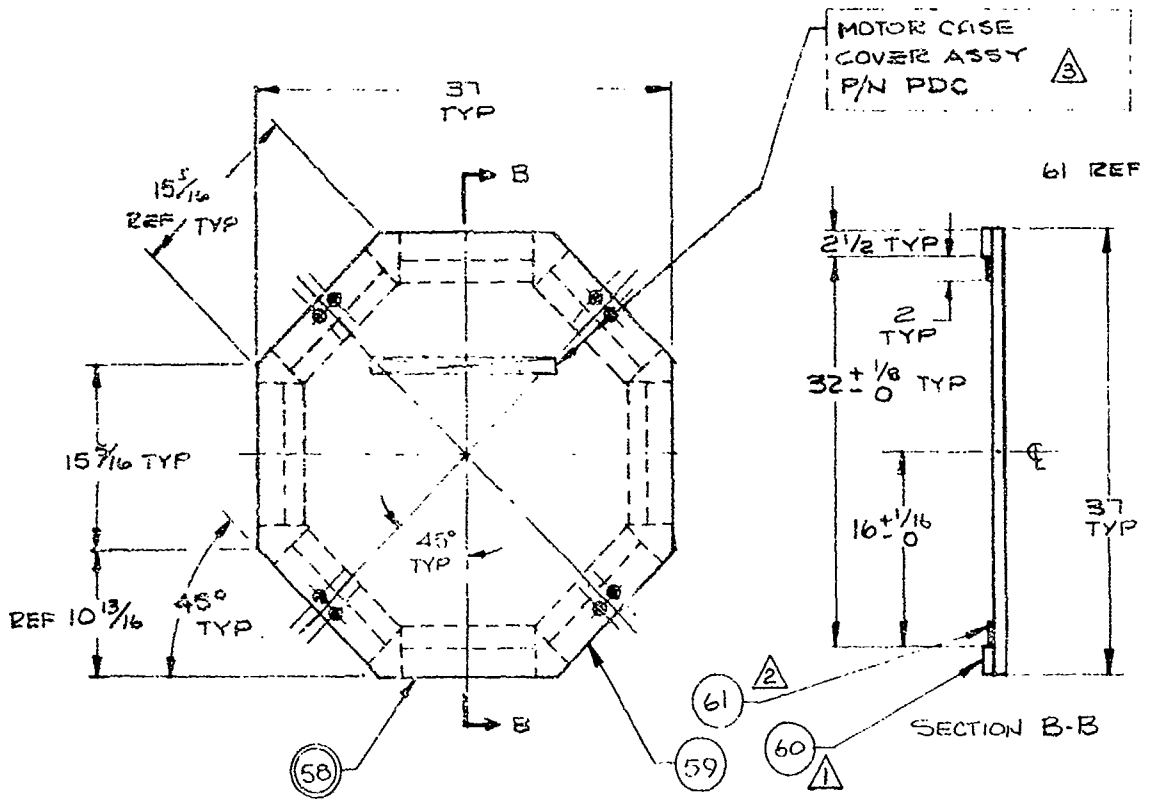

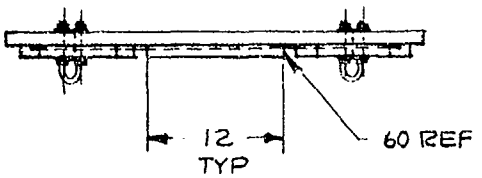

COVER ASSEMBLY
SCALE: 1" = 1'

QTY.	ITEM	
A/R	67	NA
A/R	66	GLU
A/R	65	ADH
16	64	WAS
16	63	NUT,
4	62	BOLT
8	61	RUBI
8	60	PLYW
1	59	PLYW
1	58	COVE

(3) STENCIL IN 1" HIGH CHARACTERS, BLACK COLOR

(2) BOND ITEM 61 TO ITEM 59 USING ITEM 65.

NOTES: (1) NAIL & GLUE ITEM 60 TO ITEM 59 USING ITEMS 67 & 66.

OR CASE SEGMENT, SUPER BATES	PART NO.	PD FORM NO. 2509	REV.

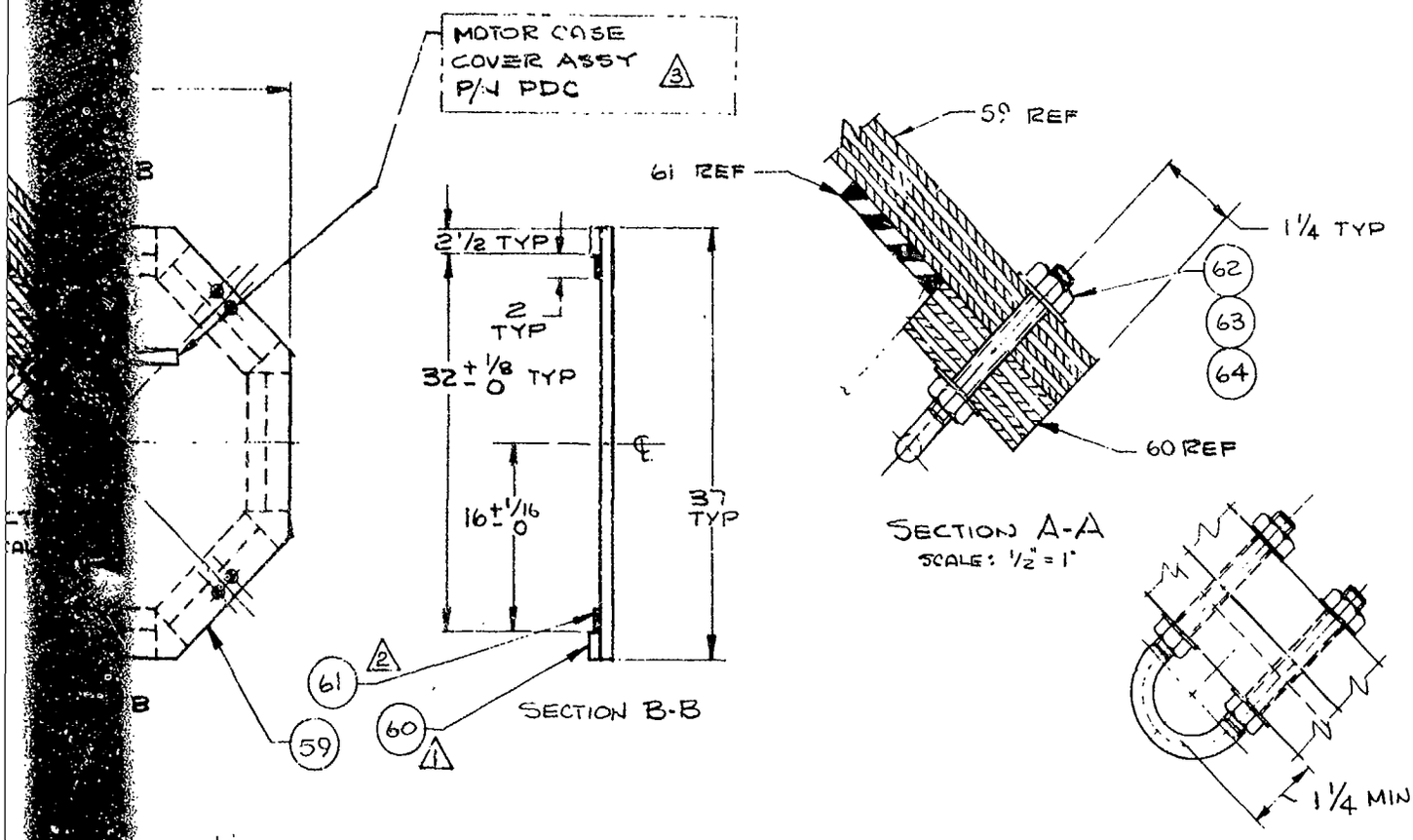

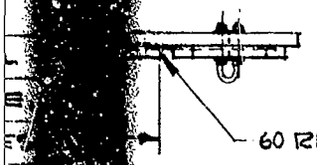

ASSEMBLY
: 1" = 1'

, BLACK COLOR
BING ITEM 65.
59 USING ITEMS 67 & 66.

QTY	ITEM	DESCRIPTION
1	58	COVER ASSY. CONSISTS OF ITEMS 59 THRU 67
1	59	PLYWOOD, D.FIR, EXTR. A/C 1 X 37 X 37
8	60	PLYWOOD, D.FIR, EXTR. A/C 1 X 12 X 2 1/2
8	61	RUBBER, NEOPRENE, SHT. 50-70 SDH 1/4 X 2 X 12
4	62	BOLT, "U", LG. TANG., CAD. PL, 1 1/4 PIPE SIZE, 3/8 X 4 1/2 LG
16	63	NUT, HEX, LOCK, STL. 3/8-16 UNC
16	64	WASHER, FLAT, STL, ZINC PL 3/8 NOM I.D.
A/R	65	ADHESIVE, CONTACT
A/R	66	GLUE, POLYVINYL
A/R	67	NAIL COMM GALV. COATED 6d

Figure 51. Shipping Container for Motor Case Segment (Sheet 5 of 7)

05899

NOMENCLATURE SHIPPING CONTAINER, MOTOR CASE SEGMENT, SUPER BATES

PART NO.

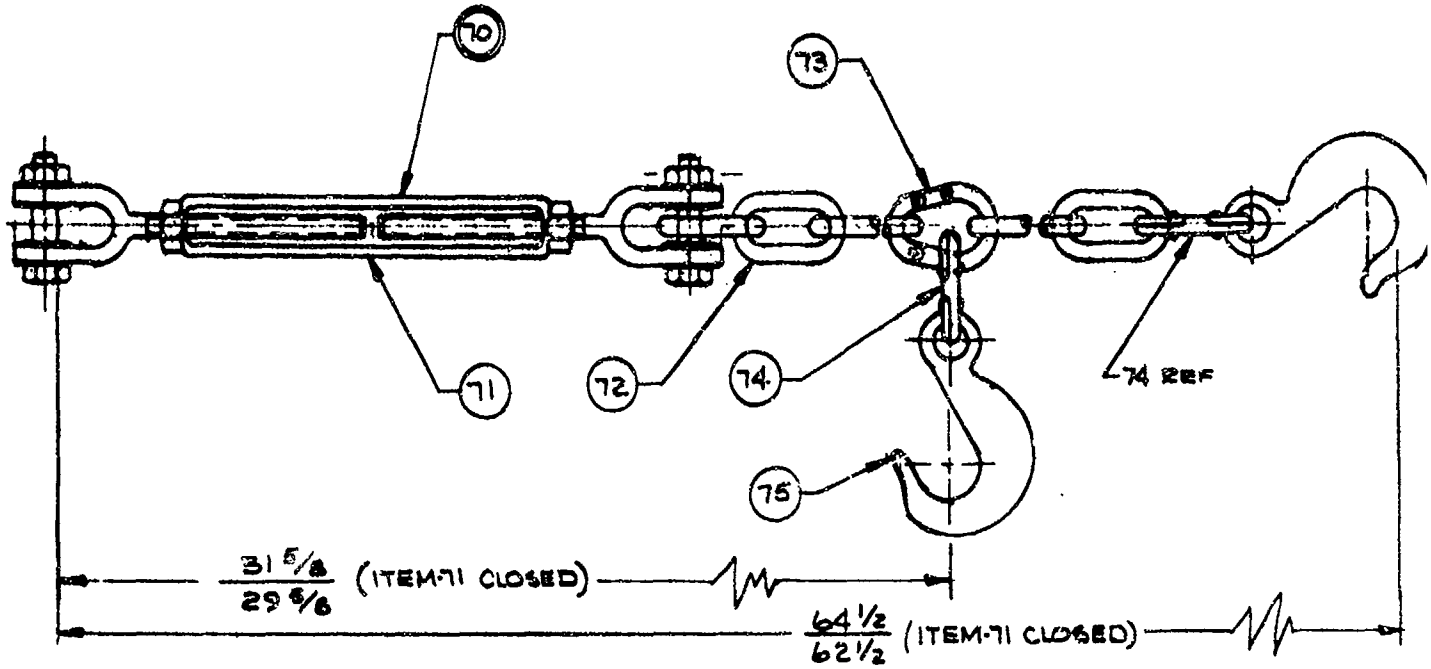

TIE DOWN ASSEMBLY
SCALE: 1/2" = 1"

QTY.	ITEM	
2	76	HOOK, EYE,
2	74	LINK, CONNEC
1	73	LINK, CONNEC
A/R	72	CHAIN, COIL "P
1	71	TURNBUCKLE, GALV. 1/2 X
⚠1	70	TIE DOWN A

NOTES: ⚠1 FOUR (4) REQUIRED PER CONTAINER ASSY., REF SHT. 2.

CASE SEGMENT, SUPER BATES	PART NO.	PD FORM NO. 2509	REV.

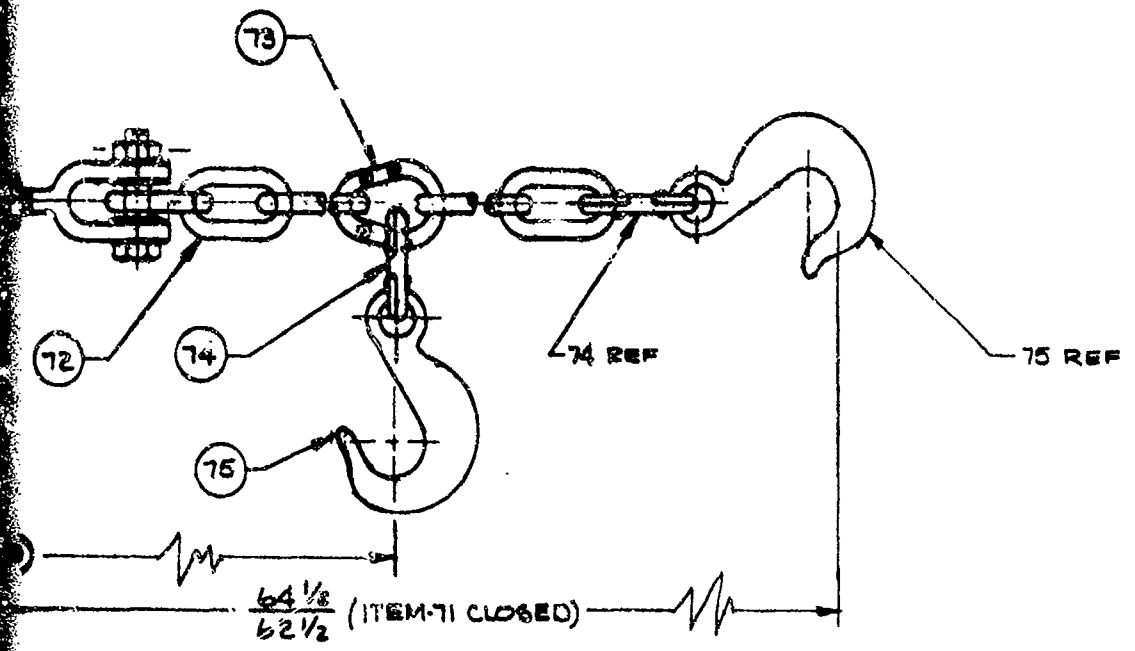

DOWN ASSEMBLY
SCALE: 1/2" = 1"

QTY.	ITEM	DESCRIPTION
2	75	HOOK, EYE, SLIP, 2500-LB MIN. SWL, 1/4 SIZE
2	74	LINK, CONNECT'G, STD., 5000-LB. MIN. SWL, 3/8 SIZE
1	73	LINK, CONNECT'G, PEAR, 5000-LB MIN. SWL, 3/8 SIZE
A/R	72	CHAIN, COIL "PROOF", 2500 LB MIN. SWL, ZINC FT, 3/8 SIZE
1	71	TURNBUCKLE, JAW & JAW, 2200-LB MIN. SWL, GALV. 1/2 X 6 SIZE
1	70	TIE DOWN ASSY. CONSIST OF ITEMS-71 THRU-75

ASSY., REF SHT. 2.

Figure 51. Shipping Container for Motor Case Segment (Sheet 6 of 7)

05900

NOMENCLATURE: SHIPPING CONTAINER, MOTOR CASE SEGMENT, SUPER BATES

PART NO.

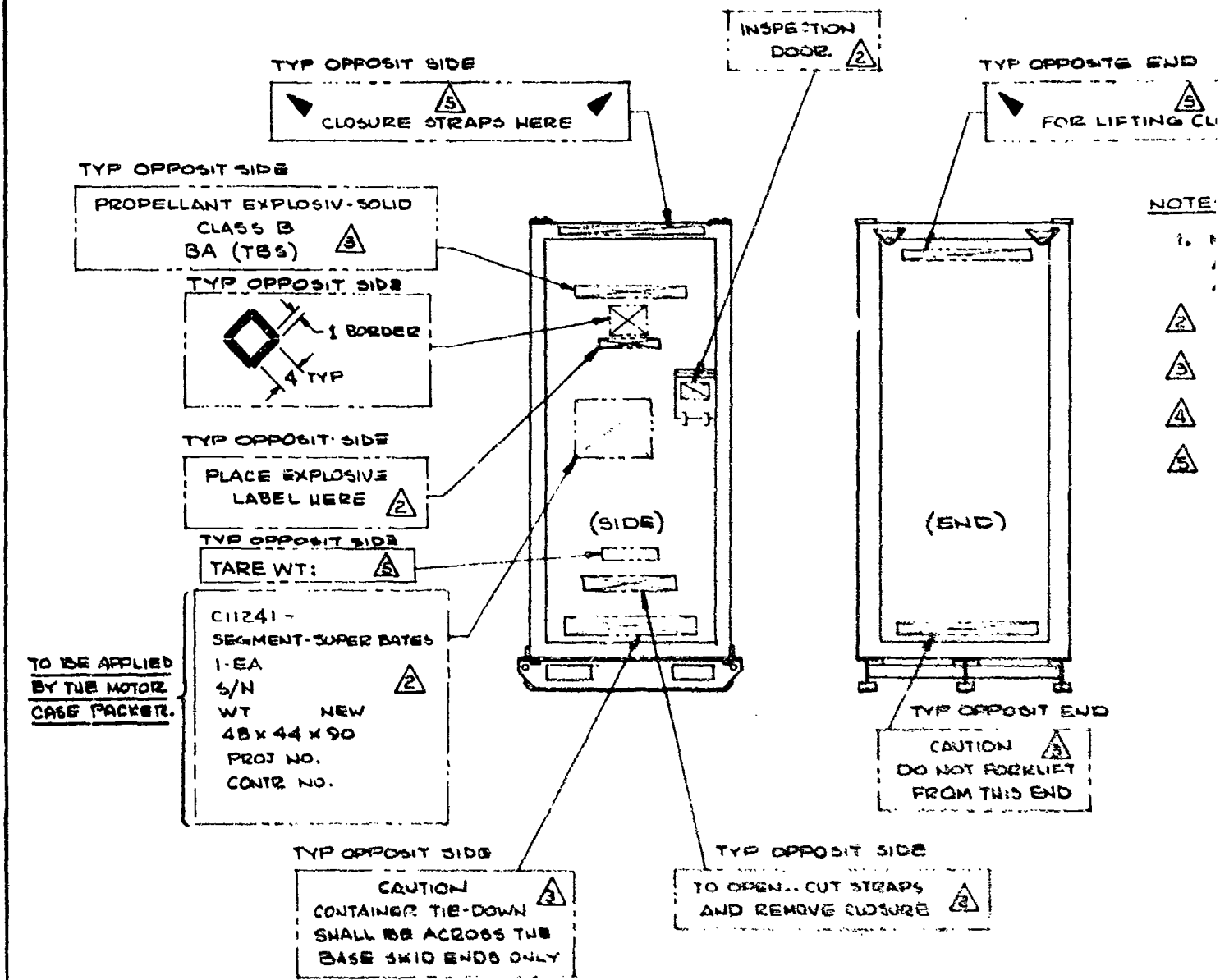

SHIPPING CONTAINER MARKING ARRANGEMENT

(NO SCALE)

QTY. REQ'D | DET.

OTOR CASE SEGMENT, SUPER BATES	PART NO.	PD FORM NO. 2509	REV.

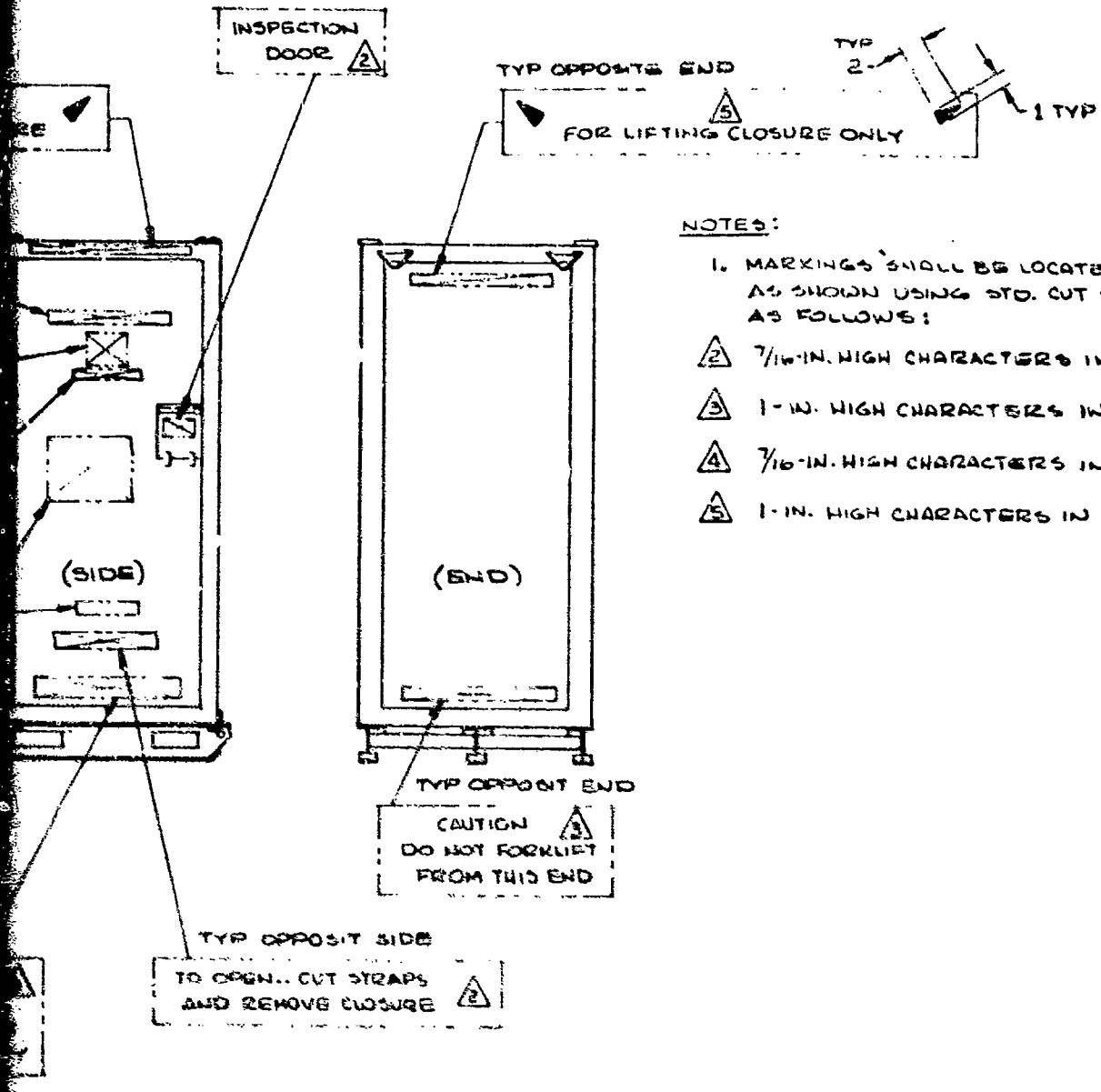

NOTES:

1. MARKINGS SHALL BE LOCATED APPROX. AS SHOWN USING STD. CUT STENCILS AS FOLLOWS:

2 7/16-IN. HIGH CHARACTERS IN BLACK COLOR.

3 1-IN. HIGH CHARACTERS IN RED COLOR.

4 7/16-IN. HIGH CHARACTERS IN RED COLOR.

5 1-IN. HIGH CHARACTERS IN BLACK COLOR.

S CONTAINER MARKING

ERANGEMENT

(NO SCALE)

QTY REQD	DET.	DESCRIPTION

Figure 51. Shipping Container for Motor Case Segment (Sheet 7 of 7)

05401

4.2 Thrust Stand Design

4.2.1 General

To evaluate rocket motor performance it is desirable to have a high frequency force measuring system that minimizes significant dynamic interaction and incorporates in the design those characteristics that provide for accurate measurement. The major problems in achieving accuracy with such a design are (1) properly isolating the individual load cells and (2) maintaining system rigidity. Since the structure and load cells deflect under load, the deflection can introduce interaction error terms into the load cells. For this reason these interaction terms must be specifically considered. Flexures and other techniques to isolate the load cell cannot be used because inclusion of these elements in the load path increases flexibility; this results in a decrease in the resonant frequency of the system.

Other conditions which can introduce errors into the system include the following:

A. Hysteresis, friction, and slop (free play)
B. Test stand redundancy
C. Interactions resulting from initial misalignments
D. Interactions resulting from axial deflections of elements under load
E. Normal or inverted pendulum effects
F. Environmental conditions
G. Induced forces resulting from dynamic action
H. Improper calibration system.

These error sources must also be investigated and corrected where feasible.

Most of the error terms listed exist to some extent in all thrust measuring systems. Most of them can be minimized by clever design and proper construction. With proper in-place calibration, calibration constants can be established and thrust coefficients and in-place characteristics can be obtained using calibration factors.

4.2.2 Design Considerations That Minimize or Eliminate Error Terms

4.2.2.1 Residual Effects - Hysteresis, friction, and slop are completely eliminated by removing as many joints as possible and preloading those that still exist. Three or more load cells, ground to a precise length, can be installed and bolted securely in place between two rigid ground surfaces. Except for areas that require disassembly or flexibility, the basic structure is welded.

4.2.2.2 Test Stand Redundancy - The test bed is basically a lightweight rigid frame supported by plate flexures connected to a solid plate foundation (see Figure 52). The flexures are designed to allow some motion in the thrust direction and to restrain the bed from motion in all other directions. Because of the rigid design, the axial deflection is small and the flexures are substantially stiffer than those normally used. Since the plate flexures offer redundancy, the redundant characteristics have to be calibrated as part of the thrust coefficient. The only redundancy in the thrust measuring system results from the flexures that support the bed.

4.2.2.3 Inverted Pendulum Characteristics - During firing, the weight suspended by the flexures is changed by the loss of propellant weight. This would normally introduce an error into the impulse measurements where the bed is supported by plate flexures. In order to eliminate this error, folded plate flexures are used. The bed is supported by one flexure in tension and in parallel with the flexure in compression so that translation of the bed in the thrust direction will be pure rectilinear motion. This will cancel the inverted pendulum effect. This technique has been used with a high degree of success in precision thrust measuring systems.

4.2.2.4 Initial Alignment - The thrust system is insensitive to alignment where three or more load cells are located symmetrically about the thrust axis. Only normal alignment precautions must be maintained since the errors introduced are proportionate to the quantity (1 cosine of the misalignment angle).

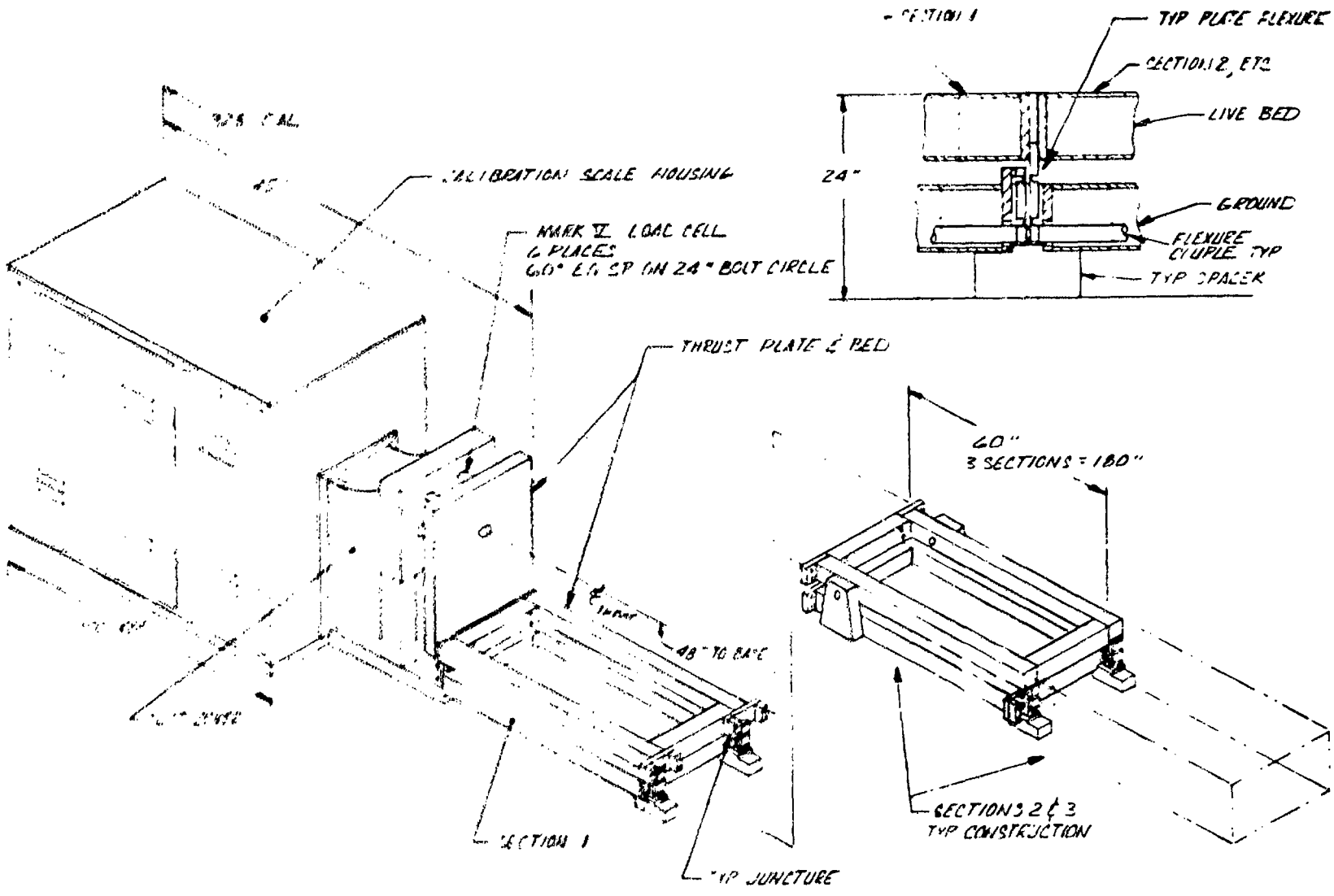

Figure 52. Super BATES 150,000-lb Thrust Stand

4.2.2.5 Deflection Under Load - Special consideration was given to designing and building an extremely rigit thrust measuring system. The load cells were chosen for minimum deflection and were installed at appropriate locations to eliminate elements in bending; thus the thrust was transferred directly into load cells mounted against a heavy steel base structure. This design essentially eliminates a major source of deflection: elements in bending. All the elements in compression are extremely rigid except for the load cells; the latter must deflect in order to measure load. Load cells are over capacity in order to minimize deflection.

The rocket motor is designed to be mounted firmly to the thrust adapter plate and bolted in place with preloaded bolts.

The thrust butt is designed with thick solid steel plates supported by heavy steel webs. In such a design, interaction terms which result from deflection can be virtually eliminated.

4.2.2.6 Environmental Conditions - The thrust stand was designed to operate in a normal ambient environment. Since the firing was to be short, the ambient conditions should not have changed appreciably during firing; therefore, no special consideration was to be given to error terms associated with the environment.

4.2.2.7 Dynamic Response - Prime consideration was given to designing for rigidity and minimizing the weight of the supported mass. By using multiple load cells coupled directly between two plates, all nonessential deflections are eliminated. This, plus the fact that the forward end of the motor is butted solidly against the thrust adapter plate, allows the system to be extremely rigid. Deflection should be in microinches. By making the resonant frequency high, the dynamic action is averaged out completely when the impulse of the motor is determined. The system is linear and repeatable, which eliminates these sources of error from the dynamic characteristics.

Since the period of the resonant frequency is short compared to the period of firing, electrical signals can be filtered easily.

The design of the support structure is clean and all elements that would induce synthetic vibration were eliminated.

The calibrator is completely disconnected from the moving structure during firing.

4.2.2.8 Calibration System - If improperly designed, the calibration system can introduce error terms into the thrust measuring calibration; therefore, the same considerations that were given to the thrust stand design were given to the calibration system.

All redundancy in the calibrating path between the calibration load cell and the thrust stand were eliminated or minimized to an insignificant value.

4.2.3 Technical Requirements

4.2.3.1 General Description - A system was designed (see Figure 52) that measures thrust over the range of 0 to 50,000 lb, 0 to 100,000 lb, and 0 to 150,000 lb within the stated accuracy.

All components were designed to carry an overload force equal to 200% of maximum thrust without damage to the thrust measuring system. In order to cover the low range requirements, three of the load cells are removed (see Figure 10 in Section 3.2). The load cell measuring system has basically two ranges: 0-100,000 lb and 0-150,000 lb.

4.2.3.2 Design Flexibility - The final design of the thrust stand will have a large degree of flexibility for positioning the load cell, aligning the motor/load cell, and easily removing and installing load cell, flexures, and motor. As shown in Figure 10, (Section 3.2), the thrust adapter plates have been removed and replaced with a smaller plate for smaller motors (or for the removal or replacement of load cells). The thrust bed is designed in three sections to accommodate

motors of various lengths (one or two sections can be removed). All joints are located with dowel pins and alignment is maintained with tooling bars so that all components can be replaced without alignment checks. Motors can be removed and installed without upsetting the alignment; however, centerlines and dowel pin locations are provided so that periodic alignment checks can be made using transit levels and scales. The load cells are dowelled and bolted in place; all locating holes are precisely jig bored in the thrust abutments so that load cells can be interchanged without positioning or realignment.

4.2.3.3 Accuracy – The design goal accuracy of the thrust system is ±0.10% of full-scale for each of the three ranges with a three-sigma confidence level based on in-place calibration. The guaranteed accuracy is ±0.15%. The overall system includes the combined accuracy of the load cells, flexure assemblies, thrust stand assembly, and calibration system. The calibration system is calibrated in place to an accuracy of 0.03% of full-scale range. Accuracy does not include signal conditioning or data acquisition.

4.2.3.4 Calibration – The thrust stand includes a deadweight calibrator with an accuracy of ±0.03% of range to calibrate the thrust measuring system. The calibrator is schematically shown in Figure 10 and described in Section 4.2.4.

The calibrator can be operated manually or from a programmed computer. It is a multiple beam arrangement whereby the weights are raised and lowered using flexure bellows. The control panel is mounted in the block house; the solenoid for actuating the bellows is mounted on the calibrator. The solenoid is potted to obtain an hermetic seal. All lines are run in conduit without plugs. Lead connections are made on a barrier strip mounted on the calibrator.

The weights are in binary coded decimals which allows selection of increments from 1,000 to 150,000 lb. The weights are certified to class C tolerances.

Class C tolerance is approximately 0.006% of weight. The calibration factor is established by calibrated load cells mounted in the pull rod. Three load cell ranges are furnished and delivered along with the calibration instrument. This equipment can be used to verify the beam balance calibrator at any future date. Flexures are used on both ends of the load cell in order to eliminate bending moments. The thrust stand is calibrated in fifteen equal steps up and down in less time than 1 min/step.

Limit stops are mounted on the beam. As long as the stop is engaged, the calibrator is prevented from applying additional loads. This safety feature prevents inadvertent application of a load in excess of that selected by the operator; it does not prevent the calibrator from running in the opposite direction to unload the system. The calibration system has the following minimum specified accuracies (at a one-sigma confidence level):

A. Linearity, ±0.03 of applied load from 50,000 to 150,000 lb
B. Hysteresis, ±0.006% of applied load
C. Repeatability, ±0.006% of applied load
D. Accuracy (including combined effects of linearity, hysteresis, and repeatability errors), within 0.08% of applied load or 0.03% of range, whichever is greater, where the ranges are 50,000 lb, 100,000 lb, and 150,000 lb.

The primary limitation of the accuracy of the calibrator is the ability to calibrate the system load cells to a higher order level.

A digital selector switch is located on the panel of the calibrator to prevent overloading of the load cell and thrust stand. The electrical circuitry prevents the application of any load in excess of that selected and dialed into the system by the operator. The calibrator is mounted on support structures completely independent of the thrust measuring system.

The control circuit for the calibrator is equipped with logic so that it can be interfaced with Hewlett-Packard's 2100 mini-computer. The interface is TTL compatible. All power supplies and other control elements are furnished with the calibrator. Switch closures on the calibrator indicate

when a weight has been applied and when the beam is balanced. Under these conditions the calibrator load can be recorded. By using proper programming the complete system can be calibrated automatically with the computer and the beam balance calibrator.

The initial performance of the calibration system and thrust stand is demonstrated at Ormond before delivery. It is also demonstrated after installation at AFRPL's test area 1-32 before acceptance.

4.2.3.5 Alignment - The thrust stand and calibration system are manufactured and aligned so that a motor can be installed to 0.1° of the longitudinal axis of the axial load cells. Tooling bars and dowel pins are included in the manufacturing; these allow disassembly and assembly without checking the alignment.

In order to prevent the thrust from being affected by the change in weight of the motor during firing, folded flexures are used which inherently cancel the pendulum effects. The flexures are compatible with the thrust range requirements and the accuracy of the system.

The load cells are ball-ball types which do not have flexures on the ends. Therefore, the ends can be drilled and tapped on the centerline of the load cell so that installation can be done without precise alignment.

4.2.3.6 Load Cell Specifications - Load cells meet the specifications discussed in Appendix A. One additional load cell is supplied as a spare part of each load cell used in the thrust stand.

4.2.3.7 Motor Attachment - Motors are mounted in cradles on the thrust stand and butted against the thrust plate. This allows the motor to be mounted without direct attachments which drill or screw into the motor. By providing different cradles, motors of various diameters and lengths can be installed.

4.2.3.8 Installation - The thrust stand and calibrator are compatible with a thrust pad having I-beams.

4.2.3.9 Electric Power - Electrical power input to the system is 115±10 volts, 60±2 cps single phase AC. Ignition pulse will be 28 volts DC.

4.2.3.10 Selection of Parts - Use of proprietary materials, components, etc., in the design of the thrust stand was avoided.

4.2.3.11 Standard Parts - On drawings standard parts are identified by their numbers. AN and MS standard parts will be used where they serve the purpose.

4.2.3.12 Commercial Parts - Commercial parts having suitable properties are used if, on the date of contract award, there are no suitable standard parts. In any case, commercial utility parts such as screws, bolts, nuts, etc., which have suitable properties are used if (1) they can be replaced by the standard parts (AN and MS) without alteration, and (2) the corresponding standard part numbers are referenced in the parts list and, if practical, on the contractor's drawings.

4.2.3.13 Materials - Materials and processes used in the manufacture of the thrust stand and its subsystem are of high quality and suitable for the purposes intended. Materials conforming to contractor's specifications are used provided the specifications are approved and provisions for adequate tests are contained in them. Approval of contractor's specifications does not constitute a waiver of inspection.

4.2.3.14 Protective Treatment - Test stand and system materials are protected from environmental conditions in a manner that in no way prevents compliance with the performance requirements of this specification. The use of any protective coating that cracks, chips, or scales with age or extremes of climate and environmental conditions is avoided.

4.2.3.15 Construction -

A. Loading

The system is constructed to withstand (1) 3-g load applied vertically downward, (2) 2-g load applied vertically upward, and (3) 1/2-g load applied horizontally.

B. Welding

Welding conforms to the recommendations of the American Welding Society and American Standard Code for the pressure vessels.

C. Fitting

Intersection of test stand structural components is made using weld-type fittings, except where otherwise specifically indicated.

D. Performance

The thrust stand, including all instrumentation components, is designed to provide the specified performance under (1) humidity at 0% to 95%, (2) temperature at $0^{\circ}F$ to $150^{\circ}F$, (3) pressure at 16 to 32 in. mercury, and (4) altitude at 0 ft to 4,000 ft.

In addition, exposure to (1) heavy rains, (2) temperatures up to 250° for short exposure time, and (3) sand and dust storms do not damage the thrust stand and its components in any manner which preclude subsequent performance to the specified levels.

4.2.4 Beam Balance Deadweight Calibrator Design

A beam balance deadweight calibrator was initially designed especially for calibrating the load cells of a single component thrust stand. The performance capabilities of this calibrator are discussed below.

4.2.4.1 Performance -

A. Load Range

The calibrator can calibrate load cells in the range from 0 to 150,000 lb in 1,000-lb increments.

B. Hysteresis Loop

The calibrator can load continuously (and in discrete increments) over the selected ranges in either ascending or descending directions; thus a hysteresis loop for the stand can be plotted. Only slight discontinuities are introduced at the load points during the change of weights.

C. Manual Operation

The load to be applied is selected using a digital switch. This in turn electrically selects the weights to be applied to the beam. The operator pushes a load button in order to apply the loads. After the loading button is pushed a motorized screw jack is actuated to restore the beam to the balanced condition. When the beam is balanced the motor stops automatically and the appropriate load is applied to the thrust stand. After each increment of load has been selected the load button is pushed.

In addition to manual operation the calibrator can be programmed and operated from the computer in the automatic mode. All interface circuitry will be TTL compatible and will be electrically isolated using lite diode switches.

D. Calibrated Weights

All weights are calibrated to class C tolerances and the calibration will be traceable to the National Bureau of Standards.

E. Accuracy

The accuracy of the calibrator is 0.03% of load over the range from 1,000 to 150,000 lb. Accuracy will include (1) load application, (2) repeatability, (3) linearity, (4) hysteresis, (5) buoyancy, and (6) gravitational effects (gravitational constants will be furnished by the customer). Overshoot is a function of dynamic loading and is not considered as an accuracy term. All accuracy is based on static calibration.

F. Certification

In order to determine the accuracy, the deadweight calibrator is calibrated using the precision load cell flexure string mounted in the tension rod between the thrust stand and the calibrator. This load cell flexure string is calibrated at Edwards Air Force Base using the precision deadweight load stack at the rocket test base. The load cell flexure string along with the digital indicator and associated leads is furnished as part of the deliverable item.

G. Stability

The calibrator can maintain any selected load from 1,000 to 150,000 lb in static equilibrium within an accuracy of 0.1% of reading without requiring external manipulation or adjustment of the equipment.

H. Instrumentation

No instruments except the calibration control system is provided. The balance of the beam is indicated by a differential transformer and a zero center meter. The zero position on the meter indicates the balance of the beam. All controls are mounted on a 19-in. rack panel that can be installed in the block house.

I. Damping

Viscose damping is incorporated in the weight-suspension mechanism to decrease beam oscillation and limit overshoot. The weights are stabilized by a guiding beam attached to the lower end of the suspension rod.

4.2.4.2 Size and Dimensions - The approximate physical dimensions are shown in Figure 10 of Section 3.2. The total weight is less than 50,000 lb with each individual component less than 25,000 lb. The calibrator is designed as an integral unit which can be set up on any firm foundation strong enough to react the loads.

4.2.4.3 Accessories - Only a computer for automatic operation is required. No other accessories are necessary.

4.2.4.4 Counterpoise – The counterpoise is provided so that the beam can be leveled manually during setup.

4.2.5 Thrust Stand Engineering Analysis

4.2.5.1 Frequency Response – Motor and stand design conditions are:

A. Motor weight (W_m) = 20,000 lb

B. Stand weight (W_s) = 8,000 lb

C. Stand deflection (Δ) = 0.03 in.

D. Thrust force (F) = 150,000 lb

E. g = 386 in./sec^2

From Newton's Third Law of Dynamics

$$F = ma$$

$$F = \frac{W}{g} (2\pi f_n)^2 \Delta$$

$$f_n = \frac{9.78F}{W\Delta}$$

$$f_n = \sqrt{\frac{9.78 \times 150{,}000}{28{,}000 \times .03}} = 50 \text{ cps}$$

50 cps > than 25 cps

$$\text{Margin of Safety} = \frac{50}{25} - 1 = 1 = 100\%$$

where

m = mass

a = acceleration

f_n = frequency response

W = total motor and stand weight

The frequency response can be obtained from the curves published in Statham Laboratories Instrument Notes No. 20 which are included as Appendix B. Damping ratio should not be greater than 0.02. For a motor with an ignition time rise of greater than 200 sec the overshoot should be less than 5%. Because the resonant frequency of the stand is so high a filter could be easily used to

obtain 0.1% final data at 2.5 cps. A signal containing 50 cps oscillation is reliably filtered. Due to the design of the stand, only thrust dynamics should induce appreciable dynamics on the thrust signal.

4.2.5.2 Motor Vibration Effects - To minimize dynamics, the motor is mounted on adjustable saddles with the forward end of the motor mounted solidly against a rigid flat plate. The flat plate is supported directly by load cells that react the load in compression without the use of flexures or other deflecting devices. In this way all the thrust load is reacted solidly over the head end of the motor (the bed only provides normal and lateral support for the motor, without encumbering the system). Thus, adverse dynamic conditions are eliminated and it is still possible to obtain reliable and accurate thrust data.

4.2.5.3 Damping Effects - The damping characteristics of the thrust measuring system are so low that the damping ratio probably is not greater than 0.02. This is necessary in order to obtain good thrust data.

4.2.5.4 Load Cell Deflections - Low deflection load cells are sandwiched directly between a flat, rigid thrust plate and a flat, rigid thrust butt in order to limit deflections to the load cells and thrust butt only. Since the deflections of the thrust plate are negligible, this configuration essentially allows the motor to push directly against the load cells located around the perimeter of the motor. Load cell deflections are less than 0.01 in.

4.2.5.5 Calibration Procedures and Equations - Absolute loads can be applied either manually or automatically to the thrust stand with the deadweight beam balance calibrator. When any selected load is applied, that load remains in effect until changed. During this period, the output signals from the load cells can be recorded; load cells can be recorded individually and summed in the computer. The only interacting terms result from the stiffness of the flexures used to support the thrust bed. This stiffness term is eliminated by in-place calibration since the thrust measuring load cell coefficients include the flexure stiffness characteristics. The load cell outputs are averaged even though the distribution of load between load cells may be unequal.

This results because the load cells are essentially linear and the rated output of all load cells is matched within 0.10% of full-scale output.

4.2.5.6 Test Stand Design - In order to improve frequency response, all unessential deflecting elements are eliminated from the design.

Although the load cells are sandwiched between two plates, bending moments that could induce extraneous signals into the load cell signal are eliminated by manufacturing radii on both ends of all load cells approximately equal to one-half the length of the load cell. Essentially, each load cell is a large ball with a diameter equal to the load cell length. Thus, when the thrust plate deflects or moves the load cells roll or rotate; this movement eliminates the application of bending moments on the load cells.

The thrust bed is mounted on flexures which provide a high order of rigidity to the thrust bed in all directions except thrust. In the thrust direction, the flexures are relatively flexible. This provides a rigid support for the motor and allows thrust measurements to be made without excessive redundancy which could compromise thrust data accuracy. Since there will be an appreciable change in weight during motor firing, folded plate flexures are used to support the thrust bed. Folded plate flexures allow rectilinear motion to the thrust stand in the thrust direction which eliminates the pendulum coefficient and resulting errors in thrust measurement. Folded plate flexures also decrease the redundancy in the thrust direction which minimizes interaction from both deflection and temperature considerations. Changes in temperature will not cause hinge binding which is encountered in systems using single plate flexures. The flexures completely eliminate error terms resulting from friction or slop that usually appear in other types of support.

The use of a high frequency stand that has been designed to eliminate error terms and provide repeatable thrust data should include accurate acquisition of data including transients and tail-off. The thrust stand frequency response is high enough to allow substantial filtering without introducing phase lag problems. Other characteristics allow accurate measurement of tail-off without drift or interaction.

The thrust stand is structurally designed with stiffness as the primary criteria. The stand has a high margin of safety for stress for the conditions of a thrust axial load of 150,00 lb with a 2:1 safety factor. Preliminary stress analyses have been performed to ensure that these safety factors have been met in the critical areas.

4.2.6 Drawings and Related Data

The component design drawings for the thrust stand and related critical materials are as follows:

No. of Sheets	Drawing No.	Drawing Title
2	14-2-0338	Calibrator Assembly
2	14-2-0339	Weight Stack Assembly
3	14-2-0340	Frame and Base Assembly, Calibrator
1	14-2-0341	Frame Assembly, Calibrator
1	14-2-0342	Base, Calibrator
1	14-2-0343	X10 Lever
1	14-2-0344	Spacer, Flexure, and Gear Motor
2	14-2-0345	Gear Motor Plate Assembly
1	14-2-0346	Flexure Spacer
1	14-2-0348	Balance Beam
1	14-2-0351	Column, 150K, 15K, and Spacer
1	14-6-0248D	Top Weight Indicator Ckt.
1	14-6-0299	Weight Stack Control
1	14-6-0283	Motor Control Schematic
3	15-4-0924	Thrust Plate Abutment
1	15-4-0926	Thrust Plate
2	15-4-0927	Thrust Bed Assembly
1	15-4-0928	Super BATES 150K
1	16-1-0204	Thrust Measuring Ckt.
1	16-1-0205	Load Cell/Indicator Wiring

Critical Materials

Duff Norton jackuator

Reliance electric motor and reducer

Large steel plates - 6 in. thick and (2) 2 in. thick

Flexure material

Load cell material

Weights

ABBREVIATIONS

AFRPL	Air Force Rocket Propulsion Laboratory
ASME	American Society of Mechanical Engineers
ASTM	American Society for Testing Materials
ATJ	graphite designation
BATES	ballistic and test evaluation system
CHAR	ballistic test motor at RPL
C/SPCS	cost/schedule planning control system
CTPB	carboxy-terminated polybutadiene
DDI	dimer acid diisocyanate
DOT	Department of Transportation
FW	fiberglass-wound UTC solid propellant motor series
GFE	Government-furnished equipment
GSI	Government source inspection
HIPPO	heavyweight high pressure test motor
HTPB	hydroxy-terminated polybutadiene
HX-735	carboxy-terminated polyester
ICBM	intercontinental ballistic missile
IDP	isodecyl pelargonate
IPDI	isophorone diisocyanate
IR&D	independent research and development
I_{sp}	theoretical specific impulse
I_{sps}	standard specific impulse at 0^{o} half-angle
L*	characteristic length
LEM	lunar excursion module
LITVC	liquid injection thrust vector control
LSBR	liquid strand burning rate
MEOP	maximum expected operating pressure
MIG	metal inert gas
MIL	military
MPI	magnetic particle inspection

MRB	material review board
MWOA	master work order authorization
MXCE	fiberite material designation for elastomeric additive carbon phenolic
NBR	Buna-N rubber
NDT	nondestructive testing
O&QR	operation and quality record
P	pressure
PBAN	polybutadiene-acrylic acid acrylonitrile
PG	pyrolytic graphite
PO	purchase order
QA	quality assurance
QC	quality control
RFQ	request for quotation
RIP	receiving inspection plan
RPO	request for purchase order
SRM	solid rocket motor
TFE	a type of Teflon
TIG	tungsten inert gas
TL	transistor logic
TTL	transistor-transistor logic
TVC	thrust vector control
UAC	United Aircraft Corporation
UARL	United Aircraft Research Laboratories
USAF	United States Air Force
UTC	United Technology Center
UTL	United Technology Center liner
UTP	United Technology Center propellant prefix
WOR	work order release

APPENDIX A. SUPER BATES DESIGN TRADE STUDY RESULTS

1.0 INTRODUCTION

This appendix presents the detailed discussions and analyses that were conducted to define the trade study results summarized in Section 3.0 of this report. It contains two major categories:

A. A technical discussion supported with pertinent data for those parameters which affect the performance of SRMs

B. The effect of these parameters and their influence on the design of the Super BATES test motor.

2.0 PERFORMANCE PARAMETER DEFINITION

The presence of particles in nozzle flow results in decreased performance due to the inability of the particle to maintain equilibrium with the gas flow. Since the transfer of heat and momentum between the particles and the gas is not instantaneous, the velocity and temperature of the two phases are not in equilibrium. The excess thermal energy in the particles, the difference in velocities between the particles and the gas, and the irreversible transfer of heat and momentum across these differences lead to decreased performance. Any change in nozzle geometry or flow conditions will affect the specific impulse efficiency of the motor.

2.1 Chamber Pressure

Chamber pressure has an important effect upon performance due to its dominating influence on flow conditions. It affects aluminum agglomeration, particle size and two-phase flow losses, boundary layer losses, and chemical recombination. The magnitude of these effects will vary with pressure.

Aluminum agglomeration has an important effect on the combustion efficiency of a motor. When an aluminum agglomerate leaves the propellant surface, its size determines the time required to burn. The burning time for an aluminum particle decreases as its size decreases. Any aluminum that is unburned when it leaves the motor reduces the efficiency of the motor. Figure 1 shows the general effect that pressure has on aluminum agglomeration; an increase in pressure results in a decrease in the agglomerate size and, therefore, a decrease in burning time. An increase in pressure will cause the aluminum agglomerate to be smaller and will increase the combustion efficiency.

The effect that pressure has on two-phase flow losses will depend upon the particle size and the drag forces on the particles. Figure 2 shows the effect that pressure has on particle size; in general, a reduction in pressure will also reduce the size of the particles. A smaller particle size will result in an improved ratio of particle drag force to mass and tend to decrease the two-phase flow losses. However, a reduction in chamber pressure also reduces the aerodynamic drag forces; this tends to increase the two-phase flow

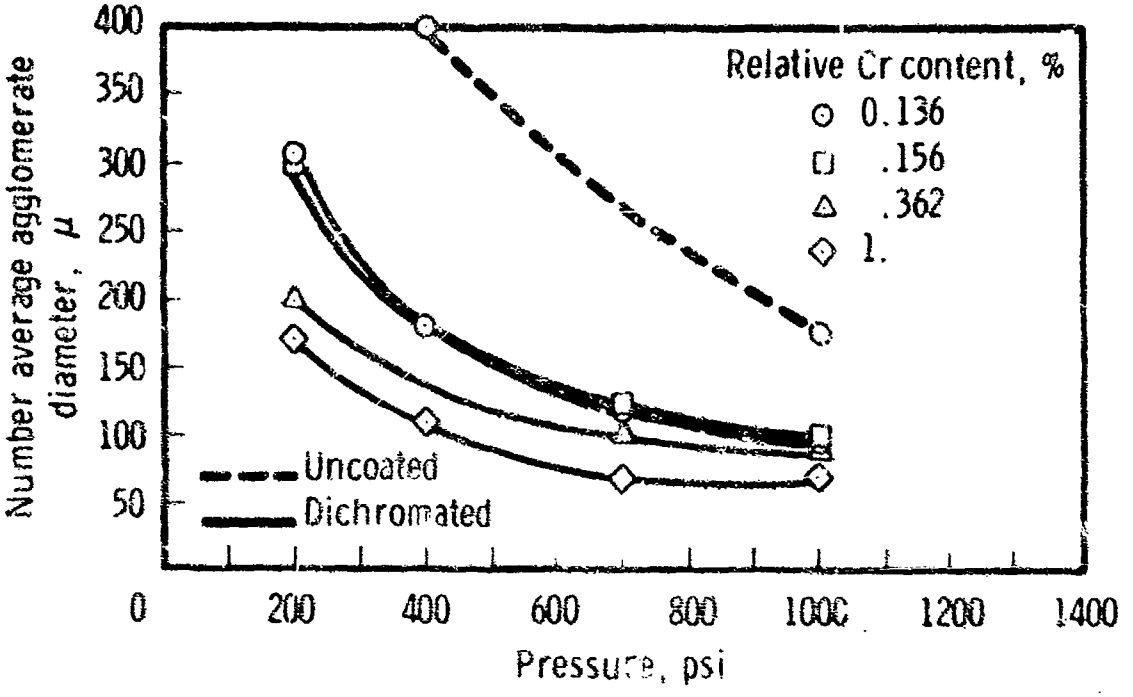

Figure 1. Variation of Aluminum Agglomerate Size with Pressure

05763

losses. Thus the trend in two-phase flow losses with pressure depends on which effect (the unfavorable reduction in drag force or the more favorable ratio of particle drag force to mass) predominates in a given motor.

Transfer of heat and momentum through a boundary layer results in performance loss. The work done against the frictional forces and the heat lost to the nozzle wall represent the source of boundary-layer losses. The local heat transfer and skin friction coefficients vary as the inverse 0.2 power of the Reynolds number, i.e.:

$$C_g,\ C_f \propto R_e^{-0.2} = (\rho_g U_g L/\mu)^{-0.2}$$

The local heat transfer rate and frictional force are given by

$$F = \tfrac{1}{2} \rho_g U_g^2 A C_f$$

$$\dot{Q} = \rho_g C_p U_g \Delta T A C_g$$

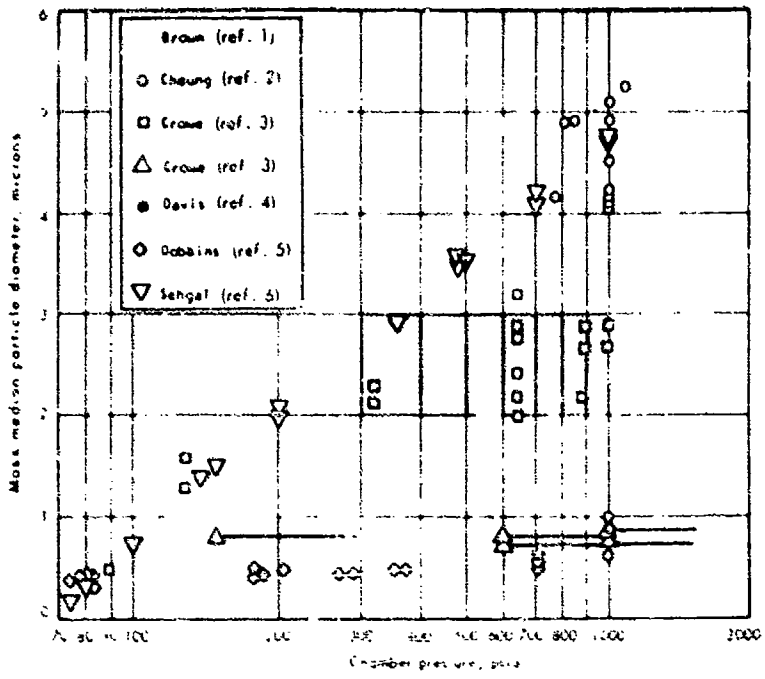

Figure 2. Measured Mass-Median Al_2O_3 Particle Diameter vs Chamber Pressure

05764

Therefore for geometrically similar nozzles, the local heat transfer and frictional force vary as

$$F, \dot{Q} \propto \rho^{0.8}$$

Or using the perfect gas law $P = \rho RT$

results in $F, \dot{Q} \propto P^{0.8}$

Since the thrust and the mass flux vary linearly with pressure, the frictional force divided by the thrust and the heat loss divided by the enthalpy flux vary as the inverse 0.2 power of the pressure. The loss in specific impulse has been shown to vary in the same way:

$$\frac{\Delta I_{sp}}{I_{sp}} \propto P^{-0.2}$$

Therefore an increase in pressure would result in a decrease in boundary layer losses. However, the change is slight.

As gas flows through a nozzle, the chemical composition of the gas tries to maintain equilibrium at the local pressure and temperature. The pressure and temperature decrease to a level where the chemical reaction rates are too slow to maintain equilibrium so the composition of the gas tends to freeze (remain fixed). The energy associated with the incomplete recombination results in performance loss. Reducing the pressure increases the performance loss associated with chemical recombination. Besides increasing the degree of dissociation of the gas, the reduced pressure causes the recombination rates to decrease. The lower recombination rates cause the composition of the gas to freeze at an earlier expansion ratio. The increase in the local dissociation along with the earlier freezing of a gas with the higher dissociation causes performance loss from the chemical recombination to increase with decreasing pressure.

Figure 3 shows the effects of the above performance losses versus the pressure; the chemical recombination losses will decrease with increasing pressure and the two-phase flow losses will increase with increasing pressure. The experimental data on the curve show the importance of the effect of aluminum agglomeration on performance. The additional loss at the lower pressures arises from the inability of the aluminum to completely burn during the firing. In any determination of performance, the effects that pressure will have are extremely important. Therefore, any ballistic testing of a motor system should try to match the chamber pressure as closely as possible.

2.2 Throat Diameter

The throat diameter has a first order effect on performance due to its influence on two-phase flow. It also has some influence on chemical recombination and boundary layer losses. The magnitude of these losses tends to decrease with increasing throat size.

The effect that throat diameter has on two-phase flow losses is a result of particle size and the flow field gradients in the nozzle. Figure 4 shows the effect that the throat diameter has on particle size. With an increase in throat diameter, the particle size increases. This increase worsens the ratio

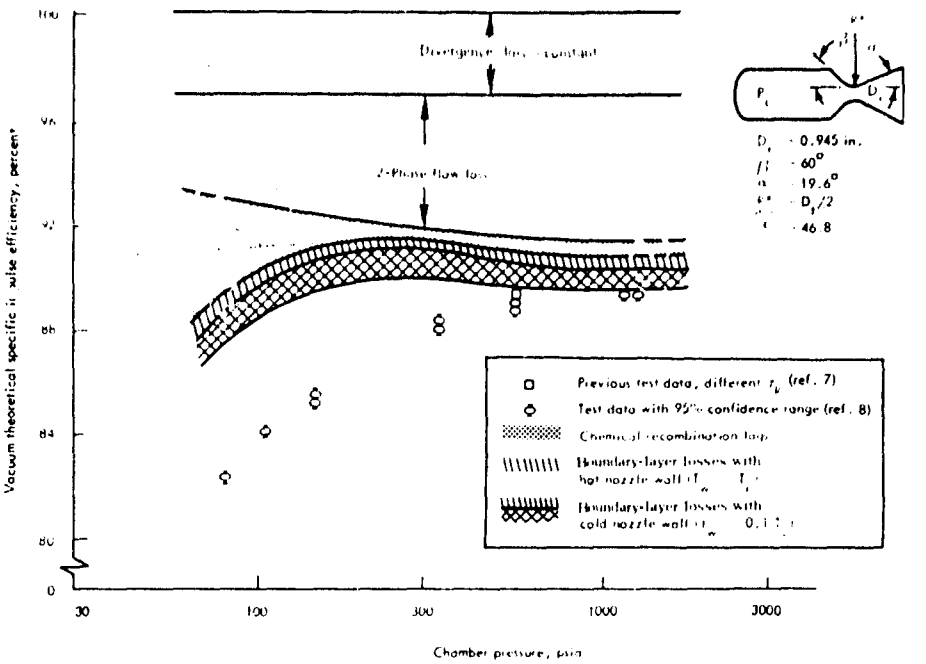

Figure 3. Typical Effect of Chamber Pressure on Vacuum Specific Impulse Efficiency 05765

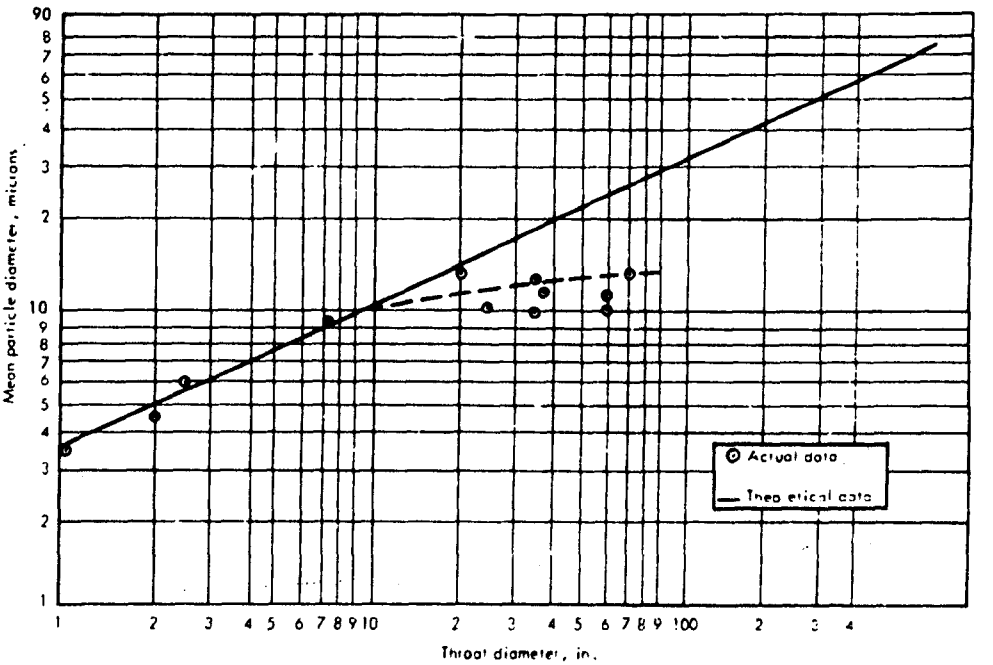

Figure 4. Correlation of Particle Size/Motor Size Data with Maximum Stable Droplet Diameter Theory 05766

of drag force to mass of the particles. This worsening condition is offset, however, by two other effects: first, the particles seem to have a maximum size of 10 to 12 microns which limits the worsening condition; second, with an increase in throat diameter geometrically similar nozzles have more gradual flow field gradients. These more gradual gradients in gas velocity, temperature, and pressure allow the gas-particle system to acquire a higher degree of equilibrium. Therefore, even though the particle size increases, the two phase flow losses decrease with an increase in throat diameter.

The chemical recombination loss also decreases with an increase in throat diameter. The more gradual gradients of temperature and pressure require lower chemical reaction rates to maintain equilibrium. This means that the chemical composition of the gas will freeze at a higher expansion ratio. The resulting lower degree of dissociation gives a lower performance loss.

The losses associated with a boundary layer arise from the work done against the friction forces and the heat lost to the nozzle wall. The local heat transfer and skin friction coefficients vary as the inverse 0.2 power of the Reynolds number, i.e.:

$$C_H,\ C_F \propto Re^{-0.2} = (\rho g U g L/\mu)^{-0.2}$$

For geometrically similar nozzles, the Reynolds number varies directly with the throat diameter since the length of the nozzle varies directly with the throat diameter. The local heat transfer and frictional forces are given by

$$F = \tfrac{1}{2}\rho g U g^2 A C_F$$

$$\dot{Q} = \rho g C p U g \Delta T\ A\ C_H$$

and the area varying as the square of the throat diameter is given by:

$$F,\ \dot{Q} \propto D_t^{1.8}$$

For a nozzle operating at a certain pressure, both the thrust and the mass flow vary as the square of the throat diameter. Therefore, the friction force

divided by the thrust and the heat loss divided by the enthalpy flux vary as the inverse 0.2 power of the throat diameter. Consequently,

$$\frac{\Delta I_{sp}}{I_{sp}} \alpha D_t^{-0.2}$$

Thus for geometrically similar nozzles, the boundary loss will decrease with an increase in throat diameter.

The combination of these effects can be seen in Figure 5 where the variation in specific impulse efficiency with throat diameter is shown. The variation in losses due to chemical recombination and the boundary layer is too small to be seen. The loss associated with two-phase flow is seen to decrease with an increase in throat diameter. The increase in efficiency becomes less and less with increasing throat diameter. Comparing the results of this graph with data from Titan III firings, an increase in throat diameter from 4 to 38 in. results in an increase in efficiency of 3%. A decrease in throat diameter from 4 to 1 in. gives a comparable decrease. In the determination of specific impulse efficiency, the effects that throat diameter have are important; however, for throat sizes greater than approximately 4 in., variations in throat diameter will begin to have less effect. The testing of a motor system should try to match the throat diameter as nearly as possible, as long as more important parameters do not suffer as a result of the matching when the diameter is greater than 4 in.

2.3 Residence Time and Characteristic Length

Residence time or L* will affect performance through its effects on unburned aluminum and particle size. Average residence time is defined from the gas laws by

$$t_r = \left(\frac{Vc}{\dot{m}}\right)\left(\frac{Pc}{RTc}\right)$$

Mass flow rate ($\dot{m}$) depends upon the throat area and pressure,

$$\dot{m} = PcAtg/C^*$$

Therefore:

$$t_r = \frac{Vc}{A_t}\frac{C^*}{gRTc} = L^*\frac{C^*}{gRTc}$$

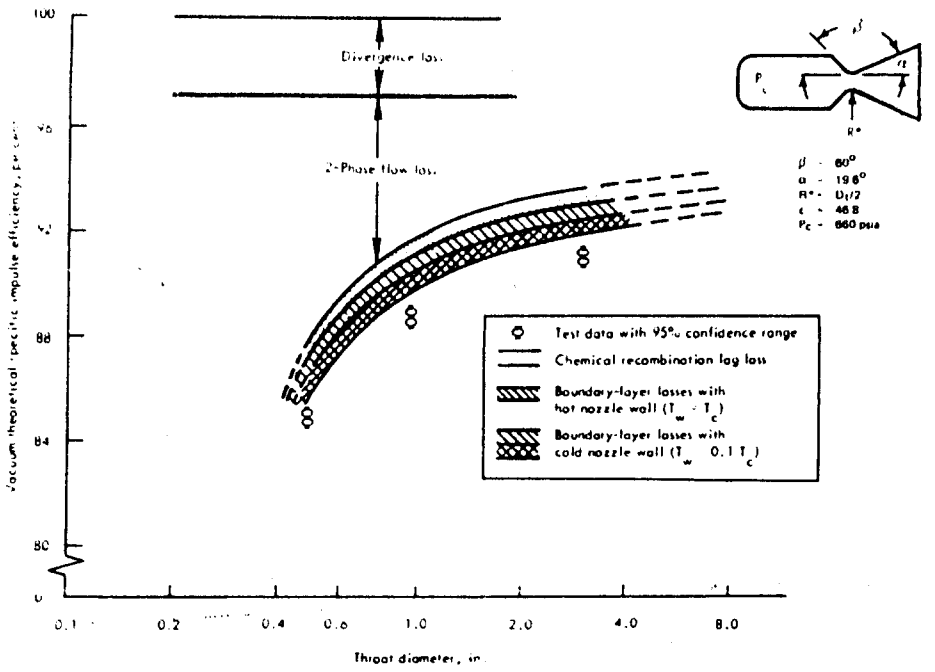

Figure 5. Typical Effect of Motor Size on Vacuum Specific Impulse Efficiency 05767

The residence time and L* vary directly. The effects of residence time are limited to a small range, and in general, efficiency will increase with increased residence time.

The effect that residence time has on particle size is seen in Figure 6 where exhaust particle size is plotted versus residence time. The particle size increases rapidly with residence time until a residence time of 20 msec is reached. For residence times above 20 msec, the particle size remains fairly constant. The particle size affects performance through its effects on two-phase flow. Two-phase flow losses will increase with particle size because the larger particles are less able to maintain thermal equilibrium and have a greater velocity lag. Therefore, two-phase flow losses increase with residence time until residence time equals 20 msec. Above 20 msec two-phase flow losses remain nearly constant.

A more important effect is the amount of unburned aluminum. Metal-particle ignition and combustion must occur within the motor residence time to avoid

performance losses. When motor residence time is too short for adequate combustion, an equilibrium condition significantly different from the theoretical one will be produced. The dependence of metal combustion on residence time is shown in Figure 7 in which the percent of unburned aluminum is plotted against residence time. Residence times under 10 msec appear insufficient for adequate metal combustion. However, residence times over 20 msec have very little effect on metal combustion; therefore, metal combustion becomes less a factor in performance.

Figure 8 shows the dependence of specific impulse efficiency on residence time. The efficiency rises sharply for residence times below 10 msec and has a very gradual rise for residence times above 20 msec. These tests were not corrected for motor heat loss, so the area of sharp decline is probably under 15 msec for residence times. The curve shows that the effects of metal combustion predominates as far as residence time is concerned. Therefore, the

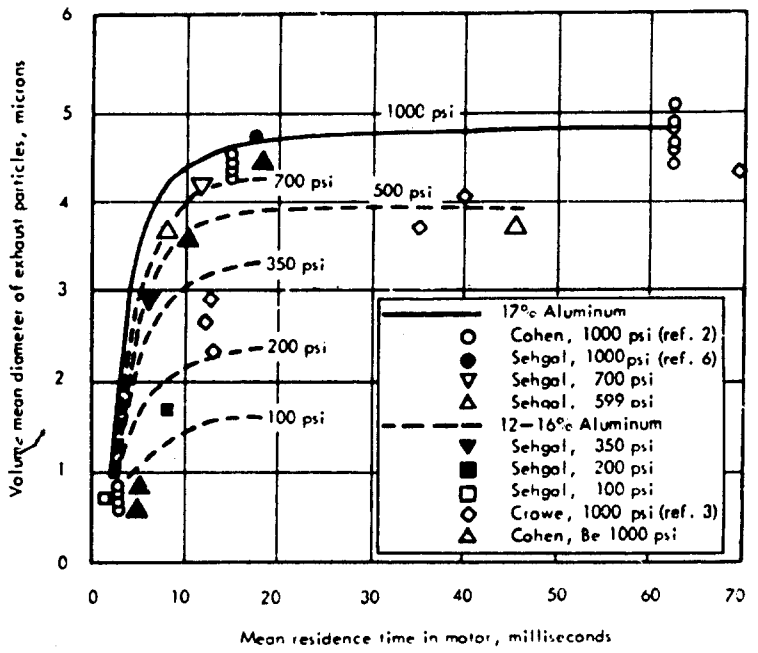

Figure 6. Effect of Residence Time on Exhaust Particle Size

05768

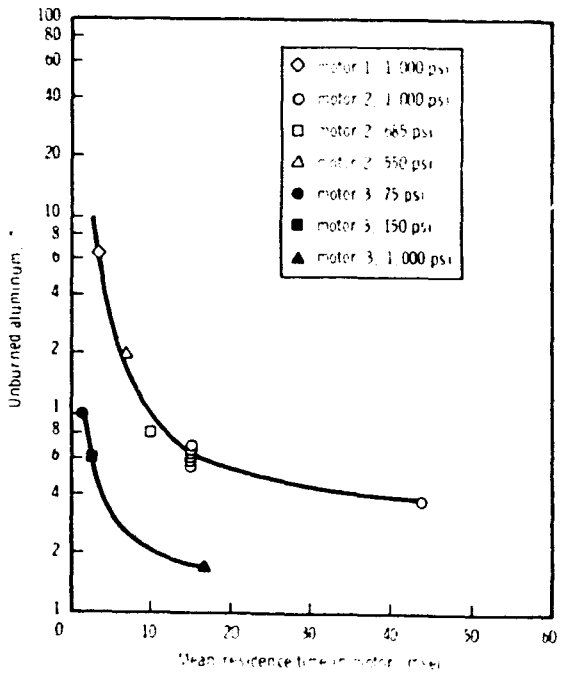

Figure 7. Effect of Residence Time on Completeness of Metal Combustion
05769

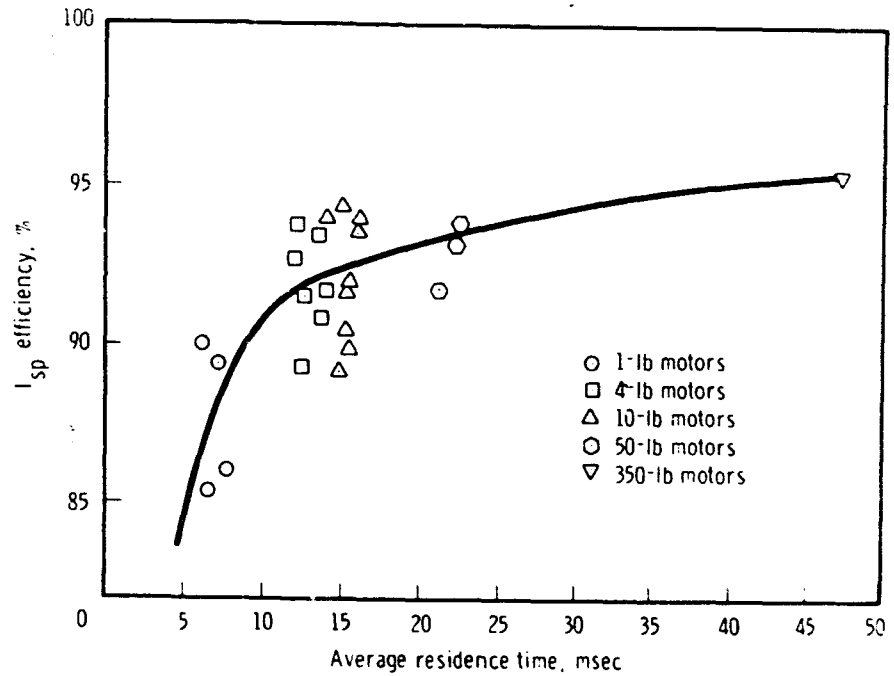

Figure 8. Effect of Residence Time of Specific Impulse Efficiency in an Al-PBAN Propellant
05770

residence time need only be considered for those systems when a mean residence time less than 20 msec prevails.

2.4 Nozzle Roughness and Erosion

The reuse of a nozzle could lead to performance loss due to nozzle roughness and erosion. The performance loss would increase with each reuse of the nozzle and severely limit the use of a nozzle for multiple testing.

During the UTC C4 EDP, a significant improvement in nozzle efficiency was observed by using a carbon-carbon exit cone material as opposed to an ablating phenolic material. Figure 9 shows a comparison of nozzle efficiency during motor firings with identical initial nozzle contours (throat diameters of 4 in.) and identical motors. The efficiency of the ablative phenolic exit cone began to drop early in the firing and remained substantially lower than the carbon-carbon exit cone for the motor duration. The efficiency improvement

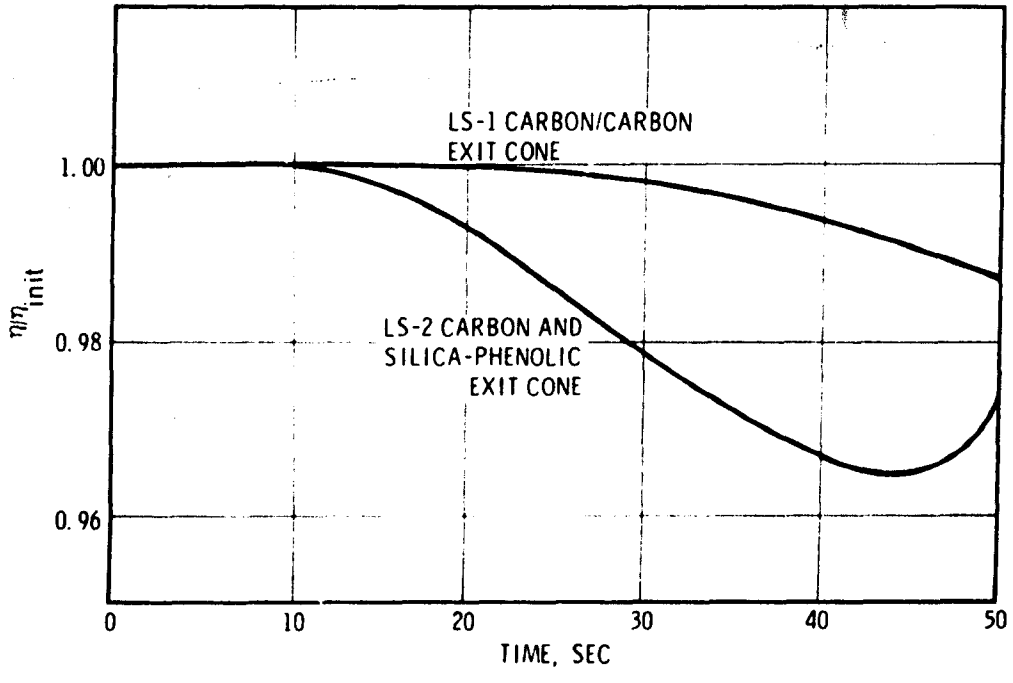

Figure 9. Effect of Ablation on Nozzle Efficiency

05771

appeared to result from reduced erosion, absence of a char layer, reduced contour discontinuities, and reduced surface roughness. Reduction in nozzle efficiency resulting from severe exit cone erosion has been observed in other investigations. In one study, the same nozzle was fired on five separate occasions. The specific impulse decreased with each successive firing, much in the same manner as continuous firing of the ablative phenolic exit cone shown in Figure 9. The trend was attributed to the cumulative erosion and char from prior firings.

The effects of nozzle roughness and erosion should, intuitively, decrease with increasing throat size. Figure 9 does show that an ablative phenolic exit cone could be used for two 5-sec firings and a carbon-carbon exit cone could be used for four 5-sec firings without serious performance degradation. However, a nozzle should be reused with care so that performance is not adversely affected.

2.5 Nozzle Submergence

The performance losses associated with nozzle submergence are due to two-phase flow effects. The particles generate under the submerged nozzle and must flow toward the forward end of the motor to reach the nozzle entrance. These particles must also make a turn of about 180^{o} to enter the nozzle. This change in direction, caused by large velocity gradients, makes these particles lag further behind in the gas flow than other like particles. This additional lag in velocity causes the performance loss.

Figure 10 shows the relationship between nozzle submergence and its associated performance loss. The loss in specific impulse increases rapidly with the percent of submergence until about 10% submergence. Above 10%, the loss increases gradually. The loss also depends upon the percentage of aluminum. An increase in the aluminum content increases the percentage loss and it also increases the slope of the gradual portion of the curve. At 10% submergence for a propellant with 21.5% aluminum, the loss in specific impulse is approximately 0.95%. Increasing the submergence to 25% increases the loss to 1.1%. It would be desirable to completely model submergence, but the

difficulty involved may make it unfeasible and an undesirable expense considering the small increase in the loss.

2.6 Nozzle Radius of Curvature

The performance loss associated with the nozzle radius of curvature is due to the acceleration of particles in two-phase flow. With a larger radius of curvature, a nozzle would have gentler velocity and temperature gradients, and the particles would have a smaller velocity lag and less thermal non-equilibrium with the gas flow. Figure 11 shows the relationship between the nozzle radius of curvature and specific impulse efficiency. The nozzle radius of curvature is a fairly important effect for radii equal to or greater than the throat radius. Limited investigations, however, have indicated that radii of curvature 0.3 to 1.0 times the throat radius have little effect on delivered specific impulse efficiency. Therefore, if the motor system has a

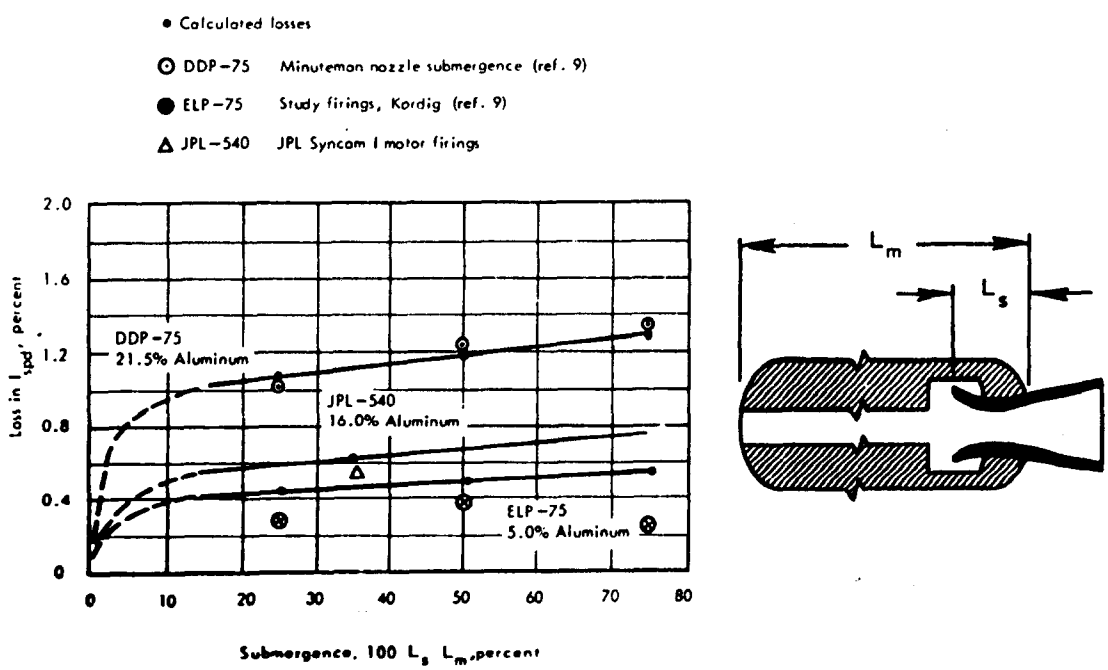

Figure 10. Typical Effect of Nozzle Submergence on Specific Impulse

05772

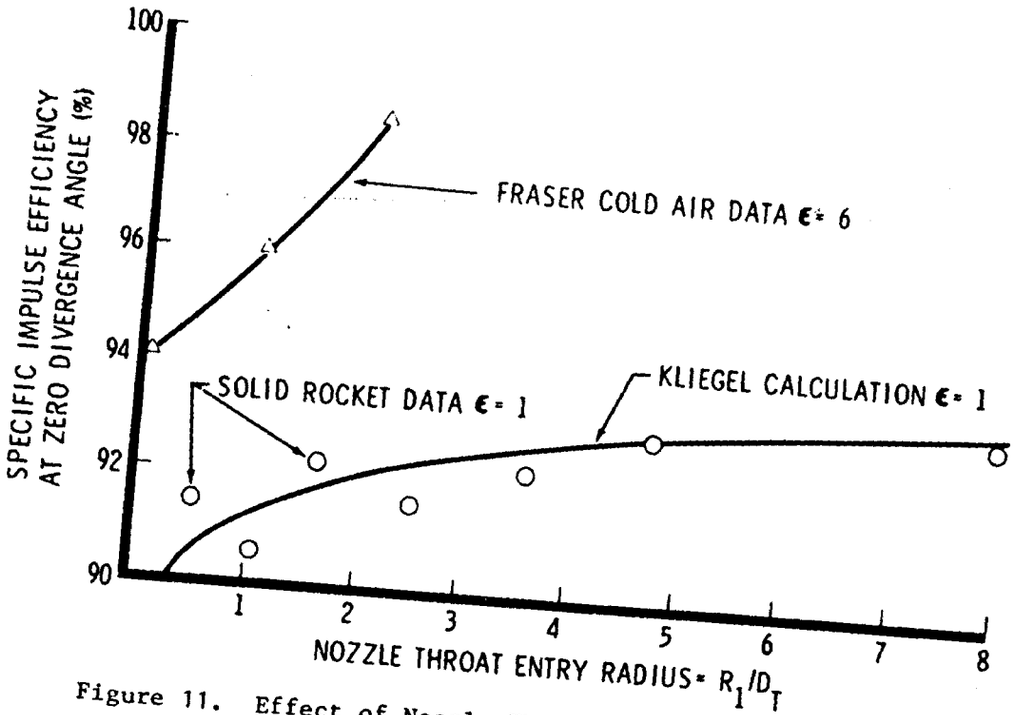

Figure 11. Effect of Nozzle Throat Contour on Efficiency

05773

throat radius of curvature less than the throat radius, the importance of modeling this effect decreases considerably.

2.7 Port to Throat Contraction Ratio

Figure 12 shows the contraction ratio's effect on specific impulse. With increasing contraction ratio and/or mass flow rate the specific impulse loss associated with this effect decreases. The Super BATES will operate with minimum mass flow rates of 100 lb/sec and a minimum contraction ratio of 2.5. At these conditions, the loss associated with port to throat contraction ratio becomes insignificant.

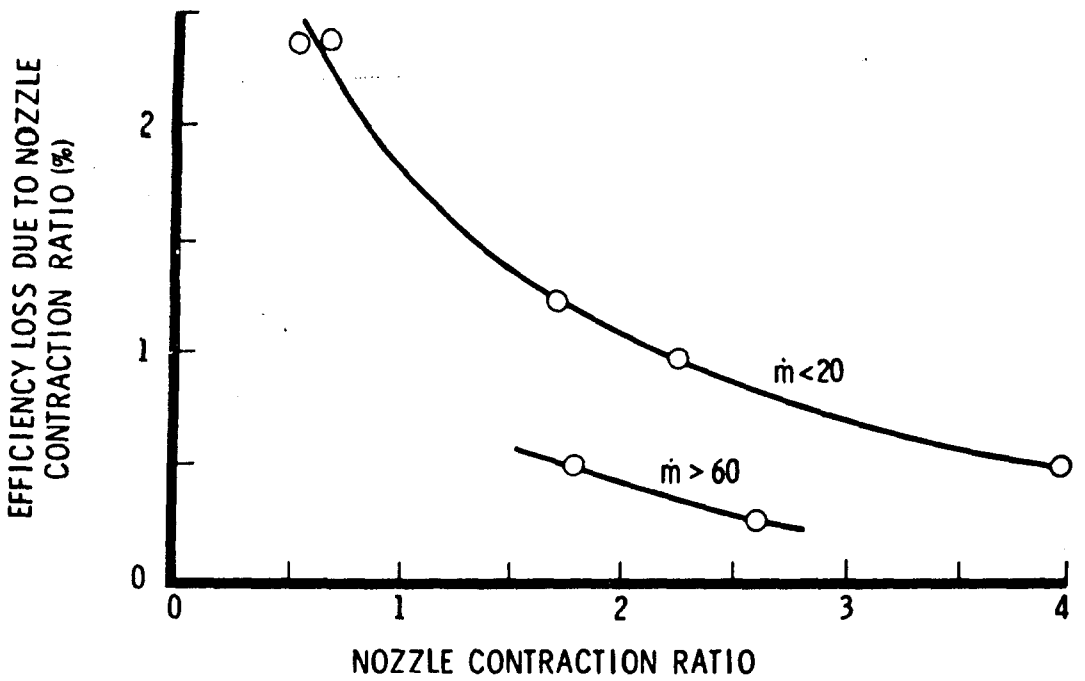

Figure 12. Effect of Contraction Ratio on Nozzle Efficiency

05774

3.0 PARAMETER EFFECT ON SUPER BATES DESIGN

3.1 Pressure Neutrality

3.1.1 Impact of Pressure Neutrality on Performance Accuracy

A study evaluated the impact of pressure variations on the accuracy of performance predictions for the Super BATES. Although a perfectly neutral trace is desirable, reasonable variations in P_c must be expected with the high pressure exponents characteristic of advanced strategic propellants. The performance accuracy corresponding to different degrees of pressure neutrality must be evaluated in light of the design compromises that may be required to achieve nearly neutral pressure traces.

Performance variations with P_c are primarily a result of pressure ratio effects on C_F and the variation of specific impulse efficiency with P_c.

P_c is one of the most important variables in modeling solid motor specific impulse. As discussed in Section 2.1, P_c controls burning rate which helps establish the size of aluminum particles ejected from the grain. Pressure also controls the diffusion of oxidizer species and the rate of combustion of the aluminum particles. P_c affects the rate of the chemical reactions occurring in the chamber and the magnitude of two-phase flow losses. Without detracting from the importance of correctly modeling full-scale motor P_c, the correlations presented in Section 2.1 do not predict large changes in specific impulse efficiency for pressure variations of even ±10%. Furthermore, the specific impulse efficiency appears to be quite linear at pressures above 300 psia. Therefore, the inaccuracy caused by a trace with pressure variations of ±10% or even slightly higher compared to a perfectly neutral trace would be less than 0.05% and would not have a significant impact on overall system performance accuracy.

P_c variations have a more significant impact on back pressure losses than on specific impulse efficiency at an 8-in. throat size. Two parameters were calculated to measure the impact of P_c variations on performance for a square wave stepped pressure trace. A square trace (half the burn time of

$\bar{P} = P + \Delta P$ and half at $P_c = P - \Delta P$) is the limiting case for any degree of pressure variation and was selected to define the maximum performance error for a given degree of non-neutrality. The first parameter, λ, shown in Figure 13 defines the maximum variation in C_F as a percent of the C_F at average pressure. For optimum nozzle expansion, λ varies from 1.5% (±0.75%) to 2.25% for P_c from 1,800 psia to 500 psia for pressure variations of ±10%. Below 500 psia λ increases more rapidly, reaching 3.25% at 200 psia. The parameter λ defines the maximum variation in instantaneous performance (excluding ignition and tailoff), but not the difficulty in measuring overall performance.

The parameter, δ, was calculated to define the performance correction required with a square wave trace to convert performance at average pressure to average delivered performance. Since performance falls off more rapidly at low pressure, the specific impulse loss at $\bar{P} - \Delta P$ is greater than the gain at $\bar{P} + \Delta P$ requiring a correction of roughly -0.10% from the specific impulse at average pressure to determine average specific impulse. The values of δ,

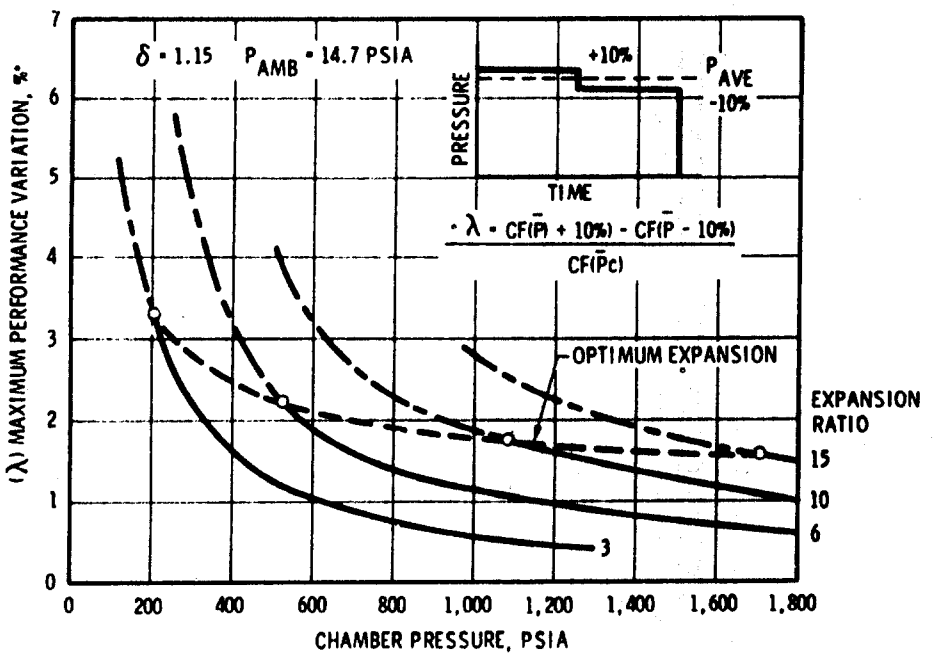

Figure 13. Performance Variation vs Pressure and Expansion Ratio for a Square Trace with 10% Neutrality

05775

the correction factor, are shown in Figure 14 versus expansion ratio and P_c for variations in P_c of ±10% with a square trace. The correction factor which can be determined for any pressure trace, will be considerably lower for the skewed parabolic traces typical of Super BATES. The correction factor at optimum expansion ratio also increases sharply below 500 psia.

The values of λ and δ were calculated for pressure variations up to ±20% to establish a recommended level of pressure neutrality for Super BATES. The results shown in Figure 15 indicate that the correction factor escalates rapidly for pressure variations above 10% while the absolute performance variation is nearly linear over the range 0 to ±20%.

Although the correction factor can be accurately calculated, large corrections are undesirable. At pressure variations of ±10%, the maximum correction factor is only about 0.12%. Consequently, simplified correlation plots with only a few curves would be adequate because interpolation errors of even 10% to 20% would amount to performance errors of only 0.01% to 0.02%. However, with P_c variations of ±20% or higher, an accurate determination of the correction factor would be required to avoid compromising the performance prediction accuracy of the motor.

Based on the correction factor curve shown in Figure 15, UTC recommends that a maximum P_c variation of ±10% be allowed for the Super BATES motor. Although the extremely small correction factor at 5% is attractive, the error resulting from a 0.12% correction at ±10% pressure should be no more than 0.02% which seems acceptable in light of the projected thrust stand accuracy (±0.10%). Clearly the design should strive for as neutral a trace as possible, but the small improvement in accuracy from ±10% P_c to ±5% P_c does not justify major compromises in the design.

3.1.2 Effect of Grain Geometry on Pressure Neutrality

The effect of propellant grain geometry on pressure neutrality was analyzed.

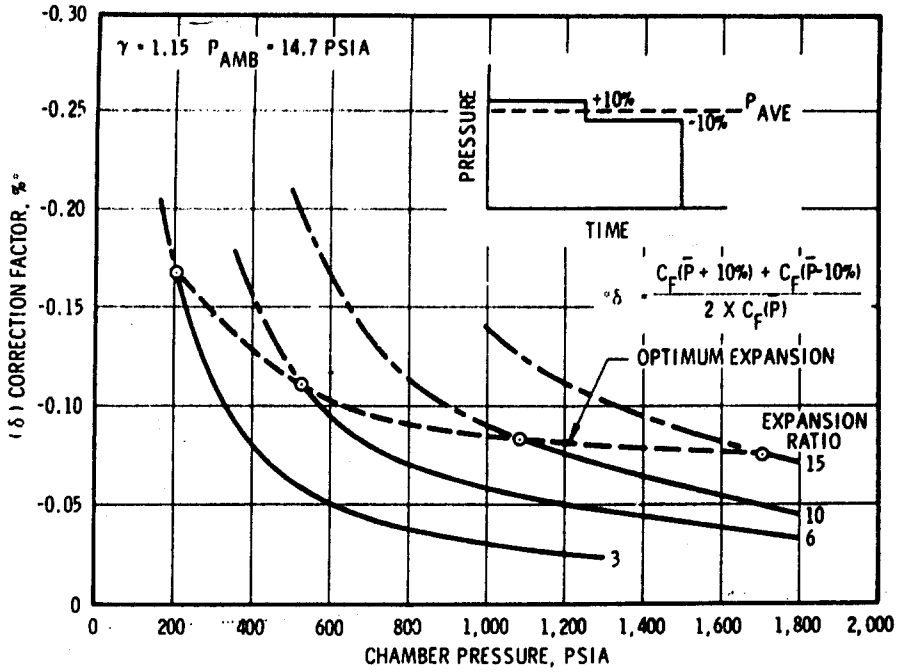

Figure 14. Square Trace Correction Factor vs Pressure and Expansion Ratio for 10% Neutrality

05776

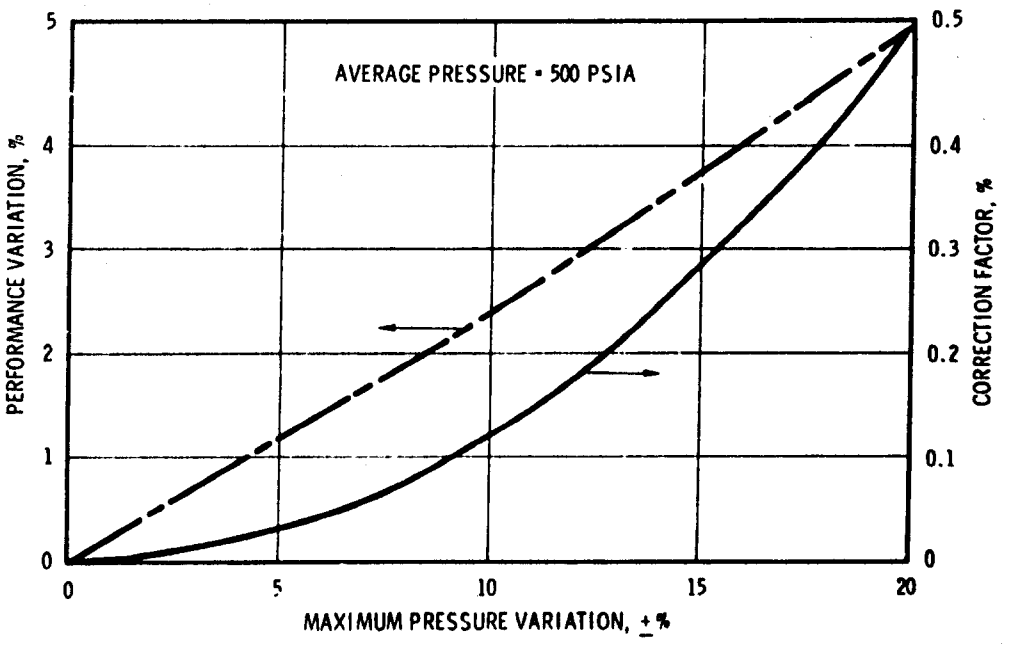

Figure 15. The Effects of Pressure Neutrality on Performance for a Square Trace

05777

Interest focused on cylindrically perforated double end burning grains because this configuration offers simplicity, web thickness flexibility, and excellent neutrality. Grain design flexibility was evaluated in terms of pressure neutrality and propellant exponent.

3.1.2.1 Derivation of Pressure Neutrality Relationships - The equations relating P_c neutrality and grain geometry were derived assuming throat erosion effects to be negligible. Variables used in the derivation are shown in the list of abbreviations and symbols at the end of this appendix.

For steady state operation the pressure and surface area can be related by equating the propellant mass flow through the nozzle with the mass leaving the grain.

$$P_c = \frac{\dot{m}\ C^*}{A_t\ g_c}$$

$$\dot{m} = \rho\ a\ P_c^{\ n}\ A_b$$

$$P_c = \left(\frac{a\ \rho\ C^*}{A_t\ g_c}\right)^{\frac{1}{1-n}} A_b^{\ \frac{1}{1-n}} = c^{\frac{1}{1-n}}\ A_b^{\ \frac{1}{1-n}}$$

Since throat area changes are small, the term in parenthesis above is a constant. Average pressure can be related to average surface area through the burning rate relationship.

$$\bar{P}_c = \frac{1}{t_b} \int_o^{t_b} P_c \, dt$$

$$\dot{r} = a P_c^{\,n} = a c^{\frac{n}{1-n}} A_b^{\frac{n}{1-n}}$$

$$dt = dw/\dot{r}$$

$$\therefore \bar{P} = \frac{1}{t_b} \int_o^{w_b} \frac{P_c^{\,1-n}}{a} \, dw = \frac{c}{t_b a} \int_o^{w_b} A_b \, dw$$

$$\bar{A}_b = \frac{1}{w_b} \int_o^{w_b} A_b \, dw$$

$$\therefore \bar{P}_c = \frac{c \, w_b}{a \, t_b} \bar{A}_b$$

This expression for average pressure can be simplified through the definition of average burning rate.

$$w_b/t_b = \bar{\dot{r}} = a \, \bar{P}_c^{\,n}$$

$$\therefore \bar{P}_c = c \, \bar{P}_c^{\,n} \, \bar{A}_b$$

Pressure variations can be expressed in terms of surface area variations which can be related to the grain design.

$$\frac{A_b}{\bar{A}_b} = \frac{P_c^{\,1-N/c}}{\bar{P}_c/c \; \bar{P}_c^{\,n}} = \eta$$

If $K(\lambda, \delta)$ is defined as $\bar{P}_c^{\,n}\,\overline{P_c^{\,n}}$ then

$$\frac{A_b}{\overline{A_b}} = \frac{P_c^{\,1-n}}{\overline{P_c^{\,1-n}}}\,K(\lambda, \delta) = \left(\frac{P_c}{\bar{P}_c}\right)^{1-n} K(\lambda, \delta)$$

An investigation showed that $\bar{P}_c^{\,n}$ and $\overline{P_c^{\,n}}$ were essentially equal for the range of grain designs being considered for Super BATES. The extreme case of a square wave pressure trace was examined to determine the maximum variation of these two pressure averages. For pressure variations of ±5% and ±10% the

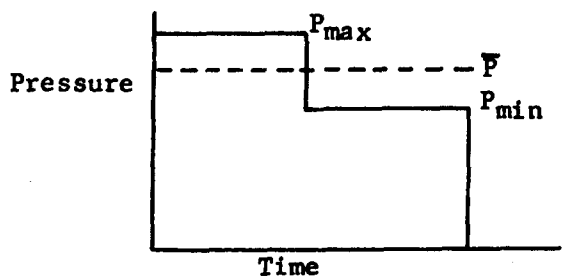

values of K and the maximum error incurred by neglecting K were calculated as shown below.

Pressure Variation, %	K Square Wave	Actual Pressure Variation for K Assumed to be Unity, %
± 5	0.9997	5.09
±10	0.9989	10.13

Since the variations for the skewed parabolic traces characteristic of the Super BATES grain will be much less than for a square wave, the pressure variations can be calculated based on surface area and average surface area without determining the K factor for each grain.

For a cylindrically perforated double end burning grain, the surface area variations can be calculated in nondimensional form directly from the geometry where $w_f = w/D$.

$$A_b = 2 \times \frac{\pi}{4}\left(D^2 - (d + 2w)^2\right) + \pi(d + 2w)(L - 2w),\ 0 \leq w \leq \frac{D-d}{2}$$

$$\frac{A_b}{\pi D^2} = \frac{1}{2}\left(1 + \frac{2\delta}{\lambda} - \frac{1}{\lambda^2}\right) - 4w_f/\lambda + 2\delta w_f - 6w_f^2,\ 0 \leq w_f \leq \frac{\lambda-1}{2\lambda}$$

The average nondimensional surface area can be calculated by integrating the above expression over the web.

$$\frac{\bar{A}_b}{\pi D^2} = \frac{2\lambda}{\lambda-1}\int_0^{\frac{\lambda-1}{2\lambda}} \frac{A_b}{\pi D^2}\, dw_f = \frac{\delta(\lambda + 1)}{2\lambda}$$

The surface area ratio η is simply the quotient of the instantaneous and average nondimensional surface areas.

$$\eta = \frac{\lambda^2\left(1 + 4\delta w_f - 12w_f^2\right) + \lambda\left(2\delta - 8w_f\right) - 1}{\delta\lambda\left(\lambda + 1\right)}$$

The variation of η with grain L/D (δ) is shown in Figure 16 for a grain B/A (λ) of 1.25. Minimum values of η occur at the optimum L/D of 1.9 for this B/A. The curves are not symmetric about the average surface area. The variations at minimum surface area are always larger than the variations at maximum surface area. For this study, pressure neutrality has been strictly defined as the maximum deviation from average pressure. Therefore, a trace whose minimum pressure was 10% below average, but whose maximum pressure was only 5% above average would still be considered to have a pressure neutrality of 10%.

The variation at maximum surface area can be calculated by taking the derivative of η with web fraction.

$$\frac{d\eta}{dw_f} = \frac{4\delta\lambda^2 - 24w_f\lambda^2 - 8\lambda}{\delta\lambda(\lambda + 1)} = 0 \text{ for } w_f = \frac{\delta\lambda - 2}{6\lambda}$$

$$\eta_{max} = \frac{\lambda^2(3 + \delta^2) + 2\delta\lambda + 1}{3\delta\lambda(\lambda + 1)} \text{ for } \frac{2}{\lambda} \leq \delta \leq \frac{3\lambda - 1}{\lambda}$$

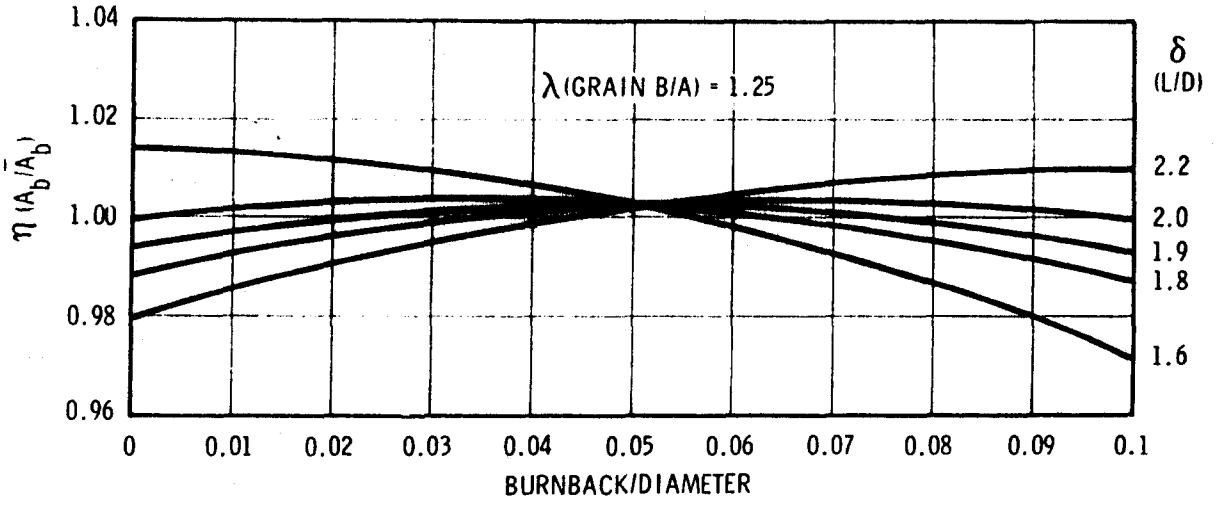

Figure 16. Surface History Characteristics

05779

The relationship for η_{max} is mathematically valid for all values of δ, but beyond the range indicated the maximum value of η will physically occur beyond the motor case or inside the actual propellant surface.

The largest surface area variations occur at the minimum point at ignition for $\delta \geq \frac{3\lambda + 1}{2\lambda}$ and at burnout for $\delta \leq \frac{3\lambda + 1}{2\lambda}$.

$$\eta = \frac{\lambda^2 + 2\delta\lambda - 1}{\delta\lambda(\lambda + 1)}, \quad \delta \geq \frac{3\lambda + 1}{2\lambda}$$

$$\eta = \frac{2(\lambda\delta - \lambda + 1)}{\delta(\lambda + 1)}, \quad \delta \leq \frac{3\lambda + 1}{2\lambda}$$

The pressure neutrality can be calculated from the surface area variations

$$P_N = 1 - P_{min}/\bar{P} = 1 - (A_{b_{min}}/\bar{A}_b)^{\frac{1}{1-n}} = 1 - \eta^{\frac{1}{1-n}} \text{ or } \eta = (1 - P_N)^{1-n}.$$

The values of δ (L/D) can be calculated for any desired value of η.

$$\delta = \frac{\lambda^2 - 1}{\eta\lambda(\lambda + 1) - 2\lambda}, \quad \delta > \frac{3\lambda + 1}{2\lambda}$$

$$\delta = \frac{2(\lambda - 1)}{2\lambda - \eta(\lambda + 1)}, \quad \delta < \frac{3\lambda + 1}{2\lambda}$$

If λ (B/A) $\leq \frac{2 - \eta}{\eta}$ then there is no maximum length.

3.1.2.2 Investigation of Grain Pressure Neutrality Characteristics – The equations developed in the previous section were used to investigate the pressure neutrality characteristics of the baseline circular perforated double end burning grain design. Based on the neutrality study presented in Section 3.1.1, pressure variations up to ±10% were considered. The grain design study showed that a pressure neutrality of considerably less than 5% could be achieved for significant ranges of motor length and web. However, a 5% limit on pressure variations would severely restrict motor operation in several areas, whereas a 10% limit on pressure variation removed these restrictions completely.

The effects of pressure variation and burning rate exponent on the maximum allowable web fraction are presented in Figure 17. Although the maximum web shows worthwhile gains from 5% to 10% pressure variation, the gains for further increases in allowable pressure variation will tend to be small. Considering the large relative increase in performance error noted in Section 3.1.1 for pressure variations beyond 10%, there seems to be little advantage in extending the allowable pressure variations beyond the recommended ±10%. The increase in allowable web for lower burning rate exponents reduces the pressure variations considerably for low values of n. Most high burning rate propellants which would require a thicker web also have high burning rate exponents. Therefore, this grain design study used a maximum exponent of 0.65 for the high energy propellants for ballistic missiles.

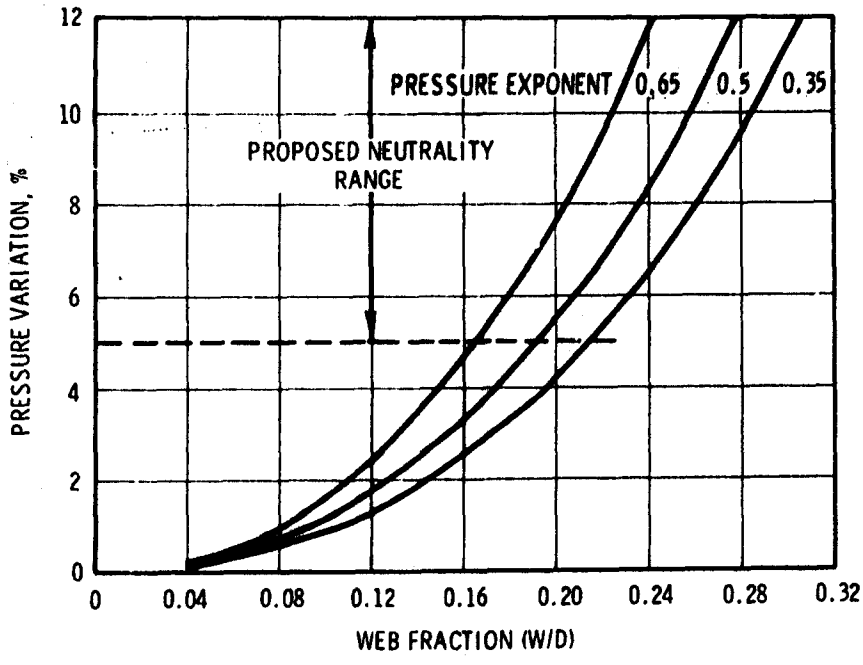

Figure 17. Minimum Pressure Variation vs Web Fraction and Pressure Exponent

05780

The allowable range of grain length for a given web is a more important design parameter than the maximum web. Figure 18 shows the variation of B/A (λ) and L/D (δ) for two pressure variations (5% and 10%) and three propellant exponents (0.35, 0.5, 0.65). The curves are sharply cusped near the maximum B/A and are relatively flat for values of L/D less than 0.8 B/A_{max} or greater than 1.15 B/A_{max}. Allowable grain length and web are shown in Figure 19 for an outside grain diameter of 28 in. A grain diameter of 28 in., which is roughly equivalent to an average port diameter of 25 in., emerged as the most attractive diameter based on the grain geometry considerations presented in this section together with the residence time, ignition transient, erosive burning, and heat transfer considerations presented in the following sections. The impact of increasing the pressure variations from 5% to 10% on allowable grain length is quite dramatic. With 5% variation the grain length is restricted to a relatively narrow range for an n of 0.65. However, with a pressure variation of 10% the grain length can vary by a factor of 2 at the nominal web of 2.5 in. and by a factor of 1.5 at the largest primary web of 3.5 in.

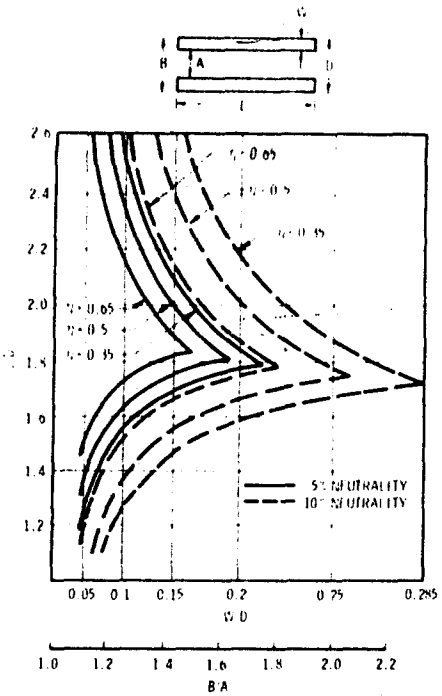

Figure 18. Combinations of B/A and L/D for 5% and 10% Pressure Neutrality

05781

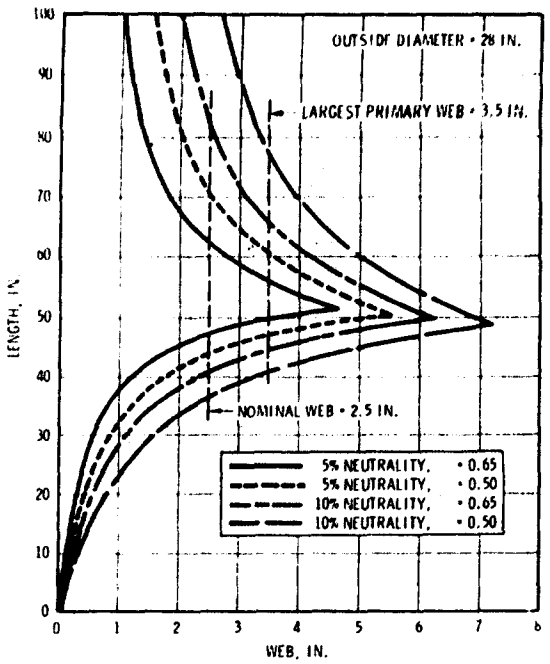

Figure 19. Propellant Length vs Web for Combination of Neutrality and Exponent Propellant

05782

Pressure neutrality helps determine the choice of grain diameter by restricting the allowable grain length variations for given propellant webs. With a grain diameter of 23 in. (average port diameter of 20 in.) the allowable grain length variation at the nominal web of 2.5 in. would fall from 40 in. (for a 28-in. OD) to only 22 in. which is inadequate to cover the full range of grain lengths for the Super BATES. With a grain diameter of 33 in. (average port diameter of 30 in.), the range of allowable grain lengths at maximum web would increase beyond the range required. Further study showed that the capabilities of a 28-in. diameter grain were sufficient to handle the full range of Super BATES grain lengths within the maximum pressure limits of ±10%. The effective grain length equals twice the actual grain length divided by the number of end surfaces burning. By using a segmented grain with the upstream face of the head end segment inhibited as needed, the number of burning end surfaces can be any integral greater than or equal to one. The resulting pressure variation curves intersect as shown in Figure 20. Over the

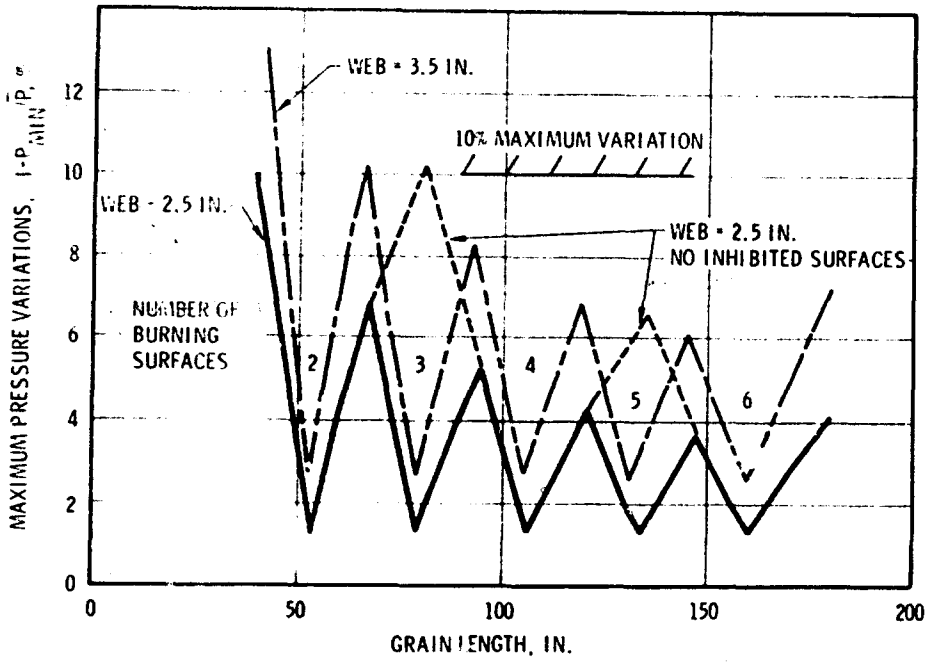

Figure 20. Pressure Neutrality vs Grain Length and Web

05783

range of grain lengths from 50 in. to 180 in. required for Super BATES, the average pressure variation at the nominal web is under 3%. Even at the largest primary web of 3.5 in., the maximum variation is only 10% with the average variation under 5%. Therefore, a 28-in.-diameter grain provides acceptable pressure neutrality characteristics over the full range of grain lengths required for Super BATES. If a particular test requires extremely low pressure variations, the values shown in Figure 20 can be further reduced. Surface histories roughly approximating fractional end surfaces can be achieved by inhibiting part of the head end face of the grain. This approach can be used to achieve reduced pressure variation for virtually all conditions.

3.2 Evaluation of Residence Time Requirements and Geometric Constraints

Chamber residence time could prove to be one of the most significant design parameters for Super BATES. Short chamber residence times are desirable to minimize the performance uncertainty during the ignition and shutdown transients. However, long residence times are desirable to allow the combustion efficiency to achieve the levels found in full-scale motors.

Residence time/performance data indicate that aluminum combustion is essentially complete after residence times as short as 10 to 15 msec. Two typical efficiency curves taken from the NASA Solid Propellant Selection Monograph are shown in Figure 21. Both curves predict small performance changes beyond 20 msec, the minimum allowable residence time for preliminary motor sizing.

Residence time given by the following equation is directly proportional to L*.

$$\tau = \frac{W_{CHAMBER}}{\dot{W}} = \frac{\rho_c \; Vol_c}{\rho^* \; A_T \; V^*} = L^* \left(\frac{\rho_c}{\rho^* \; V^*} \right)$$

For L* in inches and τ in msec, the term in parentheses is typically 0.039 msec/in. for high energy propellants. Average residence time and L* are shown in Figure 22 for a number of large SRMs. Most of the motors have average residence times between 50 and 150 msec and L* between 1,200 and 4,000 in. Actually mean residence time is somewhat misleading. Since most ballistic missiles achieve volumetric loadings of 90%, the residence time at ignition is less than 20% of the residence time when half the propellant has been expended. Therefore, several of the upper-stage motors will have initial residence times of 10 msec to 15 msec where L* effects are beginning to be important.

The Super BATES will be designed to simulate the average chamber environments of large solid motors. The high velocity, short residence time, and erosive burning conditions found in large solid motors at ignition cannot be accurately simulated in Super BATES due to the large pressure drop down the motor and the wide variation in P_c that would occur with the baseline grain design. The severe conditions often found in large solid motors at ignition soon disappear and in general do not have a major impact on average motor performance. Therefore, a Super BATES test designed to match average large motor chamber conditions will provide the most meaningful performance simulation.

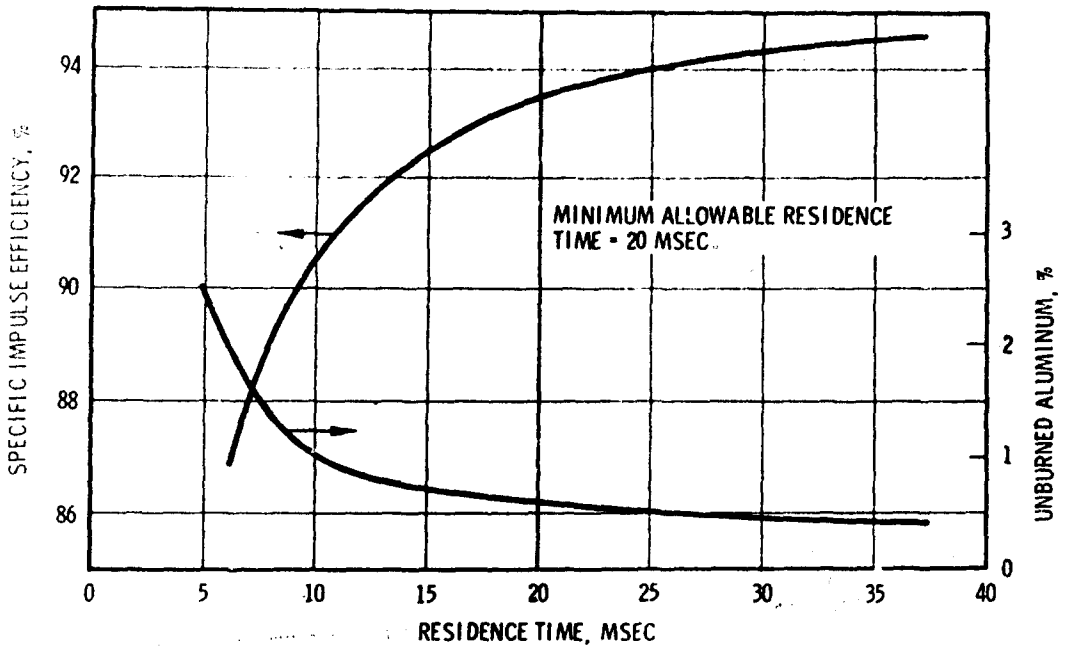

Figure 21. Typical Efficiency vs Residence Time Characteristics

05784

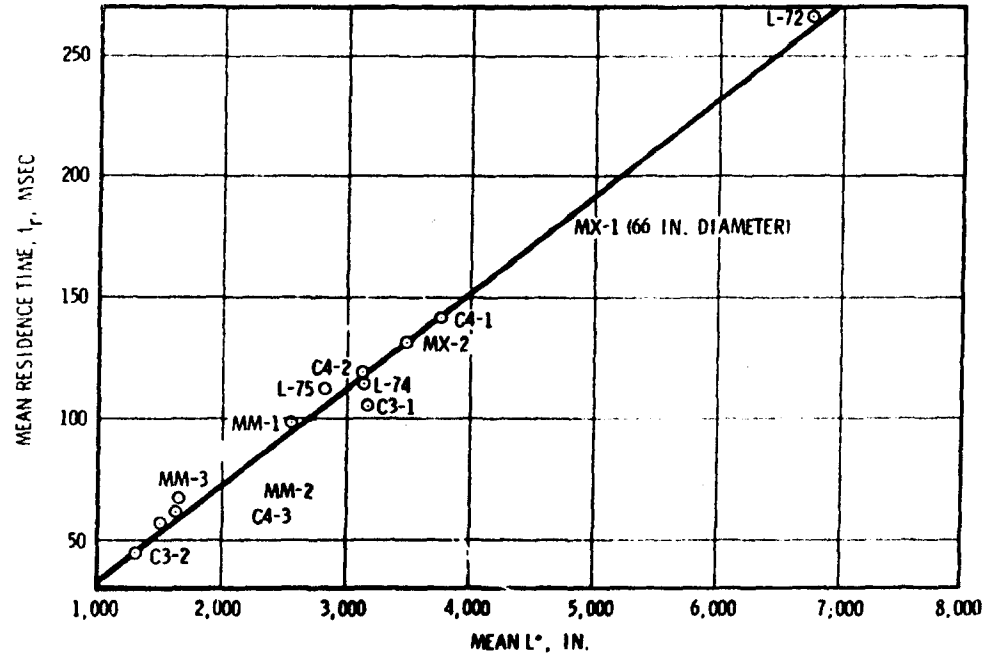

Figure 22. Residence Time and L* for Large SRMs

05785

Motor residence time and average grain dimensions were related for throat diameters from 4 in. to 12 in. For a double end-burning grain with circular port, the propellant volume in a segment is

$$\text{Volume}_{\text{Propellant}} = \frac{\pi}{4}\left[\left(\bar{D}_{\text{PORT}} + \text{Web}\right)^2 - \left(\bar{D}_{\text{PORT}} - \text{Web}\right)^2\right] \times L = \pi\ \bar{D}_{\text{PORT}}\ L\ \text{Web}$$

The average surface area is simply $\pi \bar{D}_{\text{PORT}} L$ which differs from the surface area at half web by at most a few percent. Neglecting the initial gap between grain segments, the chamber volume at half web is

$$\text{Volume}_{\text{Chamber}} = \frac{\pi}{4}\ \bar{D}_{\text{PORT}}^{\,2} \times L + 2\pi\ \bar{D}_{\text{PORT}} \times \text{Web}^2 \times N_{\text{SEGMENTS}}$$

If for conservatism the volume between segments is neglected since most of the gas-flow bypasses this largely stagnant region, then effective chamber volume as shown in Figure 23 equals $\pi/4\ \bar{D}_{\text{PORT}}^{\,2} L$. The mean characteristic length given by the following equation is directly proportional to residence time.

$$\bar{L}^* = \frac{\pi/4\ \bar{D}_{\text{PORT}}^{\,2}\ L}{\pi/4\ D_T^{\,2}} = \left(\frac{\bar{D}_{\text{PORT}}}{D_T}\right)^2 \times L$$

Selecting 20 msec as a minimum residence time determines both a minimum volume for each throat diameter and a minimum average propellant surface area for each average port diameter. As an example, for an 8-in. throat and a 25-in port, the grain length is 51 in. and the surface area is 4,005 in.^2 for a residence time of 20 msec.

Curves of minimum surface area for 20 msec residence time were generated as a function of average port diameter and throat diameter as shown in Figure 24. Constant surface area $D_p \propto D_T^{\,2}$ is given by

$$\tau \propto L^* = \frac{V_C}{A_T} = \frac{\pi/4\ \bar{D}_{\text{PORT}}^{\,2}\ L}{\pi/4\ D_T^{\,2}} = \frac{D_{\text{PORT}}\ A_b}{\pi\ D_T^{\,2}}$$

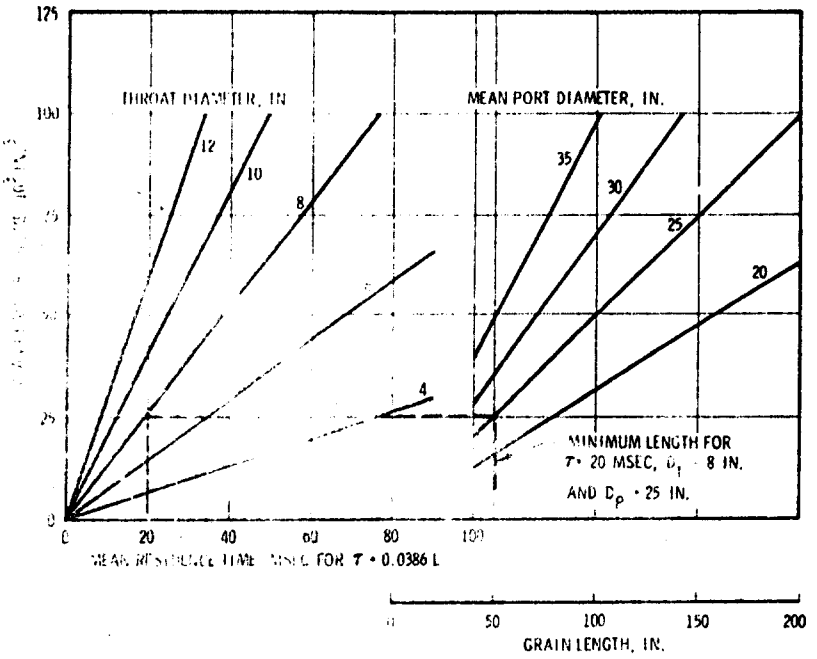

Figure 23. Residence Time/Geometry Trade

05786

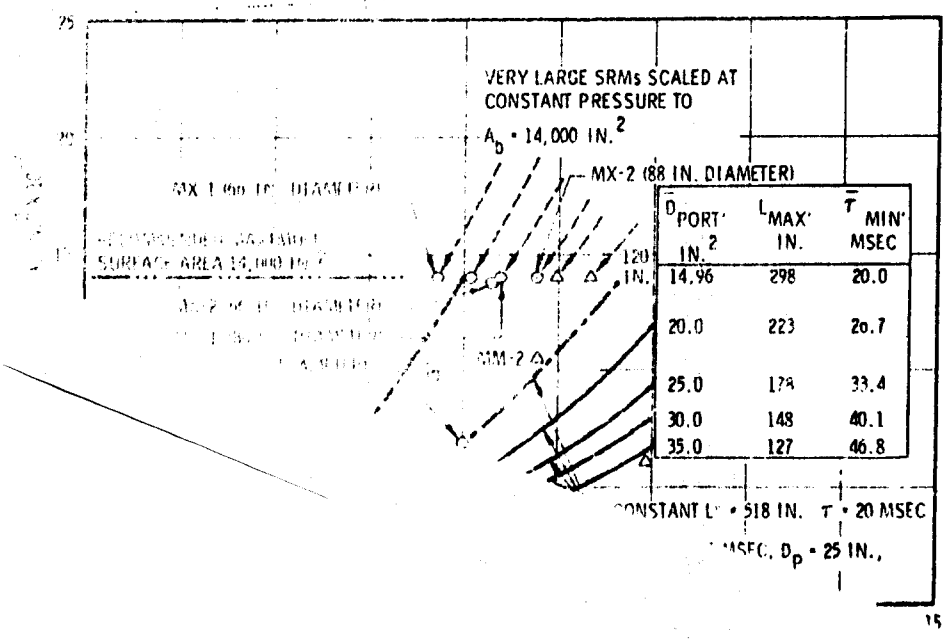

The surface area and throat diameters of candidate large solid rocket motors were located in Figure 24. The dashed line for an average port diameter of 14.96 in. represents the smallest port that could be used for a 20 msec residence time excepting the second-stage Poseidon. The second-stage Poseidon (C3) has a burning rate of roughly 0.6 in./sec (which reduced surface area) at a pressure of 330 psia (which required a large throat). This combination of high burning rate and low pressure was due to the excessively high burning rates of early double base propellants and will not likely be repeated in any future motors for ballistic missiles or large booster applications.

To hold the test motor length to a reasonable value it is necessary to scale down the very large solid motors to the Super BATES propellant and thrust capabilities. Correct chamber pressure should be maintained with throat area and surface area both reduced proportionately. At the maximum large motor burning rate (0.61 in./sec at 1,200 psia for the second-stage 88-in. MX) a surface area of 14,000 $in.^2$ gives a maximum thrust of 150,000 lb. Therefore, 14,000 $in.^2$ was selected as a preliminary maximum surface area for Super BATES. With this surface area the other very large solid motors scale down to flow rates of 300 to 500 lb/sec and throat diameters from 7.4 to 10.7 in. which are within the capabilities of the Super BATES.

An average port diameter around 25 in. looks attractive. The maximum grain length required for a surface area of 14,000 $in.^2$ is 178 in. for a 25-in. average port diameter. The motor becomes excessively long for $\bar{D}_p \leqslant 20$ in. while port diameters of 30 in. or more result in excessively large free volume. Specifically the curves drawn for a residence time of 20 msec in Figure 24 can be redrawn for longer residence times. Since $\tau \alpha \bar{D}_{PORT}$ is constant for a constant surface area, the curves will lie along the dashed 14.96-in. port diameter curve for residence times of 20 msec x $\bar{D}_{PORT}/14.96$. These values tabulated on the figure represent the minimum average residence time (corresponding to the MX-3, 88-in. diameter). All other motors would have longer average residence times. Based on the combustion efficiency curves presented in Figure 21 an average port diameter around 25 in. provides an adequate residence time (33 msec) for aluminum combustion without causing excessively long ignition and shutdown transients.

For purposes of ignition and tailoff transient evaluation a typical upper L^*/D_p bound ($= Ab/\pi D_T^2$) is shown in Figure 24. This upper bound average L* is roughly double the lower bound and encompasses virtually all the current and future large solid motors. These L* bounds do not restrict the operation of the Super BATES, but they do indicate the primary range of operation based on available motor data.

3.3 Aluminum Combustion

A study was conducted to predict the performance losses in the Super BATES attributable to incomplete combustion of the aluminum and to compare the results with similar predictions for the 15 lb and 70 lb BATES motors as well as typical full-scale motors.

A burning rate law for the aluminum agglomerates leaving the propellant surface and a model of the flow field in the chamber are required to predict particle trajectories, residence times, and combustion efficiency.

Burning times for single aluminum particles have been measured in premixed flames at atmospheric pressure,[1,2] in oxygen argon mixtures,[3] and in simulated solid propellant gases[4] at various pressures. Burning times

---

[1] R. Friedman and A. Macek, "Ignition and Combustion of Aluminum Particles in Hot Ambient Gases," Combustion and Flame, Vol. 6, 1962, p. 62.

[2] R. Friedman and A. Macek, "Combustion Studies of Single Aluminum Particles," 9th Symposium (International) on Combustion, Academic Press (New York, 1963) p. 703.

[3] R. P. Wilson, Jr., and F. A. Williams, "Experimental Study of the Combustion of Single Aluminum Particles in O_2/AR," 13th Symposium (International) on Combustion, The Combustion Institute (Pittsburg, 1971) p. 833.

[4] A. Davis, "Solid Propellants: The Combustion of Particles of Metal Ingredients," Combustion and Flame, Vol. 7, 1963, p. 359.

also have been measured for aluminum agglomerates shed from propellant strands using high-speed photography[5,6] and quenched-particle collectors[7]. The data indicate that the time required for a particle of initial diameter d_{P_o} to burn to completion may be expressed as

$$t_b = \frac{d_{P_o}{}^n}{k}$$

where n is between 1.5 and 1.8 and k depends on ambient conditions. The empirical value for n falls between the theoretical values of 2, corresponding to a vapor phase diffusion flame model, and 1, corresponding to a surface combustion model[8]. Values of k determined by various investigators are shown in Table 1. The lowest values of k, obtained at low pressure in experiments with single particles are inapplicable under SRM conditions.

The single-particle measurements of Davis were made in oxidizer-rich gases at pressures from 300 to 3,000 psia and temperatures from 1,300° to 3,200°K, and show an increase in burning rate with increasing pressure and temperature. The measurements on the burning rate of agglomerates from propellant strands by Pokhil and Belyaev are somewhat lower than Davis's data, probably due to the lower oxidizer level. Belyaev studied the effect of oxidizing species concentration and concluded that

$$k = C_1 \left(\alpha_{H_2O} + \alpha_{CO_2}\right)^{0.9}$$

---

[5] P. F. Pokhil, V. S. Logachev, and V. M. Mal'tsev, "Coalescence of Metal Particles During the Combustion of Metallized Ballistic Compositions and Fuel-Oxidizer Mixtures," Fizika Goreniya i Vzryva, Vol. 6, 1970, p. 80.

[6] P. G. Willoughby, UTC measurements, unpublished.

[7] A. F. Belyaev, B. S. Ermolaev, A. I. Korotkov, and Y. V. Frolov, "Combustion Characteristics of Powdered Aluminum," Fizika Goreniya i Vzryva, Vol. 5, 1969, pp. 207-217.

[8] R. Friedman and A. Macek, "Ignition and Combustion of Aluminum Particles in Hot Ambient Gases," ibid.

TABLE 1. ALUMINUM PARTICLE BURNING RATE CONSTANTS

Source	K, $cm^{1.8}$ sec^{-1}*	Condition
Friedman and Macek (see ref. 1 and 2)	0.004 to 0.006	Single particle, low P, C_3H_8/O_2 flame
Wilson and Williams (see ref. 3)	0.004	Single particle, low P, O_2/A_r, laser ignition
Davis (see ref. 4)	0.017 to 0.026	Single particle, high P, AP/PF strand
Pokhil (see ref. 5)	0.009 to 0.013	High P, Al/AP/PF strand
Belyaev (see ref. 6)	0.009	High P, Al/AP/PMM strand
UTC (see ref. 7)	0.08	High P, Al/AP/PBAN strand
UTC (see ref. 10)	0.15	Motor data, high P, Al/AP/PBAN propellant

* For consistency, the k values have been adjusted to correspond to a value of n = 1.8 so that $t_b = \frac{d_{p_o}^{1.8}}{k}$

where C_1 is a constant and α_{H_2O} and α_{CO_2} are the mass fractions of H_2O and CO_2.

UTC's cinematographic observation of aluminum agglomerates burning on and near the surface of a propellant strand suggest a value for k of 0.08 $cm^{1.8}$ sec^{-1},(9) almost a factor of 10 greater than observed by Pokhil and Belyaev. The reason for this apparent discrepancy is not understood at present but may be due to velocity lags and a more highly oxidizing environment in the UTC experiments.

Significantly higher values of k derived from motor data are inferred from the experimental combustion efficiencies and measured initial agglomerate size

[9] P. G. Willoughby, ibid.

distributions,[10] as shown by the last entry in Table 1. Somewhat higher burning rates might be expected in actual SRM cavities because of the higher temperature and more severe radiation environment than in the case of a propellant strand. Particle fragmentation also may occur in the motor cavity, leading to an apparent increase in agglomerate burning rate.

The aluminum burning rate in the motor cavity may also be influenced significantly by the velocity lag between the aluminum agglomerates and the accelerating gases. If the lag results in a sizable gas velocity relative to the burning particles, the flame zone would move closer to the aluminum surface, thereby causing greater heat transfer to the particle and a greater vaporization rate.

The wide discrepancies in aluminum burning rates shown in Table I were investigated to determine their effect on the design of the Super BATES. Lower values of k favor longer residence times to achieve complete combustion. Burning rate constants in the 0.009 to 0.013 $cm^{1.8}$ sec^{-1} range reported in the Russian literature by Pokhil and Belyaev could make accurate simulation of large motor combustion environments extremely difficult to achieve by ballistic test motors with comparatively low L*. Therefore, the probable range of the aluminum burning rate constant must be determined to appropriately select the size of the Super BATES and predict the level of scaling required to match large motor performance.

The size of the aluminum agglomerates leaving the propellant surface is one of the primary variables determining the fraction of unburned aluminum leaving the chamber. The mass median particle diameter, <d>, is defined by

$$\frac{\int_0^{<d>} D^3 N(D)\, dD}{\int_0^{\infty} D^3 N(D)\, dD} = 1/2$$

[10] R. W. Hermsen, and P. G. Willoughby, Unpublished measurements of aluminum agglomerate size for two propellants at various pressures; calculations of motor combustion efficiency; and comparison with experimental data. November, 1969.

where N(D) dD is the number fraction of particles with $\int_0^\infty N(D)\, dD = 1$ correlated with propellant burning rate for a wide range of solid propellants as shown in Figure 25. A preliminary trade study showed that burning rates of candidate large ballistic missiles fell mostly in the range 0.3 to 0.5 in./sec. The mass median aluminum particle diameter ranges from roughly 180μ at 0.3 in./sec to 100μ for propellant burning rates above 0.55 in./sec. A mass median particle diameter of 196μ was selected to investigate the largest particle size that would be expected over the Super BATES burning rate range of 0.3 to 1.0 in./sec.

The effects of unburned aluminum on specific impulse efficiency were determined using UTP-15,908 propellant (Figure 26). UTP-15,908 is a high energy class 7 aluminized composite propellant developed at UTC during the C4 third-stage ADP. The effects of unburned aluminum fraction (F) on both optimum and vacuum specific impulse efficiency shown in Figure 26 are typical of high energy propellants. The measured aluminum particle distribution for UTP-15,908 was shifted to match the 196 micron mass median particle size based on the lowest Super BATES burning rate of 0.3 in./sec.

The size and residence time distributions of aluminum particles were integrated over the burn time to obtain an accurate evaluation of aluminum combustion efficiency. For selected grain configurations, the velocity distribution can be expressed in closed form solution to determine a particle residence time distribution for a given mean residence time neglecting particle lags. Selecting the initial aluminum particle size distribution and the particle burning rate constant, k, the instantaneous unburned aluminum fraction (F) and specific impulse efficiency ($\eta_{I_{sp}\text{-COMBUSTION}}$) can be calculated. The latter can be integrated over the burn time to obtain the average specific impulse efficiency due to incomplete aluminum combustion in the chamber.

The predicted combustion efficiencies of the BATES and Super BATES test motors were compared with the second-stage Minuteman as a function of the aluminum burning rate constant, k, for a mass median particle diameter of 196 microns. Simulation of the second-stage Minuteman in the Super BATES required an L* near the lower bound identified in Figure 24 and therefore

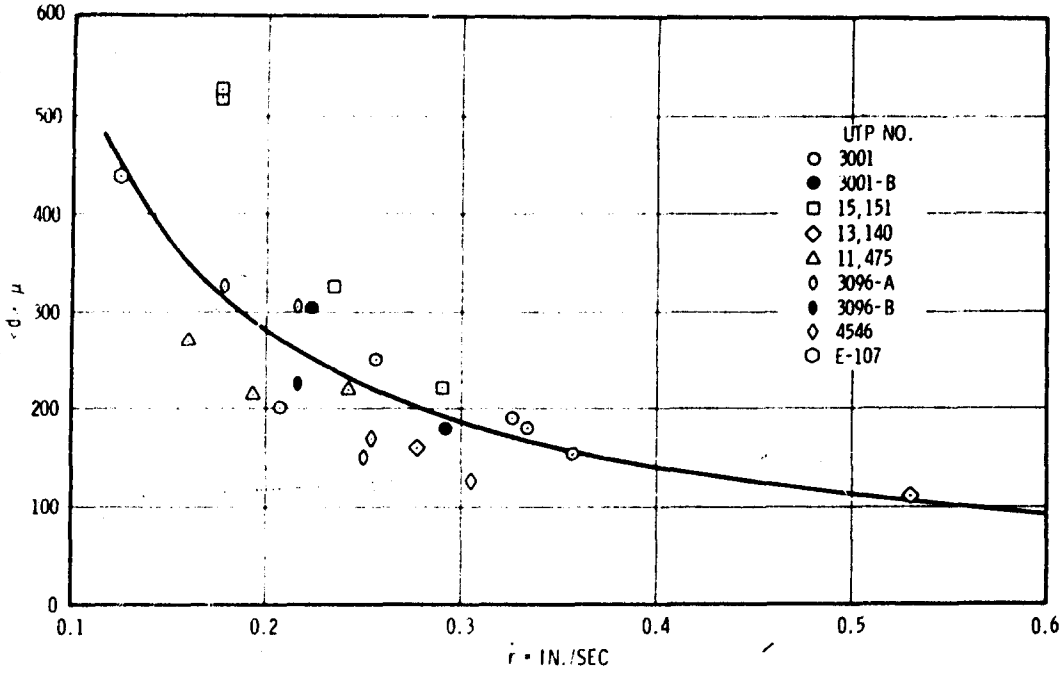

Figure 25. Mass Median Aluminum Agglomerate Diameter vs Propellant Burning Rate

05788

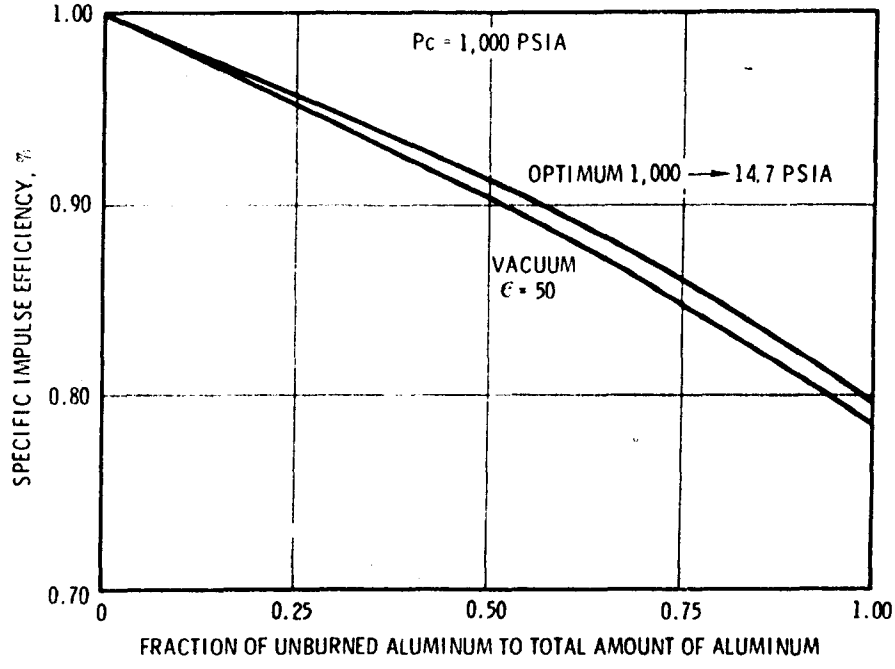

Figure 26. Effect of Unburned Aluminum on Specific Impulse Efficiency for UTP-15,908

05790

provides a critical test of the ability of Super BATES to model combustion efficiency in large solid motors.

Combustion efficiency predictions shown in Figure 27 for four test motors (25-in. and 20-in. average port diameter Super BATES, 70-lb and 15-lb BATES) exhibit similar I_{sp} efficiency characteristics. Since these test motors all have relatively low volumetric loading, they tend to operate at nearly constant combustion efficiency throughout the firing and are more sensitive to the value of k.

The efficiency characteristic for the second-stage Minuteman is typical of highly loaded operational motors. Operational motors often have low initial values of L* (under 10 in.) even though their average L* may be quite high. Therefore, a substantial fraction of the aluminum leaves the chamber unburned during the initial low L* period and very little aluminum leaves the chamber

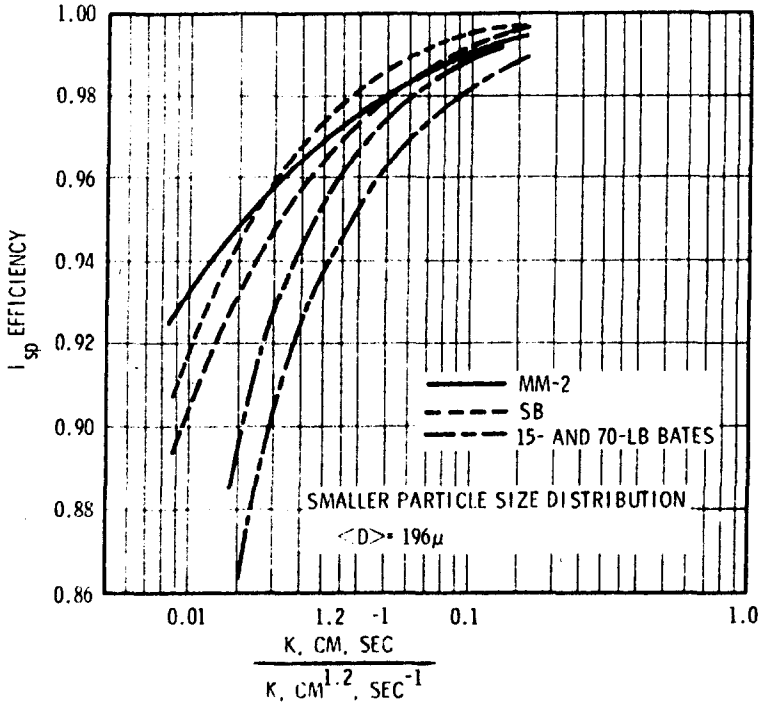

Figure 27. Effect of Incomplete Aluminum Combustion on I_{sp} Efficiency

05789

unburned during the remainder of the firing. This wide fluctuation in L* makes the combustion efficiency less sensitive to the value of k in an operational motor than in a constant L* test motor.

Combustion efficiency losses are excessively large at the low values of k (0.009 to 0.013) reported by the Russian investigators Pokhil and Belyaev. Although these experiments provide interesting insights into aluminum combustion, they apparently did not accurately model the environment in large solid motors. The radiation level in a large motor chamber would be much more intense. More important, the high flow velocities in actual motors could substantially increase the mass transfer rate and make k a function of the motor flow field. Although the equivalent value of k must lie above the Russian values, the state of knowledge on aluminum combustion is not sufficient at this time to precisely define the equivalent aluminum burning rate constant.

The Super BATES should be designed to match the combustion efficiency of large solid motors over a wide range of k values to minimize the uncertainties owing to present incomplete knowledge of aluminum combustion. A simulation by Super BATES (with 25-in. average port diameter) of the second-stage Minuteman would equal or exceed the full-scale motor combustion efficiency for values of k greater than about 0.03. A scaledown of 0.3% to 0.5% would be required to match full-scale motor efficiency. However, increased aluminum combustion in the high velocity flow fields of large motors at ignition could raise the predicted second-stage Minuteman efficiency curve and match the efficiency of a Super BATES with a 25-in. average port diameter over a wide range of k. A Super BATES simulation (with 20-in. average port diameter) of the second-stage Minuteman would fall below the full-scale motor performance over a wide range of k and consequently would not be as attractive a design as one with 25-in. average port diameter in terms of matching large motor combustion efficiency.

The BATES motors fall considerably below the combustion efficiency of large motors at low values of the aluminum burning rate constant, k. These extremely low predicted values of I_{sp} efficiency for values of k between 0.009 and 0.013 reported in the Russian literature further support the higher

values of k derived by UTC from motor firings. Even at higher values of k, the combustion efficiencies of the 70-lb BATES and especially the 15-lb BATES fall well below the level achieved in full-scale motors. The Super BATES equals or exceeds full-scale motor performance over a wide range of k values and should be able to offer a significant improvement in modeling large motor combustion efficiency.

3.4 Ignition and Shutdown Transients

An ignition and shutdown transient study was conducted to determine the effects of motor design variables on transient impulse and ensure that the Super BATES could meet the 5% transient impulse fraction specified in the SOW.

The total impulse during the ignition and tailoff transients is determined by a number of factors as shown in Figure 28. Chamber L* and propellant burning rate exponent are the most important factors. Flame propagation rate

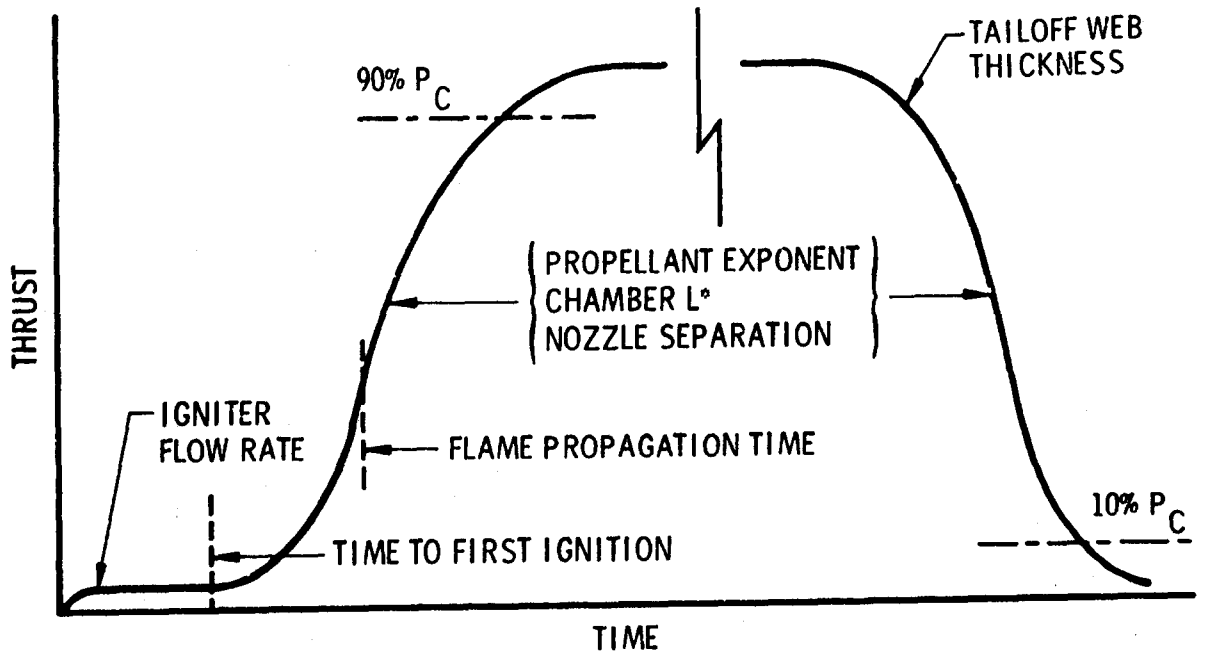

Figure 28. Factors Affecting Ignition and Tailoff Transients

05791

plays a significant role in determining the shape of the ignition transient, and tailoff web thickness is important during tailoff. The extent of separated flow during ignition and tailoff contributes disproportionately to the performance error due to the comparatively large uncertainty of the thrust with separated flow.

The upper and lower $L^* \sqrt{D_{PORT}}$ values generated in the previous section were used to establish the range of anticipated chamber L* for ignition and tailoff with a 2.5-in. web. The values of L* shown in Figure 29 only increase proportionally to grain diameter (not D_G^2) because motor length decreases with increasing port diameter. These L* bounds do not limit the operation of the Super BATES. They merely indicate the most probable range based on the large solid motors evaluated.

Propellant ignition characteristics were based on established engineering relationships. Igniter mass flux requirements depend on the propellant, but an ignition mass flux of 9.2 lb/ft^2-sec (corresponding to a convective flux of

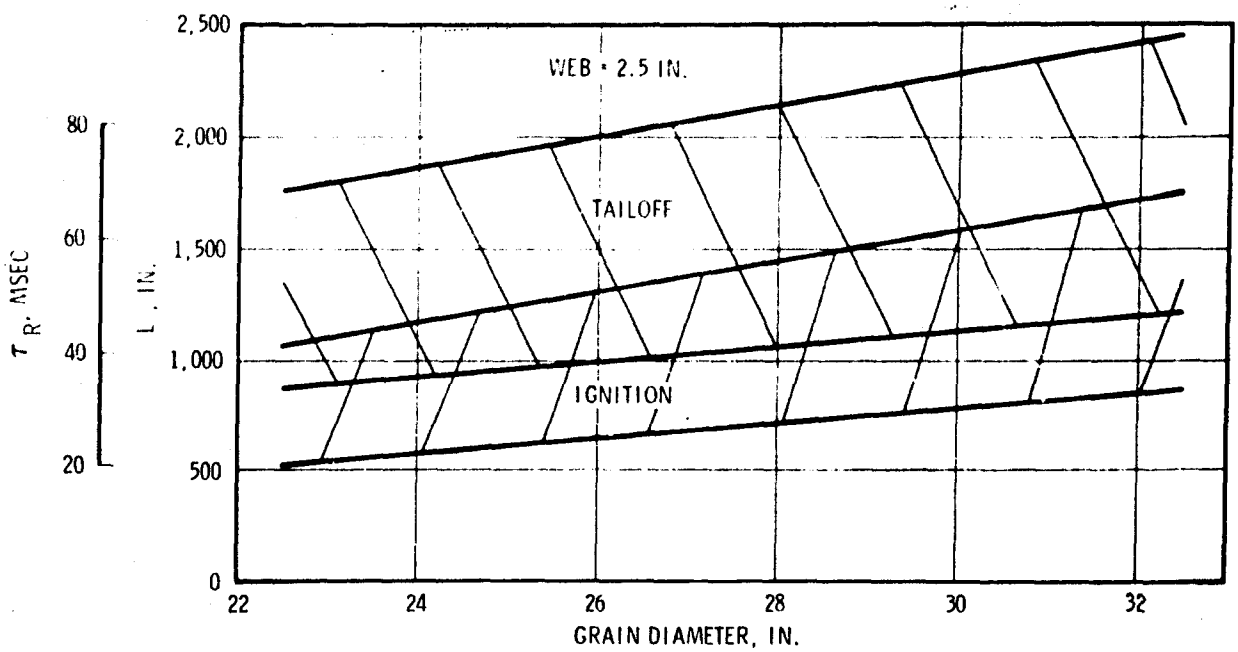

Figure 29. L* vs Grain Diameter Upper and Lower Bounds for Ignition and Tailoff

05792

100 cal/cm^2-sec) is typical for an ignition delay of 50 msec. A flow rate of 15.4 lb/sec was used based on an average port diameter of 25 in. with a 2.5-in. web. For this size port, a flame propagation time of 50 msec is a conservative value for the maximum 180-in. motor length.

Flow separation effects were examined in considerable detail to define the fraction of ignition transient impulse contributed by separated flow. The Super BATES specification limits the transient impulse fraction to 5%. If, for instance, the performance error generated by the transients is to be no more than the accuracy of the thrust stand (0.1%), then the average performance uncertainty during the transients must not exceed 2%. Based on the pressure neutrality study presented earlier a 2% uncertainty seems reasonable unless there is a large impulse uncertainty generated by the separated flow region. Equations for nozzle separation pressure were collected from several sources. The results are shown in Figure 30 together with exit pressure curves for various expansion ratios for γ = 1.15. The equations defining nozzle separation pressure are in reasonably good agreement. The expression for nozzle separation expansion ratio depends on propellant γ. For γ = 1.2 it lies much closer to the other curves.

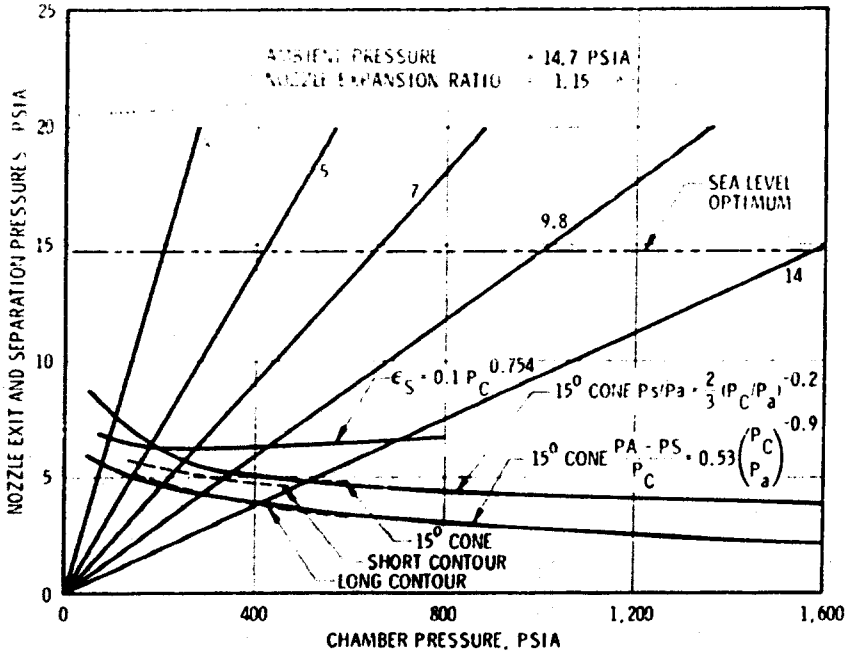

Figure 30. Nozzle Flow Separation Predictions

05793

The equation $P_S/P_A = 2/3\ (P_C/P_A)^{-0.2}$ was used to determine nozzle separation and to evaluate separated impulse fraction. The results shown in Figure 31 indicate that for large L* where transient response is important, only 7% to 9% of the ignition impulse (0.2% to 0.3% of the motor impulse for a 5% transient impulse fraction) occurs in the region of separated flow. Therefore, even relatively large uncertainties in separated flow performance (e.g., 10%) will not significantly contribute to the total performance inaccuracy (~0.025%).

Ignition transient characteristics were determined as a function of chamber L* and equilibrium pressure for a burning rate exponent of 0.65 as shown in Figure 32. Two parameters were calculated: (1) $T_{90\%}$, defined as the time from igniter signal to 90% of equilibrium pressure and (2) τ, defined as the equivalent time at full thrust (i.e., $I_{T_{IGNITION}}/F_{EQUILIBRIUM}$). Both parameters are linear with L* and increase only slightly with pressure primarily due to the decreasing igniter contribution.

The effect of residual web on the tailoff characteristics was investigated to determine grain dimensional accuracy requirements. Tailoff impulse was calculated from full pressure to 10% of full pressure. The governing parameter is residual web/burning rate at full pressure as shown in Figure 33. At a nominal burning rate of 0.5 in./sec, a tailoff web of 0.015 in. is required to hold $W/\dot{r}$ to 0.030 sec. The equivalent time τ, increases by roughly 0.02 sec from $W/\dot{r}$ of 0.030 to 0.060 sec which would require an additional motor burn time of 0.4 sec to maintain a 5% transient impulse fraction. Tailoff characteristics are replotted as a function of burnout L* in Figure 34.

The Super BATES can maintain a 5% transient impulse fraction with a grain diameter of 28 in. The time required ($T\delta$) for the transient impulse to equal any desired fraction (δ) of the total impulse is simply $(\tau_{IGNITION} + \tau_{TAILOFF})/\delta$ or in this case $T_{5\%} = 20 \times (\tau_{IGNITION} + \tau_{TAILOFF})$. The value of $T_{5\%}$ is shown in Figure 35 for the typical upper and lower L* bounds shown in Figure 29. For grain diameters of 28 in. or less, the primary burn time range of 4 to 7 sec is sufficient to keep the transient impulse fraction below 5%.

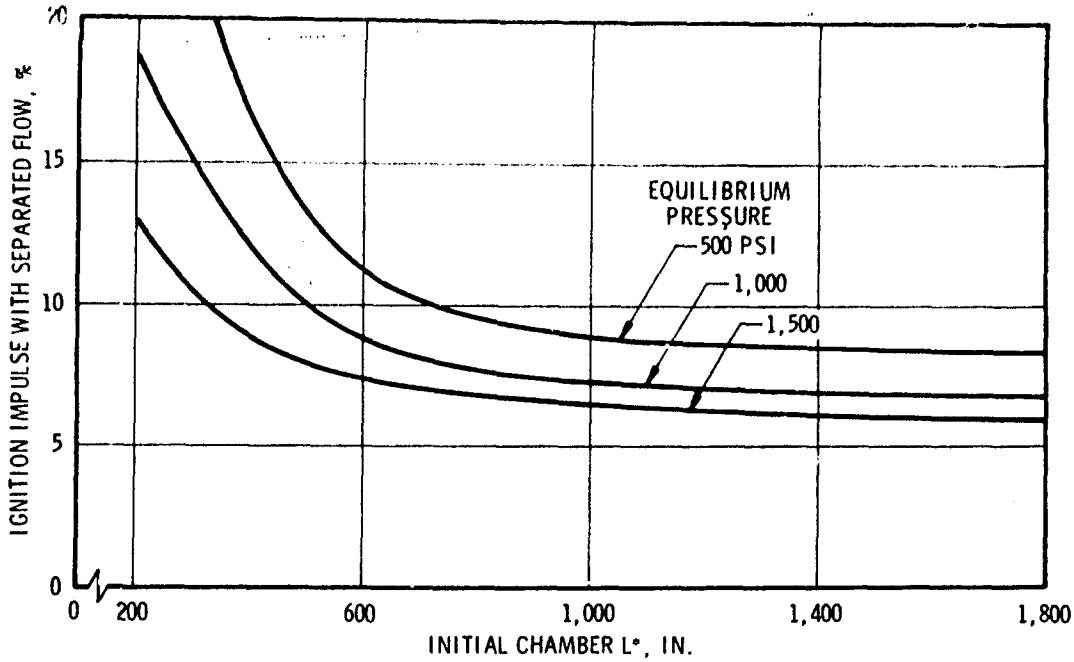

Figure 31. Separation Impulse Fraction vs L*

05794

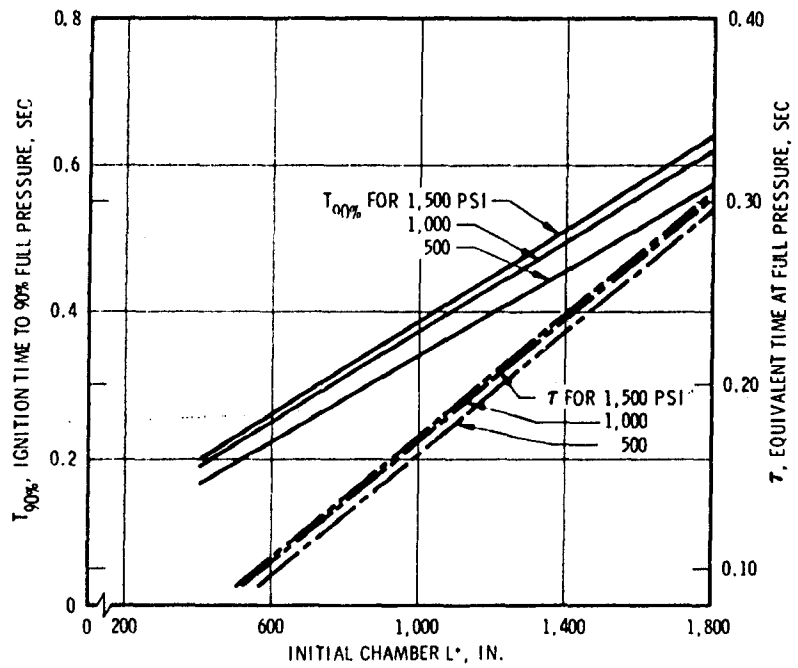

Figure 32. Ignition Times vs Initial L*

05795

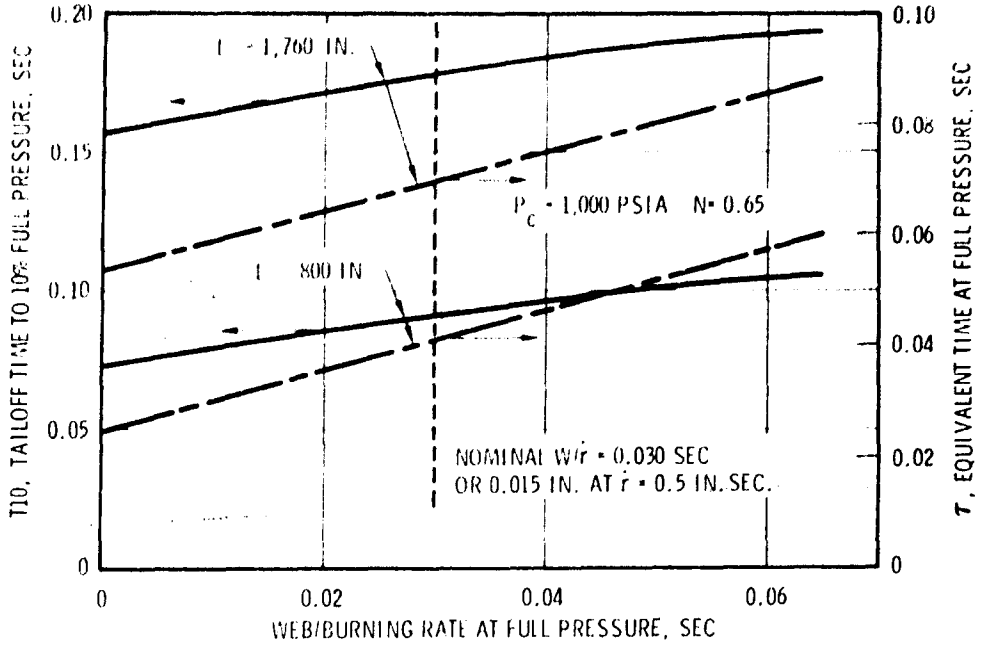

Figure 33. Tailoff Times vs Residual Web

05796

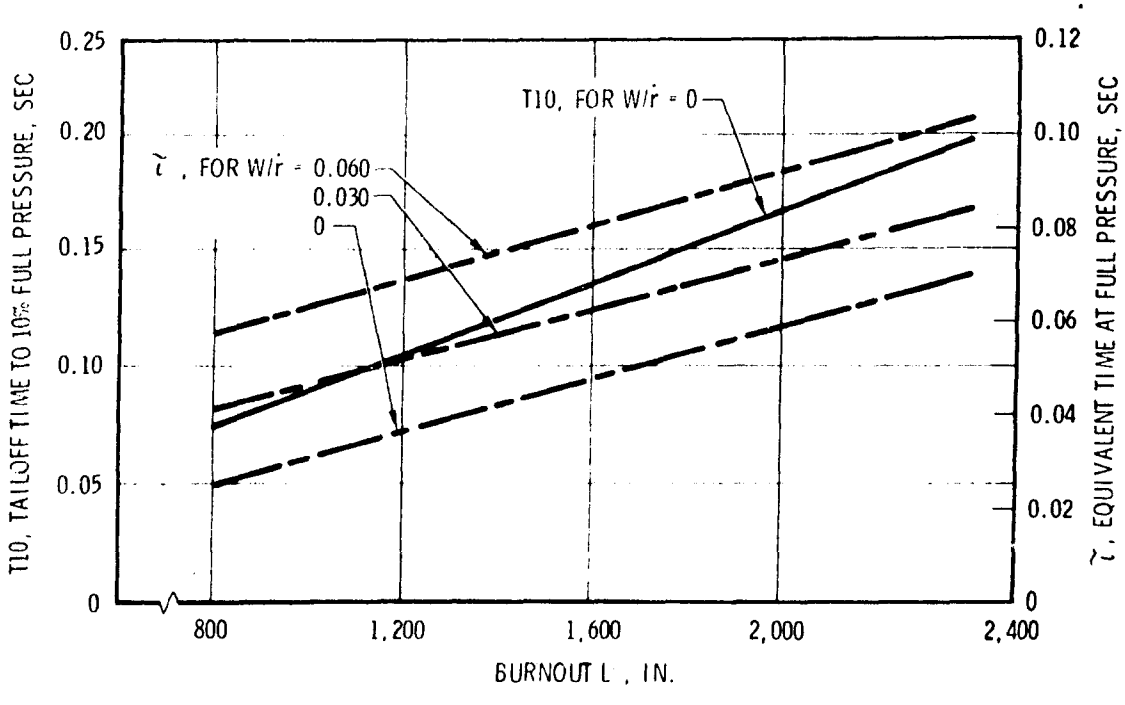

Figure 34. Tailoff Times vs Burnout L*

05797

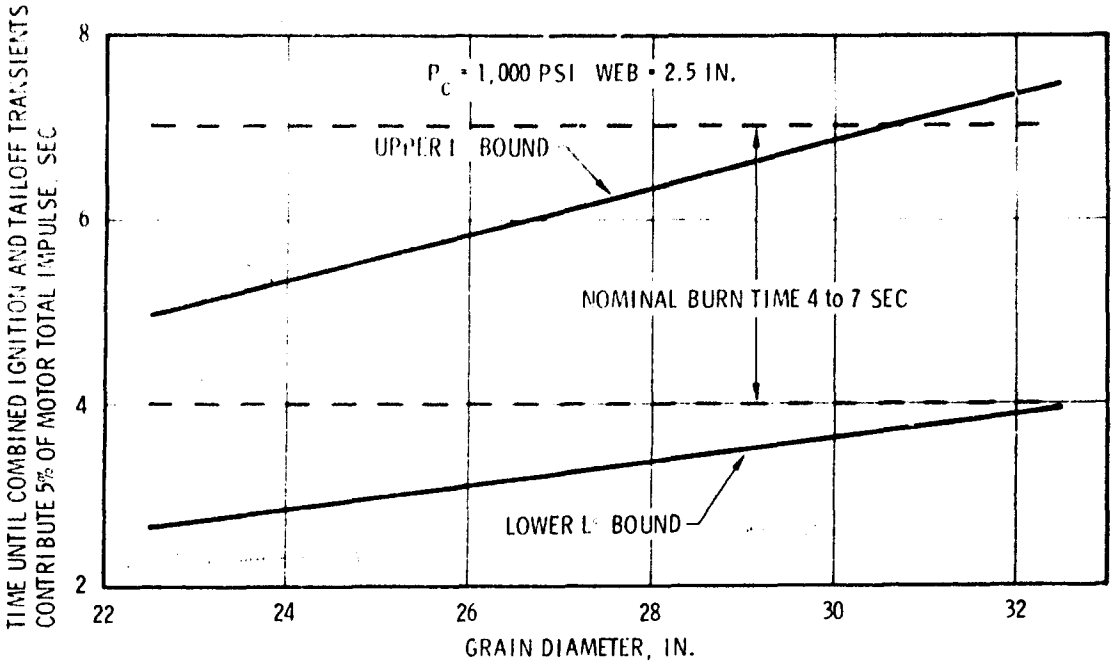

Figure 35. Required Burn Time for 5% Transient Impulse

05798

3.5 Erosive Burning Effects

A study was conducted to determine the burning rate augmentation due to propellant mass flux as a function of grain diameter. Burning rate increases when a high mass flux of gas passes parallel to the burning propellant surface. This effect, erosive burning, stems from increased heat transfer from the flame to the propellant surface. Erosive burning can become very significant when a high mass flux is coupled with a low burning rate. Under these conditions, the heat transfer is high due to the convective flow across the surface associated with the high mass flux and the low blowing from the surface since the burning rate is low. The increased heat transfer can enhance the burning rate considerably.

Several expressions have been developed to predict erosive burning. The expression developed by Lenoir and Robillard has been used extensively. Their expression combines aspects of fluid flow and heat transfer and postulates a central core of flowing combustion gases surrounded by transpiring propellant walls. The augmentation of burning rate

is related to convective heat transfer and is, therefore, dependent on the combustion gas flow rate. Their erosive burning rate expression is

$$\dot{r}_b = \dot{r} + \alpha \frac{G^{0.8}}{D^{0.2}} e^{\frac{-\beta \dot{r}_b \rho}{G}}$$

where

α, β = empirical constants

G = mass flux in port parallel to burning surface

D = hydraulic diameter of the port

$$\therefore \frac{\Delta \dot{r}}{\dot{r}} = \frac{\alpha G^{0.8}}{\dot{r} D^{0.2}} e^{\frac{-\beta \rho \dot{r}}{G}}$$

since $G = \dot{m}/A_p$

and $A_p = \frac{\pi}{4} D^2$

and $D = \frac{4 \text{ port area}}{\text{wetted perimeter}}$

Figure 36 shows the relationship between α and the hydraulic bore diameter. It shows that α continuously decreases with increasing bore diameter. β was assumed equal to 70 for all motors. While this figure only shows diameters up to 7.5 in., data for the Titan III show that $\alpha = 0$ for a 40-in. bore diameter. In this study a linear interpolation was used to arrive at an α for the range of Super BATES bore diameters.

Ballistic analysis of the proposed Super BATES grain configurations indicate erosive burning is not significant. If the mass flow rate/mass flux of the Super BATES is increased, erosive burning will be analyzed and accounted for as described above.

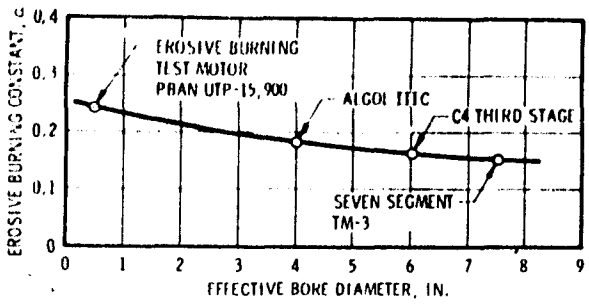

$$\dot{r} = r_0 + \left[\frac{\alpha_G^{0.8}}{D^{0.2}} \times e^{-\frac{(\beta r \rho)}{G}} \right]$$

ρ = PROPELLANT DENSITY

α = EROSIVE BURNING CONSTANT

β = EROSIVE BURNING CONSTANT (70)

$G = \dot{m}/A_p$

D = EQUIVALENT BORE DIAMETER

r_0 = BURNING RATE AT THE LOCAL CHAMBER PRESSURE

$\dot{r}$ = TOTAL BURNING RATE

Figure 36. Relationship Between α and Hydraulic Bore Diameter

05799

3.6 Heat Transfer Analysis

An analysis was conducted to determine the expected total heat transfer loss to candidate chamber and nozzle insulation materials as a function of exposure time. The thermal analysis was performed with gas properties characteristic of high energy aluminized propellants (T_F = 6,090°F, c* = 5,400 ft/sec, γ = 1.14) at a chamber pressure of 1,500 psia with an 8-in. throat and a flow rate of 450 lb/sec to determine the heat losses under a severe thermal environment. Conventional filled rubber insulation was used in the chamber. Heat fluxes in the chamber were primarily radiative even in the aft closure region due to the relative low flow velocities that existed throughout the motor. The baseline nozzle incorporated erosion resistant materials which minimized contour change during the firing even at high pressure permitting multiple reuse of the throat package to minimize nozzle cost. The submerged portion of the nozzle was insulated with silica phenolic and was exposed to the largely radiative chamber environment. The throat package consisted of carbon phenolic entrance and exit sections with pyrolytic graphite washers in the throat backed up with graphite. The exit cone was silica phenolic. Convection dominated the heat transfer in the throat and exit portions of the nozzle.

Thermal response characteristics basically fell into two classes as shown in Figure 37. The low thermal conductivity materials in the chamber and the submerged portion of the nozzle reached their equilibrium surface temperatures in a few seconds. The largely radiative environment minimized the net heat flux. variations since reradiation from the insulation was still small at surface temperatures around 3,000°F. These fast response materials are essentially in thermal equilibrium within the nominal 5-sec burn time and account for 75% of the total heat loss. The materials in the nozzle throat have relatively high thermal conductivities, respond more slowly, and reach higher surface temperatures than the chamber insulation. Furthermore, with a largely convective environment, there is a significant reduction in net heat flux as the surface temperatures increase. The response of the silica phenolic exit cone is not appreciably faster than the throat due to the low heat fluxes and completely convective environment in the exit cone. These slow response materials do not reach thermal equilibrium within the burn time of the Super BATES. However, the slow response materials in the nozzle account for only about 25% of the total heat loss, and although they may transfer twice the equilibrium heat flux over a 5-sec firing, the weighted effect on overall motor thermal equilibrium is only about 15%.

Total heat losses for a 5-sec firing were calculated for different areas of the motor to determine the magnitude and distribution of heat losses. The total heat losses shown in Table 2 are 174,400 BTU split 60/40 between the chamber and the nozzle. Heat losses to the fast response materials account for roughly 75% of the total. Heat losses to the submerged portion of the nozzle (for maximum submergence) and to the

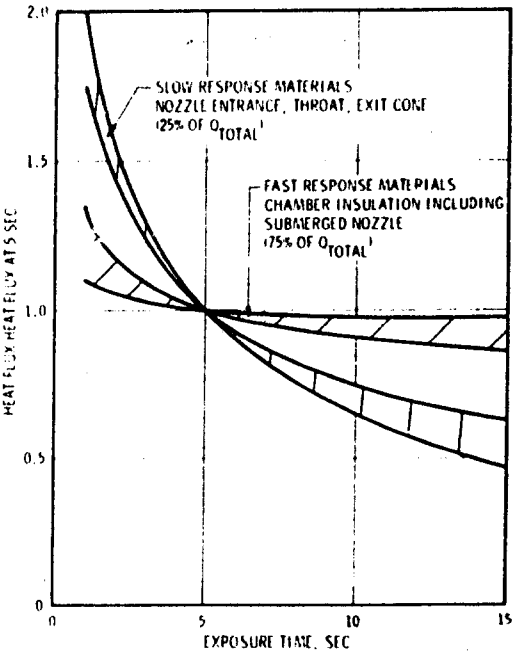

Figure 37. Super BATES Thermal Equilibrium Characteristics

05801

TABLE 2. SUPER BATES HEAT LOSS DISTRIBUTION

T_F = 6,090°F P_c = 1,500 psia D_{TH} = 8.0 in.

Location	Total Heat Flow, 5 sec, BTU		
	Fast Response	Slow Response	
Forward closure	17,300		
Slots – 3 segments	24,700		
Aft closure	22,800		
Forward case – 15 in exposed	37,600		
Total chamber	102,400		102,400
Submerged nozzle	30,500		
Throat package		20,100	
Exit cone		21,400	
Total nozzle	30,500	41,500	72,000
Total motor	132,900	41,500	174,400
Fraction	76.2%	23.8%	

forward case (for grains 15 in. shorter than the case segment length) together account for 1/3 of the total. Use of 30-in. half segments for the case is extremely beneficial in minimizing heat losses for grain lengths that do not match the integral 60-in. segment lengths. An adapter ring in the nozzle to achieve flexible nozzle submergence is also important to model both two-phase flow and heat losses due to submergence.

Heat losses were evaluated in terms of their fraction of available energy and their contribution to specific impulse efficiency. An ideal nozzle converts roughly 42% of the available chamber enthalpy into directed kinetic energy for γ = 1.15 and an expansion from 1,000 psia to 14.7 psia as:

$$\frac{\Delta h}{H_o} = \frac{V_{EXIT}^2}{2 g_c H_o} = \frac{C_p T_o \left[1 - \left(\frac{P_{EXIT}}{P_c}\right)^{\frac{\gamma-1}{\gamma}}\right]}{C_p T_o [1]}$$

For a typical theoretical optimum specific impulse of 270 sec, 1,507 BTU/lb are converted into kinetic energy in the expansion process as shown below.

$$\Delta h \ 1{,}000/14.7 = \frac{g \ I_{sp}^{2}}{2J} = 1{,}507 \text{ BTU/lb for } I_{sp} \ 1{,}000/14.7 = 270 \text{ sec}$$

From these two equations the fraction of available energy lost due to heat transfer can be estimated. For a propellant flow rate of 450 lb/sec at 1,500 psia through an 8-in. throat, the total heat loss shown in table II was 174,400 BTU for a 5-sec firing. If 42% of the thermal energy is available for conversion to kinetic energy then the loss in available energy is roughly 2.2% as shown below.

$$\frac{\Delta h \ Q}{\Delta h \ 1{,}000/14.7} = \frac{(174{,}400 \times .42)/(450 \times 5)}{1{,}507} = \frac{32.6}{1{,}507} = 2.2\%$$

Since $I_{sp} \alpha \Delta h$ the predicted specific impulse loss due to heat transfer ($I_{sp} \alpha \Delta h$) would be about 1% which is roughly half of the loss experienced in a typical 70 lb BATES firing. Based on the heat flow distribution shown earlier, the average heat losses in Super BATES should be no higher than 25% above the equilibrium rate for a full-scale motor. If the full-scale motor grain exposes large areas of the case early in the firing, the full-scale heat loss fraction could easily exceed the value for Super BATES. Therefore, a performance scale-up in Super BATES of at most 0.25% would be expected to match full-scale motor heat losses.

ABBREVIATIONS AND SYMBOLS

a	burning rate constant, $\dot{r} = aP_c^n$
A	aft
Ab	burning surface area
ADP	advanced development program
AP	ammonium perchlorate
A_t	throat area
B/A	ratio of outer grain radius to inner radius
BTU	sometimes classified, depending on use
c	constant
C*	characteristic exhaust velocity
C_F	thrust coefficient
C_H	local heat transfer coefficient
Cp	coolant heat capacity
d	inside grain diameter
D	outside grain diameter
Dp	port diameter
dpo	initial diameter of particle
D_T	throat diameter
EDP	engineering development program
f	final value
F	thrust
g	acceleration of gravity
i	initial value
I_{sp}	theoretical specific impulse
K	constant
L	length of grain
L*	characteristic length
L/D	length to diameter (ratio)
m	mass flux exponent
$\dot{m}$	mass flow rate
max	maximum value
min	minimum value
n	pressure exponent, $\dot{r} = aP_c^n$

NASA	National Aeronautics and Space Administration
P	pressure
PBAN	polybutadiene-acrylic acid-acrylonitrile
P_c	chamber pressure
PF	perchloryl fluoride
P_n	pressure neutrality = maximum $\frac{\lvert P - \bar{P} \rvert}{\bar{P}}$
Q	effective heat release in the secondary chamber
$\dot{r}$	burning rate
R	duct radius
Re	Reynolds number
RT	room temperature
SOW	statement of work
SRM	solid rocket motor
t	time
TA	triacetin
t_b	burn time
T_c	chamber temperature
T_F	flame temperature
tr	average residence time
T_W	wall temperature
Ug	velocity of gas
UTC	United Technology Center
V_c	Poisson's ratio for motor case
w	distance burned back
W_b	web of propellant
ζ	L/D
η	$A_b \sqrt{A_b}$
λ	D/d = grain B/A
μ	burnback for maximum surface area
π	3.14159
ρ	propellant density

REFERENCES

Friedman, R., and A. Macek, "Ignition and Combustion of Aluminum Particles in Hot Ambient Gases," Combustion and Flame, Vol. 6, 1962, p. 92.

Friedman, R., and A. Macek, "Combustion Studies of Single Aluminum Particles," 9th Symposium (International) on Combustion, Academic Press, New York, 1963, p. 703.

Wilson, R. P., Jr., and F. A. Williams, "Experimental Study of the Combustion of Single Aluminum Particles in O_2/AR," 13th Symposium (International) on Combustion, The Combustion Institute, Pittsburgh, 1971, p. 833.

Davis, A., "Solid Propellants: The Combustion of Particles of Metal Ingredients," Combustion and Flame, Vol. 7, 1963, p. 359.

Pokhil, P. F., V. S. Logachev, and V. M. Mal'tsev, "Coalescence of Metal Particles During the Combustion of Metallized Ballistic Compositions and Fuel-Oxidizer Mixtures," Fizika Goreniya i Vzryva, Vol. 6, 1970, p. 80.

Willoughby, P. G., unpublished UTC measurements.

Belyaev, A. F., B. S. Ermolaev, A. I. Korotkov, and Y. V. Frolov, "Combustion Characteristics of Powdered Aluminum," Fizika Goreniya i Vzryua, Vol. 5, 1969, pp. 207-217.

Hermsen, R. W., and P. G. Willoughby, unpubiished measurements of aluminum agglomerate size for two propellants at various pressures; calculations of motor combustion efficiency; and comparison with experimental data. November 1969.

Statham LABORATORIES

Instrument Notes

Number 20 *December 1951*

A major portion of our activity at Statham Laboratories is concerned with the dynamic response characteristics of instruments. The article presented in this issue of Instrument Notes has been found to be of great value to our staff members. The results apply not only to accelerometers, but also to any instruments whose behavior may be described by a linear second order differential equation.

With the kind permission of the authors and the Bureau of Standards, we are reprinting the paper for the benefit of those readers who may have missed the original publication in the Journal of Research of the National Bureau of Standards.

Response of Accelerometers to Transient Accelerations*

By Samuel Levy and Wilhelmina D. Kroll

Curves and tables are shown for the response of accelerometers to transient exciting accelerations. Three types of acceleration-time relations are considered. When plotted, they have square, triangular, and half-sine-wave shapes. The natural periods of the accelerometers for which the computations were made were approximately one, one-third, and one-fifth of the duration of the acceleration pulse. The damping coefficients of the accelerometers were 0, 0.4, 0.7, and 1.0 times the critical values. It is indicated that, to obtain an accuracy of better than 5 percent of the peak acceleration in measuring acceleration pulses having the general characteristics of the triangular or sinusoidal pulses, an accelerometer must have a natural period of about one-third the duration of the acceleration pulse, and a damping constant of about 0.4 to 0.7 of the critical value.

I. Introduction

Accelerometers are widely used to measure oscillatory and transient vibrations.

The fidelity with which these instruments respond in the case of oscillatory stimuli has been thoroughly studied [1, pp. 61 to 70]. It is found that, when the damping is between 0.6 and 0.7 of the critical value and the natural period of the accelerometer is less than about half of the period of the applied acceleration, the accuracy is satisfactory.

In the case of excitation of the accelerometer by a transient vibration, only scattered information is available regarding the reliability of the response obtained. Weiss [2] gives the response to a triangular pulse of acceleration for an accelerometer whose natural period is 0.3 the duration of the pulse and whose damping is 0, 0.3, and 0.7 of the critical value. He also gives the response to a suddenly applied constant acceleration for accelerometers with a damping ratio of 0, 0.3, 0.7, and 1.0 times the critical value. Welch [3] has determined, on the Westinghouse transient analyzer, the response to several kinds of impulses of a 50 c/s single-degree-of-freedom shock measuring instrument having various amounts of damping. On the basis of these scattered data, and information for undamped accelerometers derived by Frankland [4], Biot and Bisplinghoff [5], and others, it has been common practice to assume that an accelerometer will be acceptable in a given

* Reprinted from JOURNAL OF RESEARCH OF THE NATIONAL BUREAU OF STANDARDS, Vol. 45, No. 4, October, 1950. Research Paper 2138.
Printed in U. S. A.

application if its damping is 0.6 to 0.7 of the critical value and if its natural period is less than about half of the duration of the acceleration pulse.

The curves presented in this report were computed to obtain more systematic information regarding the accuracy of damped accelerometers in measuring transient phenomena.

II. Theory

The usual accelerometer is a single-degree-of-freedom mechanical system. Such a system is shown in figure 1. Means are provided to indicate the relative motion x of the internal mass with respect to the frame. This relative motion is taken as a measure of the acceleration, d^2y/dt^2, of the frame.

The equation of motion for the mass m, figure 1, is

$$m\frac{d^2z}{dt^2}+c\left(\frac{dz}{dt}-\frac{dy}{dt}\right)+k(z-y)=0. \tag{1}$$

With

$$z=x+y, \tag{2}$$

eq 1 becomes

$$m\frac{d^2x}{dt^2}+c\frac{dx}{dt}+kx=-m\frac{d^2y}{dt^2}, \tag{3}$$

$$\frac{d^2x}{dt^2}+\frac{c}{m}\frac{dx}{dt}+\frac{k}{m}x=-\frac{d^2y}{dt^2}. \tag{4}$$

We wish to know how faithfully the response x of the accelerometer reproduces the time history of the applied acceleration d^2y/dt^2 for pulses of acceleration of finite duration and arbitrary shape. To give the analysis a wider range of usefulness, eq 4 is written in dimensionless form by making the following substitutions:

$$\left.\begin{aligned} a&=\left(\frac{d^2y}{dt^2}\right)\Big/\left(\frac{d^2y}{dt^2}\right)_{max}\\ \tau&=t/T\\ \xi&=-kx/m\left(\frac{d^2y}{dt^2}\right)_{max}\\ D&=c/2\sqrt{mk}=c/c_c\\ R&=2\pi\sqrt{m/k}/T \end{aligned}\right\} \tag{5}$$

where

$c_c=2\sqrt{mk}$, critical value of damping coefficient,

T=duration of acceleration pulse to be measured,

$2\pi\sqrt{m/k}$="undamped" period of accelerometer,

$\left(\frac{d^2y}{dt^2}\right)_{max}$=peak value of acceleration.

Substituting eq 5 into eq 4 gives

$$\left(\frac{R}{2\pi}\right)^2\frac{d^2\xi}{d\tau^2}+\frac{RD}{\pi}\frac{d\xi}{d\tau}+\xi=a. \tag{6}$$

For a relatively high frequency accelerometer, R is a small number. Under these circumstances, the first two terms in eq 6 become negligible, and the dimensionless response ξ is equal to the dimensionless acceleration a. As R becomes larger, the first and second terms start to have an effect. The primary effect of the second term is to introduce a time lag between the response ξ and the acceleration a. The primary effect of the first term is to tend to make the response ξ oscillate in value above and below the value of the acceleration a.

III. Results

Equation 6, giving the relation between the dimensionless responses ξ and the dimensionless acceleration a, was integrated numerically for three values of the natural period ratio having approximately the values, R=1, 1/3, 1/5; for four values of the damping ratio, D=0, 0.4, 0.7, 1.0; and for the three time-histories of acceleration pulse shown in figure 2. Numerical integration, instead of direct integration, was used to give results that could be plotted directly. Small variations from the nominal values of R were used for convenience in computing. These values of R are given in table 1. A spot check of the results was made using the analytical solution of eq 6.

The numerical integration was carried out using a time increment of $1/(20\pi)$ times the natural period of the accelerometer. Eight decimal figures were used in the computation.

The results are plotted in figures 3 to 11. Figures 3, 4, and 5 give the response to a sinusoidal pulse of acceleration. Figure 3 gives the response when the natural period is about equal to the duration of the acceleration pulse. Figures 4 and 5 give similar results with the natural period about one-third and one-fifth, respectively, of the duration of the acceleration pulse. In each figure, the dimensionless applied acceleration, a, is shown by a dotted line; the response, ξ, with the damping ratio D=0 by curve 1; with D=0.4 by curve 2; with D=0.7 by curve 3; and with D=1.0 by curve 4.

Figures 6, 7, and 8 show the response to a triangular pulse of acceleration, and figures 9, 10, and 11 show the response to a rectangular pulse. In each figure, the set of curves brings out the effect of varying only the damping ratio D.

IV. Discussion

It is evident from an inspection of the figures that for none of the accelerometers considered does the time history of the dimensionless response ξ coincide with the time history of the dimensionless accelera-

TABLE 1.—*Error for accelerometers and acceleration pulses considered*

(1)	(2)	(3)	(4)	(5)	(6)	(7)	(8)
		Error				Plotted	
R	D	$\xi_{max}-a_{max}$	$\lvert\xi-a\rvert_{max}$	After shift $\lvert\xi-a\rvert_{max}$	$\Delta\tau$	Figure	Curve
HALF-SINE-WAVE PULSE							
1.014	0	0.74	1.36	1.36	0.17	3	1
1.014	0.4	.15	0.62	0.24	.22	3	2
1.014	.7	−.05	.67	.18	.25	3	3
1.014	1.0	−.18	.65	.24	.29	3	4
0.338	0	.17	.35	.35	.07	4	1
.338	0.4	.02	.20	.06	.05	4	2
.338	.7	.00	.24	.06	.07	4	3
.338	1.0	−.03	.32	.10	.11	4	4
.203	0	.10	.20	.20	.01	5	1
.203	0.4	.07	.12	.06	.02	5	2
.203	.7	.00	.15	.03	.04	5	3
.203	1.0	−.01	.20	.06	.06	5	4
TRIANGULAR PULSE							
1.014	0	0.51	1.29	1.29	0.15	6	1
1.014	0.4	.00	0.56	0.21	.21	6	2
1.014	.7	−.20	.51	.20	.22	6	3
1.014	1.0	−.32	.57	.32	.25	6	4
0.338	0	.17	.43	.43	.04	7	1
.338	0.4	.00	.18	.06	.07	7	2
.338	.7	−.06	.17	.06	.08	7	3
.338	1.0	−.11	.22	.12	.08	7	4
.203	0	.10	.25	.25	.01	8	1
.203	0.4	.00	.11	.03	.04	8	2
.203	.7	−.04	.10	.04	.05	8	3
.203	1.0	−.07	.13	.07	.07	8	4
SQUARE PULSE							
1.014	0	1.00	1.00	1.00	0.04	9	1
1.014	0.4	0.25	1.00	0.49	.19	9	2
1.014	.7	.05	1.00	.53	.22	9	3
1.014	1.0	−.01	1.00	.50	.28	9	4
0.334	0	1.00	1.00	1.00	.01	10	1
.334	0.4	.25	1.00	0.50	.06	10	2
.334	.7	.05	1.00	.50	.08	10	3
.334	1.0	.00	1.00	.50	.10	10	4
.203	0	1.00	1.00	1.00	.02	11	1
.203	0.4	0.25	1.00	0.50	.03	11	2
.203	.7	.05	1.00	.50	.04	11	3
.203	1.0	.00	1.00	.50	.06	11	4

tion a. In many cases, however, the coincidence can b markedly improved by considering the response curves to be shifted a small distance to the left. They can also be improved, in those cases where oscillatory response is present, by fairing a line through the oscillatory response. Both of these methods of record improvement are commonly employed.

The errors of the various accelerometers for the acceleration pulses considered are given in table 1. In columns 1 and 2, respectively, are given the accelerometer characteristics: R, ratio of natural period to pulse duration; and D, ratio of damping constant to critical value.

In column 3, table 1, is given the difference between the maximum value of dimensionless response, ξ, and the maximum value of the dimensionless applied acceleration, a. The error varies from 0 to 100 percent.

In column 4, table 1, is given the largest absolute value of the difference $\xi-a$ where ξ and a are evaluated at the same dimensionless time. The error varies from a minimum of 10 percent to a maximum of 136 percent.

In column 5, table 1, is given the largest absolute value of the difference $\xi-a$ after shifting the ξ curve to the left by the amount $\Delta\tau$ given in column 6. The error in this case is typical of the usual way of interpreting accelerometer records. This error varies from a minimum of 3 percent to a maximum of 136 percent. If only accelerometers with damping are considered ($D>0$), the largest error is 32 percent when the accelerometer is subjected to acceleration pulses of triangular or sinusoidal time histories.

On the basis of the few cases investigated, an optimum value of damping is indicated to be between 0.4 and 0.7 of the critical value. It is also indicated that, to obtain an accuracy of better than 5 percent of the peak acceleration in measuring acceleration pulses having the general characteristics of the triangular or sinusoidal pulses, an accelerometer must have a natural period of less than about one-third the duration of the acceleration pulse.

Acknowledgment is due to the Bureau of Aeronautics, Navy Department, whose research projects on vibration pickups have provided the impetus for the work presented in this paper. The authors also extend thanks to L. W. Roberson and I. Smith for assistance in computing the many response curves and preparing the figures and table.

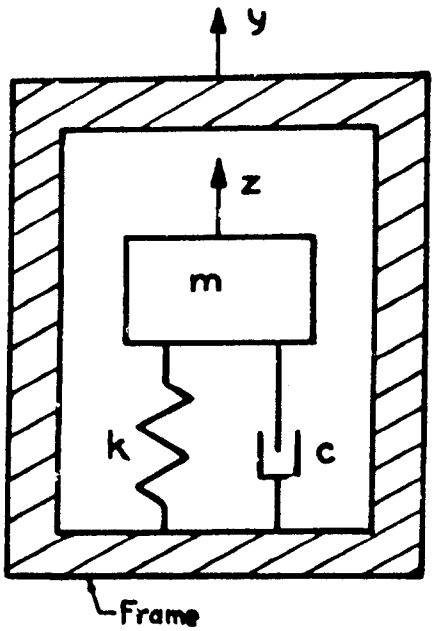

FIGURE 1. *Single-degree-of-freedom system representing accelerometer.*

Displacement of frame is y, displacement of interna lmass is z, relative displacement of internal mass with respect to frame is $x=z-y$.

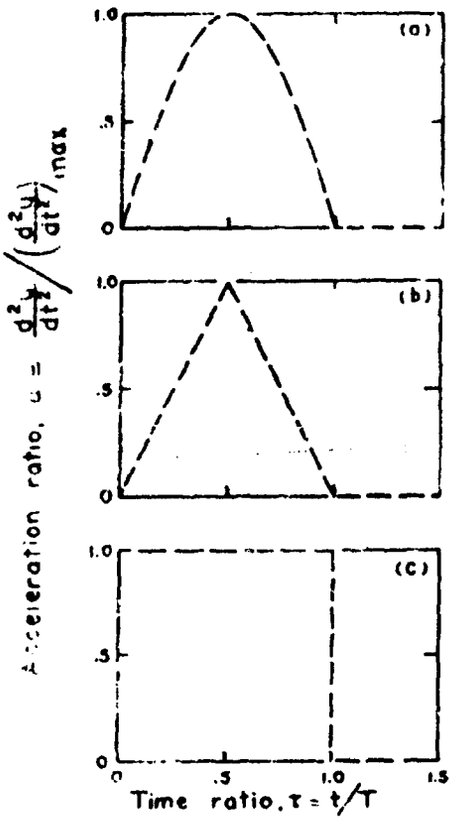

FIGURE 2. *Pulses of acceleration for which integration was carried out: (a) half-sine-wave pulse, (b) triangular pulse, (c) square pulse.*

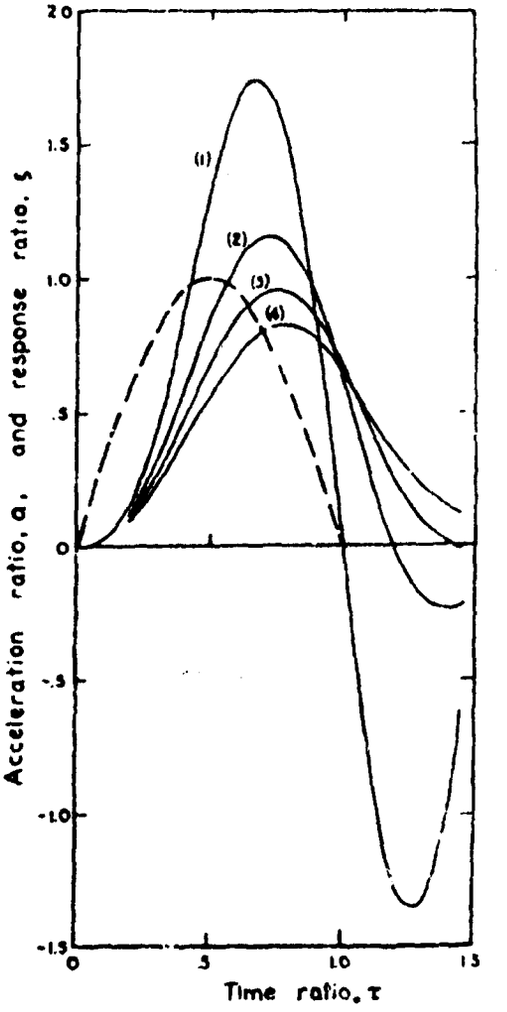

FIGURE 3. *Response to a half-sine-wave pulse of acceleration, dashed curve, of an accelerometer whose natural period is about equal to the duration of the pulse, R=1.014.*

Curve (1), damping coefficient zero, D=0; curve (2), damping coefficient 0.4 of the critical, D=0.4; curve (3), damping coefficient 0.7 of the critical, D=0.7; curve (4), damping coefficient equal to the critical, D=1.0.

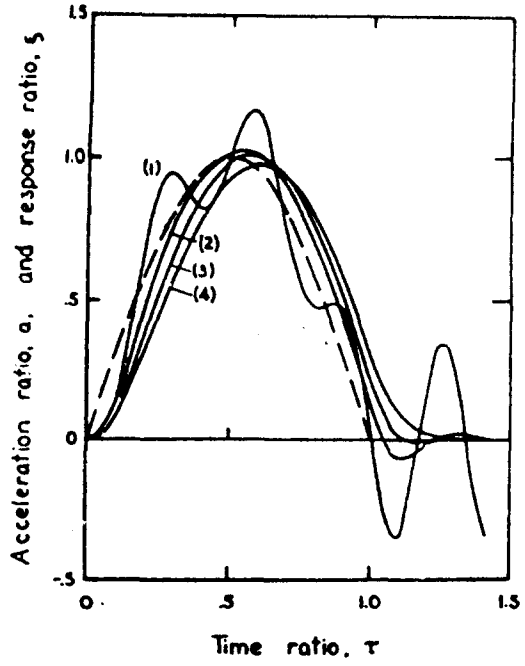

FIGURE 4. *Response to a half-sine-wave pulse of acceleration, dashed curve, of an accelerometer whose natural period is about equal to one-third of the duration of the pulse, $R=0.338$.*

Curve (1), damping coefficient zero, $D=0$; curve (2), damping coefficient 0.4 of the critical, $D=0.4$; curve (3), damping coefficient 0.7 of the critical, $D=0.7$; curve (4), damping coefficient equal to the critical, $D=1.0$.

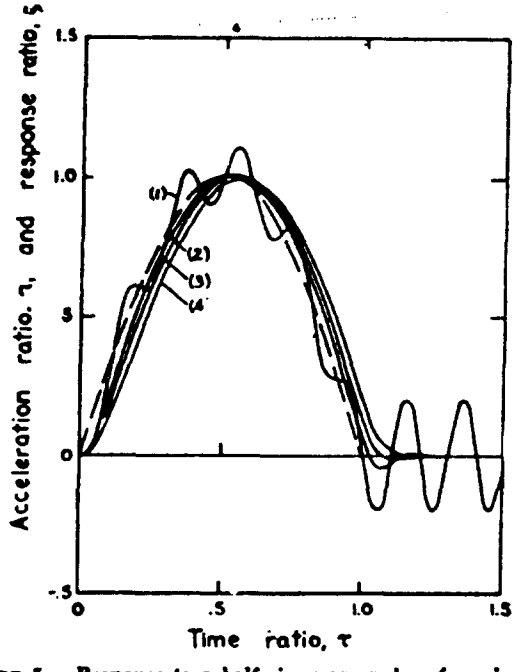

FIGURE 5. *Response to a half-sine-wave pulse of acceleration, dashed curve, of an accelerometer whose natural period is about equal to one-fifth of the duration of the pulse, $R=0.203$.*

Curve (1), damping coefficient zero, $D=0$; curve (2), damping coefficient 0.4 of the critical, $D=0.4$; curve (3), damping coefficient 0.7 of the critical, $D=0.7$; curve (4), damping coefficient equal to the critical, $D=1.0$.

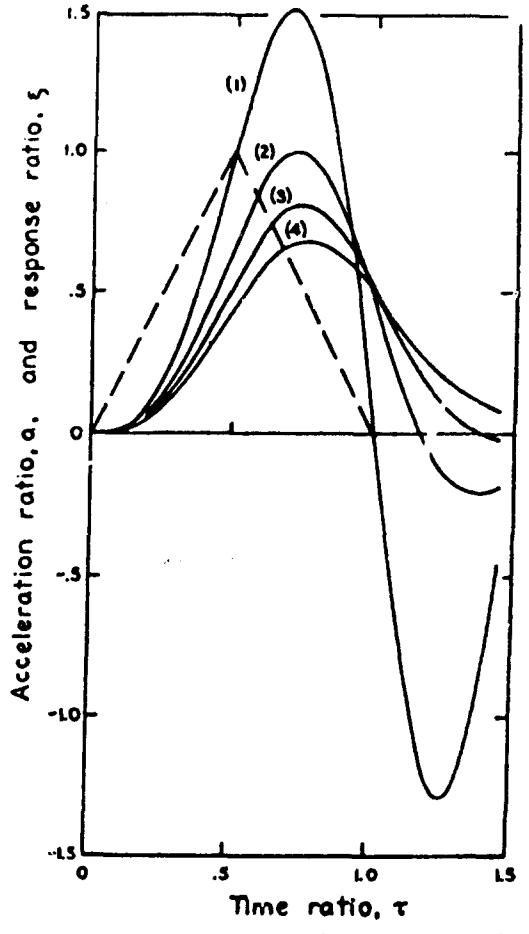

FIGURE 6. *Response to a triangular pulse of acceleration, dashed curve, of an accelerometer whose natural period is about equal to the duration of the pulse, $R=1.014$.*

Curve (1), damping coefficient zero, $D=0$; curve (2), damping coefficient of the critical, $D=0.4$; curve (3), damping coefficient 0.7 of the critical, $D=0.7$; curve (4), damping coefficient equal to the critical, $D=1.0$.

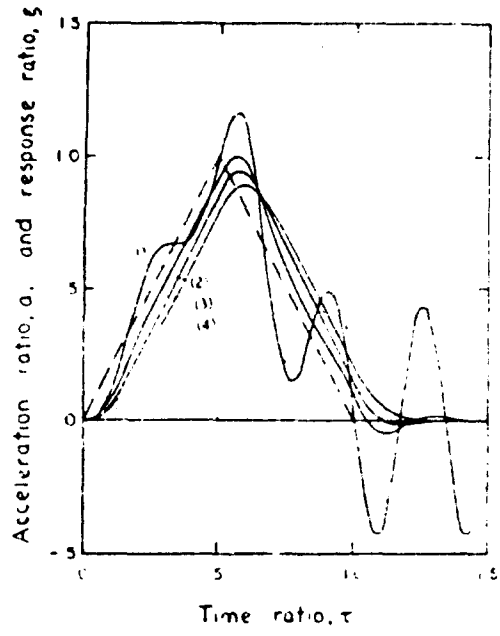

FIGURE 7. *Response to a triangular pulse of acceleration, dashed curve, of an accelerometer whose natural period is about equal to one-third of the duration of the pulse, R = 0.333.*

Curve (1), damping coefficient zero, $D=0$, curve (2), damping coefficient 0.4 of the critical, $D=0.4$; curve (3), damping coefficient 0.7 of the critical, $D=0.7$, curve (4), damping coefficient equal to the critical, $D=1.0$.

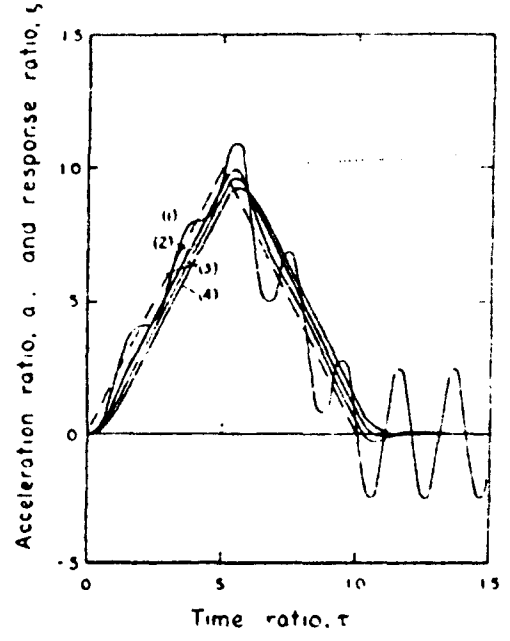

FIGURE 8. *Response to a triangular pulse of acceleration, dash curve, of an accelerometer whose natural period is about equal to one-fifth of the duration of the pulse, R = 0.203.*

Curve (1), damping coefficient zero, $D=0$, curve (2), damping coefficient 0.4 of the critical, $D=0.4$; curve (3), damping coefficient 0.7 of the critical, $D=0.7$, curve (4), damping coefficient equal to the critical, $D=1.0$.

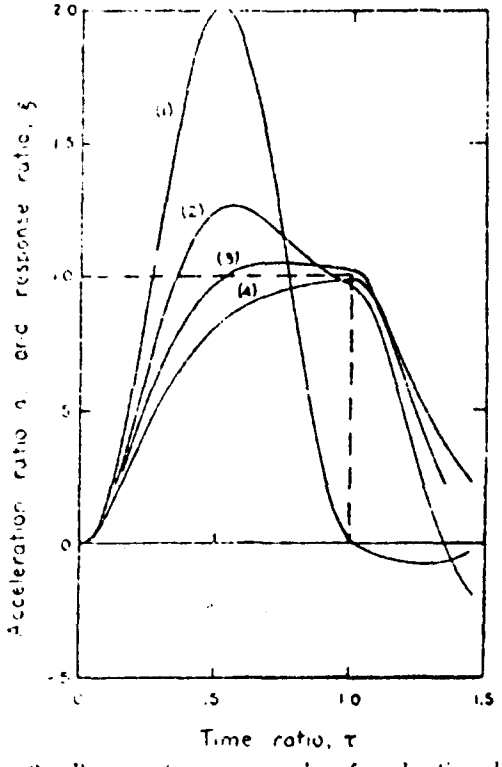

FIGURE 9. *Response to a square pulse of acceleration, dashed curve, of an accelerometer whose natural period is about equal to the duration of the pulse, R = 1.014.*

Curve (1), damping coefficient zero, $D=0$, curve (2), damping coefficient 0.4 of the critical, $D=0.4$, curve (3), damping coefficient 0.7 of the critical, $D=0.7$, curve (4), damping coefficient equal to the critical, $D=1.0$.

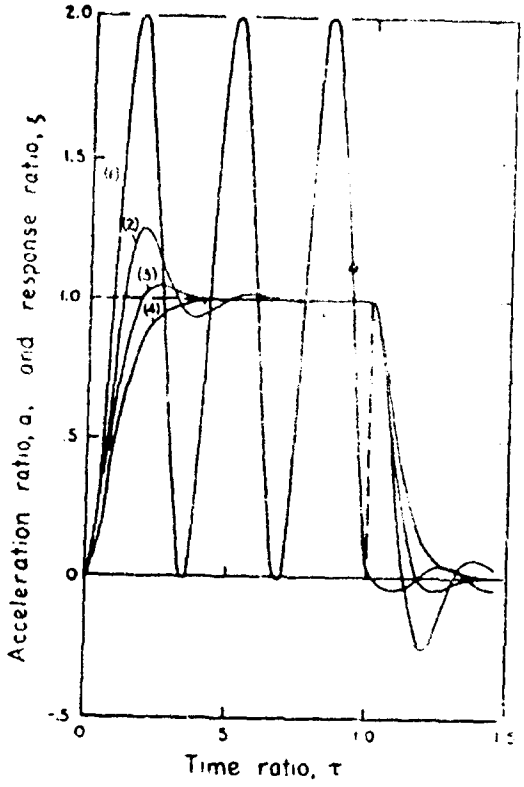

FIGURE 10. *Response to a square pulse of acceleration, dashed curve, of an accelerometer whose natural period is about equal to one-third of the duration of the pulse, $R=0.334$.*

Curve (1), damping coefficient zero, $D=0$; curve (2), damping coefficient 0.4 of the critical, $D=0.4$; curve (3), damping coefficient 0.7 of the critical, $D=0.7$; curve (4), damping coefficient equal to the critical, $D=1.0$.

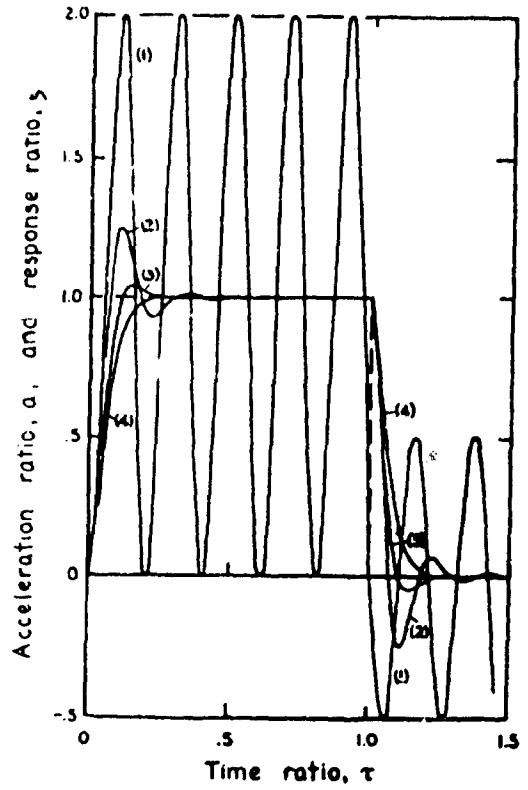

FIGURE 11. *Response to a square pulse of acceleration, dashed curve, of an accelerometer whose natural period is about equal to one-fifth of the duration of the pulse. $R=0.203$.*

Curve (1), damping coefficient zero, $D=0$; curve (2), damping coefficient 0.4 of the critical, $D=0.4$; curve (3), damping coefficient 0.7 of the critical, $D=0.7$ curve (4), damping coefficient equal to the critical, $D=1.0$.

V. References

[1] J. P. Den Hartog, Mechanical vibrations (McGraw-Hill Book Co., Inc., New York, N. Y., 1940).

[2] D. E. Weiss, Design and application of accelerometers, Proc. SESA, vol. IV, no. II, p. 89 (1947).

[3] W. P. Welch, A proposed new shock measuring instrument, Proc. SESA, vol. V, no. I, p. 39 (1947).

[4] J. M. Frankland, Effects of impact on simple elastic structures, Taylor Model Basin Rep. 481 (April 1942).

[5] M. A. Biot and R. L. Bisplinghoff, Dynamic loads on airplane structures during landing, NACA ARR No. 4H10 (Oct. 1944).

WASHINGTON, May 11, 1950.

APPENDIX C. LOAD CELL SPECIFICATIONS

1.0 SCOPE

This general specification covers the requirements of strain gage load cell transducers used to determine rocket motor thrust parameters during static testing.

2.0 REQUIREMENTS

2.1 Type

The transducer element shall be a four-arm bridge, bonded strain gage with split modular resistors for temperature and sensitivity compensation. The resistance bridge circuit shall be electro-mechanically coupled to a force sensing element.

The function shall be such that the applied force will vary the balance of the bridge in a manner to produce an electrical output signal proportional to the applied force.

2.2 Materials

The materials selected for fabrication of each transducer shall be satisfactory for use in direct water spray, temperatures from 0^{o} to 250^{o}F and highly corrosive or oxidizing atmospheres.

2.3 Physical Characteristics

The dimensions of the transducer shall be as small in size as possible without sacrificing elements of strength or function. The specification number shall be engraved on the transducer.

2.4 Electrical Connector

The connector CA 3102E-14S-6P/C22-F77 (silicon inserts) or equivalent shall provide a waterproof seal. The mating connector shall be supplied with the transducer.

The following pin connection shall apply:

Pin	Strain Gage Element
A	Positive output signal
B	Negative output signal
C	Negative excitation
D	Positive excitation
E	Shorted to B
F	Shorted to C

2.5 Calibration Certificate

Each transducer shall be accompanied by a calibration certificate which shall include the following information:

A. Identification information (including force range)
B. Linearity
C. Hysteresis
D. Repeatability
E. Combined effect
F. Sensitivity
G. Input and output resistances
H. Complete schematic of circuitry showing resistance values
I. Two resistor calibration steps and resistor values (25% FS-112, 200 ohms and 75% FS-37, 280 ohms).

3.0 OPERATION RATINGS AND ACCURACY

A. Range - 0 to 50,000 lb, 0 to 100,000 lb, 0 to 150,000 lb, (range and compression and/or tension to be specified at time of order)
B. Excitation - 10 volt nominal
C. Output - shall be standardized 3.00±3.5 millivolts full scale/volt excitation
D. Impedance characteristics - input 350±3.5 ohms at $77^{o}F \pm 3^{o}F$
output 350±3.5 ohms at $77^{o}F \pm 3^{o}F$
E. Linearity ±0.05% full scale maximum deviation from a straight line connecting the zero force and full scale force points

F. Hysteresis – ±0.03% FS maximum hysteresis loop deviation from linearity curve

G. Zero balance – ±1% FS

H. Repeatability – ±0.02% FS

I. Resolution – continuous

J. Combined effect ±0.10% FS (includes linearity, hysteresis, and repeatability errors)

K. Frequency response – ±3% or less of static value from direct current to 2,000 psi

L. 1^{o} side loading (off axis) – the error shall not exceed 0.10% of applied load

M. 3^{o} side loading (off axis) – the error shall not exceed 0.30% of applied load

N. Shock – to withstand a minimum of 30 g for 11±1 msec in each of the three major axes without damage

O. Force shock – to withstand a minimum of 10% of FS repeated force shocks to a maximum of five shocks without altering calibration data other than zero shift

P. Insulation resistance – not less than 1,000 megohms at 50 vdc

Q. Temperature and humidity

1. Thermal sensitivity – ±0.0007% FS/^{o}F from 0^{o} to 150^{o}F
2. Zero shift – ±0.0014% FS/^{o}F from 0^{o} to $+150^{o}$F
3. Humidity – meet this specification requirement at 100% humidity
4. Environmental – 0^{o} to $+250^{o}$F

R. Mechanical overload

1. A force overload of 200% shall not damage the transducer.
2. A force overload of 120% of full scale shall not prevent the transducer from meeting the operational ratings and accuracies other than zero shift.

S. The axial transducer shall be either compression or a tension-compression load cell, double bridge 350 ohms.